universität wien

DISSERTATION

Titel der Dissertation

„Quantum Mechanical Simulations of Defect Dynamics in DNA and Model Systems“

Verfasser

Felix Plasser, MSc

angestrebter akademischer Grad

Doktor der Naturwissenschaften (Dr. rer. nat.)

Wien, 2012

Studienkennzahl lt. Studienblatt:	A 091 419
Dissertationsgebiet lt. Studienblatt:	Chemie
Betreuer:	Univ.-Prof. i.R. Dr. Hans Lischka

Quantum Mechanical Simulations of Defect Dynamics in DNA and Model Systems

Felix Plasser
Institute for Theoretical Chemistry
University of Vienna

Vienna, 5 July 2012

Contents

List of Tables

List of Figures

Abstract

The purpose of this study was the examination of the dynamics of electronic defects introduced into DNA by UV irradiation or oxidative stress. Such defects may either lead to damage in the DNA structure or to deactivation without adverse effects, as determined by ultrafast processes. The simulation of such dynamics presents several challenges, related to the extended structure of DNA, the presence of non-adiabatic interactions between electronic and nuclear degrees of freedom, and complex open-shell electronic wavefunctions requiring accurate computation and a meaningful analysis. To allow for a reliable description of all these phenomena a systematic approach going from smaller model systems to realistic DNA fragments was chosen.

Simulations of charge transfer dynamics on smaller systems were performed to give a detailed examination of the influence of non-adiabatic effects and of environmental polarization. Already at this stage very interesting insight into the underlying physics of such processes could be obtained. Moreover, the applicability of the available methodologies could be assessed and several critical points were identified. Significant method development, concerned with state-averaged MCSCF gradients, with a local diabatization method for surface hopping dynamics, and with QM/MM simulations, was performed to address these points leading the way to more extended simulations. In addition an analysis procedure for excited states in systems with several coupled chromophores was devised and implemented.

By considering larger systems new insight into several complex phenomena could be obtained. Firstly, the processes leading to excimer formation in stacked π-systems were examined in the naphthalene dimer. It was found that a strongly stabilized coherent excited state was formed through interactions between exci-

tonic and CT configurations. Secondly, excitation energy transfer as well as proton coupled electron transfer in a hydrogen bonded base-pair analog were analyzed highlighting in particular non-adiabatic effects, which are involved in these processes. Finally, a realistic simulation of the absorbing states in DNA was performed, shedding new light onto several questions regarding excitonic and charge transfer character of these states that had been discussed controversially in literature.

Deutsche Zusammenfassung (German Abstract)

In dieser Arbeit wurde die Dynamik von elektronischen Defekten untersucht, die in DNA durch die Einwirkung von UV Strahlung oder oxidativem Stress entstehen können. Ultraschnelle dynamische Prozesse bestimmen, ob diese Defekte zu Schäden in der DNA führen oder ohne negative Effekte deaktiviert werden können. Die Simulation dieser Dynamik stellt wegen der ausgedehnten Struktur von DNA, wegen des Einflusses von nicht-adiabatischen Effekten, und wegen komplexer offenschaliger Wellenfunktionen der Elektronen einige Herausforderungen dar. Um all diese Phänomene zuverlässig beschreiben zu können, wurde ein systematischer Zugang gewählt, der von kleineren Modellsystemen zu realistischen DNA Fragmenten führte.

Durch Simulationen von Ladungstransfer Dynamik an kleineren Modellsystemen konnte der Einfluss von nicht-adiabatischen Effekten und Polarisation der Umgebung untersucht werden. In dieser Phase konnte schon viel interessante Einsicht in die zugrunde liegenden physikalischen Phänomene gewonnen werden. Darüberhinaus konnte die Anwendbarkeit von verschiedenen methodischen Strategien untersucht werden, wobei einige kritische Punkte identifiziert wurden. Ausgiebige Methodenentwicklung in Bezug auf SA-MCSCF Gradienten, lokale Diabatisierung für Surface Hopping Dynamik und QM/MM Dynamik wurde durchgeführt um diese Probleme zu behandeln und verlässliche Simulationen an größeren Systemen zu ermöglichen. Zusätzlich wurde eine Analyse von angeregten Zuständen in Systemen mit mehreren gekoppelten Chromophoren ausgearbeitet und implementiert.

Durch Rechnungen an größeren Systemen konnte Einsicht in verschiedene kom-

plexe Phänomene gewonnen werden. Zuerst wurden die Prozesse, die in π-stacks zur Bildung eines Excimers führen untersucht. Dabei konnte vor allem gezeigt werden, dass ein stark stabilisierter kohärenter Zustand durch Wechselwirkungen von Ladungstransfer- und excitonischen Konfigurationen entsteht. Weiters wurden in einem Modellsystem für Wasserstoff gebundene DNA Basenpaare Energietransfer und Protonen gekoppelte Elektronentransfer Prozesse untersucht, wobei vor allem der Einfluss von nicht-adiabatischen Effekten aufgezeigt werden konnte. Schließlich wurden realistische Simulationen der absorbierenden Zustände in DNA durchgeführt. Diese eröffnen neue Perspektiven zu verschiedenen Fragen bezüglich deren excitonischem und Ladungstransfer Charakter, die bisher in der Literatur kontrovers diskutiert wurden.

Chapter 1

Introduction

Deoxyribonucleic acid (DNA) is a basic building block of living cells, containing the genetic code. Electronic defects introduced into this structure by UV light or oxidative stress can potentially damage this macromolecule leading to mutations, genomic instability or carcinogenesis. [1, 2] After a defect is introduced, it is the initial molecular processes that determine whether damage or a deactivation without adverse effects occur. [2,3] Many open questions remain and conflicting results have been reported with respect to both photodynamics [3,4] and charge migration processes. [5] The purpose of this study is to shed new light onto these processes by means of quantum mechanical simulations at the molecular scale. A bottom-up approach was chosen where the relevant physical phenomena and computational methods were first explored on model systems before realistic simulations on DNA fragments were performed. Interesting insight could be obtained at every step along the way.

From a structural point of view, DNA is a closely packed double helix of aromatic bases connected via a backbone of phosphate and sugar (Figure 1.1). Intra- and interstrand interactions between DNA bases are crucial for determining the properties of the macromolecule. The precise evaluation of the involvement of these interactions for defects is still a major area of research.

The influence of UV light on isolated nucleobases is now fairly well understood thanks to a combined experimental and theoretical effort. [6–11] A major outcome

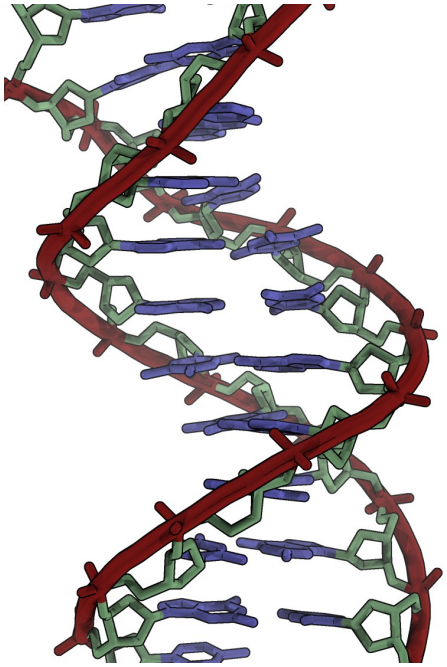

Figure 1.1: *Structure of the DNA double helix*

of this research is that all nucleobases have highly efficient channels allowing for internal conversion to the ground state before damage occurs. These processes occur on a picosecond time scale converting electronic excitation energy into vibrational energy, which can be quickly dissipated to the environment. These processes are mediated by specific strong distortions of the molecular geometry. An interesting point in this context is that minimal modifications of the molecular structure of these nucleobases may result in an inhibition of the decay processes leading to increased fluorescence quantum yields and thus a higher probability of adverse photochemical reactions. [7] Hence it has been argued that photostability may have been one of the decisive selection factors in early evolution determining the precise molecular structures of the nucleobases. [12] In single and double stranded DNA the excited state behavior is significantly altered and aside from monomer-like decay new transient signals with 10-100 ps lifetime and even nanosecond components were reported. [4, 13–16] Both, delocalization due to excitonic interactions [4, 15] and charge transfer between the bases [13, 17] are being considered as processes, which may be responsible for these changes in the dynamical behavior. A number of different results regarding these processes has been reported and many open

questions remain in this area.

Charge migration in DNA is an active area of research as well. One important question is whether charge transfer between bases occurs through incoherent hopping or through a coherent superexchange mechanism, or if both mechanisms are active at different length scales. [18,19] Moreover, the role of the environment and DNA conformation was intensively discussed. [20–22] A critical question in this context is whether electronic coupling is dominant leading to a delocalization of the charge or whether solvent reorganization localizes it and furthermore if polaron formation, i.e. large scale structural distortions induced by the charge, plays a role. [23–25]

Both areas discussed above are of highest interest. However, many open questions and contradicting results remain. The challenge from an experimental viewpoint is that the results (i.e. ultrafast transient decays) give only a very indirect indication of the actual processes. Moreover, the results reported strongly depended on the experimental technique and setup. From computation quite divergent results were reported as well, dependent on the model used. A particular problem in this context is that several approximations have to be made when considering processes of such complexity. However, without further investigations it is not quite clear what exact strategy to take and if some of the approximations may lead to artifacts. The purpose of this study was to examine the phenomena described above in a bottom-up approach. Starting with smaller model systems, a detailed investigation of the underlying physics and the applicability of existing computational models could be performed. Special challenges in this context were (i) an accurate and efficient description of the electronic structure, (ii) the inclusion of dynamical non-adiabatic interactions between electronic and nuclear degrees of freedom, (iii) the coupling to the environment, and (iv) a meaningful analysis of the electronic wavefunctions. In all of these areas significant methodological effort had to be carried out, pertaining specifically to (i) electronic energy gradients at the state-averaged multi-configurational self-consistent field level (Section 3.2), (ii) an accurate integration of the time-dependent electronic Schrödinger equation in the case of highly peaked non-adiabatic interactions (Sections 3.3 and 3.4), (iii) the computation of environmental polarization with respect to a charged molecule (Section 3.5), and (iv) an analysis of one-particle transition density matrices for

excitonic and charge transfer interactions (Section 3.6).

Aside from these methodological efforts interesting calculations have been performed on larger molecules with direct implications on processes occurring in DNA. Calculations on the naphthalene dimer gave new insight into excimer formation between π-stacked molecules, a process which was considered as a major factor increasing the decay times in stacked DNA bases (Section 3.6). [3, 26] Furthermore dynamics simulations on the 2-pyridone dimer, which can be seen as a model for a hydrogen bonded nucleobase pair, were carried out (Section 3.4). Through these simulations insight into excitation energy transfer and proton coupled electron transfer processes, which are also of highest interest in DNA (cf. Refs [4, 27]) could be obtained. Finally, a detailed investigation of the UV absorbing states in alternating DNA duplexes was performed (Section 3.7). This study may be a step toward resolving the conflicts regarding the importance of excitonic and charge transfer interactions, as outlined above.

Chapter 2

Theory and Computational Models

In this chapter a brief introduction into the underlying theory and applicable computational models will be given. A special focus will be laid on the areas discussed within the main part of this thesis: accurate and efficient electronic structure calculations, description of dynamic couplings between electronic and nuclear degrees of freedom, inclusion of environmental effects, and the analysis of electronic wavefunctions.

2.1 The Molecular Schrödinger Equation

In time-independent quantum mechanics the state of a system of N particles is described by its wave function $\Psi(r_1, ..., r_N)$ where $r_i = (x_i, y_i, z_i, \omega_i)$ denotes the three spatial and the spin coordinates of particle i. The physical meaning of the wave function lies in the fact that the probabilty distribution is given by the absolute square of the wave function, i.e. $\Psi^*(r_1, ..., r_N)\Psi(r_1, ..., r_N)$ gives the (differential) probability of finding particle 1 at r_1, particle 2 at r_2 etc.

The wave function is found as eigenfunction of the Hamiltonian operator $\widehat{H}$ by solving the Schrödinger equation

$$\widehat{H}(\Psi) = E\Psi \tag{2.1}$$

where the eigenvalue corresponds to the energy E.

The Hamiltonian operator is split into the kinetic energy operator $\widehat{T}$ related to the second spatial derivative of the wave function and the potential energy operator $\widehat{V}$, which in the case of no external potential corresponds to the potential energy $V(r_1, ..., r_N)$ resulting from interactions between the particles.

$$\widehat{H} = \widehat{T} + \widehat{V} \tag{2.2}$$

$$\widehat{T}(\Psi) = \sum_{i=1}^{N} -\frac{\hbar^2}{2m_i} \triangle_i \Psi \tag{2.3}$$

$$\widehat{V}(\Psi) = V(r_1, ..., r_N)\Psi \tag{2.4}$$

A stationary solution of the Schrödinger equation corresponds to a constant total energy. In this way it is the quantum mechanical equivalent of the energy conservation law.

The quantum-mechanical kinetic energy $\widehat{T}$ is inversely proportional to the mass of the particle m_i. In this way it can be understood that quantum effects become less important when mass increases. The Schrödinger equation is essential for describing electrons even qualitatively. Considering that the proton is about 2000 times heavier than the electron, quantum effects are less important for atomic nuclei and a classical treatment is often sufficient. However, in some cases it is important to consider zero point vibrations and tunneling phenomena.

In chemistry atomic units ($\hbar = 1$, $m_{electr.} = 1$, $e = 1$,...) are usually taken to simplify the expression. The considered particles are positively charged nuclei and negatively charged electrons. Let there be N nuclei at positions $(R_1, ..., R_N) = \mathbf{R}$ with charges Z_μ and masses m_μ ($\mu = 1, ..., N$) and n electrons at positions $(r_1, ..., r_n) = \mathbf{r}$. Then the kinetic energy operator can be rewritten according to (2.5). And the potential energy without external influence is given by (2.8).

$$\widehat{T} = \widehat{T}_{nuc} + \widehat{T}_{el} \tag{2.5}$$

$$\widehat{T}_{nuc} = \sum_{\mu=1}^{N} -\frac{1}{2m_\mu} \triangle_\mu \tag{2.6}$$

$$\widehat{T}_{el} = \sum_{i=1}^{n} -\frac{1}{2}\triangle_i \tag{2.7}$$

$$\begin{aligned} V(\mathbf{R},\mathbf{r}) &= V_{nn}(\mathbf{R}) + V_{ne}(\mathbf{R},\mathbf{r}) + V_{ee}(\mathbf{r}) := \\ &:= \sum_{\mu=1}^{N-1}\sum_{\nu=\mu+1}^{N}\frac{Z_\mu Z_\nu}{R_{\mu\nu}} - \sum_{\mu=1}^{N}\sum_{i=1}^{n}\frac{Z_\mu}{R_{\mu i}} + \sum_{i=1}^{n-1}\sum_{j=i}^{n}\frac{1}{r_{ij}} \end{aligned} \tag{2.8}$$

For the remaining discussion it is convenient to rewrite the Hamiltonian according to

$$\widehat{H} = \widehat{T}_{nuc} + \widehat{H}_{el} \tag{2.9}$$

$$\widehat{H}_{el} = \widehat{T}_{el} + \widehat{V} \tag{2.10}$$

2.1.1 The Born-Oppenheimer Approximation

Considering that $\widehat{H}_{el}$ is a Hermitian operator, it is known from functional analysis that an orthonormal basis of the Hilbert space of all possible wavefunctions can be constructed from its eigenfunctions. This basis $\mathcal{B}$ is also called the adiabatic basis and it holds that

$$\forall\phi(\mathbf{r};\mathbf{R}) \in \mathcal{B} : \widehat{H}_{el}(\phi(\mathbf{r};\mathbf{R})) = E_\phi(\mathbf{R})\phi(\mathbf{r};\mathbf{R}) \tag{2.11}$$

For the following derivation it is enough to know that this set exists. Finding such functions at fixed nuclear geometries $\mathbf{R}$ is one of the major areas in quantum chemistry. Except for very simple cases only approximative solutions exist and only a few eigenfunctions are computed. Different methods of doing that will be introduced in Section 2.2.

The total wave function $\Psi(\mathbf{R},\mathbf{r})$ is expressed in terms of these eigenfunctions as an expansion considering all nuclear geometries.

$$\Psi(\mathbf{R},\mathbf{r}) = \sum_{\phi\in\mathcal{B}} \chi_\phi(\mathbf{R})\phi(\mathbf{r};\mathbf{R}) \tag{2.12}$$

If this is inserted into the Schrödinger equation (2.1) with the definition of the Hamilton operator in (2.9) one gets the following result.

$$(\widehat{T}_{nuc} + \widehat{H}_{el} - E)(\sum_{\phi\in\mathcal{B}} \chi_\phi(\mathbf{R})\phi(\mathbf{r};\mathbf{R})) \equiv 0 \tag{2.13}$$

By applying the scalar product $\langle . \mid . \rangle$ (defined as an integration over all electronic coordinates after taking the complex conjugate of the first expression), equation (2.13) can be rewritten.

$$(2.13) \Leftrightarrow \forall \psi \in \mathcal{B} : \langle \psi | \, (\widehat{T}_{nuc} + \widehat{H}_{el} - E) \sum_{\phi \in \mathcal{B}} \chi_\phi \, |\phi\rangle = 0 \tag{2.14}$$

The three terms corresponding to the three operators can be separately evaluated by considering how the operators act on functions with different arguments.

$$\sum_{\phi \in \mathcal{B}} \langle \psi | \, (-E) \chi_\phi \, |\phi\rangle = -E \sum_{\phi \in \mathcal{B}} \chi_\phi \, \langle \psi \mid \phi \rangle = -E \chi_\psi \tag{2.15}$$

$$\sum_{\phi \in \mathcal{B}} \langle \psi | \, \widehat{H}_{el} \chi_\phi \, |\phi\rangle = \sum_{\phi \in \mathcal{B}} \chi_\phi E_\phi \, \langle \psi \mid \phi \rangle = E_\psi \chi_\psi \tag{2.16}$$

With the kinetic energy operator first the product rule with second derivatives has to be applied (2.18). Then the expression could be rewritten by using the quantum mechanical definition of the momentum as the spatial derivative of the wave function and then taking the velocity $\mathbf{v}$ (2.19).

$$\sum_{\phi \in \mathcal{B}} \langle \psi | \, \widehat{T}_{nuc} \chi_\phi \, |\phi\rangle = \tag{2.17}$$

$$= \widehat{T}_{nuc}(\chi_\psi) + \sum_{\phi \in \mathcal{B}} (\sum_{\mu=1}^{N} \frac{1}{m_\mu} \bigtriangledown_\mu \chi_\phi \, \langle \psi | \bigtriangledown_\mu |\phi\rangle + \langle \psi | \, \widehat{T}_{nuc} \, |\phi\rangle \, \chi_\phi) = \tag{2.18}$$

$$= \widehat{T}_{nuc}(\chi_\psi) - \sum_{\phi \in \mathcal{B}} (i\mathbf{v} \cdot \langle \psi | \bigtriangledown_{\mathbf{R}} |\phi\rangle + \langle \psi | \, \widehat{T}_{nuc} \, |\phi\rangle) \chi_\phi \tag{2.19}$$

With this the Schrödinger equation can be written as (cf. Ref. [28]):

$$\begin{gathered} \forall \psi \in \mathcal{B} : \widehat{T}_{nuc}(\chi_\psi(\mathbf{R})) + E_\psi(\mathbf{R}) \chi_\psi(\mathbf{R}) - \\ - \textstyle\sum_{\phi \in \mathcal{B}} (i\mathbf{v} \cdot \langle \psi | \bigtriangledown_{\mathbf{R}} |\phi\rangle + \langle \psi | \, \widehat{T}_{nuc} \, |\phi\rangle) \chi_\phi = E \chi_\psi(\mathbf{R}) \end{gathered} \tag{2.20}$$

The terms in the sum are called the "non-adiabatic couplings". They are usually very small. Neglecting them reduces (2.20) to isolated equations

$$\widehat{T}_{nuc}(\chi_\psi(\mathbf{R})) + E_\psi(\mathbf{R}) \chi_\psi(\mathbf{R}) = E \chi_\psi(\mathbf{R}) \tag{2.21}$$

This resembles the full Schrödinger equation (2.1) only that the potential V is replaced by an effective potential deriving from the electron energy. Nuclei move

on an isolated "adiabatic energy surface". This is called the Born-Oppenheimer approximation. Its validity and its exceptions will be discussed in Section 2.4. The significance of this is that the electronic (Eq. (2.11)) and nuclear (Eq. (2.21)) Schrödinger equations can be treated separately.

In a similar way translation and rotation can be separated from the nuclear degrees of freedom. In the general case there are 3 translational and 3 rotational degress of freedom and one only has to consider $3N-6$ internal coordinates (for a linear molecule $3N-5$, for an atom $3N-3=0$).

2.1.2 The Pauli Principle

A physically valid wave function does not only have to comply with the Schrödinger equation (2.1) but also with the Pauli principle. For electrons (and all other Fermions) this means that the wave function has to be antisymmetric with regard to the interchange of the coordinates of two electrons.

$$\phi(r_1,...,r_i,...,r_j,...,r_n) = -\phi(r_1,...,r_j,...,r_i,...,r_n) \tag{2.22}$$

An immediate consequence is that it is not possible that two electrons with the same spin are at the same position (i.e. $r_j = r_i$).

$$\phi(r_1,...,r_i,...,r_i,...,r_n) = -\phi(r_1,...,r_i,...,r_i,...,r_n) \tag{2.23}$$

$$\Rightarrow \phi(r_1,...,r_i,...,r_i,...,r_n) = 0 \tag{2.24}$$

2.1.3 Slater Determinants

In typical calculations the electronic wave function is expanded in terms of molecular orbitals (MO) $\omega_j(r_i)$ which are functions of the coordinates of only one electron. In the simplest case the wave function is expressed as a Hartree product. In this case electrons are statistically independent and have no effect on each other.

$$\phi(\mathbf{r}) = \omega_1(r_1)...\omega_n(r_n) = \prod_{i=1}^{n} \omega_i(r_i) \tag{2.25}$$

A more general form is considering a sum of products.

$$\phi(\mathbf{r}) = \sum_k d_k \prod_{i=1}^{n} \omega_{k(i)}(r_i) \tag{2.26}$$

With this general form wave functions that comply with the Pauli principle can be constructed as "Slater Determinants".

$$\begin{aligned}
\phi_0(\mathbf{r}) &= |\omega_1 \dots \omega_n\rangle := & (2.27)\\
&= \frac{1}{\sqrt{n!}} \begin{vmatrix} \omega_1(r_1) & \omega_2(r_1) & \dots & \omega_n(r_1) \\ \omega_1(r_2) & \ddots & & \omega_n(r_2) \\ \vdots & & \ddots & \vdots \\ \omega_1(r_n) & \dots & \dots & \omega_n(r_n) \end{vmatrix} = & (2.28)\\
&= \frac{1}{\sqrt{n!}} \sum_{\pi \in S_n} \mathrm{sgn}(\pi) \prod_{i=1}^{n} \omega_{\pi(i)}(r_i) & (2.29)
\end{aligned}$$

where in Eq. (2.29), the explicit definition of the determinant, S_n is the group of permutations and sgn(π) is +1 if π is even and -1 if π is odd. Wave functions of this sort are used with the Hartree-Fock method (Section 2.2.1).

2.1.4 Second Quantization

An efficient way to deal with Slater determinants is called Second Quantization (see e.g. Ref. [29]). In this approach for each spin-orbital ω_i a linear annihilation operator $\hat{a}_i$ is defined which removes the spin-orbital ω_i at the left of a Slater determinant if ω_i is present in the determinant and sets it equal to the "vacuum state", i.e. the zero vector, if not. In this way an n electron function is transformed into a Slater determinant which depends explicitely only on $n-1$ electronic coordinate vectors. For applying $\hat{a}_i$, first ω_i has to be moved to the left position which may change the sign of the determinant and second the orbital is removed

$$\begin{aligned}
\hat{a}_i|\omega_1 \dots \omega_{i-1}\omega_i\omega_{i+1} \dots \omega_n\rangle &= (-1)^{i-1}\hat{a}_i|\omega_i\omega_1 \dots \omega_{i-1}\omega_{i+1} \dots \omega_n\rangle := & (2.30)\\
&:= (-1)^{i-1}|\omega_1 \dots \omega_{i-1}\omega_{i+1} \dots \omega_n\rangle & (2.31)
\end{aligned}$$

The adjoint operator of $\hat{a}_i$ is written $\hat{a}_i^\dagger$. According to the definition of an adjoint operator $\hat{a}_i^\dagger$ removes an orbital from the bra. (The bra is the vector ready to form a scalar product with a ket or equivalently it could be seen as a linear functional, i.e. an element of the dual space.)

$$\begin{aligned} \langle \omega_1 \dots \omega_{i-1}\omega_i\omega_{i+1} \dots \omega_n | \hat{a}_i^\dagger &:= \langle \hat{a}_i(\omega_1 \dots \omega_{i-1}\omega_i\omega_{i+1} \dots \omega_n)| = & (2.32) \\ &= (-1)^{i-1}\langle \omega_1 \dots \omega_{i-1}\omega_{i+1} \dots \omega_n| & (2.33) \end{aligned}$$

By considering the values of the matrix elements it can be shown that annihilating an orbital in the bra is equivalent to creating an orbital in the ket. Hence $\hat{a}_r^\dagger$ acting on a ket is called the creation operator.

$$\hat{a}_r^\dagger \left|\omega_1 \dots \omega_n\right\rangle = \left|\omega_r\omega_1 \dots \omega_n\right\rangle \tag{2.34}$$

In this way excitations can be conveniently represented. For example the determinant $|\phi_i^r\rangle$ where the occupied orbital ω_i is replaced by the unoccupied orbital ω_r can be written as

$$|\phi_i^r\rangle := \left|\omega_1 \dots \omega_{i-1}\omega_r\omega_{i+1} \dots \omega_n\right\rangle = \hat{a}_r^\dagger \hat{a}_i \left|\phi_0\right\rangle \tag{2.35}$$

The order of the operators is decisive.

$$\begin{aligned} \hat{a}_i\hat{a}_r^\dagger \left|\phi_0\right\rangle = \hat{a}_i \left|\omega_r\omega_1 \dots \omega_{i-1}\omega_i\omega_{i+1} \dots \omega_n\right\rangle = & \quad (2.36) \\ = -\hat{a}_i \left|\omega_i\omega_1 \dots \omega_{i-1}\omega_r\omega_{i+1} \dots \omega_n\right\rangle = -\left|\phi_i^r\right\rangle & \end{aligned}$$

This is an example of the anticommutator relations which can be used to derive the properties of determinants without having to consider their explicit form, cf. [29].

A general definition of the annihilation operator applied to a wave function $\phi(\mathbf{r})$, that will be used below, can be given as [30]

$$\hat{a}_i\phi(\mathbf{r}) = \int \omega_i(r_1)\phi(r_1, r_2, \dots, r_n)dr_1 \tag{2.37}$$

For practical calculations it is convenient to consider spin averaged excitation operators [31]

$$\hat{E}_{rs} = \hat{a}_{r\alpha}^\dagger \hat{a}_{s\alpha} + \hat{a}_{r\beta}^\dagger \hat{a}_{s\beta} \tag{2.38}$$

i.e. one averages over orbitals with the same spatial form but opposite spin. The spin averaged double excitation and deexcitation operator is defined as

$$\hat{e}_{rstu} = \hat{E}_{rs}\hat{E}_{tu} - \hat{E}_{ru}\delta_{ts} \tag{2.39}$$

2.1.5 Density Matrices

An essential step for the calculation of molecular properties is the reduction of the information to only the necessary part, which can be achieved by computing reduced density matrices. For example the one-particle transition density matrix between two wave functions $\phi(\mathbf{r})$ and $\psi(\mathbf{r})$ is defined as

$$\gamma_1^{\phi\psi}(r_1', r_1) = \int^{n-1} \phi^*(r_1', r_2, \ldots, r_n)\psi(r_1, r_2, \ldots, r_n)dr_2 \ldots dr_n \tag{2.40}$$

and if $\phi(\mathbf{r}) = \psi(\mathbf{r})$, this is called the density matrix of $\phi(\mathbf{r})$. The matrix element of this function with respect to an orthonormal one-electron basis set $\{\omega_i\}$ is obtained as

$$P_{ij}^{\phi\psi} := \left\langle \omega_i \mid \gamma_1^{\phi\psi} \mid \omega_j \right\rangle_1 = \int \omega_i(r_1')^* \int \gamma_1(r_1', r_1)^{\phi\psi}\omega_j(r_1)dr_1dr_1' = \tag{2.41}$$

by inserting Eq. (2.40) this amounts to

$$= \int \omega_i(r_1')^* \int \left(\int^{n-1} \phi^*(r_1', \ldots, r_n)\psi(r_1, \ldots, r_n)dr_2 \ldots dr_n \right) \omega_j(r_1)dr_1dr_1' = \tag{2.42}$$

the integrals can be rearranged to yield

$$= \int^{n-1} \left(\int \omega_i(r_1')\phi(r_1', \ldots, r_n)dr_1' \right)^* \left(\int \omega_j(r_1)\psi(r_1, \ldots, r_n)dr_1 \right) dr_2 \ldots dr_n \tag{2.43}$$

If Eq. (2.37) is inserted into this expression, the following result for the one-particle density matrix in second quantization is obtained.

$$= \int^{n-1} \left(\hat{a}_i\phi(\mathbf{r})\right)^* \hat{a}_j\psi(\mathbf{r})dr_2 \ldots dr_n = \langle \hat{a}_i\phi \mid \hat{a}_j\psi \rangle \tag{2.44}$$

In summary the one-particle density matrix can be rewritten as

$$P_{ij}^{\phi\psi} = \left\langle \phi \mid \hat{a}_i^\dagger \hat{a}_j \mid \psi \right\rangle \tag{2.45}$$

which provides a straight forward way of evaluating these expressions without any explicit integrations.

In practice one usually considers the spin-averaged one particle (transition) density matrix which is defined using the operators from Eq. (2.38)

$$D_{ij}^{\phi\psi} = \left\langle \phi \mid \hat{E}_{ij} \mid \psi \right\rangle \tag{2.46}$$

A state density matrix $\gamma_1^{\phi\phi}(r_1', r_1)$ yields a Hermitian operator with the scalar product of Eq. (2.41). Hence an orbital basis $\{\tilde{\omega}_i\}$ exists in which its matrix representation is diagonal

$$\tilde{D}_{ij}^{\phi\phi} = \left\langle \tilde{\omega}_i \mid \gamma_1^{\phi\phi} \mid \tilde{\omega}_j \right\rangle_1 = \delta_{ij} n_i \tag{2.47}$$

The $\tilde{\omega}_i$ in Eq. (2.47) are called the natural orbitals (NOs) with occupations n_i. The occupations can range from zero to two for spatial orbitals (and from zero to one for spin-orbitals).

For a transition density matrix, which is not symmetric, such a decomposition does not exist in general. For this reason, the concept of natural transition orbitals has been introduced. [32–34] In this case the transition density matrix $\mathbf{D}^{\phi\psi}$ ($\phi \neq \psi$) is decomposed by a singular value decomposition (more information about this will be given in Section 3.6).

Aside from the one-particle reduced density matrix also higher order density matrices can be computed. In particular the spin-averaged two particle (transition) density matrix

$$d_{ijkl}^{\phi\psi} = \langle \phi \mid \hat{e}_{ijkl} \mid \psi \rangle \tag{2.48}$$

plays an important role. For example it can be shown that the total energy is already completely determined by the one- and two-particle density matrices. Using the definitions

$$h_{ij} = \left\langle \omega_i(r_1) \mid \widehat{T}_{el} + \widehat{V}_{ne} \mid \omega_j(r_1) \right\rangle_1 \tag{2.49}$$

$$g_{ijkl} = \left\langle \omega_i(r_1)\omega_k(r_2)) \mid \frac{1}{r_{12}} \mid \omega_j(r_1)\omega_l(r_2) \right\rangle_2 \tag{2.50}$$

the following relation holds

$$E_\phi \delta_{\phi\psi} = \mathsf{tr}(\mathbf{h}\mathbf{D}^{\phi\psi}) + \frac{1}{2}\mathsf{tr}(\mathbf{g}\mathbf{d}^{\phi\psi}) \tag{2.51}$$

An interesting point in this context is that Hohenberg and Kohn have shown that all information is in fact already contained in the electron density of a state ϕ: $\rho(r) = \gamma^{\phi\phi}(r, r)$ (cf. Section 2.2.3). [35] However, as opposed to Eq. (2.51) the exact functional for computing the energy out of only the electron density is not known.

2.1.6 The Generalized Hellmann-Feynman Theorem

The Hellmann-Feynman theorem is an essential tool for computing electronic energy gradients. In the case of practical calculations it takes the following form.

One considers a normalized wave function $\phi_{\mathbf{R}}(\mathbf{s})$ at a nuclear geometry $\mathbf{R}$, which is dependent on a set of parameters $\mathbf{s} = (s_1, \ldots, s_p)$. [1] The energy at a geometry $\mathbf{R}$, considering an arbitrary choice of parameters $\mathbf{s}$ is computed as

$$\tilde{E}_{\mathbf{R}}(\mathbf{s}) = \left\langle \phi_{\mathbf{R}}(\mathbf{s}) \mid \widehat{H}_{el,\mathbf{R}} \mid \phi_{\mathbf{R}}(\mathbf{s}) \right\rangle \tag{2.52}$$

It could also be given as a function of the density matrices (cf. Eq. (2.51)), which are in turn dependent on $\mathbf{s}$.

$$\tilde{E}_{\mathbf{R}}(\mathbf{s}) = \mathsf{tr}(\mathbf{hD}(\mathbf{s})) + \frac{1}{2}\mathsf{tr}(\mathbf{gd}(\mathbf{s})) \tag{2.53}$$

Next one considers a rule $\mathbf{s}_{\mathbf{R}}$ to determine the wave function parameters at a geometry $\mathbf{R}$ (in practice this means an electronic structure calculation). In the special case of a variational method, $\mathbf{s}_{\mathbf{R}}$ is chosen according to

$$\tilde{E}_{\mathbf{R}}(\mathbf{s}_{\mathbf{R}}) = \min_{\mathbf{s}} \left(\tilde{E}_{\mathbf{R}}(\mathbf{s}) \right) \tag{2.54}$$

Assuming that this minimum exists and that $\tilde{E}_{\mathbf{R}}(\mathbf{s})$ is differentiable, it follows from this condition that

$$\frac{\partial}{\partial s_i} \tilde{E}_{\mathbf{R}}(\mathbf{s}_{\mathbf{R}}) = 0; i = 1, \ldots, p \tag{2.55}$$

With this rule for determining $\mathbf{s}_{\mathbf{R}}$ (which may or may not be variational) the geometry dependent potential energy is defined as

$$E_{\mathbf{R}} = \tilde{E}_{\mathbf{R}}(\mathbf{s}_{\mathbf{R}}) \tag{2.56}$$

The partial derivative of this function with respect to a nuclear coordinate R_j is determined according to the chain rule

$$\frac{\partial}{\partial R_j} E_{\mathbf{R}} = \frac{\partial}{\partial R_j} \tilde{E}_{\mathbf{R}}(\mathbf{s}_{\mathbf{R}}) + \sum_{i=1}^{p} \frac{\partial}{\partial s_i} \tilde{E}_{\mathbf{R}}(\mathbf{s}_{\mathbf{R}}) \frac{\partial}{\partial R_j} \mathbf{s}_{\mathbf{R}} \tag{2.57}$$

[1] It may be noted that the wave function depends in fact on three different sets of variables, the electronic coordinates $\mathbf{r}$, the nuclear coordinates $\mathbf{R}$ and the parameters $\mathbf{s}$. In the present context it seems convenient to consider $\mathbf{r}$ only implicitly and write $\mathbf{R}$ as a subscript. However, the wavefunction might also simply be written as $\phi(\mathbf{r}; \mathbf{R}; \mathbf{s})$.

The first term may be rewritten in the form of Eq. (2.53) by using density matrices

$$\frac{\partial}{\partial R_j} E_{\mathbf{R}} = \mathsf{tr}\left(\mathbf{h}^{(R_j)}\mathbf{D}(\mathbf{s_R})\right) + \frac{1}{2}\mathsf{tr}\left(\mathbf{g}^{(R_j)}\mathbf{d}(\mathbf{s_R})\right) + \sum_{i=1}^{p} \frac{\partial}{\partial s_i}\tilde{E}_{\mathbf{R}}(\mathbf{s_R})\frac{\partial}{\partial R_j}\mathbf{s_R} \quad (2.58)$$

where the symbols $\mathbf{h}^{(R_j)}$ and $\mathbf{h}^{(R_j)}$ denote the integrals defined in Eqs (2.49) and (2.50), respectively, only that a derivative with respect to R_j is taken. [36] Using this notation the two terms comprising the electronic energy gradient can be easily identified: (i) the change of the underlying potential evaluated at the wave function parameters $\mathbf{s_R}$ and (ii) the influence of the wave function response $\partial \mathbf{s_R}/\partial R_j$ to the perturbation. The essence of the generalized Hellmann-Feynman theorem is that for a variationally determined wavefunction the second term in Eq. (2.58) vanishes according to Eq. (2.55) leaving only the first term, which can be evaluated fairly easily. Moreover, for a wavefunction where a part of the parameters are determined in a variational way, only the wavefunction response with respect to the other parameters has to be determined. A practical evaluation of this expression in the case of the SA-MCSCF method will be presented in Section 3.2.

2.2 Electronic Structure Methods

A large number of electronic structure methods with different merits and shortcomings have been formulated so far. The main consideration in this context is a compromise between accuracy and computational efficiency. But also many other considerations come into play, for example variational or non-variational optimization of the wavefunction, extensivity with respect to an increase in system size, ease of computing properties and gradients, availability of excited states, and applicability to open-shell systems. The main types of methods will be introduced here. In Section 3.1 they will be revisited from a somewhat more practical viewpoint.

2.2.1 The Hartree-Fock Method

The Hartree-Fock (HF) ansatz serves as a conceptual basis for a large number of quantum chemical methods. In HF the wave function $\phi_0(\mathbf{r})$ is written as a single

Slater determinant. With this construction the energy in terms of MO integrals is given according to

$$
\begin{aligned}
E_0 &= \left\langle \phi_0(\mathbf{r}) \mid \widehat{T}_{el} + V_{ne}(\mathbf{R},\mathbf{r}) + V_{ee}(\mathbf{r}) \mid \phi_0(\mathbf{r}) \right\rangle = && (2.59)\\
&= \sum_{a\in\mathcal{O}} \left\langle a(r_1) \mid -\frac{1}{2}\triangle_1 - \sum_{\mu=1}^{N} \frac{Z_\mu}{R_{\mu 1}} \mid a(r_1) \right\rangle + && (2.60)\\
&+ \frac{1}{2} \sum_{a,b\in\mathcal{O}} \left(\left\langle a(r_1)b(r_2)) \mid \frac{1}{r_{12}} \mid a(r_1)b(r_2) \right\rangle - \left\langle a(r_1)b(r_2) \mid \frac{1}{r_{12}} \mid b(r_1)a(r_2) \right\rangle \right)
\end{aligned}
$$

where integration in the braket is performed over the respective coordinates and $\mathcal{O}$ is the set of occupied orbitals. The expression can be derived by inserting the explicit form of the Slater determinant (Eq. (2.29)) into Eq. (2.59) or with the formalism of Second Quantization (cf. Section 2.1.4). [29, 37]

The one-electron terms in Eq. (2.60) are the kinetic energy of the electron and the electrostatic interaction of the electron distribution with the nuclei. The first two-electron term is called the Coulomb integral. It gives the average repulsion between the electron clouds and raises the HF energy. The second term, the exchange integral, is a quantum mechanical term that arises from the antisymmetry of the wave function (c.f. Sec. 2.1.2). It is non-zero only if the orbitals a and b are of the same spin. The major source of error in HF theory is that the Coulomb integral overestimates interelectronic repulsion since electrons are unphysically kept from moving out of each others' way. This energy increase is an example of the general fact that according to the variational principle the energy expectation value of any trial function has to be greater or equal to the true ground state energy.

The most common way of solving the HF equations is by expressing the MOs as linear combinations of atomic orbitals. This leads to the Roothaan-Hall equations. The problem is converted into a non-linear generalized eigenvalue equation which produces the MOs that will give the lowest possible HF energy for the specific basis set. [29, 37] According to the variational principle this should be the best estimate.

2.2.2 Post Hartree-Fock Methods

Several methods have been developed for producing wave functions beyond the Hartree-Fock approximation. The main types are configuration interaction, many-body perturbation theory, and coupled cluster. However, the boundaries are not always strict and different approaches may lead to the same final equations. Moreover combinations can be applied. [29]

Configuration Interaction and Multi-Configuration Self-Consistent Field

In configuration interaction (CI) the wave function is formed as a linear combination of several determinants usually based on a HF reference function (2.61). Let $\mathcal{O}$ and $\mathcal{U}$ denote the (ordered) sets of occupied and unoccupied orbitals, and $\phi_{ab\ldots}^{rs\cdots}(\mathbf{r})$ the excited determinants where electrons have been moved from orbitals $a, b, \ldots$ to orbitals $r, s, \ldots$. Then the CI wavefunction is given as

$$\phi(\mathbf{r})_{CI} = \phi_0(\mathbf{r}) + \sum_{a\in\mathcal{O}}\sum_{r\in\mathcal{U}} d_a^r \phi_a^r(\mathbf{r}) + \sum_{a<b\in\mathcal{O}}\sum_{r<s\in\mathcal{U}} d_{ab}^{rs}\phi_{ab}^{rs}(\mathbf{r}) + \ldots \tag{2.61}$$

The objective of CI is finding the linear expansion coefficients $d_{ab\ldots}^{rs\cdots}$ which minimize the energy and thus give the optimal result according to the variation principle. They are determined from the eigenvector of the CI matrix (i.e. the matrix collecting the matrix elements between the different Slater determinants) with the lowest eigenvalue (where the eigenvalue corresponds to the energy). Excited states are constructed from eigenvectors corresponding to higher eigenvalues.

Rather than in the basis of Slater determinants, CI may also be performed with configuration state functions (CSF). CSFs are linear combinations of Slater determinants that are already eigenfunctions of the spin operator, i.e. singlets, triplets, etc. The advantage of this procedure is that fewer terms have to be considered. However, the interactions between individual CSFs are more complicated than between simple determinants, requiring new strategies that will be discussed below.

Full CI considers the whole expansion (2.61) which goes until all the electrons are in virtual orbitals. It is the full solution for the Schrödinger equation in a given

one electron basis set. n_{CI} the number of considered determinants corresponds to all possibilities of placing n_{el} electrons into n_{orb} orbitals. It can be approximately given by the binomial coefficient

$$n_{CI} \approx \binom{n_{orb}}{n_{el}} \tag{2.62}$$

This means that the effort for a full CI calculation scales exponentially with the system size. Therefore in practical calculations Eq. (2.61) is usually truncated after a given number of excitations (most commonly two leading to the CISD method). The variational nature of the CI wavefunction leads to the fact that gradients and other molecular properties can be evaluated rather easily as explained in Section 2.1.6. However, a problem with the CI approach is a lack of extensivity. This follows from the fact that any given truncation will recover a larger part of the correlation energy in a smaller system than in a larger one. [29] A way to explain this is to consider for example that CISD is full CI for a two-electron system but truncated CI for a larger system and that there is no reason to assume that the coefficients for higher excitations should be exactly zero. And it can be understood that just for statistical reasons it is expected that higher excitations play a more important role in larger systems. An improvement is the Davidson correction which estimates the effect of quadruple excitations based on the weight of the HF determinant in the expansion. Moreover, a number of approximately extensive variations of CI (possibly in its multi-reference formulation, see below) have been suggested. [38]

CI based on a single reference determinant can only be carried out under the assumption that HF provides a good reference wavefunction. This is not the case when quasi degenerate orbitals are present or in the case of strongly distorted molecular geometries (see also Section 3.1). In such a case the orbitals can be optimized by the mutli-configuration self-consistent field (MCSCF) method, cf. e.g. Refs [31, 39]. In this case orbital and CI coefficients are optimized simultaneously for a number of active determinants or CSFs with different orbital occupations. In particular the complete active space SCF (CASSCF) method has gained popularity. In this method all configurations are considered that can be constructed when a fixed number of active electrons is arbitrarily distributed over a fixed number of active orbitals. The remaining orbitals are either kept doubly occupied or un-

occupied, respectively. The advantage of this approach is that all active orbitals are treated on the same level and rotations between these orbitals do not affect the electronic wavefunction. The disadvantage is that a large number of unfavorable highly excited configurations are considered in such a setup, which means that the expansion is larger than it would have to be. To overcome this problem the excitation number may be restricted yielding the restricted active space SCF (RASSCF) method. Alternatively occupation restrictions based on orbital groups may be performed. [31]

MCSCF may be carried out for a single state or in its state-averaging formulation (SA-MCSCF). In the latter case the orbitals are chosen in such a way as to minimize the average energy of several roots of the CI matrix. This method can provide a balanced description of several excited states and provides a good way for computing non-adiabatic couplings (Eq. (2.20)). [40] However, it should be noted that each individual state is described more accurately (at least in a variational sense) when only this one state is considered in the MCSCF procedure.

To add dynamical electron correlation to an MCSCF wavefunction, the MCSCF active space can be considered as a reference space out of which single and double excitations are allowed. This yields the multi-reference (MR)-CI method. MR-CI may either be carried out in its full uncontracted form [41] or by internally contracting the double excitations. [42] Electronic energy gradients and non-adiabatic couplings as needed for this work have only been reported in the first case. [36, 40]

For uncontracted MR-CI it is particularly suitable to use a CSF expansion to reduce the dimension of the CI vector. In this case a highly efficient, non-intuitive way of computing the coupling elements between the CSFs is based on the graphical unitary group approach (Figure 2.1). The possible occupation and spin states for each orbital are collected as nodes (also called "distinct rows") in a directed graph (the "distinct row table", DRT). CSFs are represented as walks from the bottom to the top in this graph. Interestingly, this construction allows for a highly efficient evaluation of the coupling elements between the CSFs through considering the shapes of the loops. [43] In practice the algorithm is carried out without specific interaction by the user. However, some understanding of this construction is helpful when designing specific occupation restrictions in the wavefunctions. Moreover, parallel MR-CI calculations require some understanding of the under-

lying DRT structure if efficient load balancing over a large number of computing nodes is to be carried out. [44]

Many-body perturbation theory

Many-body perturbation theory is usually carried out with the formalism introduced by Møller and Plesset (MP). [45] In this case the 0th order Hamiltonian is the HF Hamiltonian $\widehat{H}_0$, defined according to

$$\widehat{H}_0 = \sum_{i=1}^{n} \hat{f}_i \tag{2.63}$$

where $\hat{f}_i$ is the Fock operator acting on electron i. The perturbation is defined as the difference to the correct Hamiltonian. The eigenfunctions $\widehat{H}_0$ are all the determinants that can be formed from HF orbitals. The exact many body solutions can be expressed in this basis and no extra differential equations have to be solved. Because of Brillouin's theorem matrix elements between the HF determinant and singly excited determinants are zero. With only one- and two-electron operators also all the matrix elements to triply and higher excited determinants are zero. Therefore the interactions with doubly excited determinants are the only ones directly interacting with the HF reference.

The 0th order MP energy is the sum of the orbital energies, in 1st order the correct HF energy (2.60) is obtained. The first correction is in the second order leading to the popular MP2 method. According to the considerations above it can be shown that the perturbation energy $E_0^{(2)}$ is given as a quadruple sum over two-electron MO integrals (2.64) (where ε_i is the energy of orbital i). [29]

$$E_0^{(2)} = \frac{1}{4} \sum_{\substack{a,b \in \mathcal{O} \\ r,s \in \mathcal{U}}} \frac{\left| \left\langle a(r_1)b(r_2) \mid \frac{1}{r_{12}} \mid r(r_1)s(r_2) - s(r_1)r(r_2) \right\rangle \right|^2}{\varepsilon_a + \varepsilon_b - \varepsilon_r - \varepsilon_s} \tag{2.64}$$

This equation gives some qualitative insight into electron correlation. Firstly, it can be seen that correlation plays a more important role if the occupied and virtual orbitals are close in energy. Furthermore, two occupied orbitals a and b should of course have a stronger contribution to the correlation energy if the Coulomb

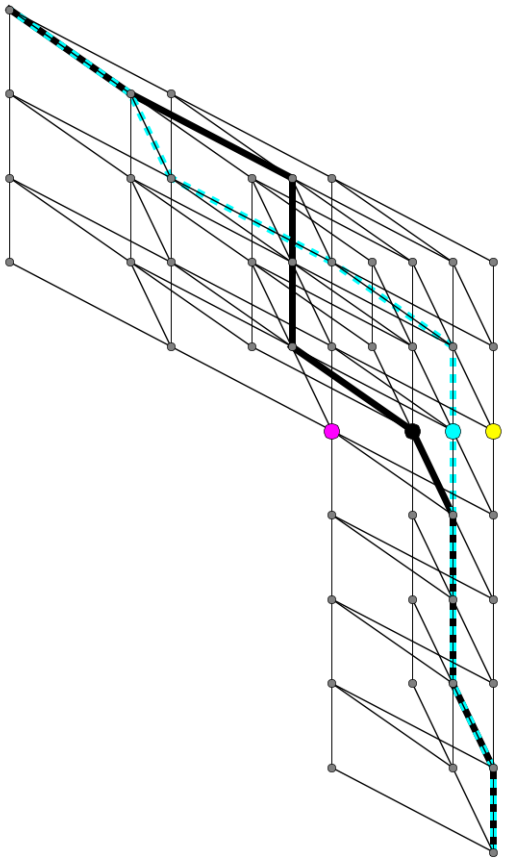

Figure 2.1: *Depiction of a distinct row table as used in the graphical unitary group approach to compute coupling elements in MR-CI wavefunctions. Two exemplary CSFs are shown as walks in this graph (black, cyan). The w, x, y, and z nodes connecting the internal and external parts of the DRT are shown in magenta, black, cyan, and yellow, respectively.*

repulsion between them is strong. Finally, it may be observed that the correlating virtual orbitals r and s have to be in close spatial proximity to their occupied counterparts.

Evaluation of the expression (2.64) can be sped up by using the resolution of the identity (RI) approximation. The idea of this approach is to express the two electron integrals in an auxiliary basis set. The resulting RI-MP2 method cuts down on computation time and storage needs. It allows for an efficient evaluation of energies, gradients and other properties. [37, 46]

Coupled Cluster Theory

Coupled cluster (CC) theory is usually formulated by means of the cluster operator $\widehat{\mathcal{T}}^{(m)}$ which in the formalism of Second Quantization may be written as

$$\begin{aligned} \widehat{\mathcal{T}}^{(m)} &= \hat{1} + \widehat{\mathcal{T}}_1 + \ldots + \widehat{\mathcal{T}}_m && (2.65)\\ \widehat{\mathcal{T}}_1 &= \sum_{a\in\mathcal{O}}\sum_{r\in\mathcal{U}} b_a^r \hat{a}_r^\dagger \hat{a}_a && (2.66)\\ \widehat{\mathcal{T}}_2 &= \frac{1}{4}\sum_{a,b\in\mathcal{O}}\sum_{r,s\in\mathcal{U}} b_{ab}^{rs} \hat{a}_r^\dagger \hat{a}_s^\dagger \hat{a}_b \hat{a}_a \\ &\ldots \end{aligned}$$

with parameters $b_{ab\ldots}^{rs\ldots}$ called the cluster amplitudes.

Using $\widehat{\mathcal{T}}^{(m)}$ CI with m excitations could be expressed according to Eq. (2.67). By contrast, in the CC ansatz the exponential of the operator is taken (2.68).

$$\begin{aligned} \phi(\mathbf{r})_{CI} &= \widehat{\mathcal{T}}^{(m)}\phi_0(\mathbf{r}) && (2.67)\\ \phi(\mathbf{r})_{CC} &= \exp(\widehat{\mathcal{T}}^{(m)})\phi_0(\mathbf{r}) && (2.68) \end{aligned}$$

Through this construction higher excitations are implicitly considered without the need of additional parameters.

$$\exp(\mathcal{T}_1) = 1 + \sum_{a\in\mathcal{O}}\sum_{r\in\mathcal{U}} b_a^r \hat{a}_r^\dagger \hat{a}_a + \frac{1}{2}\sum_{a,b\in\mathcal{O}}\sum_{r,s\in\mathcal{U}} b_a^r b_b^s \hat{a}_r^\dagger \hat{a}_s^\dagger \hat{a}_b \hat{a}_a + \ldots \quad (2.69)$$

These disconnected excitations are intended to represent the effect of statistically independent combinations of lower excitations. An advantage of this construction

is that the CC method is extensive. However, the CC equations cannot be practically solved in a variational approach, which results in the condition that the evaluation of gradients and properties is more involved.

CCS, CCSD, CCSDT, ... denote cluster expansions up to $\widehat{\mathcal{T}}_1, \widehat{\mathcal{T}}_2, \widehat{\mathcal{T}}_3, \ldots$. An approximation to these are the CCS(D), CCSD(T), ... approaches where the last order is treated in a perturbative manner. Excited states of these methods can be computed as response properties with the equation of motion formalism. [47]

An alternative approach, used for the computation of excitation energies, is in the CC2, CC3, ... series. In the CC2 approach double excitations are approximated whereas single excitations are fully retained. This approach, especially with the RI-approximation, allows for the computation of excited states of large molecules at feasible computational effort while still including some correlation energy. [48,49] A closely related approach is provided by the algebraic diagrammatic construction to second order (ADC(2)). [50] In spite of giving similar results in many cases, it is a conceptual advantage of ADC(2) with respect to CC2 that the response function is obtained as an eigenvector of a Hermitian matrix. For this reason ADC(2) is more stable in the case of intersecting excited states (no artificial complex roots are obtained) and more efficient for the calculation of properties (no eigenvalues of the transposed matrix have to be computed). [51]

2.2.3 Density Functional Theory

Compared to the wavefunction based methods just mentioned, density functional theory (DFT) considers only the electron density $\rho(r)$. Whereas the wavefunction depends on 3 spatial (+1 spin) coordinates for every electron, the density is described by only these 3(+1) coordinates in total. This allows for a significant speed up of the procedure.

A functional is a "function of a function" or more precisely a mapping from a vector space into the underlying field. The functional derivative of a functional $A[.]$ at Ψ (if it exists) can be defined as the linear functional $\langle \delta A[\Psi]|$ which fulfills the following relation.

$$\frac{d}{dt} A[\Psi + t\Phi]_{t=0} = \langle \delta A[\Psi] \mid \Phi \rangle \tag{2.70}$$

In wave mechanics the energy expectation value of a normalized wave function $\Psi(\mathbf{r})$ is given by the functional $E_W[\Psi]$ (below). The variation principle (2.72) states that for any given trial function this expectation value is larger than the true ground state energy E_0. Finding the ground state wave function can be considered as a minimization of $E_W[\Psi]$ under the constraint of $\langle \Psi \mid \Psi \rangle = 1$. This is done by searching for a Ψ with a vanishing functional derivative of the Lagrangian (2.73). The Lagrangian parameter E gives the energy expectation value.

$$E_W[\Psi] = \left\langle \Psi \mid \widehat{H}_{el} \mid \Psi \right\rangle, \langle \Psi \mid \Psi \rangle = 1 \tag{2.71}$$

$$\forall \Psi : E_W[\Psi] > E_0 \tag{2.72}$$

$$\langle \delta \left(E_W[\Psi] + E(\langle \Psi \mid \Psi \rangle - 1) \right) | = \langle 0 | \tag{2.73}$$

Hohenberg and Kohn [35] showed that similar relations also hold for the density $\rho(r)$. Their first theorem states that for a given stationary electron density there is only one possible external potential. The number of electrons is determined by the integral of the density. Together that means that with a given density the Hamiltonian and hence its lowest eigenvalue, the ground state energy, are clearly determined. Then a functional $E_D[\rho]$ must exist which gives the ground state energy of a given electron density ρ containing n electrons (2.74). The second Hohenberg-Kohn theorem states that there is a variational principle for the density with a given external potential $v(r)$ (2.75). And again a Lagrangian can be formulated (2.76). The Lagrangian parameter turns out to be the chemical potential μ. [52]

$$E_v[\rho], \int \rho(r) d^3r = n \tag{2.74}$$

$$\forall \rho : E_v[\rho] > E_0 \tag{2.75}$$

$$\left\langle \delta \left(E_v[\rho] + \mu(\int \rho(r) d^3r - n) \right) \right| = \langle 0 | \tag{2.76}$$

The difficulty of the DFT approach is that the functional E_v is not known and can only be approximated. It is straight forward to define functionals related to the external potential $V_{ext}[\rho]$ and interelectronic Coulomb repulsion of uncorrelated electrons $J[\rho]$. [52]

$$V_{ext}[\rho] = \int \rho(r) v(r) d^3r \tag{2.77}$$

$$J[\rho] = \frac{1}{2} \int \int \frac{\rho(r_1)\rho(r_2)}{r_{12}} d^3r_1 d^3r_2 \tag{2.78}$$

An approximation to the kinetic energy can be obtained in the Kohn-Sham formalism [53] which is the most widely used form of DFT. In this approach the wave function is constructed from atomic orbitals $\psi_i(r)$. The single particle kinetic energy is obtained by applying the kinetic energy operator. [54]

$$T_S[\rho] = \sum_{i=1}^{n} \left\langle \psi_i \mid -\frac{1}{2}\triangle \mid \psi_i \right\rangle \tag{2.79}$$

The assumption in Kohn-Sham DFT is that the three terms $V_{ext}[\rho], J[\rho], T_S[\rho]$ should make up the largest part of the energy. The effects that have been neglected are the electron correlation and exchange interactions. These are summarized in the exchange-correlation functional $E_{xc}[\rho]$ and the energy is given according to

$$E_v[\rho] = V_{ext}[\rho] + J[\rho] + T_S[\rho] + E_{xc}[\rho] \tag{2.80}$$

So far no approximations have been made but the problem with the approach is that E_{xc} is not known. An early parametrization that uses only local information is the local density approximation. It is mainly used in solid state chemistry. The generalized gradient approximation also includes the gradient of the density in the computation. One prominent representative, the PBE functional [55] gives good results in both solid state and molecular chemistry. A different approach is by computing the Hartree-Fock exchange (cf. Eq. (2.60)) of the Kohn-Sham orbitals and including a fraction of this into the functional. These hybrid functionals, like B3LYP [56, 57] are very popular in molecular computations. [54]

Excited states are available through the time-dependent linear response formalism (TDDFT) where excitation frequencies are computed as poles of the frequency dependent polarizability. [58] This provides a highly efficient approach for computing excitation energies in many cases. However, it should be noted that there are some known artifacts of this method, in particular when it comes to the description of CT states in spatially separated chromophores. [59] A more detailed discussion of this problem and possible solutions will be presented in Section 3.1.

2.3 Environmental Effects

Whereas highly accurate electronic structure methods exist (cf. Section 2.2), a major challenge is that these are often prohibitively expensive for larger system

sizes. For this purpose hybrid methods have been introduced that provide a connection between an accurate description of the system of interest with an inclusion of a large scale environment.

In this work a connection between quantum mechanics and classical mechanics (QM/MM) was used for this purpose. This method can be derived in the following way. [60] First, it has to be assumed that the wavefunction can be partitioned into a product of two parts: ϕ_{QM} for the core region and ϕ_{MM} for the environment.

$$\phi = \phi_{QM}\phi_{MM} \tag{2.81}$$

Then the energy is given as

$$\begin{aligned} E_\phi &= \left\langle \phi_{QM} \mid \widehat{H}_{QM} \mid \phi_{QM} \right\rangle + \\ &+ \left\langle \phi_{QM}\phi_{MM} \mid \widehat{H}_{QM/MM} \mid \phi_{QM}\phi_{MM} \right\rangle + \left\langle \phi_{MM} \mid \widehat{H}_{MM} \mid \phi_{MM} \right\rangle \\ &= E_{\phi,QM} + E_{\phi,QM/MM} + E_{\phi,MM} \end{aligned} \tag{2.82}$$

As a second approximation $E_{\phi,MM}$ is computed by a classical force field.

$$E_{\phi,MM} = V^{force-field} \tag{2.83}$$

Next, an approximation to $E_{\phi,QM/MM}$ has to be found. For this purpose the charge distribution of the MM region is usually described by point charges. Moreover, the van-der-Waals interactions between the QM and MM regions are treated by force field terms. [2] Several approaches exist for the calculation of the electrostatic interactions. [61] In the mechanical embedding approach the environmental point charges do not affect the QM wavefunction and all interaction terms are evaluated in an MM fashion (usually with charges obtained in the QM calculation). In the electrostatic embedding approach (see also Ref. [62]) the electronic wavefunction of the core system is polarized by fixed MM pointcharges. The electrostatic interactions of the QM nuclei and the electron density $\rho_{QM}(r)$ with the effective MM pointcharges q_ν are computed according to

$$E_{\phi,QM/MM} = \sum_{\substack{\mu \in QM \\ \nu \in MM}} \frac{Z_\mu q_\nu}{R_{\mu\nu}} - \sum_{\nu \in MM} \int \frac{q_\nu \rho_{QM}(r)}{\mid r - R_\nu \mid} dr \tag{2.84}$$

[2] In fact these van-der-Waals interactions derive from exchange repulsion and dispersion terms, which go beyond the approximation of Eq. (2.81). However, these terms are only included from the MM side and do not affect the electronic wavefunction.

The next step in the hierarchy of QM/MM methods is the polarizable embedding approach where MM pointcharges are allowed to change or move in response to the wavefunction of the core system, emulating a polarization of the electrons in the MM region.

Another widely used approach for the description of the environment are continuum models like the polarizable continuum model (PCM) [63] and the conductor like screening model (COSMO) [64]. The advantages of these methods are that more interaction terms and the electronic polarization of the environment can be included and that a smaller number of empirical parameters are necessary. The disadvantage is that no specific interactions (e.g. hydrogen bonds) can be taken into account.

Different strategies exist that attempt to provide an atomistic description of the environment as well as an accurate inclusion of all interaction terms. These are either concerned with parametrized effective potentials [60,65] or with frozen density embedding. [66] In the latter case also the response of the environment to an electronic excitation can be included. [67]

2.4 Dynamics Simulations

Dynamics simulations are concerned with the time-dependent behavior of a system. In this way chemical processes can be directly observed and more information is gained than by considering only the stationary points or low dimensional samples of the potential energy surface.

For exact dynamics the time-dependent Schrödinger equation has to be solved.

$$\widehat{H}(\Psi(\mathbf{R},\mathbf{r},t)) = i\hbar\frac{\partial}{\partial t}\Psi(\mathbf{R},\mathbf{r},t) \tag{2.85}$$

As far as t is concerned this is an ordinary first order differential equation and no eigenvalue problem. Formally for time-independent $\widehat{H}$ the solution is directly given with the time propagator

$$\Psi(\mathbf{R},\mathbf{r},t) = e^{\frac{it}{\hbar}\widehat{H}}\Psi(\mathbf{R},\mathbf{r},t) \tag{2.86}$$

For practical calculations there are several different strategies for an approximate treatment of the wavefunction propagation. Adiabatic dynamics are run under the assumption of the Born-Oppenheimer approximation (2.21). For non-adiabatic dynamics, coupling elements as given in Eq. (2.19) are evaluated as a post Born-Oppenheimer correction. Another approximation is treating the nuclei as classical particles as far as their kinetic energy is concerned. If this is done with the adiabatic approximation purely classical dynamics result for the nuclei. Non-adiabatic dynamics with classically moving nuclei are called a "mixed quantum-classical" approach.

2.4.1 Classical Dynamics

In the classical limit neither adiabatic quantum effects nor couplings between states are considered (cf. Eq. (2.20)). In this way nuclei are classical particles that behave according to Newton's laws. Forces are determined by the gradient of the electronic energy. This leads to a system of coupled differential equations, one for each nucleus.

$$\forall \mu \in \{1, ..., N\} : a_\mu(t) := \frac{d^2}{dt^2} R_\mu(t) = -\frac{1}{m_\mu} \nabla_\mu E_\psi(\mathbf{R}(t)) \tag{2.87}$$

A numerical solution to this is provided by the Verlet algorithm [68] or alternatively if explicit velocity is required the velocity Verlet algorithm. In the second case one starts with a geometry $\mathbf{R}(0)$ and velocity $\mathbf{v}(0)$. The two quantities are propagated according to

$$\mathbf{R}(t + \Delta t) = \mathbf{R}(t) + \mathbf{v}(t)\Delta t + \frac{1}{2}\mathbf{a}(t)\Delta t^2 \tag{2.88}$$

$$\mathbf{v}(t + \Delta t) = \mathbf{v}(t) + \frac{\mathbf{a}(t) + \mathbf{a}(t + \Delta t)}{2}\Delta t \tag{2.89}$$

where the acceleration $\mathbf{a}(t) = (a_1(t), ..., a_N(t))$ is computed from the electronic energy gradient (Eq. (2.87)).

2.4.2 Adiabatic Quantum Dynamics

Another way to approximate Eq. (2.86) is by applying the Born-Oppenheimer approximation but retaining other quantum effects. The time-dependent formulation

of Eq. (2.21) yields

$$\widehat{T}_{nuc}(\chi_\psi(\mathbf{R},t)) + E_\psi(\mathbf{R})\chi_\psi(\mathbf{R},t) = i\hbar\frac{\partial}{\partial t}\chi_\psi(\mathbf{R}) \tag{2.90}$$

and the solution with a time-independent Hamiltonian is

$$\chi(\mathbf{R},t) = e^{\frac{it}{\hbar}(\widehat{T}_{nuc}+E_\psi(\mathbf{R}))}\chi(\mathbf{R},t) \tag{2.91}$$

The major difficulty is evaluating the quantity $E_\psi(\mathbf{R})$. Only in very simple systems like harmonic or Morse oscillators it can be given in analytical form. But usually $E_\psi(\mathbf{R})$ has to be approximated by a grid where at every point an electronic structure calculation (Eq. (2.11)) has to be performed. The number of grid points scales exponentially with the number of degrees of freedom. Therefore only a small number of degrees of freedom can be explicitly considered in such an approach.

2.4.3 Non-adiabatic Dynamics

Typically in chemistry the Born-Oppenheimer approximation is valid. However, it can break down when close lying states are present or possibly when nuclear motion is fast (cf. Eq. (2.20)). Because of the rather dense distribution of excited states in many molecules, non-adiabatic corrections are needed in many cases when excited state dynamics are simulated. A clear indicator that the Born-Oppenheimer picture of having two isolated excited states is often not valid derives from the fact that many molecules exhibit a fluorescence quantum yield significantly lower than one or possibly show no detectable fluorescence at all. The states interact and non-radiative decay takes place. The energy of the excited state is turned into vibrational energy which is subsequently given to the environment. In a similar sense non-adiabatic effects are essential for the transport of electrons or excitation energy between spatially separated chromophores. In this case non-adiabatic events represent avoided transfer events, which occur when the coupling is low (see also Section 3.3). A transition between two states usually occurs close to an intersection, a place where the states are degenerate. But complete degeneracy is not required, the transition takes place because the states are close in energy and the Born-Oppenheimer approximation breaks down.

One way of simulating excited state dynamics is by using the full quantum picture. For this it is convenient to use a diabatic basis, consisting only of smoothly varying quantities. The diabatic basis functions are formed by a geometry dependent linear transformation of the adiabatic basis $\mathcal{B}$ under the condition that non-adiabatic couplings between the functions are $\mathbf{0}$. With this condition Eq. (2.20) (and its time-dependent counter part) are greatly simplified. In the next step a model potential may be formed. Then wave packet dynamics can be carried out using the multi-configuration time-dependent Hartree method. [28]

In practical calculations where only a (small) finite subset $\mathcal{B}'$ of $\mathcal{B}$ can be considered, it is not generally possible to obtain a strictly diabatic basis due to mixing with the external states. [28,69] However, if $\mathcal{B}'$ is chosen appropriately (i.e. enough states are considered), the states can still be considered diabatic for practical purposes. To obtain diabatic states one may either fit to adiabatic potential energy surfaces [70] or use additional non-adiabatic coupling elements (see also Section 3.4). [71, 72] Alternatively, property based diabatization approaches can be used, which are particularly suitable for identifying localized *initial* and *final* states of transfer processes (as used on several occasions in the remaining text). [69, 73, 74]

An alternative approach to wavepacket dynamics are on-the-fly mixed quantum-classical dynamics (MQCD) based on the surface hopping method [75] as implemented for example in the NEWTON-X molecular dynamics package. [76] Nuclei are treated as classical particles propagated with the velocity-Verlet algorithm (Eq. (2.88)). Then the time-dependent nuclear wave function $\chi_\psi(\mathbf{R}, t)$ is a moving δ-function and can be written as $\chi_\psi(\mathbf{R}(t))$ or as just $\chi_\psi(t)$ a time-dependent coefficient for the adiabatic electronic function ψ. The $\chi_\psi(t)$ are propagated according to [75]

$$i\frac{d}{dt}\chi_\psi(t) + \sum_{\phi\neq\psi}\left(\underbrace{i\mathbf{v}(t)\cdot\langle\psi \mid \nabla_{\mathbf{R}} \mid \phi\rangle}_{\text{non-adiabatic coupling}} - \underbrace{\left\langle\psi \mid \widehat{H}_{el} \mid \phi\right\rangle}_{\text{diabatic coupling}}\right)\chi_\phi(t) = E_\psi(t)\chi_\psi(t) \quad (2.92)$$

In general, non-adiabatic interaction terms as well as diabatic coupling come into play. To minimize the transitions between the states, surface hopping dynamics are usually carried out considering a set of adiabatic states $\phi \in \mathcal{B}$ where according to Eq. (2.11) the diabatic couplings vanish. A challenge in this context is that

the non-adiabatic interactions may be highly peaked. As a result special care has to be taken for the integration of the electronic coefficients. In some cases even a reduction of the timestep of the electronic structure calculations may be necessary, which may significantly increase the effort of the dynamics simulations. [77] A solution to this problem was provided in Ref. [71]: the electronic coefficients are propagated in a locally diabatic basis where the the non-adiabatic terms in Eq. (2.92) vanish and only the diabatic terms have to be considered while the dynamics still proceeds on adiabatic surfaces. In Section 3.4 it will be shown that this approach yields impressively stable and consistent results.

In surface hopping dynamics one initially specifies the number of states considered. In principle all states have an influence. But this influence is very small if the states are well separated in energy. Therefore typically only the ground state and a few lowest excited states are considered. One also needs a starting state ϕ and starting geometry and velocity. The dynamics are run by propagating the geometry (Eq. (2.88)) and velocity (Eq. (2.89)) with the velocity Verlet algorithm, and the nuclear wave function coefficients χ_ψ according to Eq. (2.92). For this purpose the gradient of the current state ϕ and the non-adiabatic derivative couplings of ϕ to all other considered states have to be computed by the electronic structure program. The complex coefficients χ_ψ do not influence the dynamics directly. However, according to their values stochastic hops to a new state ψ are performed and the dynamics continues with the forces of this state.

A similar approach from a practical viewpoint, also leading to on-the-fly dynamcis, is Full Multiple Spawning (FMS) [78]. In FMS the nuclear wave function $\chi_\psi(\mathbf{R}, t), \psi \in \mathcal{B}'$ is expressed in a basis of moving Gaussians. For each such basis function, a gradient and non-adiabatic coupling calculation as just described is performed per time step. Then the non-adiabatic nuclear Schrödinger equation in this basis is solved to get the nuclear wave function coefficients. The basis functions are propagated according to classical forces. In this way an accurate description can be obtained without the need of too many electronic structure computations. To improve the description new basis functions are introduced ("spawned") when needed, typically this is done when the non-adiabatic coupling is large.

Chapter 3

Results

In this chapter the main results of my thesis will be presented. The following sections consist of published papers, of papers submitted for publication, and of additional parts currently not in the publication process.

3.1 Review: Electronically Excited States and Photodynamics

I would like to start with a review paper concerned with excited states and photodynamics. The first part of this article is concerned with an outline of excited state phenomenology. Then methods for electronic structure calculations and dynamics are presented, with a focus on practical applicability. Finally, an extensive collection of examples is given. In all of these areas a special focus is laid on dimers and extended systems and the resulting excitonic and charge transfer interactions.

The article was published in *Theoretical Chemistry Accounts*. [79] My contribution to this project consisted mainly of the parts concerned with dimers and aggregates and the description of applications to DNA fragments and photovoltaics.

Theor Chem Acc (2012) 131:1073
DOI 10.1007/s00214-011-1073-y

REGULAR ARTICLE

Electronically excited states and photodynamics: a continuing challenge

Felix Plasser · Mario Barbatti · Adélia J. A. Aquino · Hans Lischka

Received: 12 July 2011 / Accepted: 1 August 2011

Abstract The purpose of this contribution is the description of the progress in theoretical investigations on electronically excited states in connection with photodynamical simulations made within the last years and to provide an outlook on the scope of future applications and challenges. An overview over excited-state phenomenology is given and the applicability of different computational methods is discussed. Both electronic structure- and dynamics methods are considered. The examples presented comprise the explanation of the photostability of individual DNA nucleobases, the photodynamics of DNA including excitonic and charge-transfer processes, the primary processes of vision and the broad field of photovoltaics, photodevices, and molecular machines.

Keywords Electronic structure · Excited states · Photodynamics · Nonadiabatic phenomena

Published as part of the special collection of articles celebrating the 50th anniversary of Theoretical Chemistry Accounts/Theoretica Chimica Acta.

F. Plasser · A. J. A. Aquino · H. Lischka (✉)
Institute for Theoretical Chemistry, University of Vienna, Waehringerstrasse 17, 1090 Vienna, Austria
e-mail: hans.lischka@univie.ac.at

M. Barbatti (✉)
Max-Planck-Institut für Kohlenforschung, Kaiser-Wilhelm-Platz 1, 45470 Mülheim an der Ruhr, Germany
e-mail: barbatti@kofo.mpg.de

A. J. A. Aquino · H. Lischka
Department of Chemistry and Biochemistry, Texas Tech University, Lubbock, TX 79409-1061, USA

A. J. A. Aquino
Institute of Soil Research, University of Natural Resources and Applied Life Sciences Vienna, Peter-Jordan-Straße 82, 1190 Vienna, Austria

1 Introduction

Photoinduced phenomena in molecules play an important role in many scientific and technological fields. In biological sciences, they are related to photoaging and photodamage [1–3], to vision and light detection [4, 5], to photosynthesis and light harvesting [6–8]. In technology, they are central for photocatalysis [9, 10], photovoltaics [11, 12], imaging [13, 14], photodevices, [15, 16], conventional [17, 18] and time-resolved spectroscopy [19, 20]. It would, certainly, be unrealistic to attempt examining such huge variety of fields in one review. Instead, we intend to provide an account of recent theoretical investigations, which, although restricted to a more modest variety of topics, will still illustrate a broad range of recent achievements, as well as current limitations of quantum chemical investigations of molecular excited states.

Special focus will be laid on the interactions between chromophores in π-systems, which have recently attracted substantial interest for computational studies because of many challenging questions still to be answered. Note that as a consequence of progress in computer hardware and quantum chemical algorithms, high-level quantum chemical treatment of many of the examples discussed below has become accessible only in the last years. A large number of systems of biological and technological interest exist, where interactions between chromophores play an important role. In particular, the photophysics and charge migration dynamics of DNA fragments have attracted widespread interest and many open questions remain [2, 21]. Exciton dynamics in photosynthetic complexes and other aggregates are studied to understand how the precise arrangement of the chromophores affects light harvesting efficiency and what is the role of quantum coherence [7, 22, 23]. In particular, the technique of two-dimensional

Published online: 11 January 2012

optical spectroscopy provides fascinating signatures of the quantum nature of these processes but often poses questions that cannot be answered without modeling [7, 23]. Excitonic and charge dynamics is fundamental in organic electronics. Not only migration properties of excitons and charges are of highest interest, but especially the charge separation and charge recombination steps have a crucial influence on the efficiency of photovoltaic and electroluminescent devices [24]. Another widely used application that is based on the specific properties of excitation energy transfer (EET) is the analytical technique of fluorescence resonance energy transfer, which is used to obtain time-dependent structural information on macromolecules [25].

Several physical phenomena play a role in photoexcited molecules and molecular aggregates. Electronic excitations correspond to significant changes in the electronic structure, which may in turn lead to ultrafast non-equilibrium phenomena. For a successful modeling of excited states, it is important to understand the basic physics of different classes of excited states, as well as the available computational methods and their advantages and problems with respect to the different questions to be asked. We will start in Sect. 2 by outlining excited-state phenomenology, where aside from excited states of single molecules special focus will be laid on changes that occur due to interactions between chromophores. In Sect. 3, a number of quantum chemical methods that can be used for excited states and their advantages and limitations will be discussed. Possibilities for considering dynamical phenomena and couplings between electronic and nuclear degrees of freedom will be outlined in Sect. 4. An overview of possibilities for computing excited states in dimers and aggregates will be presented in Sect. 5. Finally, Sect. 6 will feature a number of examples selected from biology and technology and special attention will be given to the applicability of different methods for these classes of systems.

2 Excited-state phenomenology

2.1 Photoinduced phenomena in molecules

Molecules can be electronically excited by irradiation at UV or visible wavelengths. The electronic excitation promotes the molecule to a non-equilibrium state, which triggers a sequence of relaxation processes. As illustrated in Fig. 1, these processes may correspond to simple vibrational relaxation on a single potential energy surface, or may involve radiationless crossings to other adiabatic states with the same spin multiplicity (internal conversion) or different spin multiplicities (intersystem crossing); alternatively, they may involve radiative transitions to other states by fluorescent or phosphorescent processes.

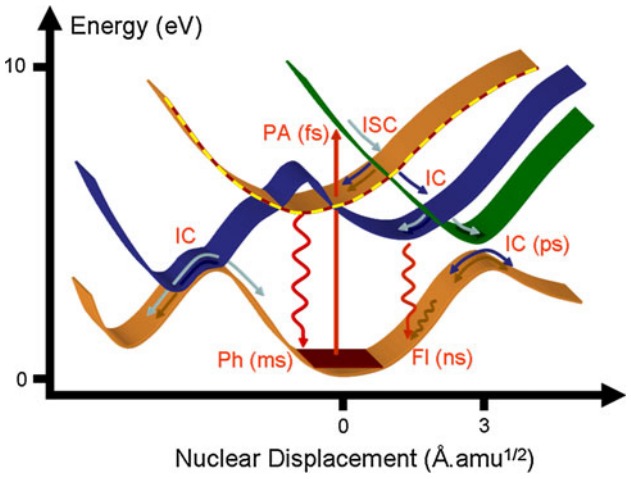

Fig. 1 Illustration of photodynamical processes occurring on ground and excited potential energy *curves* of a molecule. *PA* photoabsorption, *ISC* Intersystem crossing, *IC* internal conversion, *Fl* Fluorescence, *Ph* Phosphorescence

In any case, between the fastest processes—vibrational relaxation taking place within few tens of femtoseconds (fs), and slowest processes—phosphorescence occurring within milliseconds (ms), a span in time of more than ten orders of magnitude is found. This large variability of processes and time scales imposes, naturally, a great challenge to theoreticians, who should be prepared to employ many different approaches and methods, tailored for each special case.

Theoretical investigations of molecular excited states usually start with the determination of the vertical excitation spectrum for the ground-state minimum geometry and continue with the determination of geometries and energies of excited-state stationary structures, of coupling terms for state crossings, and of reaction pathways connecting all those structures. In comparison with ground-state research, excited-state investigations impose a new level of challenges due to the high density of closely lying states possessing different delocalization character (localized valence states, delocalized excitons, separated charge-transfer states, diffuse Rydberg states). Moreover, rather than having nearly harmonic wells separated by high energy barriers—as usually found in the ground state—excited-state surfaces are often anharmonic, with multiple wells separated by low energy barriers, allowing the molecule to reach geometrical conformations far from chemical intuition.

The development of experimental femtosecond spectroscopic techniques [26, 27] has been a driving force pushing theoretical research in excited states beyond simple assignment of vertically excited spectra. The need for theoretical models helping to deconvolute time-dependent spectra has continually motivated the research of excited-state reaction pathways and excited-state dynamics

simulations. In this context, internal conversion processes have been a main field of theoretical research in excited states. After photoexcitation, the molecule can reach regions of the configuration space where the Born–Oppenheimer approximation breaks down (see Fig. 2). In particular, degeneracy between states of the same spin multiplicity, also known as conical intersections [28, 29], creates an efficient funnel for radiationless transfer between adiabatic states. Seams of conical intersections are ubiquitous [30]; the main question to be answered is whether a specific molecule excited at a determined wavelength can reach the intersection seam or not.

Algorithms for localization of conical intersection have been developed [31–33], making their search comparable to the conventional search for stationary points. They are reviewed and benchmarked in Ref. [34]. The research of internal conversion pathways performed for a large variety of molecules has shown that the structures at conical intersections often keep close structural resemblance even between very different molecules. For instance, two examples of S_1/S_0 conical intersections are shown for two distinct molecules in Fig. 3. The substructure that causes the degeneracy between the two states is a twist-pyramidalized configuration (indicated by lines in bold) in both cases. The twist has the effect of stabilizing the $\pi\pi^*$ state and destabilizing the closed shell (cs) state, bringing them to an avoided crossing. Pyramidalization (sp^2 to sp^3 hybridization change) tunes the degeneracy [35]. Five of the most common motifs giving rise to S_1/S_0 conical intersections in organic molecules are collected and illustrated in Table 1.

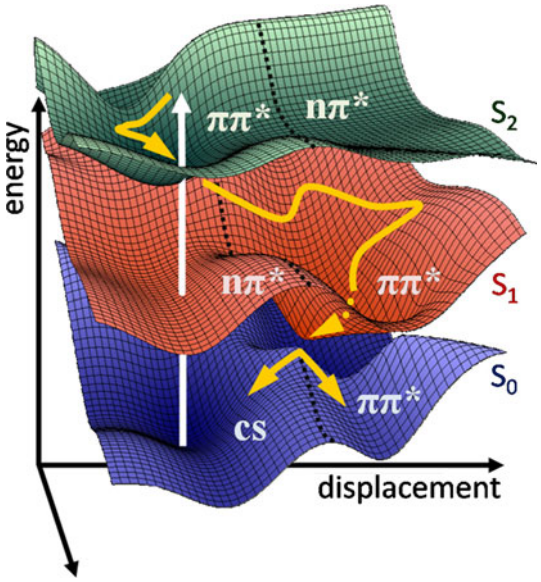

Fig. 2 Illustration of the potential energy surfaces of a molecule. The *arrows* indicate the photoabsorption (*vertical*) and the relaxation processes. Each adiabatic surface (S_0, S_1, S_2) can have different diabatic characters (cs (*closed shell*), $n\pi^*$, $\pi\pi^*$) depending on the nuclear geometry

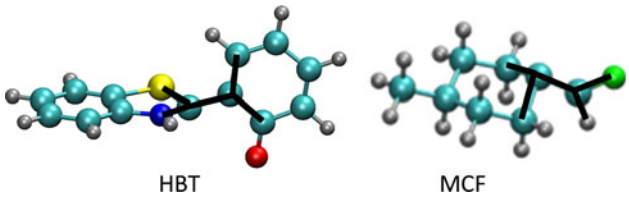

Fig. 3 Examples of twisted pyramidalized (or ethylenic) S_1/S_0 conical intersections in 2-(2′-hydroxyphenyl)-benzothiazole (HBT) [36] and 4-methylcyclohexylidene-fluoromethane (MCF) [37]. The *lines* in *bold* indicate the origin of the "primitive conical intersection"

In spite of the large variety of types of processes observed in molecular photodynamics, these motifs for conical intersections indicate that there are common patterns followed by molecules. For instance, Fig. 4 shows the state occupation during dynamics of pyrrole [38], adenine [39], and pyridone [40] according to surface hopping simulations. These state occupations belong to three distinct classes of excited-state pathways commonly observed in dynamics of organic molecules. For pyrrole, a very fast (sub-100 fs) dynamics occurs following the NH dissociation along the $\pi\sigma^*$ state. For adenine, ring puckering toward an ethylenic conical intersection along the $\pi\pi^*$ state controls the dynamics. For pyridone, the conical intersection cannot be reached efficiently, turning this molecule into a fluorescent species.

2.2 Charge transfer and excitonic interactions

If two or more chromophores interact with each other, new intriguing phenomena come into play. Strong interactions may significantly alter the character of the excited states by delocalizing them among several fragments. Additionally, defect migration plays a role even at much weaker coupling strengths and energy transfer occurs up to a spatial separation of several nanometers between chromophores [25]. Electronic defects in aggregated or bulk systems are commonly described in terms of excess electrons and holes relative to the neutral ground state. If the electron and the hole are in close contact, possibly delocalized over a few fragments, the term Frenkel exciton is commonly used. Typically, only Frenkel excitons are active in absorption and emission processes. Later, they may split into charge-transfer states, i.e., an electron and a hole on separate fragments bound by a strong mutual Coulomb interaction. Finally, complete charge separation can occur where the electron and hole migrate independently. The complete description of these phenomena is quite challenging as it is not only necessary to describe the electronic structure at

Table 1 Common motifs or "primitive conical intersections" giving rise to conical intersections between the first excited and the ground singlet states of organic molecules

Conical intersection	Primitive structure	Examples
Twisted; Twisted-pyramidalized ($\pi\pi^*$/cs)	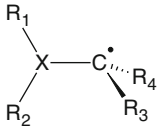	Conjugated chains (ethylene [189], polar substituted ethylenes [190], protonated Schiff bases [191], stilbene [192], azobenzene [193]) Aromatic rings (benzene [194], purines [195], pyrimidines [196])
H-migration/carbene ($\pi\pi^*$/cs)	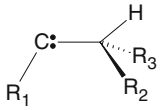	Ethylidene [197] Cyclohexene [198]
Out-of-plane O ($\pi_O\pi^*$/cs)	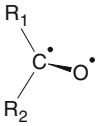	Formamide [199] Rings with carbonyl groups (pyridone [40], pyrimidines [200], guanine [201])
Bond breaking; ring opening ($\pi\sigma_{XY}^*$/cs)	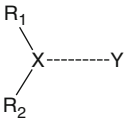	Heteroaromatic rings (pyrrole [202, 203], purines [204], thiophene [205], furan [206], imidazole [207])
Proton transfer ($\pi\pi^*$/cs)	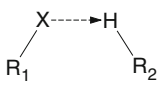	Watson–Crick base pairs [118]

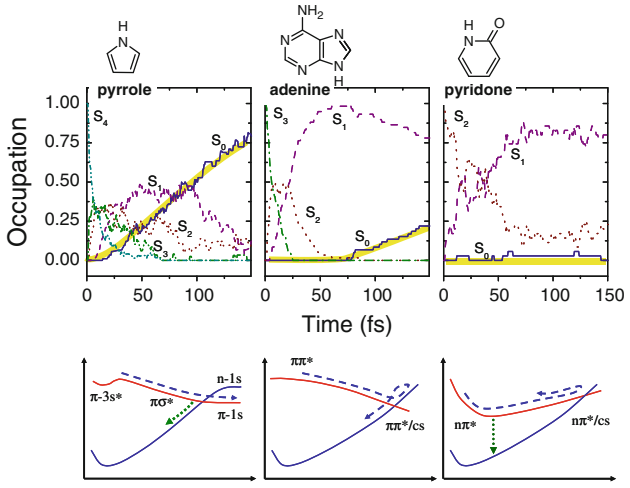

Fig. 4 State occupation during dynamics of pyrrole [38], adenine [39], and pyridone [40] and corresponding main reaction pathways. The highlighted *curve* indicates the evolution of the ground-state population

high level, but it is also essential to include the coupling between electronic and nuclear degrees of freedom. The computational description can either occur by finding the parameters for global theories or by a direct dynamical description.

In Fig. 5 the model shape of a potential energy surface (PES) of a defect located on two interacting fragments is shown, cf. Ref. [41]. The diabatic states H_{ii}^{diab} and H_{ff}^{diab} where the defect is localized on the *initial* or *final* fragments are represented by displaced parabolas. These are characterized by the reorganization energy λ, the energy required to move from one minimum geometry to the other while staying on the same diabatic surface. These diabatic curves are modulated in this example by a constant coupling H_{if}^{diab} to yield the adiabatic energy curves E_1^{ad} and E_2^{ad}. If the two fragments are different, then a non-vanishing reaction free energy $\Delta_r G$ for the defect transfer reaction will be observed. If the coupling is on the order of the reorganization energy, then the resulting adiabatic states are strongly mixed and a unique delocalized minimum is formed, Fig. 5a. If the coupling is significantly smaller, then the adiabatic states remain very similar in character to that of the localized diabatic states and only at the transition region an interaction between the states occurs, Fig. 5b. The essence of Marcus theory is to combine H_{if}^{diab}, λ, and $\Delta_r G$ to form a rate equation including non-adiabatic effects for weak coupling cases [42]. Förster theory allows connecting spectroscopically available quantities to form a rate equation of excitation energy transfer [43].

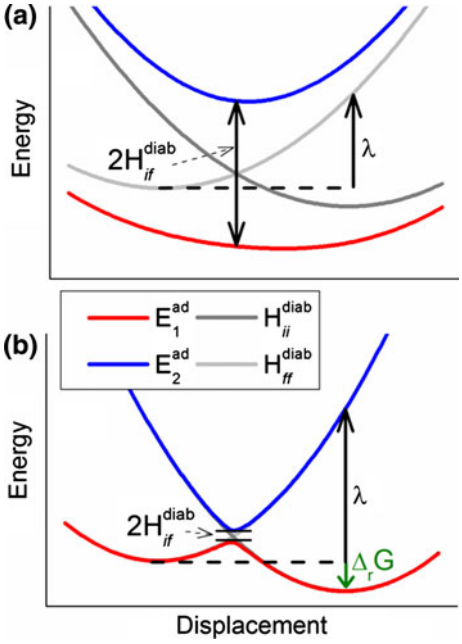

Fig. 5 Model potential energy curves for a defect delocalized over two fragments in the (**a**) strong coupling and (**b**) weak coupling cases

3 Quantum chemical method for excited states

3.1 Ab initio methods

Many ab initio methods are currently available for exited-state calculations. Some single-reference methods, such as the second-order approximate coupled-cluster (CC2) [44], algebraic diagrammatic construction (ADC) [45], and the equation-of-motion coupled-cluster (EOM-CC) [46] methods, have proven to be reliable and affordable sources for vertical excitation energy calculations, with data quality considerably superior to former common approximations such as the configuration interaction with single excitations (CIS) [47]. It should be noted that combination of CC2 and ADC(2) with the resolution-of-the-identity (RI) approximation [48, 49] has significantly increased the applicability of these methods (see below).

At strongly distorted molecular geometries or conical intersections with the ground state, the Hartree–Fock method does not provide a satisfactory reference wave function. In these cases, the usage of multiconfigurational and multireference methods is necessary, and the multiconfigurational self-consistent field (MCSCF) [50, 51], the multireference configuration interaction (MRCI) [52–54], or the complete active space perturbation theory to second-order (CASPT2) [55] can be applied. Analytical gradients are available for all these methods [56–58]. Analytical nonadiabatic couplings terms are available for MCSCF and MRCI methods [59].

Table 2 Recent reviews and benchmark investigations on excited-state calculations

Description	Refs.
Benchmark of excited states: ab initio methods	[208–211]
Benchmark of excited states: DFT-based methods	[82, 212–217]
Benchmark of excited states: semiempirical methods	[88]
Benchmark of conical intersections	[34]
Review on quantum chemical methods	[83]
Review on the QM/MM approach	[218, 219]
Review on surface hopping	[100, 220]
Review on excited-state phenomena	[157, 221–223]

Besides the high computational costs common to all these methods, another handicap affecting especially the MCSCF and the MRCI methods is their dependence on the choice of active and reference spaces [60]. Of particular concern is that larger active spaces, which are often used when a large number of orbitals is to be considered, start to include dynamic electron correlation effects for some of the electrons, which causes an imbalance by leaving the other electrons uncorrelated [61]. Additionally, convergence problems may increase computation times, and certain orbital rotations may appear for specific geometries changing the character of the MCSCF wavefunction that can lead to discontinuities in potential energy surfaces. MCSCF and MRCI often overestimate the energy of ionic states in the Franck–Condon region [62, 63]. CASPT2, on its turn, tends to underestimate the vertical spectrum [64, 65]. A collection of references to investigations benchmarking results for excited-state calculations at ab initio levels are given in Table 2.

3.2 DFT-based methods

Currently, excited-state properties can be obtained with several density functional (DFT) methods. Besides the popular time-dependent (TD) DFT [66, 67], usually computed within the linear-response approximation, other DFT-based methods, such as the restricted open-shell Kohn–Sham (ROKS) [68], restricted ensemble-reference Kohn–Sham (REKS) [69], time-dependent density functional tight-binding (TD-DFTB) [70], and DFT/MRCI [71, 72], can provide excitation energies and other properties. Among these methods, analytic energy gradients and analytic and numeric nonadiabatic couplings terms are available for TDDFT [73–78].

The result of a TDDFT calculation critically depends on the functional used. Because of its superior quality in ground-state calculations, the hybrid B3-LYP [79] functional is often used as a starting point. In a similar sense,

the generalized gradient approximation functional PBE [80] is often applied. PBE0 [81] is a parameter free hybrid extension of PBE, which was formulated with a special focus on molecular properties and excited states. Highly parameterized functionals like Truhlar's M06 series [82] give remarkable results in many cases, but have the disadvantage that the physical understanding of the functional form becomes more difficult. In practical applications, usually several functionals would be considered and computed results compared to reference values (obtained, e.g., from experiment or a high-level ab initio method) thus allowing to find an appropriate functional. A difficulty for applying TDDFT is the large number of available functionals, from which it is not trivial to find the best one for each specific case. Additionally, TDDFT lacks the possibility of systematically improving results, which is one of the major characteristics of ab initio methods.

One of the main problems with DFT-based methods has been the description of charge-transfer states [83], which can be strongly overstabilized by conventional functionals. This problem, however, has been largely attenuated by the development of asymptotically corrected functionals [82, 84, 85], but more experience may still be needed to properly evaluate these approaches. In the case of TDDFT, the single-reference character and the linear-response approximation also turn the computation of potential energy surfaces near conical intersections between the ground and the excited states problematic, if not impossible. These intersections can be described by ROKS (within a simple two-state approximation), REKS, and DFT/MRCI methods.

A collection of references to works benchmarking results for excited-state calculations at DFT-based levels are given in Table 2.

3.3 Semiempirical-based methods

As for ground-state problems, one promising option to overcome the limitations imposed by computational costs is the use of semiempirical methods. Semiempirical-based methods have been also developed for excited-state calculations. In particular, multireference problems have received special attention with the development of semiempirical configuration interaction methods employing floating-occupation of molecular orbitals (FOMO/CI) [86] and MRCI based on the graphic unitary group approach (GUGA) [87].

Results of mixed quality have been reported from the application of these methods. Good results, for instance, can be obtained for vertical excitations with the OM2/MRCI method [88]. The excited-state relaxation dynamics, however, has been often in contradiction with results obtained at ab initio levels (see, for instance, the discussion about cytosine in Sect. 6.1). Transferable, large-scale parametrization over the whole periodic table and including excited-state stationary structures and intersections is still necessary to make these methods fully reliable for excited-state calculations.

4 Methods for photodynamical simulations

4.1 Wavepacket dynamics

The full time-dependent Schrödinger equation for a molecule can be partitioned between self-consistent sets of equations for the electronic and nuclear systems [28, 89]. Then, the nuclear wavepacket of an electronically excited molecule can be propagated by grid-projection techniques [90, 91]. The problem with such methods is that only a limited small number of nuclear coordinates can be included in the calculations. Even though the situation is improved by time-dependent wavefunction expansions, like in the multiconfigurational time-dependent Hartree (MCTDH) method [89], computational costs and difficulties involved in building multidimensional potential energy and coupling surfaces still limit wavepacket propagation to small subsets of nuclear coordinates.

In spite of such limitations, excited-state wavepacket dynamics is an important tool for obtaining highly accurate spectroscopic results [89, 92] or verifying the quality of predictions obtained with trajectory-based methods [93, 94].

4.2 Trajectory-based approaches

Trajectory-based approaches for nonadiabatic dynamics simulations have been popularized in the last decade. They overcome the main problem of nuclear wavepacket propagation—the limited dimensionality due to computational costs and to difficulties of building multidimensional potential energy surfaces—by adopting a local approximation. Within the local approximation, energies, energy gradients, and coupling terms need to be computed only along a classical trajectory, rather than over the full space as the time-dependent Schrödinger equation requests. Delocalization of the nuclear wavepacket is partially recovered by the propagation of multiple independent trajectories. Nonadiabatic behavior is recovered by different approaches. Two of the most well-tested trajectory-based methods are multiple spawning [13, 95] and surface hopping [96].

While multiple spawning propagates Gaussian wavepackets centered at classical trajectories and can spawn new trajectories at nonadiabatic crossing regions, surface hopping propagates classical trajectories on the energy surface of a single state, allowing each independent

trajectory to switch between states during the propagation according to a stochastic algorithm. The multiple spawning technique has the advantage of including quantum effects for the nuclear motion more rigorously. Surface hopping is widely used because of its methodological simplicity and ease of interpretation. In many cases, multiple spawning and surface hopping should lead to similar results at similar computational costs if a proper integration of the time-dependent Schrödinger equation and some additional consistency corrections [97] are performed in the surface hopping dynamics. A recent review about the multiple spawning method can be found in Ref. [98]. Surface hopping dynamics has been reviewed in Refs. [99, 100] and a general program implementation is described in Ref. [101].

5 Computational considerations for dimers and aggregates

A significant amount of attention has been devoted to computing the electronic coupling between chromophores as the central descriptive quantity for the defect transfer process, cf. Fig. 5. There are two general approaches for computing these couplings: direct supermolecular computations and computations of interaction matrix elements between molecules considered independently. In the supermolecular approach, the coupling is obtained as half the energy splitting at resonance conditions [102]. Resonance can either be enforced by symmetry considerations, cf. Refs. [103, 104], by scanning of geometries, or by applying an external electric field [105]. It has been pointed out that simply calculating the gap without checking for resonance may significantly overestimate the coupling [103]. Alternatively, localized states in supermolecular structures may be found by property-based diabatization schemes [102, 105]. In a third approach, the parameters are obtained by considering repeat units [106]. If the two chromophores are considered separately, the task is to compute the interaction matrix element between the two excited states. If there is no overlap between donor and acceptor wave functions, exchange can be neglected and the coupling is given as the Coulomb interaction between the transition densities [107]. This electrostatic interaction can be computed according to the transition density cube method [108] or using analytical Coulomb integrals [107]. For larger separations between the chromophores it is often enough to consider the interaction of transition dipoles, which is the basis for Förster theory. If charge migration rather than energy migration properties are to be computed in a fragment-based approach, the coupling can be estimated as the matrix element between the highest occupied molecular orbitals of the fragments [103, 109]. If the couplings and other descriptive quantities are available, they can provide the background for global theories or multi-scale techniques to describe larger systems [22, 41, 110, 111].

In many cases, it is advantageous to go beyond the simple rate equations provided by Marcus and Förster theory. This was done by adapting the existing theories through inclusion of vibronic terms [41] or by explicitly considering molecular aggregates [111]. But atomistic ab initio non-adiabatic dynamics simulations, as described above, should give a direct unbiased view of the processes occurring and can naturally be applied to intermediate coupling situations where Marcus and Förster theory cannot be applied. An examination of the applicability of surface hopping dynamics for defect transport and its connection to Marcus theory is given in Ref. [104]; the underlying physics are outlined in Sect. 2 of Ref. [112]. The atomistic picture allows for an inclusion of environmental effects through QM/MM coupling schemes. In particular, electrostatic embedding (see Ref. [113] and further references therein) allows coupling the electronic polarization of the core system directly to the orientational polarization of the solvent. The strong influence of such an environmental polarization on the charge-transfer properties of DNA have been discussed in Ref. [109].

6 Applications showing current possibilities and future aspects

6.1 Nucleobases

A very active field of theoretical research in excited states has been the investigation of the behavior of nucleobases [1, 114, 115] and other nucleic-acids fragments [116–118] after UV irradiation. The main motivation has been to understand how this radiation can damage the genetic code and what intrinsic protection mechanisms DNA has developed against it. Experimental research has revealed that all nucleobases can efficiently get rid of the photoenergy at the picosecond time scale [119, 120]. Theoretical research of reaction pathways and conical intersections of nucleobases has identified the main internal conversion channels available for each nucleobase [1, 121–124]. Dynamics simulations have provided information about the efficiency of each of those reaction pathways [20, 114, 115, 125, 126].

Although the reaction pathways described by most of theoretical methods are qualitatively equivalent, results of the dynamics simulations can be quite dependent on the specific properties of the respective potential energy surfaces. Divergent results about the importance of each pathway have been found for all nucleobases. This situation is illustrated for cytosine in Table 3, which surveys the results of simulations from Refs. [114, 115, 117, 126–129].

Table 3 Gas phase dynamics results for UV-excited cytosine obtained with different methods

Dynamics	Electronic structure	Main pathway	τ (ps)	Refs.
MS	CAS (2, 2)	oop-NH_2 (65%)	~0.8	[127]
SH	OM2/MRCI	C6-puck (100%)	0.37	[115]
SH	CAS (10, 8)	Quasi-planar (64%)	0.69	[114, 128]
SH	CAS (12, 9)	Quasi-planar	~0.5[a]	[129]
SH	FOMO/AM1 (PM3)	C6-puck (77%)[b]	0.09 (0.17)	[117]
		oop-NH_2 (81%)[c]	–	
SH	ROKS	C6-puck	0.7	[126]

MS multiple spawning, *SH* surface hopping

[a] Extrapolation of the reported data with a single exponential fitting function

[b] Cytosine + sugar

[c] Isolated cytosine

It is well established that cytosine has three main reaction pathways for internal conversion after excitation into the first bright $\pi\pi^*$ singlet state [1, 124, 127]. One pathway is characterized by puckering at the C6 atom, another one is characterized by out-of-plane displacement of the amino group, and the third one is characterized by a quasi-planar distortion bringing cytosine to near a three-state conical intersection. As shown in Table 3, although all methods predict ultrafast deactivation, there is still no consensus about which pathway is the most important one.

Semi-classical simulations of the UV-photo absorption spectrum at the RI-CC2 level were carried out for each nucleobase, adenine, guanine, cytosine, thymine, and uracil in gas phase [18]. The simulation of the absorption cross section was approached by constructing a nuclear phase space distribution in the electronic ground state and then projecting it onto the electronic excited states. The ground-state distribution was prepared by means of a probabilistic sampling of the Wigner distribution for the ground-state quantum harmonic oscillator [32, 130, 131]. The spectra of adenine, guanine, thymine, and uracil (Fig. 6) showed a common characteristic by the presence of a two-band structure separated by a low intensity region. On the other hand, the cytosine spectrum is formed by a succession of three bands of increasing intensity (Fig. 6). For all five nucleobases, the bands are formed mostly by absorption into $^1\pi\pi^*$ states.

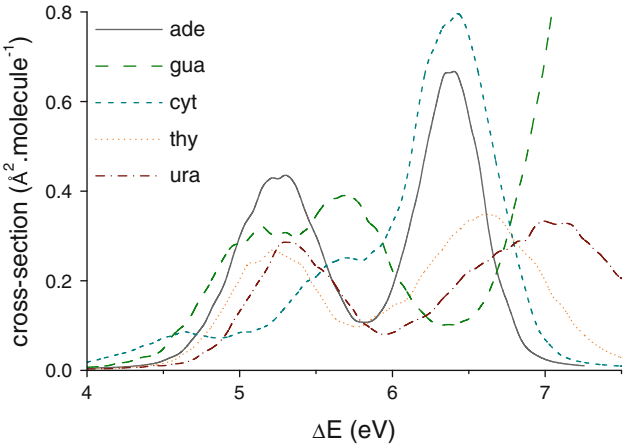

Fig. 6 Simulated absorption spectra of nucleobases using the RI-CC2 method

6.2 DNA fragments

Whereas most of the photophysics of isolated nucleobases is now quite well understood, the photodynamics of several interacting nucleobases still poses many challenges. Research on the excitonic interactions between nucleobases is driven by the observation that the photophysics of DNA is significantly different from that of isolated nucleobases. Whereas all the isolated bases decay on a picosecond time scale [119, 120], long-lived transients up to 10–100 ps [132–134] are observed in DNA, which are strongly dependent on sequence and structure [135]. In principle, both inter- and intrastrand interactions could play a significant role. It is now believed that intrastrand stacking interactions are the major factor for the increase in life time [2]. It has been suggested that UV absorption occurs into Frenkel excitonic states with a delocalization length of 3–4 bases in a homo-adenine strand [134] or probably less in more heterogenous sequences [2].

Computational studies on DNA base stacks are aimed at elucidating the processes described above. Computational challenges arise from the large system sizes to be treated, the importance of the environment, and the need of considering dynamical effects. In principle, TDDFT would be favorable for describing systems of such a size and base tetramers have been successfully treated [136], but the accuracy of TDDFT, at least in the case of standard functionals without long-range corrections, has been questioned [137]. Ab initio methods have been used for

slightly smaller systems. RI-CC2 has been used for system sizes up to base trimers [106], and the CASPT2 method could be applied to dimers [138]. It is a particular challenge to assess the involvement of charge-transfer states. TDDFT studies using a polarized continuum model emphasized the importance of charge-transfer states even when long-range corrected functionals were used [139, 140]. By contrast, a CASPT2 study concluded that Frenkel excitonic states stabilized by resonant interactions should be the most stable trapping sites [138]. Clarifications are still needed to understand these essential photophysical processes. More information may be provided by ab initio methods combined with QM/MM electrostatic embedding treatment of the surrounding DNA to treat both the electronic structure and the polarization of the environment at a high level.

Extended benchmark calculations for excitation energies, oscillator strengths, and characters of the low-lying singlet excited states of the stacked nucleobase pairs adenine–thymine (AT) and guanine-cytosine (GC) were performed by means of a selected set of density functional, B3-LYP and PBE0, and the recently developed M06-2X and M06-HF within the time-dependent density functional theory (TD-DFT) [141]. The resolution-of-the-identity second-order algebraic diagrammatic construction (RI-ADC(2)) method served as reference approach for comparison. For the AT dimer at its ground-state optimized geometry, the charge-transfer state at RI-ADC(2)/TZVP level corresponds to the excited state S_6, which is an excitation from a π orbital in adenine to a π^* in thymine. For the GC dimer, the RI-ADC(2)/TZVP the charge-transfer state corresponds to S_4, which is a π–π^* excitation from guanine to cytosine. Comparison of DFT and ADC(2) results shows that the M06-2X version provides a relatively good reproduction of the reference results. It avoids the serious overstabilization and overcrowding of the spectrum with charge-transfer states found with the B3LYP functional. Solvent effect was also investigated for the AT and GC complexes. The main observation is that the amount of charge-transfer character increases with the polarity of the solvent.

Non-adiabatic dynamics simulations have been performed for one quantum mechanically treated base in an MM base stack [142] and a short double helix [143]. The study illustrated that purely mechanical restrictions do not play a large role and that the monomer likely decay pathways are not hindered by the stacking interaction.

Interactions between Watson–Crick base pairs in DNA could lead to electron or proton transfer processes between the strands as well. The possibility of an electron-driven proton transfer in a guanine-cytosine base pair has been suggested from a static computational study [118] and further examined by dynamics simulations [116]. The effect has been found experimentally in isolated base pairs [144]. But it is now believed that interstrand interactions do not play a significant role in the photophysics of DNA strands [2, 136].

A significant amount of attention has been devoted to charge migration dynamics of DNA [21, 109, 145]. Also in this case, the question of delocalization and of transport properties arises. Aside from biological interests, charge transfer in DNA has been studied in the context of nanotechnology as a model self-assembling system with molecular recognition properties. The task in this context is to modify the properties in order to get sufficient electric conductivity [21]. It has been theoretically suggested [146] and experimentally verified [145] that charge transfer may proceed through two distinct mechanisms: direct superexchange up to a separation of about three bases and multistep hopping for larger distances. Several strategies exist for getting a detailed picture of different aspects of these processes. Models from solid state physics are able to capture the periodicity of the system but have difficulties in properly considering structural fluctuations and molecular motions [21, 147]. High-level ab initio supermolecular calculations (CASSCF, CASPT2, and MRCI) give detailed descriptions of the interactions between stacked bases [148, 149] and even non-adiabatic effects in connection with dynamics simulations, cf. Ref. [104]. However, these methods can only be applied selectively because of high computational requirements. In contrast, semiempirical DFTB calculations in connection with QM/MM inclusion of the environment allow for an efficient sampling of the conformational space and for estimating the importance of solvent degrees of freedom [109].

6.3 Retinal and model systems

Retinal, the chromophore of rhodopsins, has attracted attention from theoreticians since the 1970s [150]. It plays a main function in the transduction of a light signal into a chemical impulse via photoisomerization inside the protein cage. Theoretical research of retinal has been focused on two main aspects, first, solvatochromic effects, which allow its absorption to be tuned to different wavelengths depending on the protein-specific environment [151–154]; second, determination of isomerization mechanism occurring after photoexcitation [4, 5, 155]. Along the last decade, most of the investigations in this field dealt with retinal models [156–161], usually protonated Schiff bases neglecting the cyclohexene ring. Recently, research considering the full length retinal at quantum mechanical level has been reported [4, 5, 155].

The photoisomerization mechanism is still an issue under debate. While ab initio (CASSCF, CASPT2, MRCI) [155–157] and semiempirical (OM2/MRCI) [159] methods predict that torsion around formal double bonds is the main mechanism bringing the molecule to the conical intersection, TDDFT results predict a different scenario with a

major role played by torsion around formal single bonds [162]. Although the agreement about the torsional mode coming from most of methods seems to indicate a failure of TDDFT to deal with this molecule, recent CASPT2 and quantum Monte Carlo evaluations of excited-state potential energy surfaces of a retinal model indicated that the changes in bond length alternation in the excited state should be much smaller than that predicted by CASSCF and even MRCI, which would favor to some extent the TDDFT predictions [163].

6.4 Photovoltaics

Electronic devices based on organic chemistry have many potential advantageous properties compared to silicon-based devices. These include lower production costs, ease of processing, and mechanical flexibility [24]. In particular, the field of photovoltaics has been intensively studied with the aim of producing photovoltaic energy at a comparable or lower cost as traditional non-renewable energy sources. Computational studies are aimed at elucidating the complex nature of the excited states involved and to examine the vibronic coupling that leads to interconversion between them, partially on an ultrafast time scale. A variety of interesting classes of solar cells have been suggested. In dye-sensitized solar cells, an organic dye is used as a chromophore in direct contact with an inorganic framework and charge separation occurs at the interface between the dye molecules and inorganic nanoparticles [164, 165]. If an organic bulk phase is to be used, then the exciton migration properties play a decisive role. The poly (p-phenylene vinylene) (PPV) system and its methoxy derivative have been extensively studied in this context. A special focus was laid on coherences in energy migration [166], which were explained in terms of excitons surfing on the polymer backbone [167]. A DFT study illustrated the strong electron–phonon coupling along the bond length alternation coordinates [168], which could serve as a basis for the surfing process. Whereas bond length alternation is expected to affect on-site excitation energies, torsions may modulate the electronic couplings between the different monomer units. Using full quantum dynamics, these nuclear coordinates can be coupled with electronic degrees of freedom and valuable information about electron–phonon coupling and possible quantum coherences could be obtained, cf. the preliminary exploration of Ref. [110].

After exciton migration, charge separation has to occur at the heterojunction. This process is not well understood yet [12], but quantum dynamical studies may give insight into the electron–phonon coupling processes involved. After charge separation, the charge migration properties become the decisive feature. Computational studies on charge transport in organic systems have been concerned with the estimation of transfer parameters [103] as well as with non-adiabatic dynamics simulations [169]. A number of interesting extensions exists for making organic solar cells more efficient. Self-assembled nanoscale heterojunctions may be used for decreasing exciton migration lengths [170]. Alternatively, supramolecular assemblies with an electron donating group, a chromophore, and an electron accepting group covalently connected can eliminate the need of diffuse electron migration altogether. The properties of such a triad have been studied by DFT [171] and TDDFT [172]. Moreover, the process of multiple exciton generation from one photon can be used to increase the fundamental limits of conversion efficiency [173]. In organic molecules, this can be realized through singlet fission, i.e., one singlet exciton is split into two triplet excitons [173]. The process has been examined computationally for a pentacene dimer [174]. It is suggested that the photoexcitation occurs into a bright single excitation S_2 state, which can cross with a dark doubly excited lower lying state. After this state is reached the two molecules repel each other, and as the system dissociates the doubly excited state obtains the nature of two singlet coupled triplets [174, 175]. To describe these complex excited states, multi-reference perturbation theory was applied with a triple zeta basis set [174]. Biomimetic solar cells using porphyrin aggregates are another promising strategy [176]. In this case, a connection between large-scale theories [22] and smaller-scale parameter calculations may be suitable to provide a solid theoretical background. In general, it can be said that computational studies provide a foundation for understanding the signatures of complex excited-state processes, and may therefore aid in the design of new efficient solar cells in the different categories described.

6.5 Photodevices, phototriggers, and molecular machines

In analogy to the processes occurring in nature for retinal (see Sect. 6.3), molecular photodevices can be used for a clean and ultrafast way to control reactions and trigger processes [177]. Theoretical research in this field has been focusing on laser control of reactions, such as to induce photoisomerization [15, 178, 179], photodissociation [9, 180], and proton transfer processes [181–184]. Light-driven motors have been considered as well [185].

One of the main examples in this field is the photoisomerization of azo-molecules, especially of azobenzene [15, 178, 186, 187], whose molecular length is strongly affected by photoexcitation. In fact, theoretical investigations have played a major role in this field by means of dynamics simulations, which have revealed the intrinsically multidimensional character of the photoisomerization process, rather than a simple unidimensional one, as commonly thought.

Photoexcitation may induce electron or proton transfer within the molecule or between molecules. This process leads to a strong red shift of the emission wavelength in comparison with the absorption wavelength. Theoretical studies of excited-state intramolecular proton transfer (ESIPT) have been useful to support experimental ultrafast spectroscopic investigations. These studies have revealed, for instance, details on the transfer mechanism [181–183] and how it may trigger internal conversion processes [36, 188]. Another interesting theoretical suggestion was a reversible molecular switch based on ESIPT [184].

7 Conclusion and outlook

After photoexcitation, molecules may undergo a variety of different processes. The excited states are characterized by a significant shift in electron density, which may, for example, lead to ionic or diffuse character. In addition, excited states can interact, resulting in irregular shapes of potential energy surfaces. Ultrafast non-equilibrium processes further complicate the situation. For these reasons, excited-state calculations are still quite challenging in spite of the large effort spent in developing new computational methods. Whereas ground-state thermochemistry has evolved into a field where many questions can be routinely addressed by non-specialists, excited-state calculations usually still require a careful assessment of available methods. Not only considerations of computational efficiency play a role, but methods have to be chosen that are appropriate to describe the different kinds of excited states and processes of interest. The availability of analytic energy gradients and nonadiabatic coupling elements is also an important selection criterion.

A major goal in the development of new excited-state methods will be the increase of applicability and stability of the different approaches. Many coupled-cluster-based single-reference methods exist, which offer high-quality results at geometries close to the ground-state minimum. However, the description of conical intersections and strongly distorted geometries is still highly challenging. It would be highly desirable to have a unified approach for these multi-reference cases, rather than having to carefully choose the methodological details as is currently the case for many such problems. TDDFT serves as an attractive method because of its computational efficiency, but it suffers from different systematic errors, most prominently the overstabilization of charge-transfer states. Long-range corrected functionals offer a promising solution. Semiempirical methods offer an even computationally faster approach and appropriate multireference methods are available, but careful parameterization is usually necessary and questions about transferability arise. When choosing a dynamics method, it is necessary to compromise between computational efficiency and the level of approximation, i.e., whether nonadiabatic effects and all internal degrees of freedom have to be considered or not. Dimers and aggregates offer new challenges that may have to be addressed with efficient multi-scale methodology. While there are many successful applications of present methods, there are still many outstanding problems remaining and the development of new approaches to electronic structure calculations will play an important role.

Acknowledgments This work has been supported by the Austrian Science Fund within the framework of the Special Research Program and F41 Vienna Computational Materials Laboratory (ViCoM). FP is a recipient of a DOC fellowship of the Austrian Academy of Sciences. The calculations were performed in part at the Vienna Scientific Cluster (project nos. 70019 and 70151) of the Vienna University Computer Centre. This work was also performed as part of research supported by the National Science Foundation Partnership in International Research and Education (PIRE) Grant No. OISE-0730114; support was also provided by the Robert A. Welch Foundation under Grant No. D-0005.

References

1. Serrano-Andres L, Merchan M (2009) J Photochem Photobiol C-Photochem Rev 10:21
2. Middleton C, de La Harpe K, Su C, Law Y, Crespo-Hernandez C, Kohler B (2009) Annu Rev Phys Chem 60:217
3. Barbatti M (2011) Phys Chem Chem Phys 13:4686
4. Polli D, Altoe P, Weingart O, Spillane KM, Manzoni C, Brida D, Tomasello G, Orlandi G, Kukura P, Mathies RA, Garavelli M, Cerullo G (2010) Nature 467:440
5. Hayashi S, Taikhorshid E, Schulten K (2009) Biophys J 96:403
6. Olaso-Gonzalez G, Merchán M, Serrano-Andrés L (2006) J Phys Chem B 110:24734
7. Cheng Y, Fleming G (2009) Annu Rev Phys Chem 60:241
8. Dreuw A, Harbach P, Mewes J, Wormit M (2010) Theor Chem Acc 125:419
9. Daniel C, Full J, González L, Lupulescu C, Manz J, Merli A, Vajda Š, Wöste L (2003) Science 299:536
10. Duncan WR, Stier WM, Prezhdo OV (2005) J Am Chem Soc 127:7941
11. Shang Y, Li Q, Meng L, Wang D, Shuai Z (2011) Theor Chem Acc 129:291
12. Brédas J-L, Norton JE, Cornil J, Coropceanu V (2009) Acc Chem Res 42:1691
13. Virshup AM, Punwong C, Pogorelov TV, Lindquist BA, Ko C, Martinez TJ (2009) J Phys Chem B 113:3280
14. Groenhof G, Bouxin-Cademartory M, Hess B, deVisser SP, Berendsen HJC, Olivucci M, Robb MA (2004) J Am Chem Soc 126:4228
15. Böckmann M, Doltsinis NL, Marx D (2010) Angew Chem 122:3454
16. Habenicht BF, Prezhdo OV (2009) J Phys Chem C 113:14067
17. Petrenko T, Neese F (2007) J Chem Phys 127:164319
18. Barbatti M, Aquino AJA, Lischka H (2010) Phys Chem Chem Phys 12:4959
19. Stenrup M, Larson A (2011) Chem Phys 379:6
20. Hudock HR, Levine BG, Thompson AL, Satzger H, Townsend D, Gador N, Ullrich S, Stolow A, Martinez TJ (2007) J Phys Chem A 111:8500

21. Endres R, Cox D, Singh R (2004) Rev Mod Phys 76:195
22. Prokhorenko V, Steensgaard D, Holzwarth A (2003) Biophys J 85:3173
23. Nemeth A, Milota F, Sperling J, Abramavicius D, Mukamel S, Kauffmann H (2009) Chem Phys Lett 469:130
24. Bredas J, Beljonne D, Coropceanu V, Cornil J (2004) Chem Rev 104:4971
25. Selvin P (2000) Nat Struct Biol 7:730
26. Hertel IV, Radloff W (2006) Rep Prog Phys 69:1897
27. Zewail AH (2000) Angewandte Chemie (International Edition) 39:2586
28. Koppel H, Domcke W, Cederbaum LS (1984) Adv Chem Phys 57:59
29. Atchity GJ, Xantheas SS, Ruedenberg K (1991) J Chem Phys 95:1862
30. Truhlar DG, Mead CA (2003) Phys Rev A 68:032501
31. Bearpark MJ, Robb MA, Schlegel HB (1994) Chem Phys Lett 223:269
32. Ciminelli C, Granucci G, Persico M (2004) Chem Eur J 10:2327
33. Dallos M, Lischka H, Shepard R, Yarkony DR, Szalay PG (2004) J Chem Phys 120:7330
34. Keal TW, Koslowski A, Thiel W (2007) Theor Chem Acc 118:837
35. Michl J, Bonačić-Koutecký V (1990) Electronic aspects of organic photochemistry. Wiley-Interscience, New York
36. Barbatti M, Aquino AJA, Lischka H, Schriever C, Lochbrunner S, Riedle E (2009) Phys Chem Chem Phys 11:1406
37. Schreiber M, Barbatti M, Zilberg S, Lischka H, Gonzalez L (2007) J Phys Chem A 111:238
38. Vazdar M, Eckert-Maksic M, Barbatti M, Lischka H (2009) Mol Phys 107:845
39. Barbatti M, Lischka H (2008) J Am Chem Soc 130:6831
40. Barbatti M, Aquino AJA, Lischka H (2008) Chem Phys 349:278
41. Barbara P, Meyer T, Ratner M (1996) J Phys Chem 100:13148
42. Marcus RA (1993) Angewandte Chemie (International Edition in English) 32:1111
43. Forster T (1948) Annalen Der Physik 2:55
44. Christiansen O, Koch H, Jorgensen P (1995) Chem Phys Lett 243:409
45. Trofimov AB, Schirmer J (1995) J Phys B At Mol Opt Phys 28:2299
46. Stanton JF, Bartlett RJ (1993) J Chem Phys 98:7029
47. Foresman JB, Head-Gordon M, Pople JA, Frisch MJ (1992) J Phys Chem 96:135
48. Hättig C, Weigend F (2000) J Chem Phys 113:5154
49. Hättig C, Köhn A (2002) J Chem Phys 117:6939
50. Schmidt MW, Gordon MS (1998) Annu Rev Phys Chem 49:233
51. Shepard R (1987) The multiconfiguration self-consistent field method. In: Lawley KP (ed) Ab Initio methods in quantum chemistry II. Advances in chemical physics. Wiley, New York, pp 63
52. Buenker RJ, Peyerimhoff SD, Butscher W (1978) Mol Phys 35:771
53. Karwowski JA, Shavitt I (2003) Configuration interaction. In: Wilson S (ed) Handbook of molecular physics and quantum chemistry. Wiley, Chichester, p 227
54. Werner H-J, Knowles PJ (1988) J Chem Phys 89:5803
55. Finley J, Malmqvist PA, Roos BO, Serrano-Andrés L (1998) Chem Phys Lett 288:299
56. Lischka H, Dallos M, Shepard R (2002) Mol Phys 100:1647
57. Lengsfield BH, Saxe P, Yarkony DR (1984) J Chem Phys 81:4549
58. Celani P, Werner HJ (2003) J Chem Phys 119:5044
59. Lischka H, Dallos M, Szalay PG, Yarkony DR, Shepard R (2004) J Chem Phys 120:7322
60. Szymczak JJ, Barbatti M, Lischka H (2011) Int J Quantum Chem 111:3307
61. Slavicek P, Martinez T (2010) J Chem Phys 132:234102
62. Müller T, Dallos M, Lischka H (1999) J Chem Phys 110:7176
63. Angeli C (2009) J Comput Chem 30:1319
64. Ghigo G, Roos BO, Malmqvist P-A (2004) Chem Phys Lett 396:142
65. Bomble YJ, Sattelmeyer KW, Stanton JF, Gauss J (2004) J Chem Phys 121:5236
66. Bauernschmitt R, Ahlrichs R (1996) Chem Phys Lett 256:454
67. Casida M (1995) Time-dependent density functional response theory for molecules. In: Chong D (ed) Recent advances in density functional methods. Part I. World Scientific, Singapore, p 155
68. Frank I, Hutter J, Marx D, Parrinello M (1998) J Chem Phys 108:4060
69. Filatov M, Shaik S (1999) Chem Phys Lett 304:429
70. Elstner M (2006) Theor Chem Acc 116:316
71. Grimme S, Waletzke M (1999) J Chem Phys 111:5645
72. Beck EV, Stahlberg EA, Burggraf LW, Blaudeau J-P (2008) Chem Phys 349:158
73. Furche F, Ahlrichs R (2002) J Chem Phys 117:7433
74. Send R, Furche F (2010) J Chem Phys 132:044107
75. Tavernelli I, Curchod BFE, Rothlisberger U (2009) J Chem Phys 131:196101
76. Werner U, Mitric R, Suzuki T, Bonacic-Koutecký V (2008) Chem Phys 349:319
77. Tapavicza E, Tavernelli I, Rothlisberger U (2007) Phys Rev Lett 98:023001
78. Barbatti M, Pittner J, Pederzoli M, Werner U, Mitric R, Bonacic-Koutecky V, Lischka H (2010) Chem Phys 375:26
79. Becke A (1993) J Chem Phys 98:5648
80. Perdew J, Burke K, Ernzerhof M (1996) Phys Rev Lett 77:3865
81. Adamo C, Barone V (1999) J Chem Phys 110:6158
82. Zhao Y, Truhlar D (2008) Theor Chem Acc 119:525
83. Dreuw A, Head-Gordon M (2005) Chem Rev 105:4009
84. Peach MJG, Helgaker T, Salek P, Keal TW, Lutnaes OB, Tozer DJ, Handy NC (2005) Phys Chem Chem Phys 8:558
85. Yanai T, Tew DP, Handy NC (2004) Chem Phys Lett 393:51
86. Granucci G, Persico M, Toniolo A (2001) J Chem Phys 114:10608
87. Koslowski A, Beck ME, Thiel W (2003) J Comput Chem 24:714
88. Silva-Junior MR, Thiel W (2010) JCTC 6:1546
89. Worth GA, Cederbaum LS (2004) Annu Rev Phys Chem 55:127
90. Kosloff R (1994) Annu Rev Phys Chem 45:145
91. Schneider R, Domcke W, Koppel H (1990) J Chem Phys 92:1045
92. Worth GA, Meyer HD, Cederbaum LS (2004) Conical intersections: electronic structure, dynamics and spectroscopy. Advanced series in physical chemistry. World Scientific Publishing Company, Singapore
93. Worth GA, Hunt P, Robb MA (2003) J Phys Chem A 107:621
94. Santoro F, Lami A, Olivucci M (2007) Theor Chem Acc 117:1061
95. Ben-Nun M, Quenneville J, Martínez TJ (2000) J Phys Chem A 104:5161
96. Tully JC (1990) J Chem Phys 93:1061
97. Granucci G, Persico M (2007) J Chem Phys 126:134114
98. Martínez TJ (2006) Acc Chem Res 39:119
99. Barbatti M, Shepard R, Lischka H (2011) Computational and methodological elements for nonadiabatic trajectory dynamics simulations of molecules. In: Domcke W, Yarkony DR, Köppel H (eds) Conical Intersections: theory, computation and experiment. advanced series in physical chemistry, vol 17. World Scientific, Singapore
100. Barbatti M (2011) WIREs Comp Mol Sci 1:620
101. Barbatti M, Granucci G, Persico M, Ruckenbauer M, Vazdar M, Eckert-Maksic M, Lischka H (2007) J Photochem Photobiol. A 190:228

102. Hsu C (2009) Acc Chem Res 42:509
103. Valeev E, Coropceanu V, da Silva D, Salman S, Bredas J (2006) J Am Chem Soc 128:9882
104. Plasser F, Lischka H (2011) J Chem Phys 134:034309
105. Voityuk A, Rosch N (2002) J Chem Phys 117:5607
106. Nachtigallova D, Hobza P, Ritze H (2008) Phys Chem Chem Phys 10:5689
107. Tamura H, Mallet J, Oheim M, Burghardt I (2009) J Phys Chem C 113:7548
108. Krueger B, Scholes G, Fleming G (1998) J Phys Chem B 102:5378
109. Kubar T, Elstner M (2008) J Phys Chem B 112:8788
110. Sterpone F, Martinazzo R, Panda A, Burghardt I (2011) Zeitschrift fuer Physikalische Chemie 225:541
111. Scholes G, Jordanides X, Fleming G (2001) J Phys Chem B 105:1640
112. Brunschwig BS, Logan J, Newton MD, Sutin N (1980) J Am Chem Soc 102:5798
113. Ruckenbauer M, Barbatti M, Muller T, Lischka H (2010) J Phys Chem A 114:6757
114. Barbatti M, Aquino AJA, Szymczak JJ, Nachtigallová D, Hobza P, Lischka H (2010) Proc Natl Acad Sci USA 107:21453
115. Lan Z, Fabiano E, Thiel W (2009) J Phys Chem B 113:3548
116. Groenhof G, Schafer LV, Boggio-Pasqua M, Goette M, Grubmuller H, Robb MA (2007) J Am Chem Soc 129:6812
117. Alexandrova AN, Tully JC, Granucci G (2010) J Phys Chem B 114:12116
118. Sobolewski AL, Domcke W, Hättig C (2005) Proc Natl Acad Sci USA 102:17903
119. Crespo-Hernández CE, Cohen B, Hare PM, Kohler B (2004) Chem Rev 104:1977
120. Canuel C, Mons M, Piuzzi F, Tardivel B, Dimicoli I, Elhanine M (2005) J Chem Phys 122:074316
121. Marian CM (2007) J Phys Chem A 111:1545
122. Kistler KA, Matsika S (2007) J Phys Chem A 111:2650
123. Yamazaki S, Domcke W, Sobolewski AL (2008) J Phys Chem A 112:11965
124. Blancafort L, Bearpark MJ, Robb MA (2008) Computational modeling of cytosine photophysics and photochemistry: from the gas phase to DNA. In: Shukla MK, Leszczynski J (eds) Radiation induced molecular phenomena in nucleic acid. Challenges and advances in computational chemistry and physics. Springer, The Netherlands
125. Picconi D, Barone V, Lami A, Santoro F, Improta R (2011) Chem Phys Chem 12:1957
126. Doltsinis NL, Markwick PRL, Nieber H, Langer H (2008) Ultrafast radiationless decay in nucleic acids: insights from nonadiabatic ab initio molecular dynamics. In: Shukla MK, Leszczynski J (eds) Radiation induced molecular phenomena in nucleic acids, vol 5. Challenges and advances in computational chemistry and physics. Springer, Netherlands, p 265
127. Hudock HR, Martinez TJ (2008) Chemphyschem 9:2486
128. Barbatti M, Aquino AJA, Szymczak JJ, Nachtigallova D, Lischka H (2011) Phys Chem Chem Phys 13:6145
129. González-Vázquez J, González L (2010) Chemphyschem 11:3617
130. Bergsma JP, Berens PH, Wilson KR, Fredkin DR, Heller EJ (1984) J Phys Chem 88:612
131. Lukes V, Solc R, Milota F, Sperling J, Kauffmann HF (2008) Chem Phys 349:226
132. Crespo-Hernandez C, Cohen B, Kohler B (2005) Nature 436:1141
133. Vaya I, Miannay F, Gustavsson T, Markovitsi D (2010) Chemphyschem 11:987
134. Buchvarov I, Wang Q, Raytchev M, Trifonov A, Fiebig T (2007) Proc Natl Acad Sci USA 104:4794
135. Schwalb N, Temps F (2008) Science 322:243
136. Santoro F, Barone V, Improta R (2009) J Am Chem Soc 131:15232
137. Kozak C, Kistler K, Lu Z, Matsika S (2010) J Phys Chem B 114:1674
138. Olaso-Gonzalez G, Merchan M, Serrano-Andres L (2009) J Am Chem Soc 131:4368
139. Lange A, Herbert J (2009) J Am Chem Soc 131:3913
140. Santoro F, Barone V, Lami A, Improta R (2010) Phys Chem Chem Phys 12:4934
141. Aquino AJA, Nachtigallova D, Hobza P, Truhlar DG, Hattig C, Lischka H (2011) J Comput Chem 32:1217
142. Nachtigallova D, Zeleny T, Ruckenbauer M, Muller T, Barbatti M, Hobza P, Lischka H (2010) J Am Chem Soc 132:8261
143. Zeleny T, Hobza P, Nachtigallova D, Ruckenbauer M, Lischka H (2011) Collect Czech Chem Commun 76:631
144. Abo-Riziq A, Grace L, Nir E, Kabelac M, Hobza P, de Vries M (2005) Proc Natl Acad Sci USA 102:20
145. Giese B, Amaudrut J, Kohler A, Spormann M, Wessely S (2001) Nature 412:318
146. Jortner J, Bixon M, Langenbacher T, Michel-Beyerle M (1998) Proc Natl Acad Sci USA 95:12759
147. Ye Y, Chen R, Martinez A, Otto P, Ladik J (1999) Solid State Commun 112:139
148. Blancafort L, Voityuk A (2006) J Phys Chem A 110:6426
149. Roca-Sanjuan D, Olaso-Gonzalez G, Coto P, Merchan M, Serrano-Andres L (2010) Theor Chem Acc 126:177
150. Warshel A (1976) Nature 260:679
151. Hoffmann M, Wanko M, Strodel P, Konig PH, Frauenheim T, Schulten K, Thiel W, Tajkhorshid E, Elstner M (2006) J Am Chem Soc 128:10808
152. Wanko M, Hoffmann M, Strodet P, Koslowski A, Thiel W, Neese F, Frauenheim T, Elstner M (2005) J Phys Chem B 109:3606
153. Rohrig UF, Guidoni L, Rothlisberger U (2005) Chemphyschem 6:1836
154. Altun A, Morokuma K, Yokoyama S (2011) ACS Chem Biol 6:775
155. Altoè P, Cembran A, Olivucci M, Garavelli M (2010) Proc Natl Acad Sci 107:20172
156. Szymczak JJ, Barbatti M, Lischka H (2009) J Phys Chem A 113:11907
157. Garavelli M (2006) Theor Chem Acc 116:87
158. Sumita M, Ryazantsev MN, Saito K (2009) Phys Chem Chem Phys 11:6406
159. Keal T, Wanko M, Thiel W (2009) Theor Chem Acc 123:145
160. Weingart O, Schapiro I, Buss V (2006) J Mol Model 12:713
161. Burghardt I, Cederbaum LS, Hynes JT (2004) Faraday Discuss 127:395
162. Send R, Sundholm D (2007) J Phys Chem A 111:8766
163. Valsson O, Filippi C (2010) JCTC 6:1275
164. Oregan B, Gratzel M (1991) Nature 353:737
165. Odobel F, Le Pleux L, Pellegrin Y, Blart E (2010) Acc Chem Res 43:1063
166. Collini E, Scholes G (2009) Science 323:369
167. Bredas J, Silbey R (2009) Science 323:348
168. Nayyar I, Batista E, Tretiak S, Saxena A, Smith D, Martin R (2011) J Phys Chem Lett 2:566
169. Jones G, Carpenter B, Paddon-Row M (1998) J Am Chem Soc 120:5499
170. Park S, Roy A, Beaupre S, Cho S, Coates N, Moon J, Moses D, Leclerc M, Lee K, Heeger A (2009) Nat Photonics 3:297
171. Baruah T, Pederson M (2009) J Chem Theory Comput 5:834
172. Spallanzani N, Rozzi C, Varsano D, Baruah T, Pederson M, Manghi F, Rubio A (2009) J Phys Chem B 113:5345
173. Hanna M, Nozik A (2006) J Appl Phys 100:074510

174. Zimmerman P, Zhang Z, Musgrave C (2010) Nat Chem 2:648
175. Siebbeles L (2010) Nat Chem 2:608
176. Balaban T (2005) Acc Chem Res 38:612
177. Zhao Y, Ikeda T (2009) Smart light-responsive materials: azobenzene-containing polymers and liquid crystals. Wiley-Interscience, Hoboken
178. Carstensen O, Sielk J, Schonborn JB, Granucci G, Hartke B (2010) J Chem Phys 133:124305
179. Manz J, Sundermann K, de Vivie-Riedle R (1998) Chem Phys Lett 290:415
180. Crespo-Otero R, Barbatti M (2011) J Chem Phys 134:164305
181. Schriever C, Barbatti M, Stock K, Aquino AJA, Tunega D, Lochbrunner S, Riedle E, de Vivie-Riedle R, Lischka H (2008) Chem Phys 347:446
182. Plasser F, Barbatti M, Aquino AJA, Lischka H (2009) J Phys Chem A 113:8490
183. Aquino AJA, Lischka H, Hattig C (2005) J Phys Chem A 109:3201
184. Sobolewski A (2008) Phys Chem Chem Phys 10:1243
185. Koumura N, Geertsema E, van Gelder M, Meetsma A, Feringa B (2002) J Am Chem Soc 124:5037
186. Weingart O, Lan Z, Koslowski A, Thiel W (2011) J Phys Chem Lett 2:1506
187. Pederzoli M, Pittner J, Barbatti M, Lischka H (2011) J Phys Chem A 115:11136
188. Sobolewski AL, Domcke W, Hattig C (2006) J Phys Chem A 110:6301
189. Ben-Nun M, Martínez TJ (2000) Chem Phys 259:237
190. Barbatti M, Aquino AJA, Lischka H (2006) Mol Phys 104:1053
191. Ruiz DS, Cembran A, Garavelli M, Olivucci M, Fuss W (2002) Photochem Photobiol 76:622
192. Bearpark MJ, Bernardi F, Clifford S, Olivucci M, Robb MA, Vreven T (1997) J Phys Chem A 101:3841
193. Cattaneo P, Persico M (1999) Phys Chem Chem Phys 1:4739
194. Li Q, Mendive-Tapia D, Paterson MJ, Migani A, Bearpark MJ, Robb MA, Blancafort L (2010) Chem Phys 377:60
195. Marian CM (2005) J Chem Phys 122:104314
196. Merchan M, Gonzalez-Luque R, Climent T, Serrano-Andres L, Rodriuguez E, Reguero M, Pelaez D (2006) J Phys Chem B 110:26471
197. Barbatti M, Paier J, Lischka H (2004) J Chem Phys 121:11614
198. Wilsey S, Houk KN (2002) J Am Chem Soc 124:11182
199. Antol I, Eckert-Maksic M, Barbatti M, Lischka H (2007) J Chem Phys 127:234303
200. Perun S, Sobolewski AL, Domcke W (2006) J Phys Chem A 110:13238
201. Lan ZG, Fabiano E, Thiel W (2009) Chemphyschem 10:1225
202. Barbatti M, Vazdar M, Aquino AJA, Eckert-Maksic M, Lischka H (2006) J Chem Phys 125:164323
203. Sobolewski AL, Domcke W (2000) Chem Phys 259:181
204. Perun S, Sobolewski AL, Domcke W (2005) Chem Phys 313:107
205. Salzmann S, Kleinschmidt M, Tatchen J, Weinkauf R, Marian CM (2008) Phys Chem Chem Phys 10:380
206. Fuji T, Suzuki Y-I, Horio T, Suzuki T, Mitric R, Werner U, Bonacic-Koutecky V (2010) J Chem Phys 133:234303
207. Barbatti M, Lischka H, Salzmann S, Marian CM (2009) J Chem Phys 130:034305
208. Schreiber M, Silva MR, Sauer SPA, Thiel W (2008) J Chem Phys 128:134110
209. Silva-Junior MR, Schreiber M, Sauer SPA, Thiel W (2010) J Chem Phys 133:174318
210. Fleig T, Knecht S, Hättig C (2007) J Phys Chem A 111:5482
211. Parac M, Grimme S (2002) J Phys Chem A 106:6844
212. Silva-Junior MR, Schreiber M, Sauer SPA, Thiel W (2008) J Chem Phys 129:104103
213. Peach MJG, Benfield P, Helgaker T, Tozer DJ (2008) J Chem Phys 128:044118
214. Zhao Y, Truhlar DG (2006) J Phys Chem A 110:13126
215. Perdew JP, Ruzsinszky A, Constantin LA, Sun JW, Csonka GI (2009) JCTC 5:902
216. Jacquemin D, Wathelet Vr, Perpète EA, Adamo C (2009) JCTC 5:2420
217. Parac M, Grimme S (2003) Chem Phys 292:11
218. Lin H, Truhlar DG (2007) Theor Chem Acc 117:185
219. Senn HM, Thiel W (2009) Angew Chem Int Ed Engl 48:1198
220. Doltsinis NL (2002) Nonadiabatic dynamics: mean-field and surface hopping. In: Grotendorst J, Marx D, Muramatsu A (eds) Quantum simulations of complex many-body systems: from theory to algorithms, vol 10. NIC Series. John von Neumann Institute for Computing, Julich
221. Levine BG, Martínez TJ (2007) Annu Rev Phys Chem 58:613
222. Barbatti M, Ruckenbauer M, Szymczak JJ, Aquino AJA, Lischka H (2008) Phys Chem Chem Phys 10:482
223. Migani A, Olivucci M (2004) Conical intersections and organic reaction mechanisms. In: Domcke W, Yarkony DR, Köppel H (eds) conical intersections: electronic structure, dynamics and spectroscopy. World Scientific Publishing Company, Singapore

3.2 Gradients and Non-adiabatic Couplings for State-Averaged MCSCF

The first major methodological effort was concerned with the implementation of electronic energy gradients and non-adiabatic coupling vectors at the state-averaged multi-configuration self-consistent field (SA-MCSCF) level (see also Section 2.2.2) into the COLUMBUS package. [80] Whereas the functionality had already been available within the formalism of multi-reference configuration interaction (MR-CI) calculations, [40, 81–83] significant computational overhead was present rendering many interesting calculations impossible. By writing a direct interface between the SA-MCSCF wavefunction optimization and the gradient programs and by explicitly considering simplifications in the gradient formalism arising due to SA-MCSCF, significant improvements in the algorithm could be made as far as time, memory and the general stability of the approach are concerned.

The project was carried out with the help and supervision of H. Lischka. In addition the COLUMBUS developers T. Müller from the Jülich Supercomputing Centre and R. Shepard from Argonne National Laboratory, Illinois provided significant assistance for carrying out this work.

3.2.1 Gradients

Some general considerations regarding electronic energy gradients were described in Section 2.1.6. In the context of SA-MCSCF the important point is that the CI coefficients for each state are optimized in a variational way. However, the orbitals are chosen as to minimize the average energy and are not optimal for any individual state. Therefore not only the left term in Eq. (2.58) pertaining to the derivative of the Hamiltonian has to be evaluated, but also the response of the orbital coefficients with respect to the geometry change has to be considered.

The overall formalism for computing the MR-CI gradient is quite involved due to its generality allowing a large amount of flexibility in the MCSCF and MR-CI expansion space definitions. This formalism is described in detail in Refs [40,82,83]. In particular the derivatives of the orbital resolution conditions, which are needed

if the MCSCF and MR-CI active spaces differ, add complexity. However, for simple SA-MCSCF gradients this is not the case and the orbital resolution terms will be omitted in the following text. Considering Eq. (2.58) the important quantities aside from the density matrices are the wavefunction gradient of state ϕ

$$f_i^\phi = \partial \tilde{E}_{\mathbf{R}}^\phi(\mathbf{s_R})/\partial s_i \tag{3.1}$$

and the SA-MCSCF response $\partial \mathbf{s_R}/\partial R_k$. The $\mathbf{f}^\phi$ vector is computed from the generalized Fock matrix defined as [83]

$$F_{rs}^\phi = \sum_t h_{rt} D_{ts}^{\phi\phi} + \sum_{tuv} g_{rtuv} d_{stuv}^{\phi\phi} \tag{3.2}$$

The wave function response is computed by considering the fact that by construction, the state-averaged wavefunction gradient of the converged calculation vanishes at all geometries

$$\mathbf{f}^{ave} \equiv \mathbf{0} \tag{3.3}$$

Differentiating this equation with respect to a nuclear coordinate yields (by a similar application of the chain rule as in Eq. (2.57))

$$\frac{\partial f_i^{ave}}{\partial R_k} \mid_{\mathbf{s}=\mathbf{s_R}} + \sum_j \frac{\partial f_i^{ave}}{\partial s_j} \frac{\partial s_j}{\partial R_k} = 0 \tag{3.4}$$

where the first term is the partial derivative of the wavefunction gradient under the assumption of constant $\mathbf{s}$.

After introducing the state averaged wavefunction Hessian $\mathbf{G}^{ave}$

$$G_{ij}^{ave} = \frac{\partial f_i^{ave}}{\partial s_j} = \frac{\partial^2 E^{ave}}{\partial s_i \partial s_j} \tag{3.5}$$

Eq. (3.4) can be rewritten in matrix form

$$\frac{\partial \mathbf{s_R}}{\partial R_k} = -\left(\mathbf{G}^{ave}\right)^{-1} \frac{\partial \mathbf{f}^{ave}}{\partial R_k} \mid_{\mathbf{s}=\mathbf{s_R}} \tag{3.6}$$

When inserted into Eq. (2.58), the following expression is obtained

$$\begin{aligned} \tfrac{\partial}{\partial R_j} E_{\mathbf{R}} = \mathsf{tr}\left(\mathbf{h}^{(R_j)} \mathbf{D}(\mathbf{s_R})\right) + \tfrac{1}{2}\mathsf{tr}\left(\mathbf{g}^{(R_j)} \mathbf{d}(\mathbf{s_R})\right) - \\ - \left(\mathbf{f}^\phi\right)^T \left(\mathbf{G}^{ave}\right)^{-1} \tfrac{\partial \mathbf{f}^{ave}}{\partial R_k} \mid_{\mathbf{s}=\mathbf{s_R}} \end{aligned} \tag{3.7}$$

In the next step the coupled perturbed SA-MCSCF equation system

$$\mathbf{G}^{ave}\lambda = -\mathbf{f}^{\phi} \tag{3.8}$$

is solved to obtain the λ vector containing the response information. [84] This has to be done only once, independent of the coordinate displacement and the general equation

$$\frac{\partial}{\partial R_j} E_{\mathbf{R}} = \mathsf{tr}\left(\mathbf{h}^{(R_j)}\mathbf{D}(\mathbf{s_R})\right) + \frac{1}{2}\mathsf{tr}\left(\mathbf{g}^{(R_j)}\mathbf{d}(\mathbf{s_R})\right) + \lambda^T \frac{\partial \mathbf{f}^{ave}}{\partial R_k} \mid_{\mathbf{s}=\mathbf{s_R}} \tag{3.9}$$

is obtained. The term on the right can be expressed by using effective density matrices (consider Ref [83] for more detailed information) and the final expression for the gradient is of the form

$$\frac{\partial}{\partial R_j} E_{\mathbf{R}} = \mathsf{tr}\left(\mathbf{h}^{(R_j)}\mathbf{D}^{eff}\right) + \frac{1}{2}\mathsf{tr}\left(\mathbf{g}^{(R_j)}\mathbf{d}^{eff}\right) \tag{3.10}$$

This type of trace computation is a standard operation in quantum chemistry, implemented in several program systems. In the context of COLUMBUS the trace can be evaluated by using an interface to either the DALTON [85] or the MOLCAS [86] program packages.

3.2.2 Non-adiabatic couplings

The computation of non-adiabatic coupling terms proceeds in a similar fashion as compared to electronic energy gradients only that a few additional terms need to be computed. [40] The non-adiabatic coupling between the states ϕ and ψ along a coordinate R_k is defined as

$$h_k^{\phi\psi} := \left\langle \phi \mid \frac{\partial}{\partial R_k}\psi \right\rangle = \tag{3.11}$$

If the wavefunctions are of CI type, based on a set of configuration state functions (CSF) γ_i, the expression can be rewritten as

$$= \left\langle \sum_i c_i^{\phi}\gamma_i \mid \frac{\partial}{\partial R_k}\sum_j c_j^{\psi}\gamma_j \right\rangle = \tag{3.12}$$

After applying the product rule, the expression decomposes into two parts $h^{\phi\psi}_{k,\mathrm{CI}}$ and $h^{\phi\psi}_{k,\mathrm{CSF}}$, related to the change in the CI vector and the CSF expansion, respectively.

$$= \underbrace{\sum_{i,j} c_i^{\phi} \frac{\partial c_j^{\psi}}{\partial R_k} \underbrace{\langle \gamma_i \mid \gamma_j \rangle}_{\delta_{ij}}}_{:=h^{\phi\psi}_{k,\mathrm{CI}}} + \underbrace{\sum_{i,j} c_i^{\phi} c_j^{\psi} \left\langle \gamma_i \mid \frac{\partial}{\partial R_k} \gamma_j \right\rangle}_{:=h^{\phi\psi}_{k,\mathrm{CSF}}} \tag{3.13}$$

$h^{\phi\psi}_{k,\mathrm{CI}}$ can be rewritten by considering that $\mathbf{c}^{\phi}$ and $\mathbf{c}^{\psi}$ are eigenvectors of the CI-matrix $\mathbf{H}$

$$\mathbf{H}\mathbf{c}^{\psi} = E^{\psi}\mathbf{c}^{\psi} \tag{3.14}$$

After differentiating this equation with respect to R_k, the equation reads

$$\frac{\partial \mathbf{H}}{\partial R_k}\mathbf{c}^{\psi} + \mathbf{H}\frac{\partial}{\partial R_k}\mathbf{c}^{\psi} = \frac{\partial E^{\psi}}{\partial R_k}\mathbf{c}^{\psi} + E^{\psi}\frac{\partial}{\partial R_k}\mathbf{c}^{\psi} \tag{3.15}$$

By multiplying by $\left(\mathbf{c}^{\phi}\right)^T$ from the left the following expression is obtained

$$\left(\mathbf{c}^{\phi}\right)^T \frac{\partial \mathbf{H}}{\partial R_k}\mathbf{c}^{\psi} + E^{\phi}\left(\mathbf{c}^{\phi}\right)^T \frac{\partial}{\partial R_k}\mathbf{c}^{\psi} = 0 + E^{\psi}\left(\mathbf{c}^{\phi}\right)^T \frac{\partial}{\partial R_k}\mathbf{c}^{\psi} \tag{3.16}$$

This can be rearranged as

$$h^{\phi\psi}_{k,\mathrm{CI}} = \frac{1}{E^{\psi} - E^{\phi}}\left(\mathbf{c}^{\phi}\right)^T \frac{\partial \mathbf{H}}{\partial R_k}\mathbf{c}^{\psi} \tag{3.17}$$

This shows that $h^{\phi\psi}_{k,\mathrm{CI}}$ is closely related to the electronic energy gradient of the CI wavefunction. The term is computed in close analogy to the gradients only that transition density matrices instead of density matrices are used. [40]

The $h^{\phi\psi}_{k,\mathrm{CSF}}$ term pertains to the response of the underlying CSF expansion with respect to the change in geometry. A part of this contribution is also computed with the CI gradient program. [40] However, for the remaining contributions additional terms are needed: the anti-symmetric contribution of the one-particle transition density matrix and half differentiated overlap integrals between atomic orbitals. The former are now directly computed in the MCSCF program, the latter are available from the DALTON program. [85]

3.2.3 Implementation

Several points had to be considered for the implementation of the SA-MCSCF gradients and non-adiabatic couplings. First, the state specific density and transition density matrices for the states of interest had to be computed. This was accomplished by adapting the existing routines for considering the coupling elements in the graphical unitary group approach, realized through a "formula tape" (see also Section 2.2.2). These MCSCF density matrix elements exhibit a fairly sparse structure. If i, j, k, l are indices of doubly occupied orbitals and p, q are active orbitals the following relations hold. [31]

$$D_{ij}^{\phi\psi} = 2\delta_{ij}\delta_{\phi\psi} \tag{3.18}$$

$$d_{ijpq}^{\phi\psi} = 2D_{pq}^{\phi\psi}\delta_{ij}\delta_{\phi\psi} \tag{3.19}$$

$$d_{ipjq}^{\phi\psi} = -1/2D_{pq}^{\phi\psi}\delta_{ij}\delta_{\phi\psi} \tag{3.20}$$

$$d_{ijkl}^{\phi\psi} = \left(4\delta_{ij}\delta_{kl} - \delta_{ik}\delta_{jl} - \delta_{il}\delta_{jk}\right)\delta_{\phi\psi} \tag{3.21}$$

Moreover, all elements containing virtual orbitals or an odd number of doubly occupied orbitals vanish. By considering these relations, the MCSCF density matrix construction can be carried out quite efficiently.

Aside from the density matrix construction significant speed-ups in other parts of the algorithm could be achieved as well. In particular the Fock matrix construction (Eq. (3.2)) was rewritten in order to explicitly consider the fact that only density matrix elements with internal indices had to be considered. For this purpose not only the summation procedure but also the data structure of the direct access files had to be modified.

Subsequently in the algorithm the effective density matrices $\mathbf{D}^{eff}$ and $\mathbf{d}^{eff}$ containing non-vanishing elements with at most one external orbital come into play. A proper data structure for constructing these density matrices and for computing the effective Fock matrix deriving from them was assured.

An additional point in the algorithm was concerned with the fact that as opposed to MR-CI only MO integrals with at most two external indices are needed in the formalism (for example in the effective Fock matrix construction of Eq. (3.2) there is at most one external index for the density matrix and therefore at most two for

the integrals). The corresponding changes in the integral transformation program were carried out by T. Müller.

Through the direct computation of density matrices in the MCSCF program also a quicker route to properties of SA-MCSCF wavefunctions was made available. Changes in the program flow to allow for this were implemented as well.

3.2.4 Performance

In this section the performance of the new code is examined using two examples. First, a calculation of guanine will be presented, using SA-CASSCF(10/7) with state averaging over 3 states using the 6-31G* basis set (corresponding to 164 basis functions) and without using explicit symmetry (Figure 3.1). Two gradients and one non-adiabatic coupling vector were computed to represent one step of the optimization of a conical intersection or of a dynamics simulation, i.e. a type of calculation that has to be performed for several consecutive times in practical applications. The computations were carried out with the COLUMBUS 5.9.2 and the newly developed COLUMBUS 7.0 versions. In the former SA-MCSCF couplings were included by formally considering that SA-MCSCF can be seen as an MR-CI calculation with zero excitations. Using this construction, no extra programming effort was necessary after MR-CI gradients had been implemented. However, as shown below this may yield significant computational overhead. With COLUMBUS 5.9.2 the calculation described demanded about 34 minutes of walltime (Figure 3.1 left). The largest single component (13 min) was related to the computation of atomic integrals (cf. Eqs (2.49) and (2.50)), where in particular the derivative integrals were time consuming. Moreover, the artificial MR-CI step took about six minutes (including the four-index AO-MO transformation) and additional four minutes were consumed by the CI density computation step, where in particular an indirect algorithm used for computing the transition densities was time consuming. The remaining computation time is related to the orbital response calculation as carried out with the `cigrd.x` program (mostly deriving from Eqs (3.2) and (3.8)) and the MO-AO transformation of the density matrix elements. In the center column of Figure 3.1 the same calculation is shown, with COLUMBUS 7.0 while still using the artificial MR-CI step. The calculation time is significantly reduced

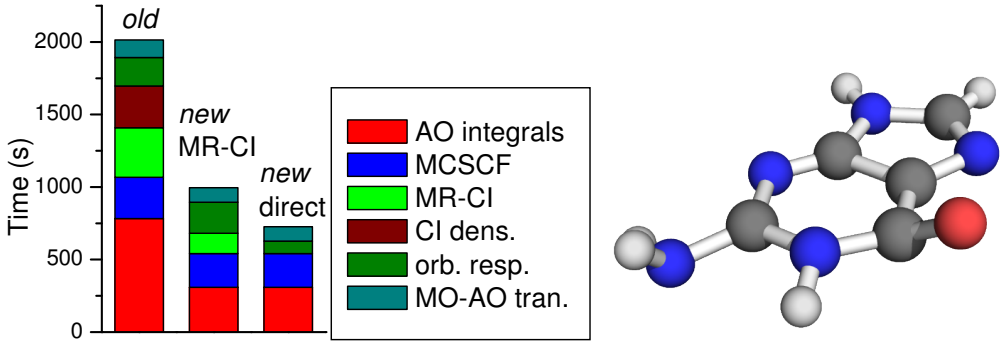

Figure 3.1: *Timing example of the new SA-MCSCF code considering Guanine in a SA(3)-CASSCF(10/7)/6-31G* calculation: the old and new programs are compared where in the latter case calculations with and without an intermediate MR-CI step were performed.*

(to about 17 min), owing mostly to a speed-up in the integral evaluation and an improved calculation of the MR-CI transition densities, both of which derives from programming work carried out by T. Müller. Using the tools developed here, it was additionally possible to skip the artificial MR-CI step and furthermore reduce the timing of the orbital response calculation, reducing the total time to about 12 min.

The second example considered was concerned with calculations on a Watson-Crick bonded guanine-cytosine base pair. For this purpose a SA-CASSCF(4/6) calculation with state averaging over 4 states was performed. Calculations were performed in C_s symmetry. The 6-31G, 6-31G*, and 6-31+G* basis sets with 191, 286, and 362 basis functions, respectively, were considered. The timing for one step in a geometry optimization of the ground state was considered. These calculations were carried out with the COLUMBUS 7.0 program using the algorithm with the intermediate MR-CI step as well as the direct SA-MCSCF gradient as implemented within this work. When using the 6-31G basis set, both algorithms perform satisfactorily but some computational overhead is present: with and without intermediate MR-CI step the timing amounts to about 14 and 10 min, respectively. When using the larger 6-31G* basis set the computational effort is increased significantly. The step, which is mostly affected, is the orbital response

Table 3.1: *Walltimes (seconds, CPU-times in parentheses) of the main steps involved in the orbital response calculations.*

	6-31G		6-31G*	
step	MR-CI	direct	MR-CI	direct
2-el. int. sort	28 (15)	4 (4)	233 (57)	18 (11)
Fockmatrix ($\mathbf{F}^{\phi}$) [a]	51 (22)	4 (4)	423 (108)	10 (10)
Equ. system [b]	13 (10)	15 (5)	210 (32)	39 (14)
density update	5 (5)	2 (2)	88 (15)	5 (4)
eff. Fockmatrix [c]	20 (20)	9 (9)	674 (111)	86 (41)
total	119 (73)	33 (24)	1638 (325)	159 (82)

[a] Eq. (3.2)

[b] Eq. (3.8)

[c] analogous to Eq. (3.2) but with eff. density matrix

calculation after the MR-CI step: the timing of this procedure is almost increased by a factor of 15 as compared to the 6-31G basis set, constituting the most time-consuming step in this calculation. By contrast in the optimized program this step amounts to virtually no additional effort to the computation as compared to the integral evaluation and MCSCF wavefunction optimization. An analysis of the major steps leading to the difference in performance between the two algorithms is presented in Table 3.1. The first observation in this context is that the new program yields significant improvements in all five major time consuming steps. This happens on the level of CPU time because the number of terms evaluated is reduced by discarding terms, which are zero in the case of SA-MCSCF. Moreover the ratio between CPU-time and walltime is improved. This follows from the fact that the direct access files containing the integral and density distributions were reduced in size to contain only the relevant terms, thus significantly reducing the amount of disc I/O necessary. For comparison, also the timings of a calculation using the 6-31+G* basis set presented (in this case only using the direct algorithm). By using 24 GB of shared memory and the high performance file system of the Vienna Scientific Cluster, this larger calculation can be carried out at a reasonable effort. An important point in this context is that the orbital response calculation consumes less time than even one MCSCF iteration.

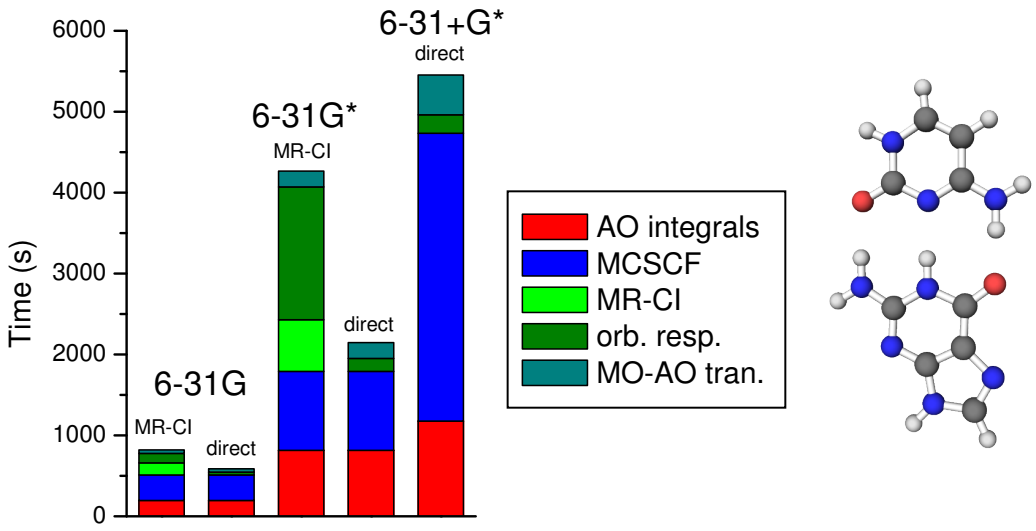

Figure 3.2: *Timing example of the new SA-MCSCF code considering a GC base pair in a SA(4)-CASSCF(4/6) calculation with different basis sets: calculations with and without an intermediate MR-CI step were performed using* COLUMBUS *7.0.*

In summary it could be shown that the new code may significantly reduce computation times for SA-MCSCF gradient and non-adiabatic coupling evaluations. This is true in particular for larger basis sets with a significant number of virtual orbitals. In the cases shown the orbital response step demanded only negligible computational effort as compared to the remaining steps. In addition to the developments described in this work, a significant speed-up was also gained through improvements in the derivative integral evaluation code, carried out at the same time. These developments open possibilities for new highly interesting applications that were inconceivable with the older program version.

3.3 Semiclassical Dynamics Simulations of Charge Transport in the Ethylene Dimer Radical Cation

The first paper published within this project was concerned with charge transfer dynamics in stacked π-systems. The ethylene dimer radical cation was chosen as a model system, which was favorable in several ways. Due to the small size an extensive testing of computational models was possible and because of the smaller number of degrees of freedom meaningful sampling of the active coordinates could be achieved. The work provided major insight into the general physics of charge transport as well as into its description with surface hopping dynamics. The results of the simulation were compared with non-adiabatic Marcus theory, giving a quite satisfactory agreement between both approaches. However, a possible shortcoming of surface hopping dynamics in its standard formalism was identified, which may be present when the couplings are too highly peaked. This problem and its solution will be discussed in more detail in the next section.

The article was published in the *Journal of Chemical Physics*. [87] My contribution to this project was carrying out the computations and to a large part I also provided the connections between the dynamical surface hopping and the global Marcus theory type representation of the processes occuring.

Semiclassical dynamics simulations of charge transport in stacked π-systems

Felix Plasser[a] and Hans Lischka[b]
Institute for Theoretical Chemistry – University of Vienna, Waehringerstrasse 17, A 1090 Vienna, Austria

(Received 18 August 2010; accepted 23 November 2010; published online 20 January 2011)

Charge transfer processes within stacked π-systems were examined for the stacked ethylene dimer radical cation with inclusion of a bridge containing up to three formaldehyde molecules. The electronic structure was treated at the complete active space self-consistent field and multireference configuration interaction levels. Nonadiabatic interactions between electronic and nuclear degrees of freedom were included through semiclassical surface hopping dynamics. The processes were analyzed according to fragment charge differences. Static calculations explored the dependence of the electronic coupling and on-site energies on varying geometric parameters and on the inclusion of a bridge. The dynamics simulations gave the possibility for directly observing complex charge transfer and diabatic trapping events. © *2011 American Institute of Physics*. [doi:10.1063/1.3526697]

I. INTRODUCTION

The dynamics of charge migration in molecular systems have attracted widespread interest. For example, the transport of electron holes has been studied in DNA because of its relation to oxidative damage[1] but also because DNA might provide interesting prototypes for nanoelectronics.[2] Charge dynamics plays an important role also in organic electronics.[3] Therefore, it is highly desirable to get more detailed physical insight into this important class of processes. Based on computational studies and charge injection experiments it has been proposed that a coherent superexchange mechanism with no or little[4] involvement of the bridge is involved between stacked nucleobases if the bridge length is three bases or less whereas charge transfer over longer distances should occur through an incoherent hopping mechanism.[5]

The general features of a system governed by a defect localized on two interacting fragments are shown in Scheme 1. The on-site energies of the initial and final charge-localized (diabatic) states H_{ii}^{diab} and H_{ff}^{diab} are represented as displaced parabolas along the reaction coordinate ξ. The reorganization energy λ, is the energy needed for moving the system from one diabatic minimum to the other while maintaining the initial diabatic character (in a symmetric system this is equivalent to the vertical excitation at one minimum). The interaction between the two diabatic states is given by the coupling matrix element H_{if}^{diab}. Diagonalization of the two-dimensional $\mathbf{H}$ matrix yields the adiabatic energies E_1^{ad} and E_2^{ad} of the ground and first excited electronic states. In the case of strong interaction [$H_{if}^{\text{diab}} > \lambda/2$; Scheme 1(a)], E_1^{ad} as a function of ξ possesses one symmetric minimum where the eigenfunction of $\mathbf{H}$ is delocalized. If the interaction is weaker [$H_{if}^{\text{diab}} < \lambda/2$; Scheme 1(b)], two minima are present where the charge is localized on either side. If the coupling is strong, the states are well separated and adiabatic dynamics on the ground state occurs. In the weak coupling limit, on the other hand, the diabatic character is nearly always preserved and the interaction between the states can be treated as a small perturbation. In this case, the rate of transfer can be described by the semiclassical Marcus–Levich–Hush (MLH) equation.[6–9] A more detailed explanation of this relation and its connection to our dynamics simulations will be given in Sec. II. Extensions of the MLH equation include corrections for quantum effects for selected normal modes, but these are usually important only for low temperatures (below 100 K) or in the Marcus-inverted region.[7,8,10] No simple approach exists in the region of $H_{if}^{\text{diab}} \approx \lambda/2$.[10] This region which may be treated by explicit nonadiabatic dynamics simulations is the focus of this work.

In the usual approach, the parameters are estimated from static calculations and then inserted into the MLH equation.[11] One difficulty in this procedure is the fact that the description of open-shell cationic systems is highly challenging and there are problems with many of the standard methods in quantum chemistry. A major problem is an artificial localization of the hole, which means that the wave function obtained does not represent the true adiabatic ground state of the system. This has been observed in the case of polycyclic organic radical cations for unrestricted Hartree–Fock,[12] as well as for single reference configuration interaction and second-order Møller–Plesset perturbation theory.[13] Unrestricted B3LYP gave the opposite trend of overstabilizing the charge-delocalized structures.[12] Several indirect approaches have been developed in an attempt to overcome these deficiencies. To avoid the problems of describing the charged system directly, calculations have been carried out in the neutral systems and one-electron Koopmans'-type considerations were used for calculating the CT parameters.[14–16] Other ideas involve spin-flipping to give equal orbital occupations or unrestricted Hartree–Fock to represent diabatic states.[16] Diabatization may be induced through constrained density functional theory as well.[11,17] In spite of the fact that all these ways to approach the problem give good results in

[a]Electronic mail: felix.plasser@univie.ac.at.
[b]Electronic mail: hans.lischka@univie.ac.at.

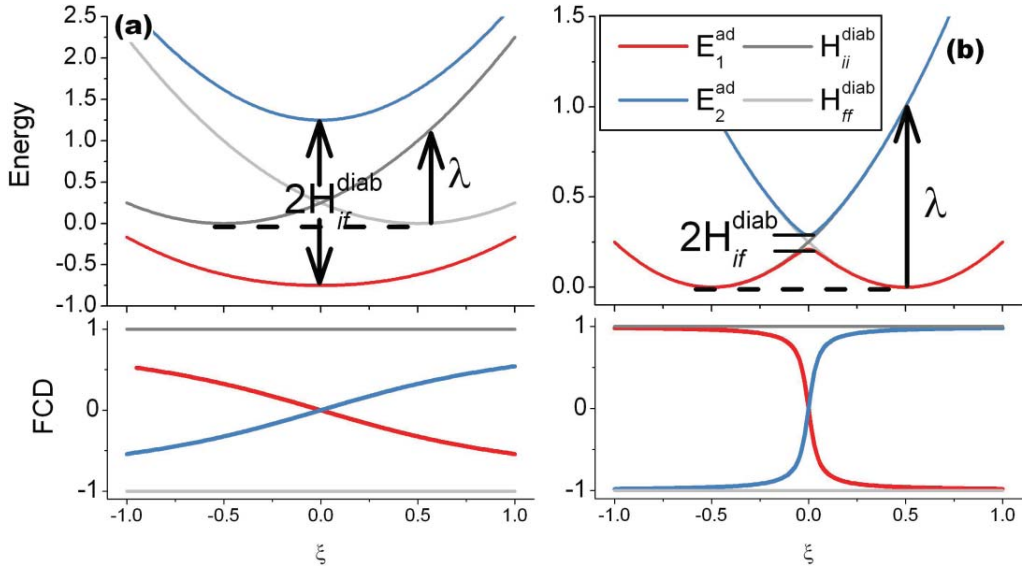

SCHEME 1. Model potential energy curves and fragment charge differences (FCD) plotted against the reaction coordinate ξ for a defect distributed over two interacting fragments for the cases of (a) strong and (b) weak coupling.

some cases, they suffer from the fact that *ad hoc* assumptions are needed. Recent investigations show that there is reasonable agreement but that Koopmans' theorem overestimates the energy gaps.[18] Another problem is the static approach relying on the assumptions made in the derivation of the MLH equation, i.e., validity of the weak coupling limit, constant coupling, and a fixed form of the potential. Force-field molecular dynamics in connection with semiempirical methods have been performed to efficiently sample the large conformational spaces of the DNA structure and to calculate the electronic coupling elements,[4,15] but these methods suffer from the fact that they do not couple nuclear and electronic dynamics in a consistent way. Note that models from solid state physics have been used as well, in particular for DNA. Then molecular motion and aperiodicity can cause difficulties.[2,19]

In this work, nonadiabatic dynamics simulations are used to directly couple the nuclear and electronic dynamics. The ethylene dimer radical cation with insertion of a bridge of up to three formaldehyde molecules (Scheme 2) is examined with the goal to model the principal features of charge migration in DNA. The reason for this choice is that this system is well suited for studying charge-hopping between π-systems and is also small enough to allow accurate investigation of the energy surfaces and extended dynamics simulations. The complex offers the possibility to study the major physical effects through changes in CC bond length alternation and intermolecular distance.

The use of multireference *ab initio* electronic structure computations is coupled to semiclassical dynamics. This type of approach has been used very successfully in the field of photodynamics (see, e.g., Ref. 20). But to our knowledge, *ab initio* direct descriptions of charged systems[13,18,21] and semiclassical dynamics in this context[12,22] have been performed only rarely. We perform state-averaged complete active space self-consistent-field computations (SA-CASSCF), which allow for a high-level explicit treatment of the quasi-degeneracies of the two charged states involved. Dynamical electron correlation is added through the multireference configuration interaction approach (MR-CI). The nonadiabatic coupling between electronic and nuclear degrees of freedom is directly included through semiclassical surface hopping dynamics.[23] In this way it is possible to treat the electronic structure and nonadiabatic effects simultaneously at a high level, including all internal degrees of freedom and the whole spectrum of coupling strengths between the adiabatic and nonadiabatic limits can be treated.

II. METHODS

In this section, we first briefly introduce the surface hopping method and discuss its applicability to defect dynamics. Then we elucidate how deeper physical insight may be gained

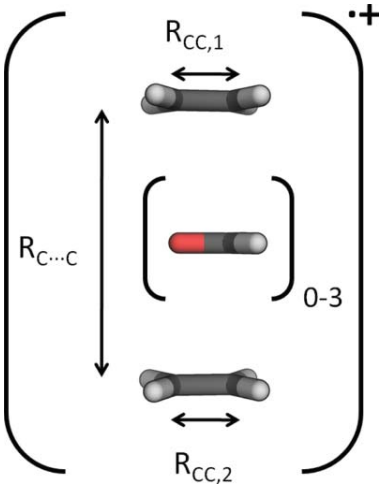

SCHEME 2. Molecular structure of $[Et.–(FA)_n–Et.]^+$ ($n = 0$–3) complexes studied in this work and definition of internal coordinates.

from this dynamics and how the results may be compared with the physical models in use.

Within the surface hopping method, nuclear motion is treated by classical dynamics coupled to forces coming from an electronic structure calculation. Several electronic states are considered simultaneously, each one associated with a complex amplitude A_k. The electronic Schrödinger equation (considering adiabatic states) is propagated in the following way:

$$\dot{A}_k(t) = -\sum_{l \neq k} A_l(t) e^{i\gamma_{kl}} \dot{\mathrm{R}} \cdot \mathrm{h}_{kl}, \tag{1}$$

$$\gamma_{kl}(t) = \frac{1}{\hbar} \int_0^t \left(E_k^{\mathrm{ad}}(\mathrm{R}(t)) - E_l^{\mathrm{ad}}(\mathrm{R}(t)) \right) dt, \tag{2}$$

$$h_{kl}^{(j)}(\mathrm{R}) = \left\langle \Psi_k^{\mathrm{ad}} \middle| \frac{\partial}{\partial R_j} \middle| \Psi_l^{\mathrm{ad}} \right\rangle. \tag{3}$$

The adiabatic electronic energies E_k^{ad} and the nonadiabatic couplings $\mathbf{h}_{kl}$ are needed for propagating the amplitudes A_k. The electronic energy gradient of the "active" or "current" state is needed for propagating the geometry $\mathbf{R}$. E_k^{ad}, $\mathbf{h}_{kl}$, and the gradient of the "active" state are computed with an appropriate electronic structure method. The essence of surface hopping is that the system follows a classical trajectory on the respective "active" state surface, while the electronic wave packet evolves according to Eq. (1). In the case of population transfer, the "active" state is changed in a stochastic manner. With this approach, the time dependent quantum mechanical coupling between nuclear and electronic degrees of freedom can be modeled in a framework of independent trajectories. For more information, see Refs. 23 and 24.

For a physical interpretation it is helpful to consider the dynamics in a two state model (cf. Refs. 8 and 14).

$$\begin{pmatrix} \Psi_1^{\mathrm{ad}} \\ \Psi_2^{\mathrm{ad}} \end{pmatrix} = U \begin{pmatrix} \Psi_i^{\mathrm{diab}} \\ \Psi_f^{\mathrm{diab}} \end{pmatrix} \tag{4}$$

$$U = \begin{pmatrix} \cos(\eta) & -\sin(\eta) \\ \sin(\eta) & \cos(\eta) \end{pmatrix} \tag{5}$$

The adiabatic ground state Ψ_1^{ad} and first excited state Ψ_2^{ad} are formed as linear combinations of two charge localized "diabatic" states Ψ_i^{diab} and Ψ_f^{diab}. The diabatic states are chosen such that Ψ_i^{diab} has the charge on the "initial" fragment and Ψ_f^{diab} on the "final" fragment. Such a construction based on physical observables will usually diminish the nonadiabatic couplings between these states and "diabaticity" should be present in this sense.[11,25] In principle, all quantities of Eqs. (4) and (5) are geometry dependent but the first approximation is to view the diabatic states as independent on molecular geometry which would, of course, make the nonadiabatic couplings vanish completely.[26] It is generally not possible to construct a set of strictly diabatic states starting from adiabatic states.[11] Therefore, a large number of approximate diabatization schemes exist.[11] In this work, the fragment charge difference (FCD) method [where Δq_i denotes the charge difference (in atomic units) between the two fragments in state i] is used for the characterization of the charge-localized states.[14,16] Under the assumption of (4), i.e., that there are just two orthogonal diabatic states involved, the following relation between the mixing angle η and the FCDs of the ground ($i = 0$) and excited ($i = 1$) state is obtained:[14]

$$-\Delta q_1(\mathbf{R}) = \Delta q_0(\mathbf{R}) = \cos(2\eta(\mathbf{R})). \tag{6}$$

Analogously to (4), the Hamiltonian may be transformed between the adiabatic and diabatic basis.

$$\begin{pmatrix} E_1^{\mathrm{ad}} & 0 \\ 0 & E_2^{\mathrm{ad}} \end{pmatrix} = U^{\mathrm{T}} \begin{pmatrix} H_{ii}^{\mathrm{diab}} & H_{if}^{\mathrm{diab}} \\ H_{if}^{\mathrm{diab}} & H_{ff}^{\mathrm{diab}} \end{pmatrix} U. \tag{7}$$

All quantities of Eq. (7) are geometry dependent. However, in analogy to the Condon approximation it is often assumed that the interaction matrix element H_{if}^{diab} is constant for fixed intermolecular distance.[10] It can then be computed as half of the energy gap at resonance conditions.[16] Note that under this assumption no conical intersection between the adiabatic states is expected to be present, as the gap may never go below $2\ H_{if}^{\mathrm{diab}}$. The geometry dependence of the on-site energies H_{ii}^{diab} and H_{ff}^{diab} can be approximated by parabolas around the respective minima (Scheme 1).[10]

Our surface hopping simulations include two adiabatic states, which can be thought of as linear combinations of the charge localized diabatic states. An adiabatic trajectory moving from one minimum (where $\eta = 0$) to the other minimum ($\eta = \pi/2$) would necessarily transfer the charge. Physically, such a charge transfer corresponds to electron tunneling. In the case of small electronic coupling H_{if}^{diab} (typically because of large spatial separation), the electron tunneling speed may be on the same order or even much slower than nuclear motion. It is therefore necessary to integrate the electronic Schrödinger equation along with the nuclear motion. Surface hopping, as described earlier, is an efficient method for such nonadiabatic treatment. Electron tunneling occurs in connection with an adiabatic nuclear dynamics [Scheme 3(a)], whereas an avoided tunneling event, i.e., diabatic trapping, is represented through two consecutive surface hops [cf. Scheme 3(b) and Ref. 22].

To get better understanding of these events it is helpful to reformulate the surface hopping equations in the two-state model. If, as described earlier, the nonadiabatic coupling between the diabatic states vanishes, the nonadiabatic coupling between the adiabatic states corresponds to the change in the mixing angle η [see also Eqs. (2.18)–(2.22) of Ref. 27].

$$h_{12}^{(i)}(\mathbf{R}) = \frac{\partial \eta(\mathbf{R})}{\partial R_i}. \tag{8}$$

Then the amplitude propagation [cf. Eq. (1)] may be rewritten

$$-\frac{\dot{A}_1(t)}{A_2(t)} = e^{i\gamma_{12}(t)} \frac{\partial \eta}{\partial t}(t). \tag{9}$$

In this formulation it can be seen that a quick change in η (relative to the speed of change in γ_{12}) is compensated by a corresponding change in the A_i's leading to no change in the diabatic character of the total time dependent electronic wave function. A charge transfer only occurs if the change in the

relative phase factor γ_{12} (which is proportional to the energy gap) is faster than the change in η.

For the analysis of the dynamics, kinetic equations as derived by Brunschwig *et al.*[8] were considered. One starts with the Eyring equation

$$k_{\mathrm{CT}} = \kappa_{\mathrm{el}} \nu e^{-\frac{\Delta G^{\neq}}{kT}}, \tag{10}$$

where κ_{el} is the electronic transmission coefficient, ν is the frequency of the active vibration, and $\Delta G^{\neq}$ is the Gibbs free activation energy. In the next step, under the assumption that the diabatic coupling is negligible, $\Delta G^{\neq}$ can be written in terms of the reaction free energy $\Delta_{\mathrm{r}}G$ and the reorganization energy λ as[9]

$$\Delta G^{\neq} = \frac{\lambda}{4}\left(1 + \frac{\Delta_r G}{\lambda}\right)^2. \tag{11}$$

In the case of a symmetric reaction potential, i.e., $\Delta_{\mathrm{r}}G = 0$, Eq. (11) reduces to

$$\Delta G^{\neq} = \frac{\lambda}{4}. \tag{12}$$

To obtain κ_{el}, one starts from the Landau[28]–Zener[29] probability

$$P_{12} = 1 - \exp\frac{-4\pi^2\left(H_{if}^{\mathrm{diab}}\right)^2}{h\mathrm{Vs}} \tag{13}$$

of performing a charge transfer (i.e., remaining on the same adiabatic surface) per single passage over the transition state where **V** is the velocity, and **s** the difference in slopes. Eq. (13) may be rewritten as

$$P_{12} = 1 - \exp\left(\frac{-\left(H_{if}^{\mathrm{diab}}\right)^2}{h\nu}\sqrt{\frac{\pi^3}{\lambda kT}}\right) \tag{14}$$

to obtain a form with more readily available quantities.[8,30]

P_{12} is the probability of a CT for a single passage over the transition state. If this CT is avoided the system has switched from the ground to the excited state. The excited state may relax through an additional *TS passage* leading to a recrossing and diabatic trapping situation. Alternatively, the system may switch to the CT product state after one or more *TS passages* in the excited state. Therefore, it may be seen that the probability κ_{el} of CT per *global TS* crossing event is higher than per single passage. Assuming that the events are independent of each other (i.e., there is no electronic coherence) and that the transition probability is the same for every TS passage, it can be written as (see also Refs. 8 and 12):

$$\begin{aligned}\kappa_{\mathrm{el}} &= P_{12} + (1 - P_{12})P_{12}(1 - P_{12}) \\ &\quad + (1 - P_{12})P_{12}^3(1 - P_{12}) + \cdots \\ &= \frac{2P_{12}}{1 + P_{12}},\end{aligned} \tag{15}$$

where the first two terms in the sum correspond to the respective processes of Scheme 3(a) and 3(c), and the remaining terms correspond to higher order events. As shown in Ref. 8, the quantities derived earlier can be combined to form the well-known Marcus–Levich–Hush equation for the charge transfer reaction constant. In this work, we will specifically focus on the electronic transmission coefficient κ_{el} and the related quantity P_{12}. These quantities are evaluated as relations between the following four elementary processes (two geometrical and two charge-transfer cases):

1. *Transition state (TS) passage*: Single passage over the TS with a sign change in the generalized reaction coordinate ξ. This coordinate is identified with the FCD (always taken for the same adiabatic state, e.g., D_0) as function of the nuclear coordinates, i.e., $\Delta q_0 = \Delta q_0(\mathbf{R})$.
2. *TS global*: This process starts in the ground state with the charge on one side and describes the overall process of reaching the TS and finally arriving in one of the potential wells of the ground state again (crossing or returning).
3. *Active charge transfer (CT)*: This is a charge transfer event in the "active" state related to a single *TS passage*. It occurs for an adiabatic process (if there is no change of state).
4. *Real CT*: This is a process related to *TS global*, which starts with the charge in the ground state on one side and finally ends with the charge in the ground state on the other side (in between several *TS passages* with or without *active CTs* may have happened).

In Scheme 3, we illustrate these processes for the hierarchy of *global TS* events arranged according to the number of *TS passages* taking place. The simplest example [Scheme 3(a)] is the adiabatic charge transfer moving from one minimum to the other, always remaining on the adiabatic ground state. The ground state FCD curve (full black line) illustrates the *TS passage* with the required sign change in the charge as discussed in item 1 above. The *active CT* is represented by the sign change of the red circles (FCD in the active state). The process is also connected with a *real CT*, i.e., a net charge transfer from one minimum to the other. The energy gap, presented on top of the FCD plot, is reduced to $2\ H_{if}^{\mathrm{diab}}$ at the avoided crossing. The diabatic trapping situation (two *TS passages*) in Scheme 3(b) starts in the left minimum. Along with the first *TS passage* (first sign change of the black FCD curve), there is a surface hopping to the excited state (a change in the adiabatic state that preserves the diabatic character) and the charge remains on the same fragment (no sign change of the FCD, red circles, and therefore, no *active CT*). On the second *TS passage*, the system hops back to the ground state into the original energy minimum. During this whole process, there is no *CT* (*real* or *active*). The next event [Scheme 3(c)] contains three *TS passages*. It starts like Scheme 3(b) but the system remains in the excited state during the second *TS passage* and the charge is transferred in the excited state (sign change of the FCD, red circles, active state is in D_1). A third *TS passage* with a hopping to the ground state brings the system diabatically to the right minimum, completing the *real CT*. The following event in this hierarchy (not shown in Scheme 3) would contain four *TS passages*, the first one with a hop to the excited state followed by two *active CTs* in the excited state and a hop to the ground state on the fourth *passage* followed by a relaxation to the initial minimum. There would be no net charge transfer and therefore no *real CT*.

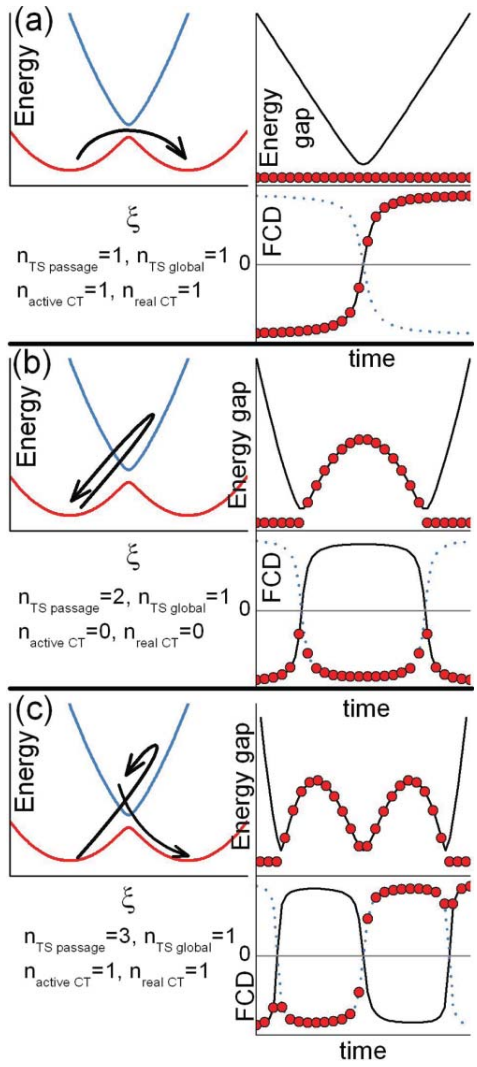

SCHEME 3. Schematic depiction of global processes around the crossing region. Left plots show the processes with respect to the reaction coordinate ξ (blue: excited state, red: ground state). Right plots show the corresponding time evolution of the energy gap and fragment charge difference (FCD) (blue dots: excited state, black line: ground state, red circles: "active" state). (a) Represents an adiabatic charge transfer; (b) a diabatic trapping situation; and (c) a higher order process, finally leading to a charge transfer.

The four processes defined earlier (*TS passage*, *TS global*, *active CT*, and *real CT*) were used to analyze the charge transfer and trapping events during the dynamics. The microscopic P_{12} probability corresponds to the fraction of *TS passages* leading to *active CTs*. It is, therefore, obtained as the ratio between the numbers of these two processes counted during the dynamics:

$$P_{12} = \frac{\mathrm{n}_{activeCT}}{\mathrm{n}_{TSpassage}}. \tag{16}$$

The macroscopic transmission coefficient κ_{el}

$$\kappa_{el} = \frac{\mathrm{n}_{realCT}}{\mathrm{n}_{TSglobal}} \tag{17}$$

is computed as the ratio between the number of *TS global* and *real CT* events. To compare theory and results, we may check if relation (15) holds with respect to these two quantities.

III. COMPUTATIONAL DETAILS

A symmetric face-to-face arrangement of the ethylene dimer radical cation [Et.–Et.]$^+$ and of this system with 1–3 formaldehyde molecules inserted [Et.–(FA)$_n$–Et.]$^+$ ($n = 1$–3) with parallel molecular planes was constructed (Scheme 2). Computations on the [Et.–Et.]$^+$ complex were generally performed with C_{2v} symmetry with the z-axis going through the molecular planes, and the y-axis parallel to the molecular CC axes (note that in the case of equal CC bond lengths the complex actually possesses D_{2h} symmetry). The main parameters of interest were the *inter*molecular C$\cdots$C distances $R_{\mathrm{C}\cdots\mathrm{C}}$ (kept at equal values for both sides) and the bond length alternation coordinate ΔR, which was formed as a difference between the two *intra*molecular CC distances

$$\Delta R = R_{CC,1} - R_{CC,2}. \tag{18}$$

Up to three formaldehyde molecules were inserted between the two ethylene molecules. The maximum symmetry of C_{2v} was chosen for the symmetric geometry, i.e., $\Delta R = 0$ (z-axis parallel to the molecular axes and the x-axis perpendicular to the molecular planes). In the displaced case, i.e., $\Delta R \neq 0$, C_{s} symmetry was used (y-axis parallel to the molecular axes and the x-axis perpendicular to the molecular planes).

State-averaged complete active space self-consistent-field (CASSCF) computations were performed for the [Et.–Et.]$^+$ and [Et.–(FA)$_n$–Et.]$^+$ ($n = 1$–3) complexes with three electrons in the four orbitals formed from the two π and two π^* orbitals of the ethylene molecules with state averaging over the doublet ground and first excited states (SA(2)-CASSCF(3/4)). State averaging was performed to get a balanced description of the two states that were obtained by removing an electron from the respective π orbital. It has been noted that this procedure can overcome spurious charge localization which many other methods suffer from.[13] This corresponded to two A_1 states in [Et.–Et.]$^+$ (C_{2v}), one B_1 and one A_1 state for the symmetric (C_{2v}), and two A′ states for the displaced (C_{s}) [Et.–(FA)$_n$–Et.]$^+$ ($n = 1$–3) complexes.

Dynamic electron correlation was taken into account through multireference configuration interaction with single and double excitations (MR-CISD). Based on previous experience gained with MRCI calculations on π systems,[31] appropriate reference spaces have been chosen. Unless specified differently, the reference space was identical to the CAS(3/4) of the preceding CASSCF calculation. To allow for a consistent treatment of different symmetry groups, no generalized interacting space restrictions were imposed and all irreducible representations of the respective symmetry group were allowed as reference symmetries. Higher-order excitations[32,33] were taken into account in single point calculations by means of corrections proposed by Pople *et al.*[34] (+P). The 6–31G*[35] and 6–311+G*[36] basis sets were used. Fragment charge differences were obtained by summing over Mulliken charges. The electronic structure computations were performed with the COLUMBUS[37] program package using electronic integrals computed with DALTON.[38]

Optimizations of [Et.–Et.]$^+$ were performed in the C_{2v} subspace, thus retaining a face-to-face arrangement. Three distances 3.0, 5.0, and 7.0 Å were chosen for $R_{\mathrm{C}\cdots\mathrm{C}}$ in

order to represent the cases of strong, intermediate, and weak coupling. For these structures, the intramolecular coordinates were optimized for the D_{2h} geometry (with $\Delta R = 0$) as well as the full minimum in C_{2v}. For the [Et.–(FA)$_n$–Et.]$^+$ (n = 1–3) complexes an intermolecular distance of 3.5 Å between adjacent molecules was chosen and a face-to-face arrangement was selected. For $n = 1$ and 2, intramolecular coordinates were optimized for the symmetric C_{2v} structure and the C_s minima. For $n = 3$, the stack was constructed without further optimization.

Nonadiabatic surface hopping dynamics simulations with Tully's fewest-switches algorithm[23] were carried out with the NEWTON-X[39,40] package. An empirical decoherence correction as described in Ref. 41 with a decay parameter of 0.1 Hartree was included to permit a more realistic treatment of recrossings through the transition region. Electronic energies, gradients, and nonadiabatic couplings[33,42] were computed at the SA(2)-CASSCF(3/4) level with the 6–311+G* basis set for [Et.-Et.]$^+$ and 6–31G*[43] for [Et.–FA–Et.]$^+$. A time step 0.5 fs was chosen. Fifty trajectories with a simulation time of 1 ps each were computed for each of the complexes. The initial conditions were chosen from a Wigner distribution of the harmonic vibrational ground state of the charge localized minimum as described in Ref. 39. To maintain a face-to-face configuration with maximal π-stacking, a restraining potential was applied to restrict relative motion of the molecules in the [Et.–Et.]$^+$ and [Et.–FA–Et.]$^+$ complexes. A harmonic potential in terms of all six, respectively 12, intermolecular normal coordinates with respect to displacement from the reference geometry was added using a spring constant of 0.5 a.u.

An automated dynamics analysis was performed to obtain P_{12} and κ_{el} [Eqs. (16) and (17)]. In the discussion, the following quantities will be used: Δq_0 for the FCD of the adiabatic ground state and Δq_{act} for the FCD of the active state of the Surface Hopping dynamics. In the analysis, a charge delocalization threshold $\alpha = 0.5$ a.u. and a relaxation time $\tau = 3$ fs are included to eliminate spurious results related to the stochastic nature of the dynamics. A *TS passage* was defined to occur if initially the condition $\Delta q_0 < -\alpha$ ($>\alpha$) held for a period of time of at least τ and then $\Delta q_0 > \alpha$ ($<-\alpha$) for at least τ. In an analogous way, an *active CT* was defined to happen if initially $\Delta q_{act} < -\alpha$ ($>\alpha$) for least τ and then $\Delta q_{act} > \alpha$ ($<-\alpha$) for at least τ. A *TS global* event starts if the trajectory is in the ground state and a *TS passage* occurs, it ends if the trajectory is again in the ground state for at least 2τ. It was considered a *real CT* if initially the trajectory was in the ground state and $\Delta q_{act} < -\alpha$ ($>\alpha$) for at least τ and then $\Delta q_{act} > \alpha$ ($<-\alpha$) with the trajectory again in the ground state for at least τ. Note that there are also times where none of the above conditions are fulfilled, e.g., $-\alpha < \Delta q < \alpha$. These parts are ignored in the analysis.

IV. RESULTS AND DISCUSSION

A. Energy surfaces

The geometrical parameters of the optimized complexes are presented in Table I (complete Cartesian geometries and energies are given in S1–S4 of the Supplemental Material[44]). For [Et.–Et.]$^+$, $R_{C\cdots C} = 3.0$ Å, there is one symmetric minimum of D_{2h} symmetry with a delocalized wave function at $R_{CC,1} = R_{CC,2} = 1.375$ Å. In all other cases considered, this symmetric structure was unstable and two minima existed with the charge localized on the longer CC bond. Only a weak dependence of the optimized $R_{CC,1}$ and $R_{CC,2}$ values on the specific complex considered was observed. Moreover, these values were similar to the ones for the isolated ethylene molecule and ethylene radical cation. Only in the [Et.–Et.]$^+$, $R_{C\cdots C} = 5.0$ Å case there is a slight reduction in ΔR (i.e., a trend toward the symmetric minimum) because of stronger coupling present. The geometrical data are not very sensitive to the inclusion of dynamic electron correlation through the MR-CISD method.

The major energetic parameters derived from these calculations (as described in the following paragraph) are collected in Table II. The electronic coupling between the diabatic states H_{if}^{diab} is the decisive quantity for determining the nonadiabatic electron transfer rate.[10,26] Here it is obtained as half the energy gap at the symmetric geometry $\Delta R = 0$.

TABLE I. Structural parameters computed at the SA-CASSCF level of theory (MR-CISD values in parentheses).[a]

		Symm ($\Delta R = 0$)		Relaxed		
Complex	$R_{C\cdots C}$ (Å)	R_{CC} (Å)		$R_{CC,1}$ (Å)	$R_{CC,2}$ (Å)	
Et.[b]				1.338 (1.342)		D_{2h}
(Et.)$^+$[b]					1.403 (1.417)	D_{2h}
[Et.–Et.]$^+$[b,d]	3.00	1.375 (1.378)	D_{2h}	–	–	
[Et.–Et.]$^+$[b]	5.00	1.377 (1.379)	D_{2h}	1.353 (1.345)	1.400 (1.414)	C_{2v}
[Et.–Et.]$^+$[b]	7.00	1.376 (1.378)	D_{2h}	1.343 (1.343)	1.409 (1.414)	C_{2v}
[Et.–FA–Et.]$^+$[c]	7.00	1.376 (1.376)	C_{2v}	1.345 (1.341)	1.407 (1.410)	C_s
[Et.–FA–FA–Et.]$^+$[c]	10.5	1.376	C_{2v}	1.343	1.408	C_s

[a]For definition of coordinates see Scheme 2.
[b]6–311+G* basis set.
[c]6–31G* basis set.
[d]Relaxed structure is symmetric in ΔR.

TABLE II. Energetic parameters of [Et.–(FA)$_n$–Et.]$^+$, (n = 0–3) complexes computed at the SA-CASSCF level of theory (MR-CISD+P values in parentheses).

Complex	$R_{C\cdots C}$ (Å)	H_{if}^{diab} (eV)	Barrier (eV)	λ (eV)
[Et.–Et.]$^+$[a]	3.00	1.1	–	–
[Et.–Et.]$^+$[a]	5.00	7.9E−2 (7.4E−2)	0.006 (0.018)	0.233 (0.314)
[Et.–Et.]$^+$[a]	7.00	4.2E−3 (4.3E−3)	0.042 (0.072)	0.236 (0.281)
[Et.–FA–Et.]$^+$[b]	7.00	3.8E−2 (3.8E−2)	0.028 (0.044)	0.239 (0.294)
[Et.–FA–FA–Et.]$^+$[b]	10.5	2.1E−3	0.059	0.247
[Et.–FA–FA–FA–Et.]$^+$[b]	14.00	1.0E−4	0.058	0.223

[a]6–311+G* basis set.
[b]6–31G* basis set.

The coupling decreases significantly with distance $R_{C\cdots C}$. In contrast, inclusion of an intermediate formaldehyde increases the coupling at constant $R_{C\cdots C}$. For example, at $R_{C\cdots C}$ = 7.0 Å the value is raised by a factor of about 10, reaching almost the coupling of the [Et.–Et.]$^+$ complex at $R_{C\cdots C}$ = 5.0 Å. For these structures, the couplings at the CASSCF level are almost identical to those of the MR-CISD+P benchmarks. The barrier of the adiabatic reaction is the most influential feature for the nuclear part of the dynamics. It was computed as the difference between ground state energy at symmetric and minimum energy geometry. The barrier for [Et.–Et.]$^+$ at $R_{C\cdots C}$ = 7.0 Å is 0.042 eV. At shorter intermolecular distances, the electronic coupling reduces this value. The barrier for [Et.–(FA)$_n$–Et.]$^+$ (n = 2,3) is somewhat larger (0.058 eV), probably because of the additional degrees of freedom present. The reorganization energy λ, computed as the energy gap between D_0 and D_1 at the minimum geometry, is presented as well. For the barrier and reorganization energy, the MR-CISD+P values are somewhat increased compared to the CASSCF values. In the cases of weaker coupling it can be seen that the relation of Eq. (12) is fulfilled, i.e., the energy barrier amounts to a fourth of the reorganization energy (Table II).

In Fig. 1, the electronic coupling between the ethylene monomers H_{if}^{diab} as a function of the intermolecular distance $R_{C\cdots C}$ is presented. In accordance with the physical model,[10] an exponential decay with increasing intermolecular distance is observed. No significant difference between CASSCF and MR-CISD+P can be seen. A direct comparison of the values

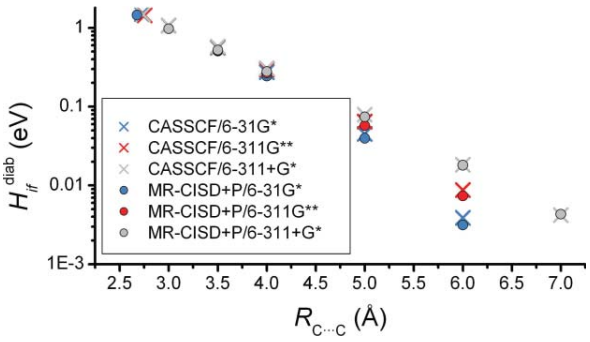

FIG. 1. Dependence of the electronic coupling on the intermolecular distance $R_{C\cdots C}$ in [Et.–Et.]$^+$, computed at the SA(2)-CASSCF(3/4) and MR-CISD+P levels with different basis sets.

(see Supplemental Material S5) shows that there is a small reduction of the gaps by about 10% when dynamical electron correlation is included. This trend has been reported in Ref. 18 as well. At small $R_{C\cdots C}$, basis set effects are negligible. At larger distances, diffuse functions become important showing that an accurate asymptotic behavior of the orbitals is important for describing the interaction.

A two-dimensional plot of the adiabatic potential energy surface of the ground state was computed at the SA(2)-CASSCF(3/4)/6–311+G* level (Fig. 2). It was constructed by first optimizing the symmetric structure at different $R_{C\cdots C}$ values. At each of these structures, the CC bond alternation [ΔR, Eq. (18)] was scanned keeping the remaining internal coordinates fixed. It is expected that $R_{C\cdots C}$ will mainly affect the coupling H_{if}^{diab} [i.e., a modulation between Scheme 1(a) and 1(b)], whereas ΔR should affect the diagonal elements H_{ii}^{diab} and H_{ff}^{diab}. At small $R_{C\cdots C}$ values, a strong coupling behavior is observed in Fig. 2. In this area, the symmetric geometry ($\Delta R = 0$) is stable with respect to changes in ΔR. At $R_{C\cdots C}$ = 2.74 Å, a pronounced symmetric minimum is located which is stabilized by 1.06 eV relative to the noninteracting system. The switch to weak coupling occurs at about $R_{C\cdots C}$ = 4.5 Å. At larger intermolecular separations, the symmetric geometry becomes unstable and two equivalent asymmetric minima are present.

A cut of this surface at $R_{C\cdots C}$ = 5.0 Å is presented in Fig. 3 (only the symmetry unique part, $\Delta R \geq 0$ is shown). In Fig. 3(a), the energies (relative to the noninteracting system) are presented. The adiabatic ground state energy surface is very flat in the neighborhood of the symmetric geometry with a shallow minimum of only 0.003 eV. Diabatic energies were computed according to Eqs. (5) and (7) with the mixing angle η taken from Eq. (6). At the symmetric geometry, one obtains $H_{ii}^{diab} = H_{ff}^{diab}$ (cf. Scheme 1) but through a change in ΔR, this degeneracy is lifted. The lower energy state forms a minimum with a well depth of 0.053 eV at ΔR = 0.06 Å. The gap at this geometry is 0.204 eV. It represents the reorganization energy between the diabatic states. The FCD is plotted in Fig. 3(b). At $\Delta R = 0$, the wave function is delocalized for symmetry reasons and the FCD is zero accordingly. With increasing asymmetry there is a gradual localization of the charge. An FCD of 0.75 is reached at about ΔR = 0.055 Å. In the ground state, the positive charge is localized on the ethylene molecule with the longer CC bond. The excited state shows the same degree of localization with the positive charge

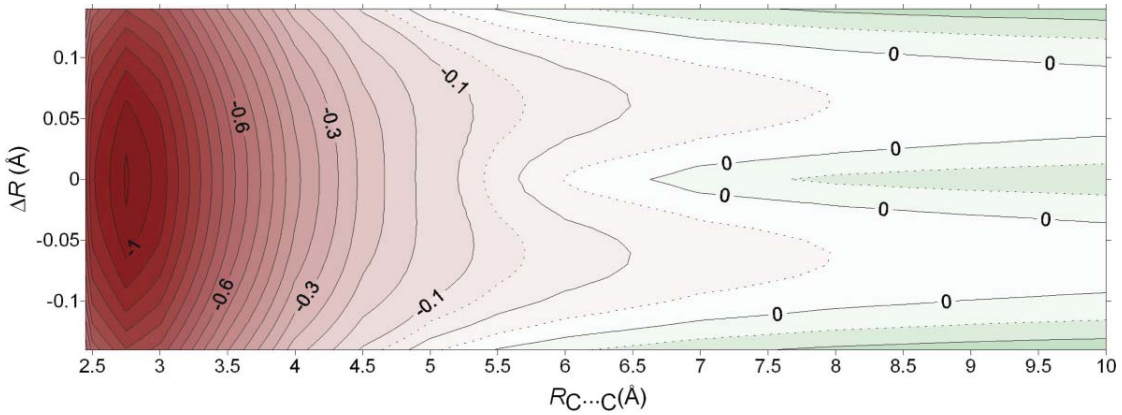

FIG. 2. Doublet ground state potential energy surface of [Et.–Et.]$^+$ (eV) with respect to intermolecular distance $R_{C\ldots C}$ and bond alternation ΔR.

located on the other ethylene molecule. In Fig. 3(c), the component of the nonadiabatic coupling vector along the bond alternation ΔR is shown. The maximum coupling of 11.7 Å^{-1} occurs at $\Delta R = 0$. It gradually decreases as the wave function becomes localized. At 0.05 Å, which is close to the energy minimum, the coupling has decreased to half the maximum value. This means that there still exists quite appreciable coupling throughout the whole region of interest in ΔR. In the two-state model, the coupling should be obtainable from the FCD [Eq. (8) with η derived from Eq. (6)]. This curve is plotted in Fig. 3(c). Very good agreement of the model curve with the directly computed coupling is obtained. It is interesting to compare these plots to the equivalent plots at the larger separation $R_{C\ldots C} = 7.0$ Å (Fig. 4). The general shape is very similar but several features are significantly altered due to the weaker coupling. There is almost no energy splitting and the adiabatic state energies are very close to the charge-localized ones [Fig. 4(a)]. Localization occurs much quicker with displacement in ΔR: an FCD value of 0.75 is already reached at $\Delta R = 0.003$ Å [Fig. 4(b)]. Another striking feature is the nonadiabatic coupling [Fig. 4(c)], which has a much more pronounced peak. The maximum at $\Delta R = 0$ is 227 Å^{-1}. A decrease to half of this value occurs already at about $\Delta R = 0.0025$ Å.

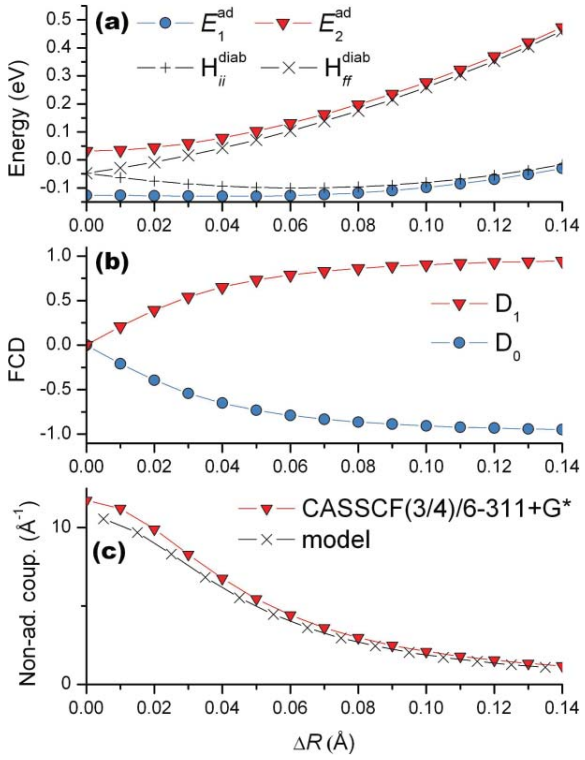

FIG. 3. Adiabatic and diabatic SA-CASSCF energies relative to the noninteracting system, fragment charge differences (FCDs), and nonadiabatic couplings projected on ΔR [analytical and according to the model of Eq. (8) in the text] of [Et.–Et.]$^+$ for an intermolecular distance of $R_{C\ldots C} = 5.0$ Å.

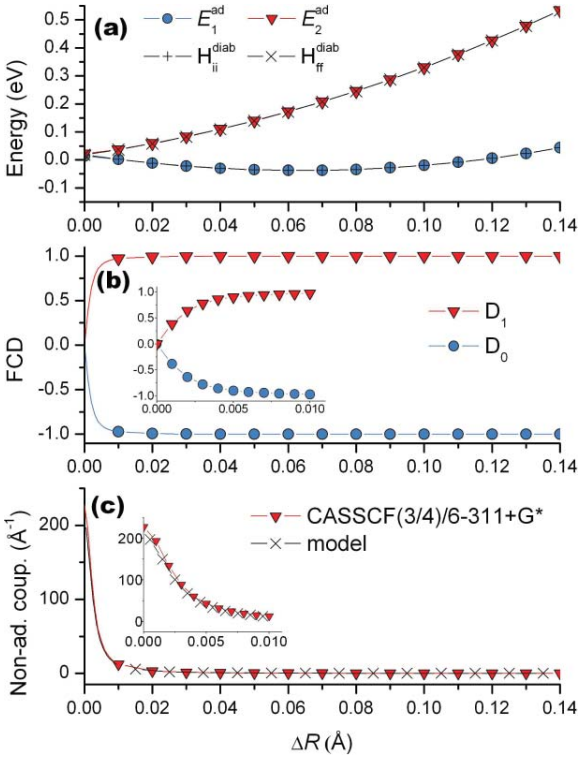

FIG. 4. Adiabatic and diabatic SA-CASSCF energies relative to the noninteracting system, FCDs, and nonadiabatic couplings projected on ΔR [analytical and according to the model of Eq. (8)] of [Et.–Et.]$^+$ for an intermolecular distance of $R_{C\ldots C} = 7.0$ Å.

TABLE III. Relative energies, bridge charges, and character of the first six doublet electronic states of the [Et.–FA–Et.]$^+$ complex considering ionizations out of the π and π^* orbitals.

SA(6)-CASSCF(5/6)				MR-CISD(5/6)+P			
Symm.	Energy (eV)	Ch. on FA	Character	Symm.	Energy (eV)	Ch. on FA	Character
$1\,^2B_1$	0	0.013	$(\pi^-)^1$	$1\,^2B_1$	0	0.013	$(\pi^-)^1$
$1\,^2A_1$	0.087	−0.004	$(\pi^+)^1$	$1\,^2A_1$	0.075	−0.004	$(\pi^+)^1$
$2\,^2B_1$	3.887	0.000	mult.-ref.	$2\,^2B_1$	4.100	0.585	mult.-ref.
$2\,^2A_1$	3.920	0.004	mult.-ref.	$3\,^2B_1$	4.124	0.314	mult.-ref.
$3\,^2B_1$	4.165	0.864	$(\pi^{FA})^1$	$2\,^2A_1$	4.243	0.003	mult.-ref.
$3\,^2A_1$	6.094	0.005	mult.-ref.	$3\,^2A_1$	6.435	0.000	mult.-ref.

In the [Et.–FA–Et.]$^+$ system it is of special interest in which way the bridging formaldehyde is involved in the charge transport. For that reason, the π and π^* orbitals of FA were included in the calculation to estimate their participation in the charge transfer process. CASSCF(5/6) computations were performed which included five electrons in the π and π^* orbitals of each of the three molecules. The first six electronic states were analyzed at the symmetric geometry, i.e., the TS structure of the charge transfer reaction (Table III). MR-CISD+P calculations were performed as well. At the CASSCF level, the first two states are formed by removing an electron from the bonding and antibonding linear combinations of the ethylene π orbitals, respectively. They are separated by a gap of 0.087 eV, i.e., $H_{if}^{\mathrm{diab}} = 0.043\,eV$. This is somewhat larger than the value presented in Table II where only two states were considered in the averaging procedure. Two more states, which are also close in energy, follow at about 4 eV. They have a multireference character where the hole is mainly localized in the ethylene π and π^* orbitals. Ionization of the FA molecule, a $(\pi^{FA})^1$ configuration, corresponds to the fifth state of the system with a relative energy of 4.165 eV. A sixth state with multireference character follows at 6.094 eV. Except for the $(\pi^{FA})^1$ state there is only negligible charge on the bridging molecule. The MR-CISD+P results are quite similar. The couplings are again somewhat reduced (cf. S5 of the Supplemental Material). Both CASSCF and MR-CI calculations agree that no charge on formaldehyde appears up to 4 eV above the ground state. This confirms the picture of an inactive bridge. Rather than playing an active role in the process, the formaldehyde molecule is apparently only involved through reducing the tunneling potential as compared to the vacuum.

B. Dynamics

To simulate the dynamics of the charge-transfer processes, 50 surface-hopping trajectories of 1 ps duration were computed for [Et.–Et.]$^+$ at a separation of $R_{C\ldots C} = 5.0$ Å and for [Et.–FA–Et.]$^+$ at $R_{C\ldots C} = 7.0$ Å. Through restrains on the intermolecular degrees of freedom as described in the Computational Details an almost ideal face-to-face configuration was maintained through the whole course of the dynamics. A sample 300 fs section of the dynamics of [Et.–Et.]$^+$ is shown in Fig. 5. In Fig. 5(a), the energy gap between the two

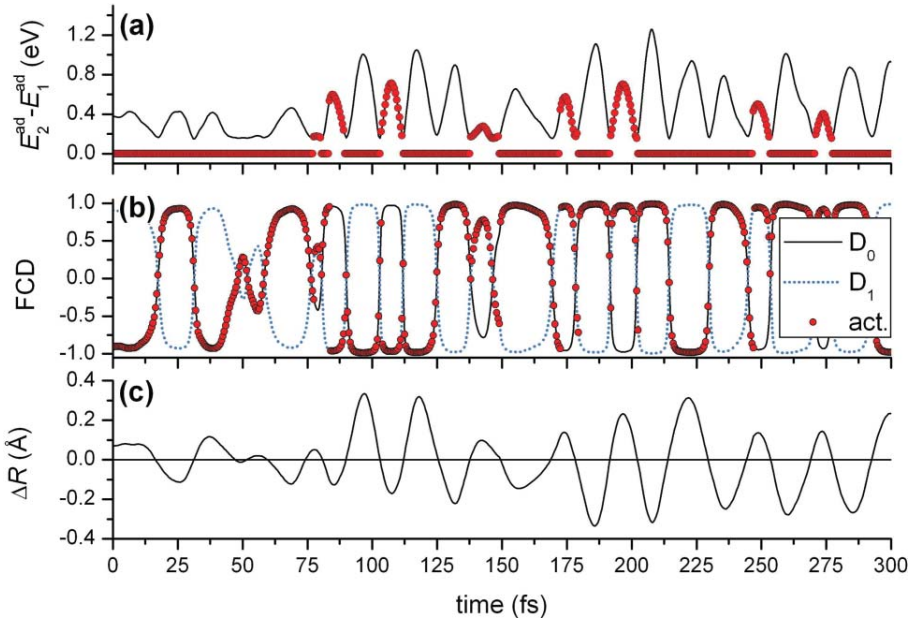

FIG. 5. Energy gap [(a), red circles on the upper line indicate that the system is in the excited state], fragment charge difference (FCD) (b), and CC bond alternation (c) plotted against time for a [Et.–Et.]$^+$ trajectory with $R_{C\ldots C} = 5.0$ Å.

states is plotted. Circles on the upper line are used to indicate that the system is in the excited state. A large gap indicates that the structure is close to a minimum. A reduction in the gap corresponds to approaching the crossing region. It is noted that the gap never goes to zero. This can be understood from the fact that, as mentioned earlier, the diabatic coupling (H_{if}^{diab}) remains fairly constant with restrained intermolecular degrees of freedom. Therefore, an intersection cannot be reached. The gap remains above 0.1 eV for more than 99% of the time in all trajectories (cf. $2H_{if}^{\text{diab}} = 0.158$ eV at the equilibrium geometry, Table II). In Fig. 5(b), the evolution of the FCD against time for the D_0 and D_1 states is presented. The current state of the dynamics is marked with circles. In Fig. 5(c), the time behavior of the CC bond alternation ΔR is shown. This dynamics is now analyzed in terms of the processes defined in Sec. II. A *TS passage* corresponds to a crossing between the FCD curves in Fig. 5(b) (cf. Scheme 3). This happens 20 times in the presented section (18.5, 32.5, 60.5, 91.0, 103.5, 112.5, 126.0, 139.5, 148.5, 170.5, 179.0, 192.5, 202.5, 215.0, 230.5, 245.5, 254.0, 271.0, 278.0, and 293.0 fs). A *TS passage* is usually accompanied also by a sign change of ΔR as shown in Fig. 5(c). However, there is no strict correspondence between these two types of events, as several internal coordinates play a role. In particular, the torsion around the CC bond was seen strongly affecting the relative energetics. This can be understood by the fact that the force constant for this motion in ethylene is strongly altered when removing an electron. The vibrational frequency of this mode changes from 1085 cm^{-1} in the neutral ethylene molecule to 482 cm^{-1} in the cation. In the completely adiabatic case, every *TS passage* would lead to a transfer of charge, i.e., an *active CT* [Scheme 3(a)]. As Scheme 3(b) shows, nonadiabatic coupling between electronic and nuclear motion may inhibit this transfer and lead to a diabatic trapping event. In the plot shown, this type of event occurs, e.g., between 100 and 115 fs where the active state FCD always remains negative even though 2 *TS passages* (103.5 and 112.5 fs) occur. Because of this trapping, only eight *active CTs* (18.5, 32.5, 60.5, 84.0, 126.0, 215.0, 230.5, and 293.5 fs) occur in the section shown. The events of macroscopic interest should start and end in the ground state. In the part shown in Fig. 5, there are 14 *TS global* events (starting at 18.5, 32.5, 60.5, 91.0, 103.5, 126.0, 139.5, 170.5, 192.5, 215.0, 230.5, 245.5, 271.0, and 293.5 fs). Eight r*eal CTs* occur (18.5, 32.5, 60.5, 91.0, 126.0, 215.0, 230.5, and 293.5 fs). From these events κ_{el} and P_{12} were computed according to Eqs. (16) and (17). The averaging was performed for all trajectories, giving statistics over 2559 *TS passages*. The results are presented in Table IV. Approximate results according to Eq. (14) are shown as well using plausible parameter values as follows: H_{if}^{diab} and λ were taken from Table II; $\nu = 1600$ cm^{-1} (as a typical C=C stretch) was chosen; for the effective temperature half the zero-point energy (kinetic energy according to virial theorem) of the C=C vibration was substituted, i.e., $kT = h\nu/4$. Table IV shows that the resulting P_{12} is somewhat larger than the one computed from the dynamics. Very good agreement between the observed value of κ_{el} and the value predicted by Eq. (15) is observed. The overall rate of electron transfer in this complex was 18.7 ps^{-1}.

TABLE IV. Kinetic properties for dynamics of $[\text{Et.–Et.}]^+$ with intermolecular distance $R_{\text{C}\cdots\text{C}} = 5.0$ Å and $[\text{Et.–FA–Et.}]^+$ with $R_{\text{C}\cdots\text{C}} = 7.0$ Å.

	$[\text{Et.–Et.}]^+$		$[\text{Et.–FA–Et.}]^+$	
	Simulation	Eq. (14)	Simulation	Eq. (14)
P_{12}	0.517	0.804	0.287	0.308
$2P_{12}/(1+P_{12})$	0.682	0.891	0.446	0.471
κ_{el}	0.671		0.401	

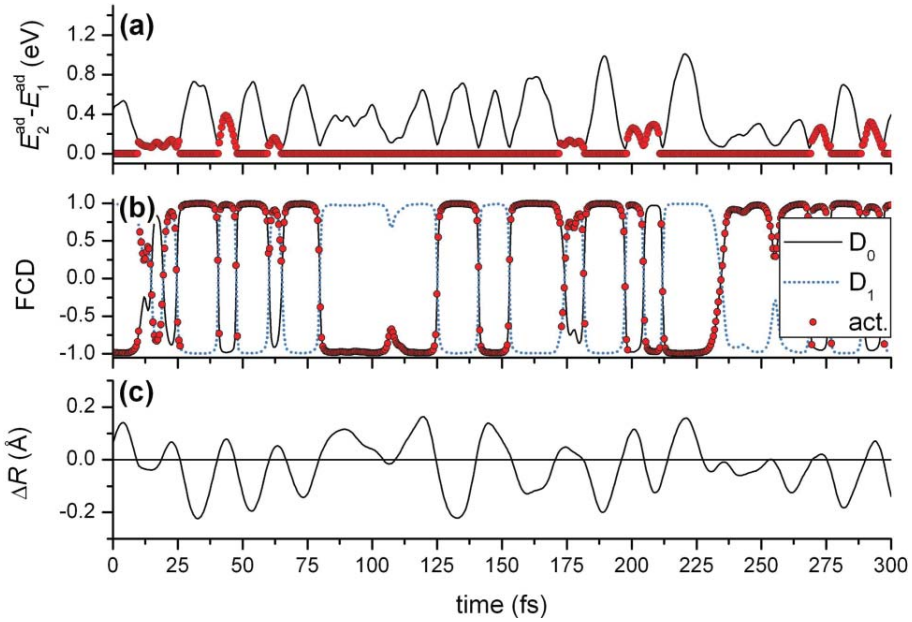

FIG. 6. Energy gap [(a), red dots on the upper line indicate that the system is in the excited state], fragment charge difference (FCD) (b), and CC bond alternation (c) plotted against time for a $[\text{Et.–FA–Et.}]^+$ trajectory with $R_{\text{C}\cdots\text{C}} = 7.0$ Å.

In Fig. 6, the analogous plot for the dynamics of the [Et.–FA–Et.]$^+$ complex is shown. The appearance is quite similar to that of the previous case because the coupling H_{if}^{diab} and reorganization energy λ have comparable values (cf. Table II). The dynamics starts with a *TS global* event, which may be identified as the process shown in Scheme 3(c): there are three *TS passages* (15.5, 20.5, and 25.0 fs), one *active CT* (20.5 fs), and in total a net transfer of charge (a *real CT*). This is followed by two diabatic trapping events [41.0–48.0 fs and 61.0–66.0 fs, cf. Scheme 3(b)] and an adiabatic transfer [80.5 fs, Scheme 3(a)]. The net charge on FA was never more than 0.004*e*. This shows again the picture of an inactive bridge, comparable to the static analysis presented earlier (cf. Table III). In relation to Refs. 4 and 5, we may conclude that a coherent superexchange mechanism without involvement of the bridge takes place here. The charge transfer parameters for this situation are shown in Table IV. The agreement between the static and dynamic descriptions is satisfactory. In particular, the trend between the two complexes is correctly reproduced, i.e., that the charge transfer probability in the second complex is somewhat lower than in the first one. The directly determined value of κ_{el} is slightly smaller than that predicted by Eq. (15). In total, an electron transfer rate of 10.6 ps^{-1} was obtained.

Dynamics calculations with an intermolecular distance of $R_{\text{C}\ldots\text{C}} = 3.0$ Å were performed as well. This case represents a strong coupling situation and purely adiabatic dynamics in the ground state was obtained. The gap was constant at about 2 eV. The hole was always quite delocalized, the absolute value of the FCD never exceeded 0.5. The corresponding graphics is presented in Supplemental Material (S6). The weak coupling case of $R_{\text{C}\ldots\text{C}} = 7.0$ Å, with a theoretical transition probability of about 99.5% per *TS crossing* [Eq. (14)], was examined as well. Because of the highly peaked nonadiabatic coupling [cf. Fig. 4(c)] a very short time-step of well below 0.1 fs would be needed to accurately sample this in the standard formalism. To overcome this problem, surface-hopping based on a locally diabatic representation of the wave function[45] is being implemented into NEWTON-X to allow for efficient accurate sampling of these kinds of processes.

V. CONCLUSIONS

Semiclassical dynamics simulations of charge transfer based on *ab initio* multireference electronic structure methods have been performed for the stacked ethylene dimer radical cation system with insertion of up to three formaldehyde molecules, with the goal of obtaining detailed understanding of the different transfer mechanisms. Computations at the CASSCF and MR-CISD levels allowed for an accurate description of the radical cationic systems including explicit calculation of nonadiabatic coupling between different electronic states. The dynamics of the electron transfer was computed at the level of semiclassical surface hopping with consideration of all nuclear degrees of freedom. Analysis of these simulations and comparison to idealized models, in particular the fragment charge difference (FCD) method, gave interesting insight into the different processes.

The electronic coupling strength within the ethylene dimer radical cation was modulated through the intermolecular distance and the on-site energies through CC bond alternation. Potential energy curves were analyzed in terms of charge delocalization and special focus was given to the nonadiabatic couplings. The CASSCF approach already gave reliable results. Inclusion of dynamic electron correlation through MR-CISD+P slightly reduced electronic couplings (by about 10%) and had a somewhat larger effect on reorganization energies. In the strong coupling region at an intermolecular distance of $R_{\text{C}\ldots\text{C}} = 3.0$ Å, a conventional adiabatic dynamics occurred in a potential characterized by one energy minimum. In the intermediate coupling region, i.e., [Et.–Et.]$^+$ at $R_{\text{C}\ldots\text{C}} = 5.0$ Å and [Et.–FA–Et.]$^+$ at $R_{\text{C}\ldots\text{C}} = 7.0$ Å, interesting complex higher order charge transfers and diabatic trapping situations were observed. These have been analyzed in terms of idealized model processes (Scheme 3). The results were compared to the electronic transmission factor of the Marcus–Levich–Hush theory. In particular, satisfactory agreement and similar trends concerning the dependence of the charge-transfer probability on the intermolecular distance was found between the two methods. Moreover, the simulations of the [Et.–FA–Et.]$^+$ complex showed that FA acts as an inactive bridge molecule there.

The present calculations are intended to initiate general approaches for investigating full nonadiabatic simulations of the dynamics of electronic defects. The currently used direct multireference *ab initio* procedures are restricted to a molecular size comparable to two or three stacked DNA bases. Additionally, quantum mechanics/molecular mechanics (QM/MM) methods[46] may be used to provide a realistic description of environmental effects. Such calculations are intended to serve as benchmarks for subsequent applications to larger systems using simpler, but more cost-effective methods, also allowing significantly longer simulation times.

ACKNOWLEDGMENTS

This work has been supported by the Austrian Science Fund within the framework of the Special Research Programs F16 (Advanced Light Sources) and F41 (ViCoM) and Project P18411-N19. FP is a recipient of a DOC fellowship of the Austrian Academy of Sciences. Computer time at the Vienna Scientific Cluster (project nos. 70019 and 70151) is gratefully acknowledged.

[1] D. B. Hall, R. E. Holmlin, and J. K. Barton, Nature **382**(6593), 731 (1996).
[2] R. G. Endres, D. L. Cox, and R. R. P. Singh, Rev. Mod. Phys. **76**(1), 195 (2004).
[3] F. Garnier, G. Horowitz, X. Z. Peng, and D. Fichou, Synth. Met. **45**(2), 163 (1991); H. E. Katz, A. J. Lovinger, J. Johnson, C. Kloc, T. Siegrist, W. Li, Y. Y. Lin, and A. Dodabalapur, Nature **404**(6777), 478 (2000).
[4] E. Hatcher, A. Balaeff, S. Keinan, R. Venkatramani, and D. N. Beratan, J. Am. Chem. Soc. **130**(35), 11752 (2008).
[5] J. Jortner, M. Bixon, T. Langenbacher, and M. E. Michel-Beyerle, Proc. Natl. Acad. Sci. USA **95**(22), 12759 (1998); B. Giese, J. Amaudrut, A. K. Kohler, M. Spormann, and S. Wessely, Nature **412**(6844), 318 (2001).
[6] N. S. Hush, Trans. Faraday Soc. **57**(4), 557 (1961).
[7] J. Jortner, J. Chem. Phys. **64**(12), 4860 (1976).
[8] B. S. Brunschwig, J. Logan, M. D. Newton, and N. Sutin, J. Am. Chem. Soc. **102**(18), 5798 (1980).
[9] R. A. Marcus, Angewandte Chemie—International Edition in English **32**(8), 1111 (1993).

[10]P. F. Barbara, T. J. Meyer, and M. A. Ratner, J. Phys. Chem. **100** (31), 13148 (1996).
[11]T. Van Voorhis, T. Kowalczyk, B. Kaduk, L. P. Wang, C. L. Cheng, and Q. Wu, Annu. Rev. Phys. Chem. **61**, 149 (2010).
[12]G. A. Jones, B. K. Carpenter, and M. N. Paddon-Row, J. Am. Chem. Soc. **120**(22), 5499 (1998).
[13]L. Blancafort, F. Jolibois, M. Olivucci, and M. A. Robb, J. Am. Chem. Soc. **123**(4), 722 (2001).
[14]A. A. Voityuk and N. Rosch, J. Chem. Phys. **117**(12), 5607 (2002).
[15]T. Kubar, P. B. Woiczikowski, G. Cuniberti, and M. Elstner, J. Phys. Chem. B **112**(26), 7937 (2008).
[16]C. P. Hsu, Acc. Chem. Res. **42**(4), 509 (2009).
[17]A. de la Lande and D. R. Salahub, J. Mol. Struct.: THEOCHEM **943**(1–3), 115 (2010).
[18]L. Blancafort and A. A. Voityuk, J. Phys. Chem. A **110**(20), 6426 (2006).
[19]Y. J. Ye, R. S. Chen, A. Martinez, P. Otto, and J. Ladik, Solid State Commun. **112**(3), 139 (1999).
[20]G. A. Worth, P. Hunt, and M. A. Robb, J. Phy. Chem. A **107** (5), 621 (2003); B. G. Levine and T. J. Martinez, Ann. Rev. Phys. Chem. **58**, 613 (2007); M. Barbatti, M. Ruckenbauer, J. J. Szymczak, A. J. A. Aquino, and H. Lischka, Phys. Chem. Chem. Phys. **10**(4), 482 (2008); M. Barbatti, B. Sellner, A. J. A. Aquino, and H. Lischka, in *Radiation Induced Molecular Phenomena in Nucleic Acid*, edited by M. K. A. L. Shukla, J. (Springer Science + Business Media B.V., 2008).
[21]E. Cauet and J. Lievin, J. Phys. Chem. A **113**(36), 9881 (2009).
[22]L. Blancafort, P. Hunt, and M. A. Robb, J. Am. Chem. Soc. **127**(10), 3391 (2005).
[23]J. C. Tully, J. Chem. Phys. **93**(2), 1061 (1990); S. Hammes-Schiffer and J. C. Tully, J. Chem. Phys. **101**(6), 4657 (1994).
[24]M. Barbatti, R. Shepard, and H. Lischka, in *Conical Intersections: Theory, Computation and Experiment*, edited by W. Domcke, D. R. Yarkony, and H. Köppel (World Scientific, Singapore, 2010), Vol. 17.
[25]J. E. Subotnik, R. J. Cave, R. P. Steele, and N. Shenvi, J. Chem. Phys. **130**, 234102 (2009).
[26]M. D. Newton, Chem. Rev. **91**(5), 767 (1991).
[27]H. Koppel, W. Domcke, and L. S. Cederbaum, Adv. Chem. Phys. **57**, 59 (1984).
[28]L. Landau, Phys. Z. Sowjetunion **2**, 46 (1932).
[29]C. Zener, Proc. R. Soc. London **137**(833), 696 (1932).
[30]J. M. Saveant, J. Phys. Chem. B **106**(36), 9387 (2002).
[31]P. G. Szalay, A. Karpfen, and H. Lischka, Chem. Phys. **130**(1–3), 219 (1989); P. G. Szalay, A. G. Csaszar, G. Fogarasi, A. Karpfen, and H. Lischka, J. Chem. Phys. **93**(2), 1246 (1990); M. Barbatti, J. Paier, and H. Lischka, J. Chem. Phys. **121**(23), 11614 (2004).
[32]P. J. Bruna, S. D. Peyerimhoff, and R. J. Buenker, Chem. Phys. Lett. **72**(2), 278 (1980).
[33]R. Shepard, in *Modern Electronic Structure Theory*, edited by D. R. Yarkony (World Scientific, Singapore, 1995), Vol. 1, p. 345.
[34]J. A. Pople, R. Seeger, and R. Krishnan, Int. J. Quantum Chem. S**11**, 149 (1977).
[35]P. C. Harihara and J. A. Pople, Theoretica Chimica Acta **28**(3), 213 (1973).
[36]R. Krishnan, J. S. Binkley, R. Seeger, and J. A. Pople, J. Chem. Phys. **72**(1), 650 (1980).
[37]H. Lischka, R. Shepard, I. Shavitt, R. M. Pitzer, M. Dallos, T. Mueller, P. G. Szalay, F. B. Brown, R. Ahlrichs, H. J. Boehm, A. Chang, D. C. Comeau, R. Gdanitz, H. Dachsel, C. Ehrhardt, M. Ernzerhof, P. Hoechtl, S. Irle, G. Kedziora, T. Kovar, V. Parasuk, M. J. M. Pepper, P. Scharf, H. Schiffer, M. Schindler, M. Schueler, M. Seth, E. A. Stahlberg, J.-G. Zhao, S. Yabushita, Z. Zhang, M. Barbatti, S. Matsika, M. Schuurmann, D. R. Yarkony, S. R. Brozell, E. V. Beck, J.-P. Blaudeau, M. Ruckenbauer, B. Sellner, F. Plasser, and J. J. Szymczak, COLUMBUS, an ab initio electronic structure program, Release 5.9.1, www.univie.ac.at/columbus (2006).
[38]T. Helgaker, H. J. A. Jensen, P. Jørgensen, J. Olsen, K. Ruud, H. Ågren, T. Andersen, K. L. Bak, V. Bakken, O. Christiansen, P. Dahle, E. K. Dalskov, T. Enevoldsen, H. Heiberg, H. Hettema, D. Jonsson, S. Kirpekar, R. Kobayashi, H. Koch, K. V. Mikkelsen, P. Norman, M. J. Packer, T. Saue, P. R. Taylor, and O. Vahtras, DALTON, an *ab initio* electronic structure program, Release 1.0 (1997).
[39]M. Barbatti, G. Granucci, M. Persico, M. Ruckenbauer, M. Vazdar, M. Eckert-Maksic, and H. Lischka, J. Photochem. Photobiol., A **190**(2–3), 228 (2007).
[40]M. Barbatti, G. Granucci, M. Ruckenbauer, M. Persico, and H. Lischka, NEWTON-X: A package for Newtonian dynamics close to the crossing seam, version 1.1.4b, (2007).
[41]G. Granucci and M. Persico, J. Chem. Phys. **126**(13), 134114 (2007).
[42]R. Shepard, H. Lischka, P. G. Szalay, T. Kovar, and M. Ernzerhof, J. Chem. Phys. **96**(3), 2085 (1992); H. Lischka, M. Dallos, and R. Shepard, Mol. Phys. **100**(11), 1647 (2002); M. Dallos, H. Lischka, R. Shepard, D. R. Yarkony, and P. G. Szalay, J. Chem. Phys. **120**(16), 7330 (2004); H. Lischka, M. Dallos, P. G. Szalay, D. R. Yarkony, and R. Shepard, J. Chem. Phys. **120**(16), 7322 (2004).
[43]W. J. Hehre, R Ditchfield, and J. A. Pople, J. Chem. Phys. **56**(5), 2257 (1972).
[44]See supplementary material at http://dx.doi.org/10.1063/1.3526697 for geometries and total energies of the complexes considered, a collection of electronic couplings at different levels of theory, and a dynamics analysis of $[Et.\text{-}Et.]^+$ with 3.0 A intermolecular distance.
[45]G. Granucci, M. Persico, and A. Toniolo, J. Chem. Phys. **114**(24), 10608 (2001).
[46]D. Bakowies and W. Thiel, J. Phys. Chem. **100**(25), 10580 (1996); M. Ruckenbauer, M. Barbatti, T. Muller, and H. Lischka, J. Phys. Chem. A **114**(25), 6757 (2010).

3.4 Surface Hopping Dynamics using a Locally Diabatic Formalism

As outlined in the last section, a special challenge in the simulation of defect dynamics is that frequent crossings between weakly coupled states may occur. Highly peaked non-adiabatic couplings, which are present in such a case, cause a special challenge for accurate dynamics simulations. A possible solution to this problem lies in a locally diabatic propagation of the wave function (with the dynamics still proceeding on adiabatic surfaces). [71] The purpose of this work was the implementation of this local diabatization method into the NEWTON-X program package and testing its performance with respect to existing methods based on an adiabatic propagation of the wavefunction. Moreover, two interesting examples were considered: (i) the stacked ethylene dimer radical cation at 7.0 Å intermolecular separation, a situation were because of the large separation electron transfer is almost impossible (ii) the hydrogen-bonded 2-pyridone dimer, which showed complex dynamics exhibiting excitation energy transfers as well as proton coupled electron transfers.

This project was carried out in collaboration with M. Persico and G. Granucci of the University of Pisa after a research visit in March 2010. In addition J. Pittner provided significant work with respect to the implementation of wavefunction overlaps at the TDDFT level. One part of my work was concerned with providing an interface of the different computer codes provided by these researchers to the NEWTON-X program package. For this work I received the help of M. Barbatti. Then, my task was to test the methodologies and run the simulations. The paper was submitted to the *Journal of Chemical Physics* (17 May 2012). [88]

Surface hopping dynamics using a locally diabatic formalism: charge transfer in the ethylene dimer cation and excited state dynamics in the 2-pyridone dimer

Felix Plasser,[a] Giovanni Granucci,[b] Jiri Pittner,[c] Mario Barbatti,[d] Maurizio Persico,[b] Hans Lischka[a,e]

[a] *Institute for Theoretical Chemistry – University of Vienna,*

Waehringegrstrasse 17, A 1090 Vienna, Austria.

[b] *Dipartimento di Chimica e Chimica Industriale, Universita di Pisa,*

via Risorgimento 35, 56126 Pisa, Italy.

[c] *J. Heyrovský Institute of Physical Chemistry, Academy of Sciences of the Czech Republic, v.v.i., Dolejškova 3, 18223 Prague 8, Czech Republic*

[d] *Max-Planck-Institut für Kohlenforschung, Kaiser-Wilhelm-Platz 1, 45470 Mülheim an der Ruhr, Germany.*

[e] *Department of Chemistry and Biochemistry, Texas Tech University, Lubbock, TX 79409-1061, USA*

Abstract

In this work the advantages of a locally diabatic propagation of the electronic wave function in surface hopping dynamics proceeding on adiabatic surfaces are presented providing very stable results even in challenging cases of highly peaked nonadiabatic interactions. The method was applied to the simulation of transport phenomena in the stacked ethylene dimer radical cation and the hydrogen bonded 2-pyridone dimer. Systematic tests showed the reliability of the method, in situations where standard methods relying on an adiabatic propagation of the wave function and explicit calculation of the nonadiabatic coupling terms exhibited significant numerical instabilities. Investigations of the ethylene dimer radical cation with an intermolecular distance of 7.0 Å provided a quantitative description of diabatic charge trapping. For the 2-pyidone dimer a complex dynamics was obtained: a very fast (< 10 fs) initial S_2/S_1 internal conversion; subsequent excitation energy transfers with a characteristic time of 207 fs; and the occurrence of proton coupled electron transfer (PCET) in 26% of the trajectories. The computed characteristic excitation energy transfer time of 207 fs is in satisfactory agreement with the experimental value of 318 fs derived from the vibronic exciton splittings in a monodeuterated 2-pyridone dimer complex. The importance of nonadiabatic coupling for the PCET related to the electron transfer was demonstrated by the dynamics simulations.

1. Introduction

Ultrafast dynamical processes play an important role in many fields of Chemistry, Physics and Molecular Biology such as in the photophysics of biomolecules and defect transport in organic semiconductors.[1-4] These processes are often governed by nonadiabatic couplings between electronic and nuclear degrees of freedom, presenting a special challenge in their simulation. Several computational strategies have been introduced for this purpose (cf. e.g. Refs [5,6]): wave packet methods[7,8]; trajectory based simulations[9,10] and global models[5,11-13] building on the concepts of Fermi's golden rule, Marcus and Förster theory.[14-17] From these methods trajectory surface hopping has gained significant popularity because of its conceptual simplicity, ease of interpretation and due to the fact that all degrees of freedom can be included without prior assumptions regarding active modes.[9,18-25] In this contribution a particular focus will be laid on the application of surface hopping to charge and energy transport phenomena (cf. Refs [24,26,27]). Such calculations impose special challenges as the transport process is represented by interactions between several states located on different fragments and frequent state crossings. Especially systems with weak interchromophore coupling (for example because of large spatial separation) may be difficult to describe accurately. In this case a very low physical transfer probability has to go along with a high hopping probability between the adiabatic states (cf. Ref [27]). It is, of course, highly desirable that the general surface hopping approaches described above are able to treat the dynamics for any interchromophore coupling strength properly.

To illustrate the potential problems, in Figure 1 a model of an avoided crossing in a nuclear displacement coordinate ξ is presented. The adiabatic energies are computed by diagonalizing the model Hamiltonian

$$\mathbf{H}(\xi) = \begin{pmatrix} \left(\xi - \frac{1}{2}\right)^2 & c \\ c & \left(\xi + \frac{1}{2}\right)^2 \end{pmatrix} \tag{1}$$

for different values of a constant diabatic coupling c. The nonadiabatic coupling in the ξ coordinate follows from the derivative of the mixing angle with respect to the nuclear displacement coordinate ξ (cf. Refs [7,27,28]). It forms a peak in the crossing region. As c is lowered (light grey lines), the adiabatic states start to approach each other more closely and at the same time, the coupling becomes increasingly peaked. Note that the area below the coupling curve always remains constant at $\pi / 2$, and therefore, an increase of the peak height occurs together with the narrowing of the peak. In the limit of $c = 0$, which means that an intersection between the two energy curves occurs, the coupling becomes a δ-function. For numerical results and a more detailed discussion of the underlying equations, consider e.g. Refs [7,27]. The extremely narrow shape of the nonadiabatic coupling clearly presents a numerical challenge for using it for the propagation of the electronic wave function. In fact the problem is split into two parts[10] related to the sampling and interpolating of the coupling vector, as well as a numerically accurate propagation of the electronic coefficients. In particular it should be pointed out that a mere reduction of the timestep length used in the process of propagating the electronic coefficients is not sufficient if the interaction terms are not represented correctly. But an accurate sampling of the nonadiabatic terms may necessitate an increase in the number of electronic structure calculations, which means that in some cases the computational effort for dynamics simulations may be enlarged by an order of magnitude or more (see also Ref. [29]). In this contribution, it will be shown that these problems can be

overcome by using a locally diabatic representation of the electronic states, which contains only smoothly varying quantities (whereas the nuclear motion still proceeds on adiabatic surfaces).[18] The method is tested here for transfer processes, but it may provide significant improvements also in other situations where highly peaked nonadiabatic interactions are present and, as a consequence, conversion probabilities between diabatic states are low. The case of spin-forbidden transitions, as an example of this phenomenon, is discussed in Ref. [30] contained in this special issue.

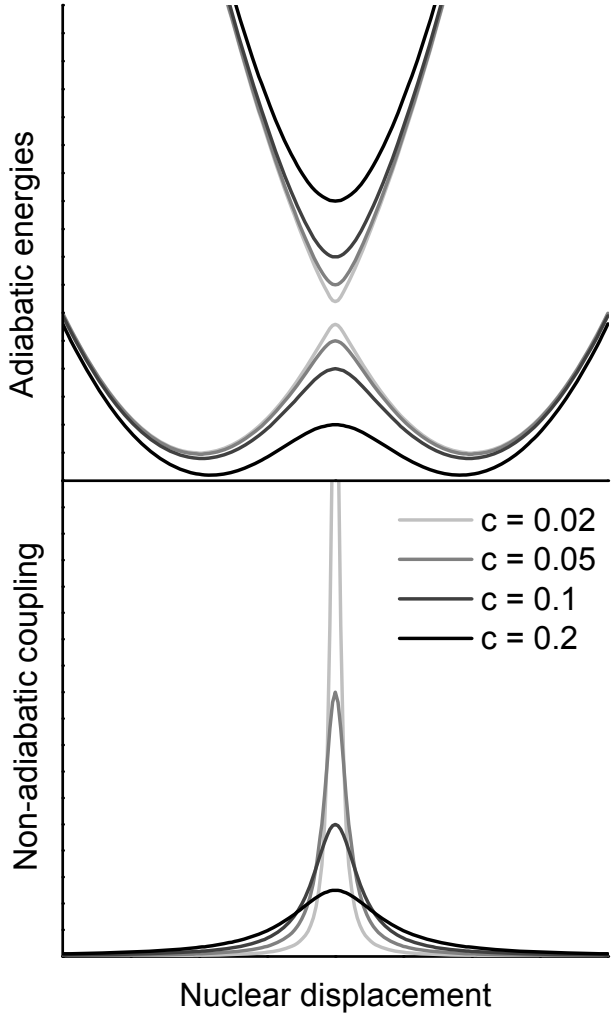

Figure 1. Model for an avoided crossing at different coupling strengths *c* (see the text for a description of the formula used). The adiabatic energies of the two states involved, as well as the nonadiabatic coupling between them is shown.

As an initial step results obtained from an analytic model will be presented. Then two interesting problems will be used to test and apply the local diabatization method. First, charge transport in the stacked ethylene dimer radical cation $[Et.\text{-}Et.]^+$ will be considered. This system serves as an important model system, where the main features of charge transport can be studied. This work will be concerned in particular with the weakly coupled case present at an intermolecular separation of 7.0 Å. In our previous study using the standard Tully surface hopping method in an adiabatic basis with utilizing nonadiabatic coupling vectors, it was not possible to properly treat this case due to highly peaked nonadiabatic

coupling vectors.[27] This challenging situation will be revisited here and used as a benchmark case for the different methods of integrating the electronic wave function. The second example is concerned with the 2-pyridone dimer $(2\text{-PY})_2$ (Figure 2 (a)). This system can be seen as a model DNA base pair where both, the processes of energy transfer as well as a potential proton coupled electron transfer (PCET) can be studied.[31,32] However, compared to DNA bases this system is significantly simpler, making it a suitable target for experimental and theoretical investigations.

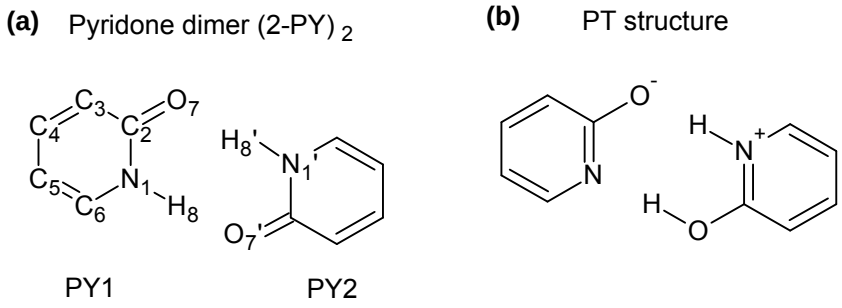

Figure 2. Structural representation and numbering scheme of the 2-pyridone dimer (a) and the zwitterionic structure present after a single proton transfer (b).

2. Methods

2.1. Propagation of the electronic wave function

In the surface hopping approach,[9,33] nuclear motion is treated by classical dynamics according to forces coming from an electronic structure calculation. Interactions between the states are treated through stochastic hoppings between the surfaces. The total time-dependent wave function $\Psi(\mathbf{R},t)$ at time t (nuclear coordinates $\mathbf{R}$ are written explicitly here, electronic coordinates are implicitly considered in the matrix elements), is written as a time-dependent linear combination of N_s adiabatic electronic eigenstates $\varphi_i(\mathbf{R}(t))$.

$$\Psi(\mathbf{R},t) = \sum_{i=1}^{N_s} c_i(t)\,\varphi_i\big(\mathbf{R}(t)\big) \tag{2}$$

and the coefficients are propagated according to[9]

$$\frac{\mathrm{d}}{\mathrm{dt}} c_j(t) = -\mathrm{i}\hbar^{-1} c_j(t) E_j(t) - \sum_{i=1}^{N_s} c_i(t)\,\sigma_{ji}(t) \tag{3}$$

where E_j(t) is the energy of the j-th adiabatic state. The nonadiabatic interaction matrix element is given as

$$\sigma_{ji}(t) = \left\langle \varphi_j\big(\mathbf{R}(t)\big) \middle| \frac{\partial}{\partial \mathrm{t}} \middle| \varphi_i\big(\mathbf{R}(t)\big) \right\rangle \tag{4}$$

Traditionally σ_{ij} is evaluated in terms of the nonadiabatic coupling vector

$$\sigma_{ji}(t) = \dot{\mathbf{R}}(t) \cdot \langle \varphi_j(\mathbf{R}) | \boldsymbol{\nabla} | \varphi_i(\mathbf{R}) \rangle_{\mathbf{R}=\mathbf{R}(t)} \tag{5}$$

where $\boldsymbol{\nabla}$ denotes the vector of all first derivatives with respect to the nuclear coordinates. Using Eq. (5) in connection with Eq. (3), will be called "NAC" in the following text. Alternatively, the overlaps of the wave functions between two successive time steps

$$S_{ji}(t) = \langle \varphi_j(\mathbf{R}(t - \Delta t)) | \varphi_i(\mathbf{R}(t)) \rangle \tag{6}$$

may be used.[21,34-36] The coupling can be estimated from linear extrapolation as

$$\sigma_{ji}(t) \approx \frac{1}{4\Delta t}\left(3S_{ji}(t) - 3S_{ij}(t) - S_{ji}(t - \Delta t) + S_{ij}(t - \Delta t)\right) \tag{7}$$

Inserting this into Eq. (3), corresponds to a scheme where wave function overlaps are used in a linear extrapolation formalism (OVL).[34,36] The difficulty in both the NAC and OVL schemes is that, as explained above, close to conical intersections the σ_{ij} are highly peaked and electronic structure calculations have to be performed with a very small timestep Δt to accurately sample this peak. The problem can be overcome by using a different propagation technique where the Hamiltonian matrix between two time steps is interpolated in a locally diabatic basis.[18] At the beginning of each time step the locally diabatic functions $\eta_i(t)$ are set equal to the adiabatic functions

$$\eta_i(t) = \varphi_i(t) \tag{8}$$

The row vector $\{\eta_i(t + \Delta t)\}$ defining the locally diabatic functions at the end of the time step is constructed according to

$$\{\eta_i(t + \Delta t)\} = \{\varphi_i(t + \Delta t)\}\mathbf{T}^{-1} \tag{9}$$

where the transformation matrix $\mathbf{T}$ is constructed by a Löwdin orthogonalization[37] of the $\mathbf{S}(t + \Delta t)$ matrix (Eq. (6)). Using $\mathbf{T}$, the diabatic Hamiltonian $\mathbf{H}$ at time step $(t + \Delta t)$

$$\mathbf{H}(t + \Delta t) = \mathbf{T}\mathbf{E}(t + \Delta t)\mathbf{T}^{-1} \tag{10}$$

is computed by transforming the diagonal matrix containing the adiabatic energies $\mathbf{E}(t + \Delta t)$. Through this construction the dynamic couplings (σ_{ij}) in the locally diabatic basis should become negligible (as far as the coupling with the states φ_i, $i > N_s$ can be neglected) and are replaced in Eq. (3) by the smoothly varying matrix elements H_{ij}. Then the coefficient vector $\mathbf{c}(t)$, can be easily propagated in the diabatic basis and finally back transformed to the adiabatic basis:

$$\mathbf{c}(t + \Delta t) = \mathbf{T}^{-1}\exp\left(-\mathrm{i}\hbar^{-1}\frac{\mathbf{E}(t) + \mathbf{H}(t + \Delta t)}{2}\Delta t\right)\mathbf{c}(t) \tag{11}$$

In summary, local diabatization (LD) provides a way of propagating the wave function without explicit reference to the dynamic couplings (σ_{ij}) and it will be shown that especially in cases where these are highly peaked, LD provides a significantly more stable integration, than the NAC and OVL algorithms discussed above. It should be noted here that the LD formalism only affects the electronic amplitudes and possible state switches, but the nuclei are

propagated on the adiabatic potential surfaces just like in the other methods. In particular, if there are no state switches, all three methods produce identical nuclear trajectories.

2.2. Analysis of charge transfer dynamics

The microscopic properties of the charge transfer dynamics are analyzed as outlined in Ref. [27] to allow for a statistical summary of the dynamics and a comparison with the underlying ideas of Marcus theory. The first quantity considered is the probability of an adiabatic charge transfer per single passage through the transition region. It is reformulated from the Landau-Zener probability as[38]

$$P_{12} = 1 - \exp\left(\frac{-\left(H_{if}^{\mathrm{diab}}\right)^2}{\mathrm{h}\nu}\sqrt{\frac{\pi^3}{\lambda \mathrm{k}T}}\right) \tag{12}$$

where H_{if}^{diab} is the diabatic coupling, ν the harmonic frequency of the active vibration, λ the reorganization energy, T the absolute temperature, and h and k the Planck and Boltzmann constants, respectively. If, after starting in the ground state, this adiabatic transfer failed, the system will continue in the excited state. In the excited state relaxation process there is an additional chance for a charge transfer and hence the global electronic transmission factor is larger than P_{12}. It is given as[27,38]

$$\kappa_{\mathrm{el}} = \frac{2P_{12}}{1 + P_{12}} \tag{13}$$

2.3. Phenomenological analysis of excited states

For the analysis of the excited states we use a recently developed method, which is based on the one electron transition density matrix,[39] cf. also Refs [40,41]. This method provides well defined, automatized descriptors for properties like the position, delocalization and charge transfer character of the wave function even in difficult cases (e.g. delocalized orbitals, many contributing configurations). First, charge transfer numbers for an excited state are computed

$$\Omega_{AB} = \frac{1}{2}\sum_{\substack{a\in A\\ b\in B}} \left(\mathbf{D}^{[\mathrm{AO}]}\mathbf{S}^{[\mathrm{AO}]}\right)_{ab}\left(\mathbf{S}^{[\mathrm{AO}]}\mathbf{D}^{[\mathrm{AO}]}\right)_{ab} \tag{14}$$

from the transition density matrix between this state and the ground state $\mathbf{D}^{[\mathrm{AO}]}$ and the overlap matrix $\mathbf{S}^{[\mathrm{AO}]}$, both expressed in the atomic orbital (AO) basis. The summations go over the basis functions on fragments A and B, respectively.

Using the charge transfer numbers (Eq. (14)) the position of the exciton in the dimer can be defined as

$$POS = \frac{3}{2} + \frac{\Omega_{22} - \Omega_{11}}{2\Omega} \tag{15}$$

where the symbol Ω is used to represent the normalization factor

$$\Omega = \Omega_{11} + \Omega_{12} + \Omega_{21} + \Omega_{22} \tag{16}$$

From Eq. (15) it can be seen that *POS* is equal to one and two, for states localized on monomer one ($\Omega_{11} = \Omega$) and monomer two ($\Omega_{22} = \Omega$), respectively. For excitonic delocalized states ($\Omega_{11} = \Omega_{22} = \Omega/2$) and charge separated states ($\Omega_{11} = \Omega_{22} = 0$), *POS* = 3/2.

The excitonic delocalization may be defined as a participation ratio expression (cf. Refs [42,43])

$$PR = \frac{\Omega^2}{2}\left(\frac{1}{\sum_A(\sum_B \Omega_{AB})^2} + \frac{1}{\sum_B(\sum_A \Omega_{AB})^2}\right) \tag{17}$$

where the summation goes over the two molecules (*A*=1,2; *B*=1,2). For localized ($\Omega_{11} = \Omega$ or $\Omega_{22} = \Omega$) and directed charge transfer states ($\Omega_{12} = \Omega$ or $\Omega_{21} = \Omega$) this measure amounts to one. For excitonic delocalized states ($\Omega_{11} = \Omega_{22} = \Omega/2$) or charge resonance states ($\Omega_{12} = \Omega_{21} = \Omega/2$) or a combination of these two types *PR* = 2.

Whereas the *POS* and *PR* values were used to describe the position and delocalization of the exciton, electron transfer was monitored by fragment charge differences (FCD) computed from Mulliken populations.[44]

3. Computational Details

The charge transfer dynamics in the ethylene dimer radical cation $[Et.\text{-}Et.]^+$ was performed in accordance with the investigations reported in Ref. [27]: A symmetric face-to-face arrangement of $[Et.\text{-}Et.]^+$ was constructed using intermolecular separations of 5.0 Å and 7.0 Å. Surface hopping dynamics simulations were performed at the state-averaged complete active space space self-consistent field (CASSCF) level with three electrons in the two π and two π* orbitals of the two molecules and with state averaging over the two lowest doublet states (SA(2)-CASSCF(3/4)). The 6-311+G* basis set was used.[45] In a first testing stage short trajectories of about 20 fs simulation time, which exhibited one passage through the crossing region, were considered. Five initial conditions each were chosen for $[Et.\text{-}Et.]^+$ at the 5.0 Å and 7.0 Å intermolecular separations and all three methods (NAC, OVL, LD) with different timestep lengths were tested. This amounted to 75 simulation runs in total. In order to observe the primary mixing between the adiabatic states and to exclude stochastic features, no surface hoppings were allowed and no decoherence correction was applied in these test runs. For a statistical analysis, the following quantities were considered. The mean of a set of similar trajectories was computed as

$$\mu(\Delta t, M) = \frac{1}{N}\sum_{k=1}^{N} c_{\Delta t,M}^{(k)} \tag{18}$$

where $c_{\Delta t,M}^{(k)}$ denotes the adiabatic population of the ground state after one passage through the crossing region for initial condition *k* (i.e. *c* is used as a short notation for $c_0(t_{\text{ref}})$ of Eq. (2)), timestep length Δ*t* and method *M* (*M* = NAC, OVL, LD). Additionally the mean absolute error for a timestep length Δ*t* and method *M* was computed as

$$\varepsilon(\Delta t, M) = \frac{1}{N}\sum_{k=1}^{N}\left|c_{\Delta t,M}^{(k)} - c_{\mathrm{ref}}^{(k)}\right| \tag{19}$$

The reference was chosen as the average between the results of using nonadiabatic coupling vectors and local diabatization for the smallest timestep considered (Δt_{min})

$$c_{\mathrm{ref}}^{(k)} = \frac{c_{\Delta t_{min},\mathrm{NAC}}^{(k)} + c_{\Delta t_{min},\mathrm{LD}}^{(k)}}{2} \tag{20}$$

where the Δt_{min} was 0.2 fs in the case of an intermolecular separation of 5.0 Å, and 0.1 fs in the case of 7.0 Å.

After testing the methods, a production run of 49 surface hopping trajectories with 1 ps duration and a timestep of 0.5 fs was performed using the LD method and applying a decoherence correction with a decay parameter of 0.1 Hartree.[46] As in Ref. [27] a restraining potential was applied to fix the relative arrangement of the molecules.

Following Ref. [32], calculations on the 2-pyridone dimer were performed using time-dependent density functional theory (TDDFT)[47,48] with the BHLYP functional containing 50% Hartree-Fock exchange.[49,50] The SVP basis set[51] with added diffuse functions (SVP+sp)[52] was used. First, test runs using the OVL and LD methods were performed. Aside from the timestep lengths (Δt), two parameters affecting the duration of CI-overlap computations significantly had to be tested, the screening threshold β_{max} (the maximal value of the CI coefficient function β_{IJ} in Eq. (15) of Ref. [36], for which the corresponding overlap term is still computed) and the number of orbitals treated as a frozen core (n_{core}). For the final dynamics simulations, the LD method with $\Delta t = 0.5$ fs, $\beta_{max} = 1\text{E-}4$, $n_{\mathrm{core}} = 38$ was used. When using these thresholds reliable nonadiabatic interactions can be obtained (as shown below) at only a fraction of the computational time of the TDDFT energy and gradient calculation. Three excited states were considered in the dynamics. The initial conditions were constructed from the Wigner distribution of the vibrational ground state of the hydrogen bonded dimer (cf. Ref [20]). The initial state of the dynamics was chosen randomly according to the relative oscillator strengths of the first two excited states. This amounted to 100 trajectories started from the S_2 state and 33 from the S_1 state. The trajectories were run for 300 fs. When computing the time dependent state distribution (see below), special attention was paid to trajectories, which could not successfully be run for 300 fs, a situation which occurred in many cases because after PCET the S_1/S_0 gap approached zero. In such a case the state of the last successful time step was taken for the remaining time steps. Wave function overlaps for nonadiabatic interactions between TDDFT excited states were computed based on the TDDFT response functions, which have the same formal structure as configuration interaction with single excitations (CIS).[47]

In $(2\text{-PY})_2$ proton transfer was monitored by means of interatomic distances. A proton transfer was considered if the N_1-H_8 (N_1'-H_8') distance was longer than the H_8-O_7' (H_8'-O_7) distance (Figure 2). In the dynamics, a proton transfer process was counted if this situation lasted for at least 2 fs. Charge and excitation energy transfer processes were analyzed following the lines described in Ref. [27]: Charge (excitation energy) transfer in $[\text{Et.-Et.}]^+$ ($(2\text{-PY})_2$) was monitored by using the FCD (*POS* value). A charge (excitation energy) transfer from molecule one to molecule two was registered if initially for at least 3 fs the dimer was in the D_0 (S_1) state and the FCD (*POS* value) was smaller than -0.5 (1.05), and later on, for at

least 3 fs, the dimer would be again in the D_0 (S_1) state, but now with an FCD (*POS* value) greater than 0.5 (1.95). The transfer from molecule two to molecule one was defined in an analogous fashion.

The excited state analysis described in Section 2.3 was carried out using the transition densities of the formal CIS wave functions[47] which were computed for the wave function overlaps as described above. Fragment charge differences[44] between the two molecules were computed from the Mulliken populations. In the case of proton transfers the fragments were adjusted to reflect the movement of the proton.

An analysis in terms of normal mode displacements, as described in Refs [53,54] was performed as well. For each trajectory k and time t the Cartesian difference vector $\mathbf{x}(k,t)$ between that structure and the ground state reference geometry ($\mathbf{x}_0$) was converted to $\mathbf{y}(k,t)$ in the normal mode basis by the relation

$$\mathbf{y}(k,t) = \mathbf{V}^{-1}(\mathbf{x}(k,t) - \mathbf{x}_0) \tag{21}$$

where $\mathbf{V}^{-1}$ is the transformation matrix from Cartesian to normal coordinates computed at $\mathbf{x}_0$. For all non-totally symmetric modes the absolute value of the displacement was taken since motions into both directions are equivalent. To characterize the $\mathbf{y}(k,t)$ vectors, they were first averaged over all trajectories and second the standard deviation over time of this time-dependent average was computed.

SA-CASSCF calculations were performed with the COLUMBUS 7.0 program package.[55-61] TDDFT computations were carried out using TURBOMOLE.[48,62] For the dynamics simulations and wave function overlap computations the NEWTON-X program package[20,36,63,64] was used.

4. Results and discussion

4.1. Model system

Before proceeding to simulations of molecular systems, the performance of the three integration formalisms NAC, OVL and LD was tested with respect to the Landau-Zener (LZ) model for an avoided crossing. A one-dimensional time-dependent diabatic model Hamiltonian between two states was defined according to

$$\mathbf{H}(t) = \begin{pmatrix} 0 & c \\ c & s\xi(t) \end{pmatrix} \tag{22}$$

$$\xi(t) = v(t - t_0) \tag{23}$$

where the diabatic coupling c, the slope s, and the velocity v are assumed to be constant. Under these assumptions the LZ asymptotic expression for the diabatic transition probability

$$P_{12} = 1 - \exp\left(-\frac{4\pi^2 c^2}{h|sv|}\right) \tag{24}$$

is exact. The nonadiabatic coupling between the adiabatic functions $h(\xi)$ has a Lorentzian shape with a full width at half maximum of $|4c/s|$. In analogy, the characteristic time τ to pass through the crossing region can be defined as

$$\tau = \left|\frac{4c}{sv}\right|. \tag{25}$$

In the model calculations the values $c = 0.0033$, $s = 0.66$ and $v = 0.002$ (all data in atomic units) were chosen. This corresponds to $P_{12} \approx 0.0505$ and $\tau = 20$ a.u. (about 0.48 fs). An integration of this model using the NAC, OVL, and LD using different timestep lengths Δt was performed. In each case an average over 10 calculations was performed using different crossing times t_0 according to

$$t_0 = \Delta t\left(n + \frac{k}{10}\right) \tag{26}$$

$$k = 0, \ldots, 9$$

where the integer n was chosen such that $vn\Delta t$, the distance traveled before reaching the crossing, was about 5 a.u. With this construction, trajectories with $k = 0$ directly reached the diabatic crossing point, whereas the others sampled points around it. The integrations were started at $t = 0$ assigning a probability of one to one of the two adiabatic states and ended at $t = 200$ fs. The final probability of the adiabatic state initially populated was then identified with P_{12}. In Figure 3 the relative error of this value with respect to the exact LZ value of P_{12} is shown. For short timesteps ($\Delta t << \tau$) all three methods give good results. When Δt approaches τ, the results of NAC and OVL diverge. By contrast LD shows impressive stability up to $\Delta t \approx 4\tau$, which is a case where the whole region of non-negligible nonadiabatic interaction is passed within only a fraction of the timestep.

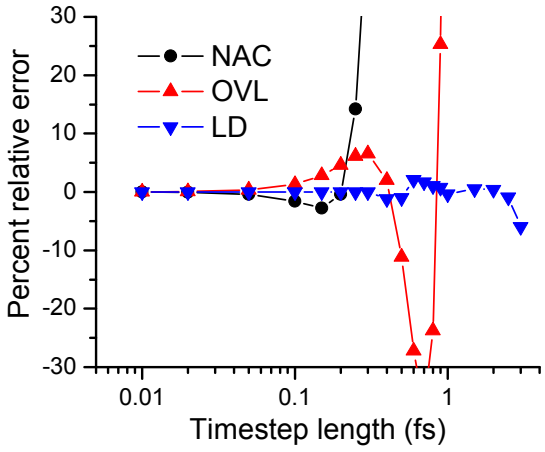

Figure 3. Landau-Zener model system: relative error for the asymptotic diabatic transition probability as a function of the integration timestep. Presented results are for the three algorithms NAC, OVL and LD as described in the main text.

In summary the fundamental stability of the LD method in the case of highly peaked nonadiabatic interactions between two states could be shown. It should however be noted that, as opposed to NAC, the LD and OVL formalisms are potentially subject to inaccuracies coming from the interactions with "external" states (i.e. the states φ_i with $i > N_s$), which were not included in this test.

4.2. Ethylene dimer radical cation

The first system considered was the ethylene dimer radical cation, which serves as a convenient model for charge transport in stacked π-systems. The complex was considered with intermolecular separations of 5.0 and 7.0 Å, which corresponds to intermediate and weak coupling situations, respectively. In an initial step, a test of the available methods for integration of the electronic Schrödinger equation was performed. For this purpose an analysis of dynamics runs with about 20 fs duration containing one passage through the crossing region was carried out. The quantity of interest was the ground state population at the end of the dynamics. The mean $\mu(\Delta t,M)$ (Eq. (18)) and mean absolute error $\varepsilon(\Delta t,M)$ (Eq. (19)) over five different initial conditions were computed for different timestep lengths Δt and the three methods described above M = NAC, OVL, LD.

For an intermolecular separation of 5.0 Å the diabatic coupling is 0.079 eV, leading to an extended region of weak nonadiabatic coupling (cf. Figure 1, c = 0.2).[27] The mean values $\mu(\Delta t,M)$ of the ground state population after one passage through the crossing region are presented in Figure 4. On average, slightly more than half the population remained in the ground state. For NAC and LD there was a very good agreement with the value of 0.544 within ± 0.002 for both timestep lengths whereas for OVL slightly smaller values of 0.527 for Δt = 0.5 fs, and 0.538 for Δt = 0.2 fs were found. In all cases the mean absolute errors $\varepsilon(\Delta t,M)$ with respect to the average of NAC and LD at Δt = 0.2 fs (cf. Computational Details) were about two orders of magnitude smaller than the mean population transfer, meaning that all methods provide a stable integration for this system. The largest error, at 4 % of the total population transfer, was found for OVL (Δt = 0.5 fs). In summary, it can be said that all methods perform satisfactory, but that NAC and LD seem to be somewhat superior to OVL.

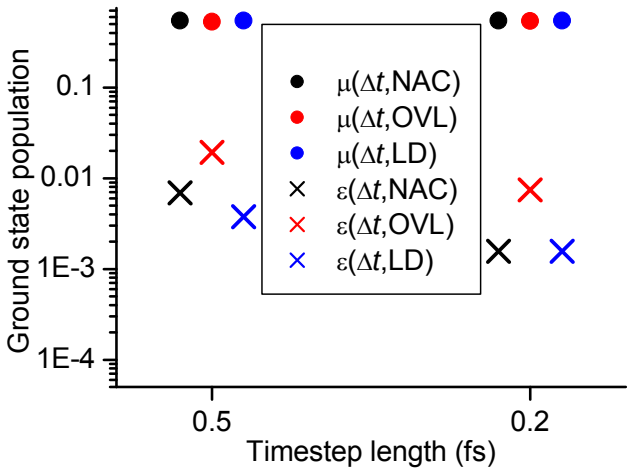

Figure 4. Mean values μ and mean absolute errors ε of the ground state population after one passage through the crossing region for the ethylene dimer radical cation at an intermolecular separation of 5.0 Å, using different simulation methods.

Second, the probability of charge transfer in the ethylene dimer radical cation was computed at an intermolecular separation of 7.0 Å (Figure 5). With a diabatic coupling of only 0.0042 eV this is an example of a weak coupling region of electron transfer.[27] The shape of the nonadiabatic coupling relates to c = 0.02 in Figure 1. In practice, the coupling vector was so highly peaked that with Δt = 0.5 fs for most trajectories there was only one time step

with significant nonadiabatic coupling when passing through the crossing region. Considering Section 4.1 this corresponds to the case of $\tau \approx 0.5$ fs, meaning that NAC and OVL should require significantly smaller timesteps for reliable results. In the calculation with $\Delta t = 0.5$ fs NAC provides an average charge transfer probability of 0.307 because the numerical integration of the electronic Schroedinger equation clearly missed the peak of the nonadiabatic coupling in some of the trajectories. The charge transfer probability is overestimated by two orders of magnitude compared to the value for $\Delta t = 0.1$ fs. OVL performs somewhat better at the longest timestep length ($\mu = 0.094$) but is still quite far from the result obtained at a smaller timestep length. LD provides very stable values, ($\mu = 0.002$) for all timestep lengths considered. At $\Delta t = 0.1$ fs, the LD value almost coincides with NAC, whereas OVL yields an average transfer probability of about twice as much ($\mu = 0.005$). Here, LD clearly yields the most stable integration algorithm and the results show impressive consistency over the different timestep lengths. A dynamics simulation using the NAC method and $\Delta t = 0.1$ fs could be reliable as well but this would correspond to a five-fold increase in computation time.

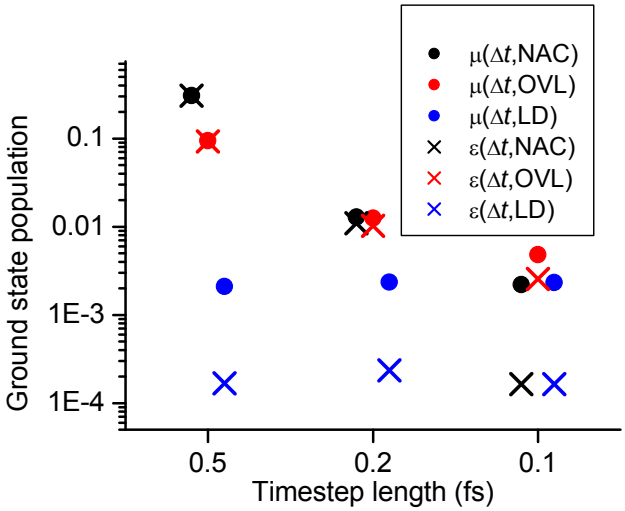

Figure 5. Mean values μ and mean absolute errors ε of the ground state population after one passage through the crossing region for the ethylene dimer radical cation at an intermolecular separation of 7.0 Å, using different simulation methods.

After the above considerations, we chose LD ($\Delta t = 0.5$ fs) as the method to perform more extended dynamics simulations on $[Et.\text{-}Et.]^+$ for an intramolecular separation of 7.0 Å. These simulations provide an extension to Ref. [27], where dynamics at 3.0 Å (strong coupling region) and 5.0 Å (intermediate coupling region) were performed. The weak coupling case of 7.0 Å, which had to be omitted because no satisfactory method of integrating the coefficients was available at that time, will be considered now. A representative 300 fs section of the dynamics of this system is shown in Figure 6. For the first 100 fs the trajectory remains around one of the minima in the double well potential. The fragment charge difference (FCD) always stays very close to one, representing a complete localization of the charge. The energy gap oscillates and in three instances the system moves close to the crossing region (represented by a small energy gap) but does not cross the transition state. The first crossing appears after about 100 fs. However, the charge is not transferred and a diabatic trapping situation is obtained through two consecutive surface hoppings (this corresponds to Scheme 3 (b) in Ref. [27]). It may be noted here that in regions surrounding nonadiabatic events, some apparent

discontinuities are present. However, these are only related to the discrete and stochastic nature of the dynamics, and a change in FCD lasting for only one or two time steps cannot be counted as a charge transfer (cf. the Computational Details for the precise algorithm used to identify CT events). For the remaining trajectory, more such events occur. But there is no actual transfer of charge.

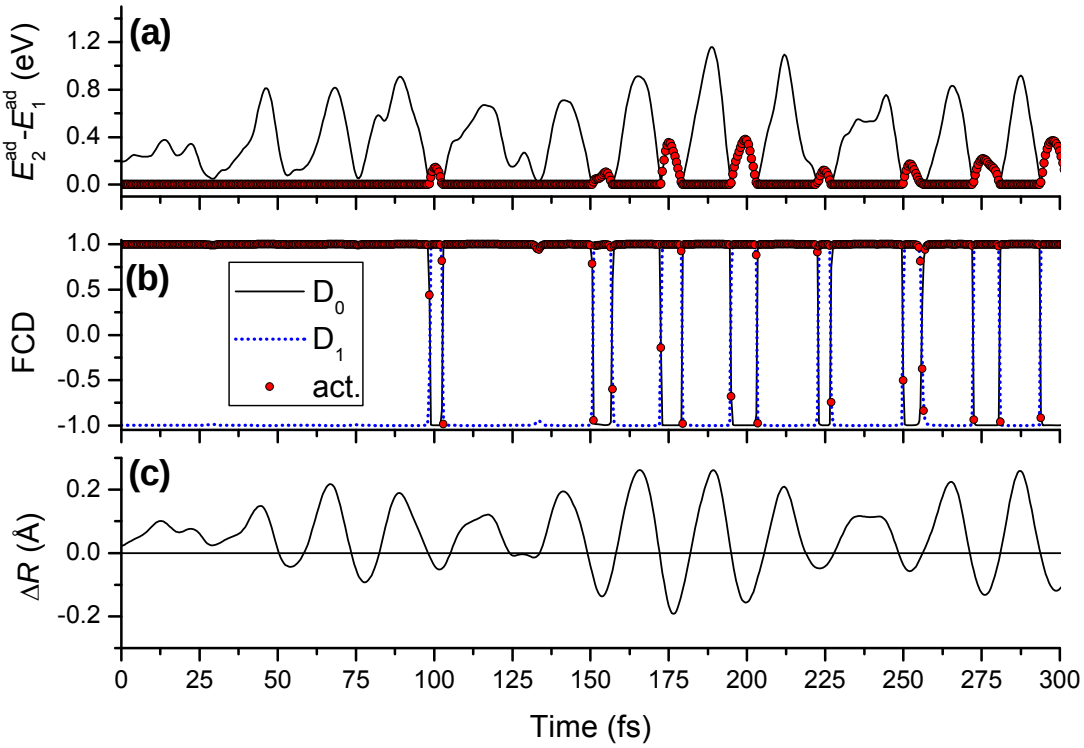

Figure 6. Energy gap (a) (red circles on the upper line indicate that the system is in the excited state), fragment charge difference (FCD) (b), and CC bond alternation ΔR (c) plotted against time for a $[Et.\text{-}Et.]^+$ trajectory with an intermolecular separation of 7.0 Å.

In Table 1, the electronic transmission factor κ_{el} is given for the intermolecular distance of 7.0 Å in $[Et.\text{-}Et.]^+$ derived from LD dynamics simulations for 49 trajectories. For comparison the dynamics simulations of Ref. [27] for $[Et.\text{-}Et.]^+$ at an intermolecular separation of 5.0 Å, as well as simulations of this system with an inserted formaldehyde molecule $[Et.\text{-}FA\text{-}Et.]^+$ are presented. The cases investigated before were situated in the intermediate coupling region with an electronic transmission factor of about 50%. In contrast the $[Et.\text{-}Et.]^+$ complex at 7.0 Å intermolecular distance is clearly a weak coupling case ($\kappa_{el} \approx 1\%$), which corresponds to an electron transfer rate of 0.16 ps^{-1}. The agreement with the Marcus theory type model (Eqs (12) and (13)) is excellent. Out of 842 accesses to the transition state in the different trajectories, only 8 led to a charge transfer. The diabatic trapping was realized by 1964 surface hoppings in the simulations. In summary, it could be seen that the LD approach was able to filter spurious charge migration events quantitatively.

Table 1. Electronic transmission factors (κ_{el}) for $[Et.\text{-}Et.]^+$ with intermolecular distances of $R_{C\cdots C}$ = 5.0 Å and $R_{C\cdots C}$ = 7.0 Å, and $[Et.\text{-}FA\text{-}Et.]^+$ with $R_{C\cdots C}$ = 7.0 Å.

	$[Et.\text{-}Et.]^+$ (5.0 Å) [a]	$[Et.\text{-}FA\text{-}Et.]^+$ [a]	$[Et.\text{-}Et.]^+$ (7.0 Å)
Simulation	0.671	0.401	0.010
Model[b]	0.891	0.471	0.010

[a] Results from Ref. [27]

[b] Eq (13) in the text

4.3. 2-pyridone dimer

The hydrogen bonded 2-pyridone dimer $(2\text{-PY})_2$ has been considered as a model DNA base pair. Two interesting processes, which are also relevant to DNA can be studied: excitation energy transfer between the molecules as well as a possible proton coupled electron transfer, which may lead to non-radiative decay.[31,32] The electronic coupling between the two $\pi\pi^*$ states in $(2\text{-PY})_2$ was estimated at about 0.05 eV from CIS transition moments[31] or 0.07 eV from TDDFT dimer splitting calculations.[32] The experimentally observed splitting was smaller by one order of magnitude at about 0.003 eV[31]. However it should be noted that the latter is the coupling between vibronic states which is obtained as the product between the electronic coupling and a Franck-Condon factor[31,65] and it is clearly possible that this Franck-Condon factor, representing the overlap between the ground state vibrations in the two equivalent strongly symmetry broken S_1 minima, is only on the order of 5%. In the further course of this discussion it should be remembered that our simulations were performed in a basis of electronic eigenfunctions, whereas the experimental interpretation is more readily performed using vibronic eigenstates. An attempt to reconcile the two representations will be performed where applicable.

The dynamics simulations were performed with the TDDFT/BHLYP method. The reliability of this approach was tested for all tautomers by comparison with second order approximate coupled cluster calculations (CC2).[32] It can therefore be assumed that this approach should provide a good description in particular of the EET dynamics. Describing the PCET process is more challenging because charge transfer transitions play a significant role and because of the fact that in the subsequent dynamics the S_1/S_0 gap is significantly lowered. Moreover, complex nonadiabatic effects may come into play.[66] However, interesting qualitative insight may be obtained from these calculations. Moreover, direct dynamics simulations can provide important complementary information with respect to the quite involved global models applied for describing PCET processes.[66]

Before the actual dynamics simulation was started, the effects of the parameters of the overlap computation were explored. This was necessary to assure a stable integration of the electronic coefficients while still operating at an acceptable computational cost. The timestep length Δt, as well as two parameters affecting the performance of the overlap computation were considered (cf. Computational Details). A collection of results considering different values of these parameters for five distinct initial conditions and integration with the OVL and LD methods is presented in Table 2. First, it can be observed that in the OVL approach there are some instabilities as far as both the timestep length as well as the parameters of the CI-overlap computation are concerned. In contrast to that, LD yields remarkably stable results, in particular for the initial conditions denoted k = 1-4. The stability of LD with respect to timestep length is probably related to the favorable treatment of highly peaked nonadiabatic interactions, as discussed above. The fact that also highly screened overlap matrices are correctly interpreted by LD may be attributed to the fact that in the Löwdin orthogonalization

procedure yielding the **T** matrix the screened terms are recovered through a proper renormalization. In the last case (k = 5) a particularly challenging example was chosen where in a process with two different nonadiabatic interactions, the population of S_2 was equally distributed between S_1 and S_3. In this case some small variations in the S_2 population are present also within the LD approach. Another point to consider is that even at the smallest timestep no quantitative agreement between OVL and LD could be reached. The computation of analytic TDDFT nonadiabatic coupling vectors has been reported[67-70] but not implemented in the program systems available to us. Therefore this discrepancy could not be evaluated further. In any case, there is good qualitative agreement between the two approaches. In particular, it is noted that the LD method using Δt = 0.5 fs, β_{max} = 1E-4, n_{core} = 38 provides reliable results. This parameter set is used in the subsequent dynamics simulations.

Table 2. Population of the S_2 state after a nonadiabatic event for five different initial conditions k, computed using different parameters in the integration process.[a]

Method	Δt	β_{max}[b]	n_{core}[c]	$c_{\Delta t, M}^{(k)}$				
	fs			k = 1	k = 2	k = 3	k = 4	k = 5
OVL	0.5	5E-3	38	0.1022	0.223	0.359	0.1242	0.0719
OVL	0.5	1E-4	38	0.0584	0.178	0.302	0.1024	0.0822
OVL	0.5	1E-4	28	0.0702	0.193	0.318	0.1095	0.0791
OVL	0.5	5E-5	28	0.0598	0.179	0.303	0.1041	0.0815
OVL	0.5	1E-5	0	0.0514	0.167	0.291	0.0992	0.0834
OVL	0.2	5E-5	0	0.0420	0.167	0.299	0.0600	0.0673
OVL	0.1	5E-5	0	0.0340	0.164	0.297	0.0535	0.0656
LD	0.5	5E-3	38	0.0143	0.141	0.271	0.0403	0.0938
LD	0.5	1E-4	38	0.0147	0.140	0.270	0.0407	0.0852
LD	0.5	1E-4	28	0.0147	0.140	0.270	0.0413	0.0861
LD	0.5	5E-5	28	0.0150	0.140	0.269	0.0413	0.0846
LD	0.5	1E-5	0	0.0150	0.140	0.270	0.0416	0.0829
LD	0.2	5E-5	0	0.0148	0.138	0.268	0.0443	0.0725
LD	0.1	5E-5	0	0.0148	0.138	0.268	0.0443	0.0721

[a] The trajectories were started in the S_2 state. In the dynamics two excited states were considered for k=1,2,3; three for k=4; and four for k=5.
[b] Screening threshold according to Eq. (15) of Ref. [36]
[c] number of core orbitals frozen in the overlap

First, two trajectories will be presented in detail to illustrate the possible processes occurring. Data for a trajectory where the pyridine dimer remains in the initial tautomeric form is presented in

Figure **7**, whereas in Figure 8 a case that undergoes PCET is shown. Such a process was previously postulated from both TDDFT and CC2 calculations.[32] In these plots a detailed description of the different electronic states is shown: relative energies with respect to the ground state at the respective geometry; *POS* values representing EET; and the fragment charge differences representing charge transfer. Moreover, N-H bond distances are presented to monitor a possible proton transfer. Both trajectories are started in the S_2 state.

Figure **7** shows that the early dynamics is determined by a hopping to the S_3 state at 2.0 fs and back to S_2 at 4.5 fs. An analysis of the FCDs reveals that this event is determined by a crossing in diabatic character (S_2 temporarily gains the charge transfer character of S_3), and

that this corresponds to a diabatic trapping situation, avoiding charge transfer. A short time after that, at 11.0 fs, a decay to S_1 occurs and the exciton is subsequently localized on PY1 (*POS* ≈ 1.0). The exciton remains on PY1 until about 125 fs when a transfer two PY2 occurs. This transfer is characterized by staying a short time in S_2: a hopping to S_2 occurs at 129.0 fs; EET (a change in the *POS* value from one to two) occurs in this state at about 135.5 fs; relaxation to S_1 and trapping of the exciton on PY2 occurs at 142.5 fs (This type of transfer process was explained in more detail in Scheme 3 (c) of Ref. [27]). During the process just described there are some additional discontinuities and short time intervals of partial electronic delocalization. These are related to the fact that in

Figure **7** the *POS* value of the active adiabatic state of the surface hopping dynamics is plotted, which is only a stochastic representation of the true wave packet. By contrast, the *POS* value of the coherent electronic wave function (Eq. (2)) should be a more smoothly varying quantity, representing the transfer process in a more balanced fashion. Around 235 fs there is another nonadiabatic event including a hopping to the S_2 state. However, after relaxation to the S_1 state the exciton is again localized on PY2, i.e. in summary this event does not correspond to a transfer of excitation energy.

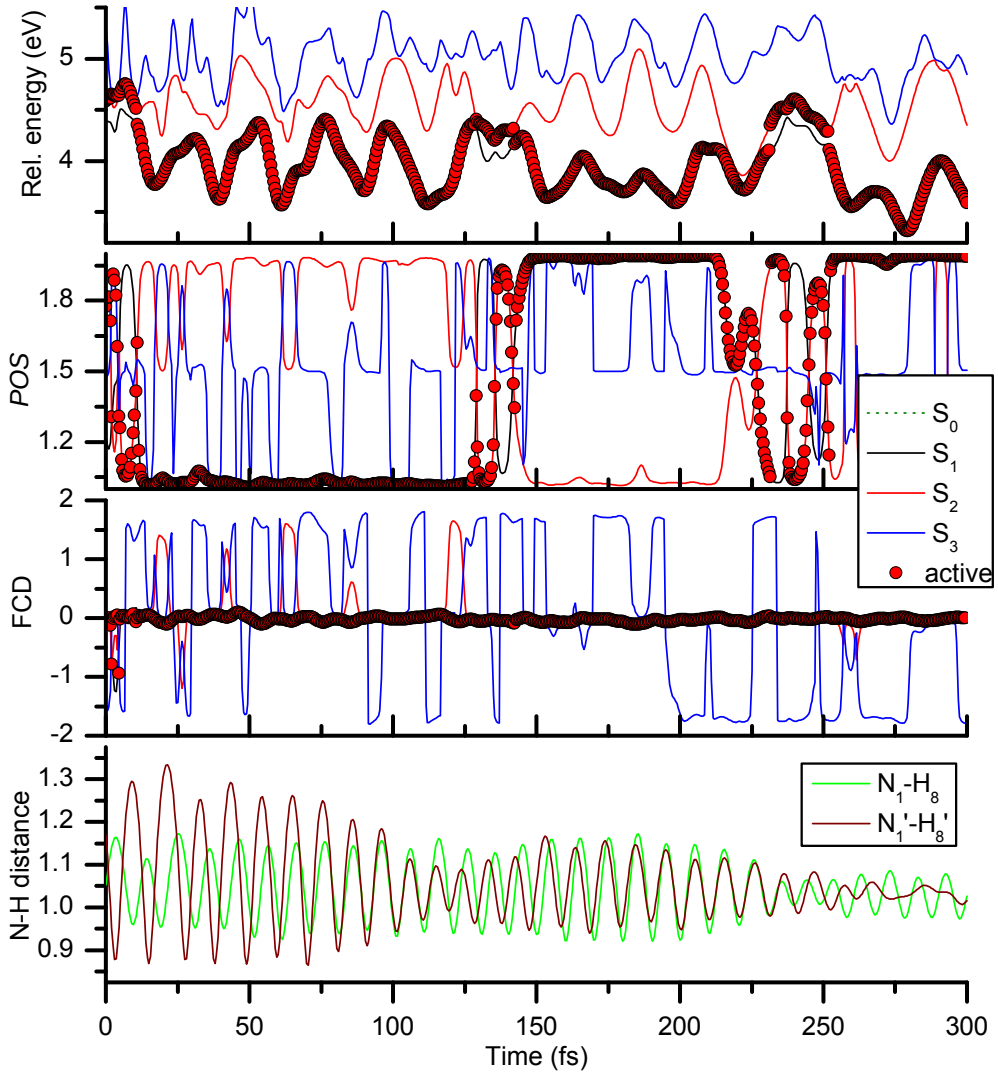

Figure 7. Relative energies, *POS* values, fragment charge differences (FCD) for the lowest four singlet states (the active state is marked with red circles) and N-H bond lengths of a trajectory of the 2-pyridone dimer, which remains in the initial tautomeric form.

For comparison, a trajectory undergoing electron coupled proton transfer is analyzed as well (Figure 8). Such a process represents 26% of our trajectories. The trajectory is started in the S_2 state with *POS* = 1.0. In the initial phase of the dynamics there is a hopping to S_1 after 5.5 fs and a backhopping to S_2 after 8.0 fs. At 12.0 fs a hopping to S_3 occurs, which is probably related to the diabatic crossing of the *POS* values. Shortly after that (14.0 fs), a proton transfer from PY1 to PY2 occurs (i.e. the H_8 atom is now closer to O_7' than to N_1). The FCDs reveal that after this event the S_0, S_2, and S_3 states are of zwitterionic nature, whereas S_1 has a biradical character. The active state after proton transfer is first S_3 then S_2. The diabatic character remains as a zwitterionic state with an excitation on PY2 (the molecule with the extra proton). A back proton transfer along the hydrogen bond, which had remained intact, occurs at 20 fs with a concurrent hopping into S_1. At the next period of the N_1-H_8 vibration another proton transfer occurs at 30 fs. This time the system remains in the S_1 state, which obtains a biradical character. Thus in summary a proton and an electron were transferred from PY1 to PY2, and charge neutrality between the fragments was obtained. However, it should be noted that during this process the S_1 state probability was temporarily reduced to 34% and

in one time step a high hopping probability to S_2 of 74% was obtained. This means that also in this case there was a high likelihood for a diabatic electron trapping. After this proton coupled electron transfer, the structure is strongly stabilized and the N_1-H_8 hydrogen bond broken, significantly reducing the chance for a back transfer. Considering the FCD values, it can be seen that the ground state (dotted line) possesses zwitterionic nature, whereas the three excited states considered are all of biradical nature, i.e. these are reached by charge transfer transitions from the ground state. In the subsequent course of the dynamics the S_1/S_0 energy gap is significantly lowered. In agreement with the CC2 calculations of Ref. [32], we find that an ultrafast internal conversion after the PCET is likely to occur. However, a precise computation of decay times cannot be performed as the reliability of our approach in connection with the PCET process is not certain (as far as the description of the charge transfer transitions as well as of the S_1/S_0 intersection is concerned).

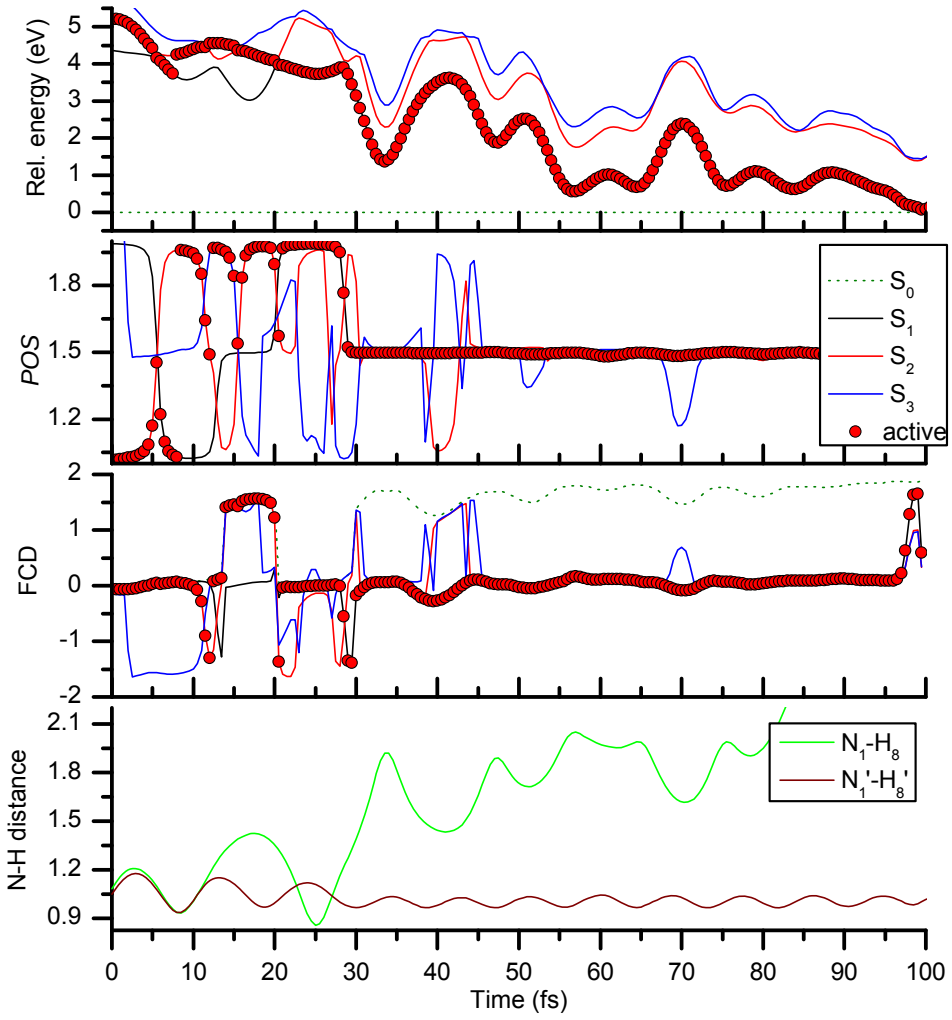

Figure 8. Relative energies, *POS* values, fragment charge differences (FCD) for the lowest four singlet states (the active state is marked with red circles) and N-H bond lengths of a trajectory of the 2-pyridone dimer, which undergoes a proton coupled electron transfer.

Having thus presented the underlying processes, the general evolution of the dynamics will be discussed. In Figure 9 the S_1, S_2, S_3 populations of the initial $(2\text{-PY})_2$ tautomer, as well as the population of the proton transfer (PT) structure is shown (cf. Figure 2). At t = 0 fs the

populations of S_1 and S_2 are 25% and 75% respectively, according to their ratio in oscillator strengths. The early dynamics is characterized by an ultrafast decay from S_2 to S_1 and already after 5.0 fs these states exhibit equal population. In the subsequent dynamics the population of S_2 is equilibrated at about 8% due to a dynamical process consisting of short recrossings to this state, as shown for example in

Figure **7** around 135 fs and 235 fs. This dynamical mixing of the S_2 and S_1 states in the semi-classical dynamics can be seen as the corresponding phenomenon to vibronic mixing between these states, as reported from experiment.[31] During the whole course of the dynamics, also a slight involvement of the S_3 state is present. Whereas this value never exceeds a few percent, preliminary tests indicated that including this state is decisive for an accurate description of the dynamics, where it appears to be in particular important for correctly describing a possible diabatic electron trapping after proton transfer (for example Figure 8 around 15 fs). Ultrafast PCET is seen as well in these simulations, leading to a biradical excited state of the PT structure (Figure 2 (b)). This process is characterized by an initial sharp rise (after 50 fs already 17% of the trajectories are in this structure) and a subsequent significant slowdown (18% after 100 fs; 21% after 200 fs; and 26% after 300 fs).

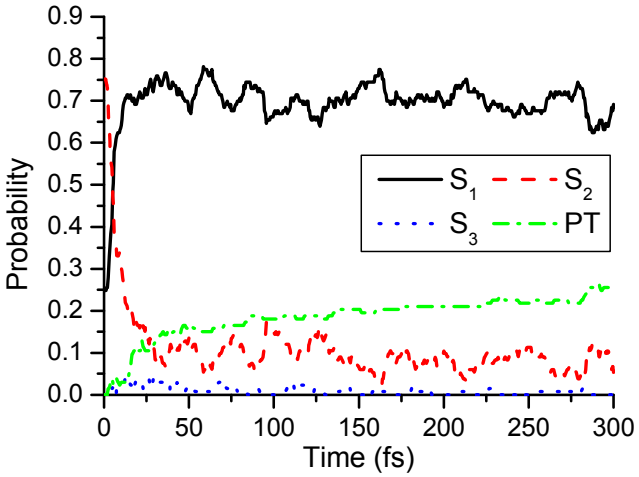

Figure 9. Development of the state distribution during the 300 fs after photoexcitation in the 2-pyridone dimer. S_1, S_2, and S_3 mark the respective state of the initial tautomer, whereas PT corresponds to the structure where one proton is transferred.

Another interesting property of the dynamics is the excitonic delocalization, represented by the *PR* value (Eq. (17)). This value is one for localized or (directed) charge transfer states and two for completely delocalized states. The average development of this quantity is presented in Figure 10. The initial average value (± the sample standard deviation over the different trajectories), corresponding to the Franck-Condon excitation lies at $PR = 1.31 \pm 0.28$. Then a brief initial small spike follows as the trajectories relax into the symmetric S_2 minimum, reaching a maximum of $PR = 1.42 \pm 0.32$ at 3.0 fs. Subsequently, due to switching into the S_1 state, the wave function quickly localizes after less than 50 fs reaching an equilibrium of about $PR \approx 1.1$.

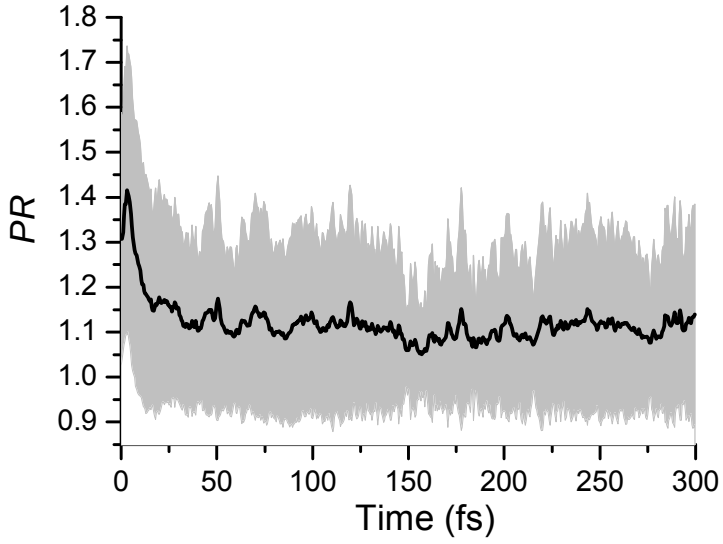

Figure 10. Development of the excitonic participation ratio (*PR*) during the 300 fs after photoexcitation in the 2-pyridone dimer. The average (black line) as well as the standard deviation (grey area) are shown.

To represent the molecular motions in more detail, we perform an analysis of coherent normal mode motions, as explained in the Computational Details. A summary of the lower frequency modes up to 1067 cm^{-1} is presented in Figure 11. The most prominent motions are the two totally symmetric intermolecular modes ν_4 (106 cm^{-1}, "shearing") and ν_6 (166 cm^{-1}, "stretching"). Three more totally symmetric modes show significant activity: two in-plane ring deformation modes ν_{15} (581 cm^{-1}) and ν_{26} (896 cm^{-1}); and the C-H in plane bending mode ν_{35} (1067 cm^{-1}). The strong activity of the intermolecular in-plane mode ν_5 (108 cm^{-1}, "opening") of B_u symmetry reflects the symmetry breaking in the dynamics, which yields the localized exciton. This mode is also strongly displaced in the case of proton transfers. It is interesting to compare these results to experiment. Whereas quantum mechanical effects of the nuclear vibrations are not included in our simulations, our results can still be set in qualitative relation to optical spectra, in the sense that it is just the Franck-Condon active modes, which should show coherent motion after excitation. The two intermolecular low energy modes ν_4 and ν_6 were also observed most prominently in two-color resonant two-photon ionization spectra, and activity of ν_5 was reported as well.[31] In dispersed fluorescence experiments, also activity of the modes denoted here ν_{15} and ν_{26} was reported.[31] In summary it can be seen that the semi-classical dynamics exhibit similar normal mode activity as the experimental absorption and emission spectra. In Figure 12 the time dependence of the normal mode motions is presented. The shearing mode (Figure 12 (a)) exhibits a motion separating the two molecules with a maximum separation at about 200 fs and a backward motion afterwards. Also stretching (Figure 12 (b)) starts right after the excitation and proceeds in a coherent way, where the maximum is reached after about 125 fs and backward motion after that. The in-plane deformation mode ν_{15}, which is in particular related to the C_2-C_5 distances on each molecule, shows an inital C_2-C_5 contraction followed by a coherent ringing with a period of about 60 fs.

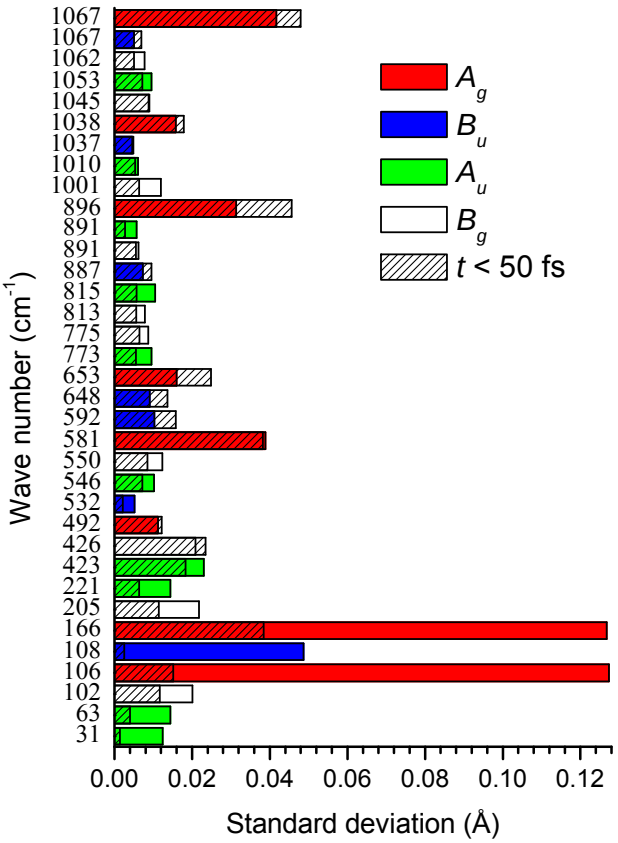

Figure 11. Coherent normal mode activity during the dynamics as measured by the standard deviation of the averaged displacement vectors with respect to the ground state equilibrium structure. Modes and wave numbers of the ground state equilibrium structure are considered. Color coding is according to the symmetry of the mode; diagonal lines mark activity occurring within the first 50 fs. In-plane modes belong to the A_g and B_u symmetries, out-of-plane modes to A_u and B_g.

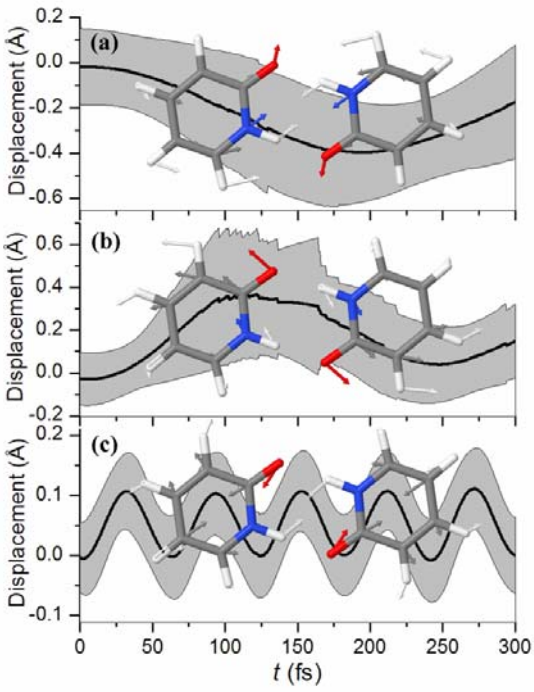

Figure 12. Time evolution of mean displacements for three selected totally symmetric normal modes: ν_4 (106 cm^{-1}, "shearing") (a), ν_6 (166 cm^{-1}, "stretching") (b), ν_{15} (581 cm^{-1}, in-plane ring deformation) (c). Zero indicates the ground state equilibrium value, positive values indicate a displacement in the direction of the arrows, negative values in the opposite direction. Grey areas indicate ± one standard deviation around the mean.

It is of special interest to discuss the transfer processes in more detail. For an analysis of EET the 99 the trajectories, which remained in the initial $(2\text{-PY})_2$ tautomeric form were analyzed. In these cases 142 EET events occurred in total, leading to a transfer time of 207 fs. An experimental reference for this value of 318 fs was derived from the vibronic exciton splittings in a monodeuterated $(2\text{-PY})_2$ complex.[31] The agreement between these two values is quite good and suggests that the TDDFT/BHLYP approach can describe the process correctly. Moreover, this fact could reconcile the discrepancy regarding excitonic couplings that was pointed out in Ref. [32]: Whereas the computed purely electronic couplings are on the order of 0.07 eV, experimental vibronic couplings of 0.003 eV were reported. However, considering the data presented above, it can be seen that when the whole dynamical process is considered, very similar transfer times are obtained in both representations.

In our simulations, a PCET leading to a stabilized PT structure occurred in 26% of the trajectories (cf. Figure 9). These are mostly occurring in the early part of the dynamics. The subsequent slowdown is probably caused by the fact that after excitation the hydrogen bonds

are elongated[32] and as presented above (Figure 11, Figure 12) that major intermolecular motions displace the complex from its initial tightly bound structure. It can therefore be assumed that the number of PCET events would not be much larger if the trajectories were run for a longer time. The simulations are therefore consistent with experiment in the sense that a large fraction of the excited complexes does undergo normal fluorescence. The dynamical behavior that went along with these transfers may be of special interest. Aside from PCETs there was a large number of quick back and forth proton transfer events (as shown for example in Figure 8 around t = 15 fs). These were usually accompanied by surface hoppings, yielding a diabatic trapping of the electron. Therefore a zwitterionic structure was formed, which quickly stabilized by transferring the proton back. In the 133 trajectories simulated 30 such proton back transfers occurred. This highlights the fact that PCET is a process with significant nonadiabatic interactions and cannot be completely understood when only adiabatic potential energy surfaces are considered.

A summary of the processes occurring after photo excitation is presented in Figure 13. Internal conversion from S_2 to S_1 occurs within the first 10 fs. Then the symmetry broken S_1 minima are populated. EET between these two equivalent minima occurs on a time scale of 207 fs. Furthermore, we found that PCET may occur, leading to a biradical excited state of the PT structure, which would subsequently relax to an area with a small S_1/S_0 gap. An interesting phenomenon in this context was that in about half of the PT events, a diabatic trapping of the electron involving two consecutive surface hoppings occurred, and a subsequent backwards PT restored the initial tautomer. In spite of this trapping situation 26% of the trajectories did exhibit PCET in the present simulations.

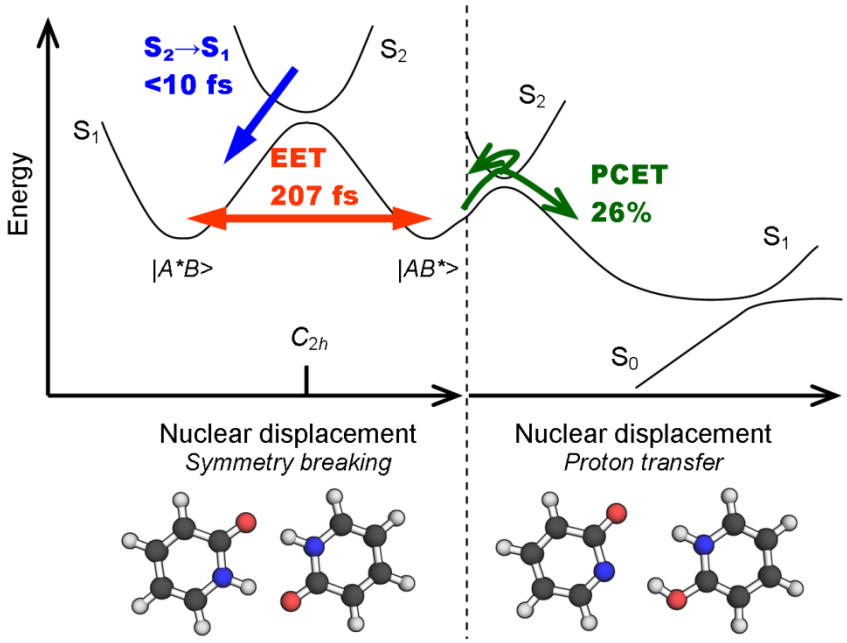

Figure 13. General scheme of processes occurring in the 2-pyridone dimer after photoexcitation as computed with TDDFT/BHLYP dynamics of 300 fs duration.

Finally, possible implications on DNA base pairs will be discussed. EET in $(2\text{-PY})_2$ has been considered as a model for interstrand EET in DNA.[31] In this context it could be said that the time of 207 fs (experimental value: 318 fs)[31] can be seen as a lower bound for the energy transfer time, applicable in the case of two identical molecules and no involvement of

environmental degrees of freedom. PCET in DNA is of special interest as it has been considered as a possible decay channel in UV excited DNA base pairs and model systems.[71-74]

In this work it was observed that in many cases a diabatic trapping of the electron mediated by S_2/S_1 crossings occurred, which lowered the chance of PCET compared to a purely adiabatic treatment. Whereas the PCET itself was observed here, the dynamics after this process, i.e. the possible decay from a biradical S_1 state to the ground state has been examined for a guanine-cytosine Watson-Crick base pair.[73] Also for this situation a diabatic trapping, realized through S_1/S_0 recrossings, was observed.[73] Thus, in summary it can be concluded that nonadiabatic electron transfer dynamics may play a key role in deciding whether or not a PCET channel is accessible.

5. Conclusions

The local diabatization method for surface hopping dynamics was investigated with a focus on the simulation of transport phenomena. It was applied to the stacked ethylene dimer radical cation as well as the hydrogen bonded 2-pyridone dimer. Systematic tests using these systems as well as an analytical model showed that this method can provide very stable results even in challenging cases of very fast nonadiabatic events. In contrast, when using nonadiabatic coupling vectors or wave function overlaps with linear extrapolation in an adiabatic representation of the wave function, significant instabilities were observed when the nonadiabatic interactions were highly peaked. Simulations on the stacked ethylene dimer radical cation with an intermolecular distance of 7.0 Å were performed to represent a case where due to a large spatial separation electron transfer was significantly inhibited. In agreement with the Marcus theory type model an electronic transmission factor of $\kappa_{el} = 1\%$ was obtained, whereas in the remaining 99% of the barrier crossings a diabatic trapping situation was assured through two consecutive surface hoppings.

In the 2-pyridone dimer a complex dynamics (see Figure 13 for a summary) was observed including excitation energy transfer as well as the possibility for a proton coupled electron transfer. The trajectories could be characterized by a very fast (< 10 fs) initial S_2/S_1 internal conversion. For a subsequent excitation energy transfer between the two localized S_1 minima, a characteristic time of 207 fs was obtained, which is in good agreement with the experimental value of 318 fs.[31] 26% of the trajectories exhibited ultrafast proton coupled electron transfer, which may subsequently lead to an internal conversion to the ground state. Whether or not this process really plays a decisive role cannot be conclusively answered without more extensive computations or experiments. However, interesting insight into the process could be gained and it could be shown that PCET does not only depend on the adiabatic energy surfaces related to the proton transfer but that also nonadiabatic effects associated with the electron transfer play a crucial role. The implications of these findings on hydrogen bonded DNA base pairs were discussed as well.

Acknowledgment

F. Plasser is a recipient of a DOC fellowship of the Austrian Academy of Sciences. This work has been supported by the Austrian Science Fund within the framework of the Special Research Program and F41 Vienna Computational Materials Laboratory (ViCoM). Support was also provided by the Robert A. Welch Foundation under Grant No. D-0005. The authors also acknowledge the technical support and computer time at the Vienna Scientific Cluster

(projects 70019 and 70151). J. Pittner acknowledges support by the Granting Agency of the Czech Republic (Project No. 208/12/0559).

References

(1) Middleton, C. T.; de La Harpe, K.; Su, C.; Law, Y. K.; Crespo-Hernandez, C. E.; Kohler, B. *Annu. Rev. Phys. Chem.* **2009**, *60*, 217.

(2) Barbatti, M.; Aquino, A. J. A.; Szymczak, J. J.; Nachtigallová, D.; Hobza, P.; Lischka, H. *Proc. Natl. Acad. Sci. U. S. A.* **2010**, *107*, 21453.

(3) Lewis, F. D.; Zhu, H. H.; Daublain, P.; Fiebig, T.; Raytchev, M.; Wang, Q.; Shafirovich, V. *J. Am. Chem. Soc.* **2006**, *128*, 791.

(4) Brédas, J.-L.; Norton, J. E.; Cornil, J.; Coropceanu, V. *Acc. Chem. Res.* **2009**, *42*, 1691.

(5) Izmaylov, A. F.; Mendive-Tapia, D.; Bearpark, M. J.; Robb, M. A.; Tully, J. C.; Frisch, M. J. *J. Chem. Phys.* **2011**, *135*.

(6) Plasser, F.; Barbatti, M.; Aquino, A. J. A.; Lischka, H. *Theor. Chim. Acta* **2012**, *131*, 1073.

(7) Koppel, H.; Domcke, W.; Cederbaum, L. S. *Adv. Chem. Phys.* **1984**, *57*, 59.

(8) Worth, G. A.; Cederbaum, L. S. *Annu. Rev. Phys. Chem.* **2004**, *55*, 127.

(9) Tully, J. C. *J. Chem. Phys.* **1990**, *93*, 1061.

(10) Levine, B. G.; Coe, J. D.; Virshup, A. M.; Martinez, T. J. *Chem. Phys.* **2008**, *347*, 3.

(11) Barbara, P. F.; Meyer, T. J.; Ratner, M. A. *J. Phys. Chem.* **1996**, *100*, 13148.

(12) Scholes, G.; Jordanides, X.; Fleming, G. *J. Phys. Chem. B* **2001**, *105*, 1640.

(13) Abramavicius, D.; Palmieri, B.; Voronine, D. V.; Sanda, F.; Mukamel, S. *Chem. Rev.* **2009**, *109*, 2350.

(14) Dirac, P. A. M. *Proc. R. Soc. London, A* **1927**, *114*, 243.

(15) Fermi, E. *Notes on Quantum Mechanics*; University of Chicago Press: Chicago, IL, 1961.

(16) Forster, T. *Annalen Der Physik* **1948**, *2*, 55.

(17) Marcus, R. A. *Angew. Chem., Int. Ed. Engl.* **1993**, *32*, 1111.

(18) Granucci, G.; Persico, M.; Toniolo, A. *J. Chem. Phys.* **2001**, *114*, 10608.

(19) Doltsinis, N. L.; Marx, D. *Phys. Rev. Lett.* **2002**, *88*, 166402.

(20) Barbatti, M.; Granucci, G.; Persico, M.; Ruckenbauer, M.; Vazdar, M.; Eckert-Maksic, M.; Lischka, H. *J. Photochem. Photobiol., A* **2007**, *190*, 228.

(21) Mitric, R.; Werner, U.; Bonacic-Koutecky, V. *J. Chem. Phys.* **2008**, *129*, 9.

(22) Tavernelli, I.; Tapavicza, E.; Rothlisberger, U. *THEOCHEM* **2009**, *914*, 22.

(23) Richter, M.; Marquetand, P.; Gonzalez-Vazquez, J.; Sola, I.; Gonzalez, L. *J. Chem. Theory Comput.* **2011**, *7*, 1253.

(24) Nelson, T.; Fernandez-Alberti, S.; Chernyak, V.; Roitberg, A. E.; Tretiak, S. *J. Phys. Chem. B* **2011**, *115*, 5402.

(25) Barbatti, M.; Shepard, R.; Lischka, H. Computational and Methodological Elements for Nonadiabatic Trajectory Dynamics Simulations of Molecules. In *Conical Intersections: Theory, Computation and Experiment*; Domcke, W., Yarkony, D. R., Köppel, H., Eds.; World Scientific Singapore, 2011; Vol. 17.

(26) Blancafort, L.; Hunt, P.; Robb, M. A. *J. Am. Chem. Soc.* **2005**, *127*, 3391.

(27) Plasser, F.; Lischka, H. *J. Chem. Phys.* **2011**, *134*, 034309.

(28) Baer, M. *Phys. Rep.* **2002**, *358*, 75.

(29) Nelson, T.; Fernandez-Alberti, S.; Chernyak, V.; Roitberg, A. E.; Tretiak, S. *J. Chem. Phys.* **2012**, *136*, 054108.
(30) Granucci, G.; Persico, M.; Spighi, G. *J. Chem. Phys.* **2012**, *DOI: 10.1063/1.4707737*.
(31) Muller, A.; Talbot, F.; Leutwyler, S. *J. Chem. Phys.* **2002**, *116*, 2836.
(32) Sagvolden, E.; Furche, F. *J. Phys. Chem. A* **2010**, *114*, 6897.
(33) Barbatti, M. *WIREs: Comp. Mol. Sci.* **2011**, *1*, 620.
(34) Hammes-Schiffer, S.; Tully, J. C. *J. Chem. Phys.* **1994**, *101*, 4657.
(35) Tapavicza, E.; Tavernelli, I.; Rothlisberger, U. *Phys. Rev. Lett.* **2007**, *98*, 023001.
(36) Pittner, J.; Lischka, H.; Barbatti, M. *Chem. Phys.* **2009**, *356*, 147.
(37) Lowdin, P. O. *J. Chem. Phys.* **1950**, *18*, 365.
(38) Brunschwig, B. S.; Logan, J.; Newton, M. D.; Sutin, N. *J. Am. Chem. Soc.* **1980**, *102*, 5798.
(39) Plasser, F.; Lischka, H. *J. Chem. Theory Comput.*, *submitted for publication*.
(40) Luzanov, A. V.; Zhikol, O. A. *Int. J. Quantum Chem.* **2010**, *110*, 902.
(41) Tretiak, S.; Mukamel, S. *Chem. Rev.* **2002**, *102*, 3171.
(42) Pipek, J.; Mezey, P. G. *Int. J. Quantum Chem.* **1988**, *34*, 1.
(43) Czader, A.; Bittner, E. R. *J. Chem. Phys.* **2008**, *128*, 035101.
(44) Voityuk, A. A.; Rosch, N. *J. Chem. Phys.* **2002**, *117*, 5607.
(45) Krishnan, R.; Binkley, J. S.; Seeger, R.; Pople, J. A. *J. Chem. Phys.* **1980**, *72*, 650.
(46) Granucci, G.; Persico, M. *J. Chem. Phys.* **2007**, *126*.
(47) Casida, M. Time-dependent density functional response theory for molecules. In *Recent advances in density functional methods, Part I*; Chong, D., Ed.; World Scientific: Singapore, 1995; pp 155.
(48) Bauernschmitt, R.; Ahlrichs, R. *Chem. Phys. Lett.* **1996**, *256*, 454.
(49) Becke, A. *J. Chem. Phys.* **1993**, *98*, 5648.
(50) Lee, C.; Yang, W.; Parr, R. G. *Phys. Rev. B: Condens. Matter* **1988**, *37*, 785.
(51) Schafer, A.; Horn, H.; Ahlrichs, R. *J. Chem. Phys.* **1992**, *97*, 2571.
(52) Aquino, A. J. A.; Tunega, D.; Haberhauer, G.; Gerzabek, M. H.; Lischka, H. *J. Phys. Chem. A* **2002**, *106*, 1862.
(53) Plasser, F.; Barbatti, M.; Aquino, A. J. A.; Lischka, H. *J. Phys. Chem. A* **2009**, *113*, 8490.
(54) Plasser, F. Dynamics simulation of excited state intramolecular proton transfer (http://othes.univie.ac.at/4414/). Master Thesis, 2009.
(55) Lischka, H.; Shepard, R.; Brown, F. B.; Shavitt, I. *Int. J. Quantum Chem.* **1981**, *S15*, 91.
(56) Lischka, H.; Shepard, R.; Pitzer, R. M.; Shavitt, I.; Dallos, M.; Muller, T.; Szalay, P. G.; Seth, M.; Kedziora, G. S.; Yabushita, S.; Zhang, Z. Y. *Phys. Chem. Chem. Phys.* **2001**, *3*, 664.
(57) Shepard, R.; Lischka, H.; Szalay, P. G.; Kovar, T.; Ernzerhof, M. *J. Chem. Phys.* **1992**, *96*, 2085.
(58) Lischka, H.; Dallos, M.; Shepard, R. *Mol. Phys.* **2002**, *100*, 1647.
(59) Lischka, H.; Dallos, M.; Szalay, P. G.; Yarkony, D. R.; Shepard, R. *J. Chem. Phys.* **2004**, *120*, 7322.
(60) Lischka, H.; Shepard, R.; Shavitt, I.; Pitzer, R. M.; Dallos, M.; Mueller, T.; Szalay, P. G.; Brown, F. B.; Ahlrichs, R.; Boehm, H. J.; Chang, A.; Comeau, D. C.; Gdanitz, R.; Dachsel, H.; Ehrhardt, C.; Ernzerhof, M.; Hoechtl, P.; Irle, S.; Kedziora, G.; Kovar, T.;

Parasuk, V.; Pepper, M. J. M.; Scharf, P.; Schiffer, H.; Schindler, M.; Schueler, M.; Seth, M.; Stahlberg, E. A.; Zhao, J.-G.; Yabushita, S.; Zhang, Z.; Barbatti, M.; Matsika, S.; Schuurmann, M.; Yarkony, D. R.; Brozell, S. R.; Beck, E. V.; Blaudeau, J.-P.; Ruckenbauer, M.; Sellner, B.; Plasser, F.; Szymczak, J. J. *COLUMBUS, an ab initio electronic structure program, release 7.0* **2011**, www.univie.ac.at/columbus.

(61) Lischka, H.; Mueller, T.; Szalay, P. G.; Shavitt, I.; Pitzer, R. M.; Shepard, R. *WIREs: Comp. Mol. Sci.* **2011**, *1*, 191.

(62) Ahlrichs, R.; Bar, M.; Haser, M.; Horn, H.; Kolmel, C. *Chem. Phys. Lett.* **1989**, *162*, 165.

(63) Barbatti, M.; Pittner, J.; Pederzoli, M.; Werner, U.; Mitric, R.; Bonacic-Koutecky, V.; Lischka, H. *Chem. Phys.* **2010**, *375*, 26.

(64) Barbatti, M.; Granucci, G.; Ruckenbauer, M.; Plasser, F.; Pittner, J.; Persico, M.; Lischka, H. *NEWTON-X: a package for Newtonian dynamics close to the crossing seam* **2011**, www.newtonx.org.

(65) Wessel, J. E.; Syage, J. A. *J. Phys. Chem.* **1990**, *94*, 737.

(66) Reece, S. Y.; Nocera, D. G. *Annu. Rev. Biochem.* **2009**, *78*, 673.

(67) Chernyak, V.; Mukamel, S. *J. Chem. Phys.* **2000**, *112*, 3572.

(68) Hu, C. P.; Hirai, H.; Sugino, O. *J. Chem. Phys.* **2007**, *127*, 9.

(69) Tavernelli, I.; Tapavicza, E.; Rothlisberger, U. *J. Chem. Phys.* **2009**, *130*, 10.

(70) Send, R.; Furche, F. *J. Chem. Phys.* **2010**, *132*, 044107.

(71) Sobolewski, A. L.; Domcke, W.; Hättig, C. *Proc. Natl. Acad. Sci. U. S. A.* **2005**, *102*, 17903.

(72) Abo-Riziq, A.; Grace, L.; Nir, E.; Kabelac, M.; Hobza, P.; de Vries, M. *Proc. Natl. Acad. Sci. U. S. A.* **2005**, *102*, 20.

(73) Groenhof, G.; Schafer, L. V.; Boggio-Pasqua, M.; Goette, M.; Grubmuller, H.; Robb, M. A. *J. Am. Chem. Soc.* **2007**, *129*, 6812.

(74) Schultz, T.; Samoylova, E.; Radloff, W.; Hertel, I. V.; Sobolewski, A. L.; Domcke, W. *Science* **2004**, *306*, 1765.

3.5 Dynamics of Charge Transport in Solution

This section is concerned with the simulation of the interplay between the polarization of the solute and the environment in the case of charge transfer dynamics. This part is currently not considered for publication.

3.5.1 Introduction

The interplay between solute and solvent polarization is a decisive process determining the dynamics of charges in solution. A special challenge in this context is that a high level description of the solute is necessary while also a large scale description of the environment has to be provided. Such a task is possible through hybrid strategies and in particular the QM/MM methodology appears to be suitable. [89] In this work the charged system is explicitly described by the ab-initio SA-MCSCF level of theory. The influence of the solvent is included by an electrostatic embedding approach. [62] Activation free energies are computed by two different approaches: (i) using an averaged solvent electrostatic potential (ASEP, cf. Refs [90, 91]) for applying Marcus theory, and (ii) explicit free energy perturbation. The analysis proceeds by consideration of different adiabatic-to-diabatic transformations. For (i) a new scheme for coarse graining of a pointcharge distribution was used. Moreover, direct QM/MM dynamics are performed to obtain a time-dependent description.

Two model systems are considered here: the stacked ethylene dimer radical cation $[Et\text{–}Et]^+$ and the same system with two additional stacked formaldehyde molecules $[FA\text{–}Et\text{–}Et\text{–}FA]^+$, both in aqueous solution (Figure 3.3). In these systems counterbalancing effects between a strong electronic coupling and solvent reorganization can be observed, the former favoring a delocalization of the charge the latter working toward localizing it.

3.5.2 Methods

To carry out this study several methodological considerations were necessary relating to the diabatic character of the states, to the computation of the activation

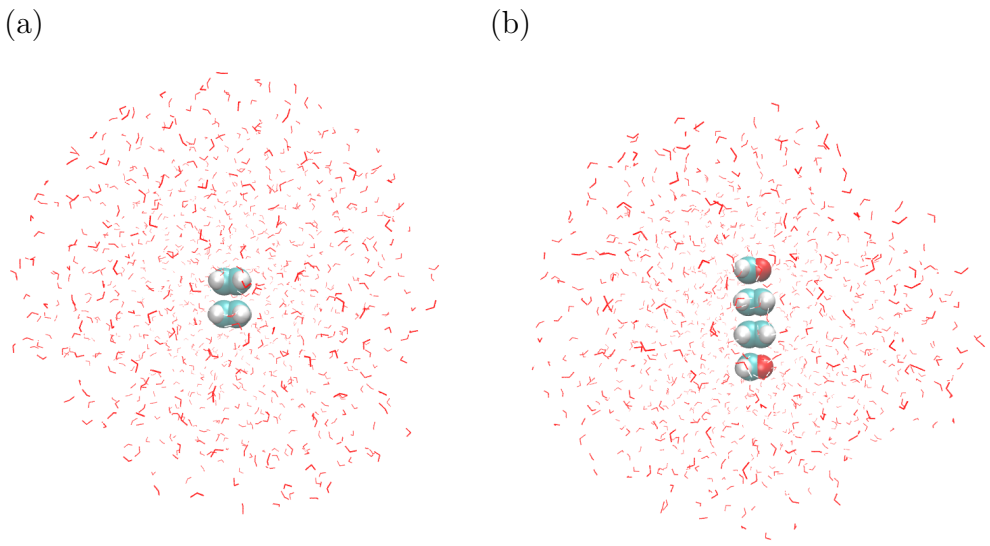

Figure 3.3: *Graphical representation of the* $[Et–Et]^+$ *(a) and* $[FA–Et–Et–FA]^+$ *(b) systems considered in this section.*

free energy, and to a coarse graining of the pointcharges to allow for an efficient description of the environment. In this section the major equations are outlined. The detailed procedure will be described in the next section.

Electronic coupling and diabatic energies

First it will be explained how to create an approximately diabatic representation of the states. This is necessary for computing electronic couplings if no resonance conditions are present. Moreover, a connection between the computations in-vacuo and in solution can be performed (see also Ref. [92]). A two state model consisting of two adiabatic states ϕ and ψ is assumed. These are obtained from the "initial" Ψ_{i}^{loc} and "final" Ψ_{f}^{loc} localized diabatic states according to a unitary transformation (see also Section 3.3)

$$\begin{pmatrix} \phi \\ \psi \end{pmatrix} = \mathbf{U} \begin{pmatrix} \Psi_{\mathrm{i}}^{loc} \\ \Psi_{\mathrm{f}}^{loc} \end{pmatrix} \tag{3.22}$$

$$\mathbf{U} = \begin{pmatrix} \cos(\eta) & -\sin(\eta) \\ \sin(\eta) & \cos(\eta) \end{pmatrix} \tag{3.23}$$

With this construction the Hamiltonian matrix in the localized basis $\mathbf{H}^{loc}$ is obtained from the adiabatic energies according to

$$\mathbf{H}^{loc} := \begin{pmatrix} H_{\mathrm{ii}} & H_{\mathrm{if}} \\ H_{\mathrm{if}} & H_{\mathrm{ff}} \end{pmatrix} = \mathbf{U} \begin{pmatrix} E_\phi & 0 \\ 0 & E_\psi \end{pmatrix} \mathbf{U}^{-1} \tag{3.24}$$

To actually evaluate this expression the mixing angle η is needed. In this work the fragment charge difference (FCD) [73] method is used for this purpose. First the FCDs Δq are expressed in the adiabatic and localized diabatic representations.

$$\mathbf{\Delta q}^{ad} := \begin{pmatrix} \Delta q_\phi & \Delta q_{\phi\psi} \\ \Delta q_{\phi\psi} & \Delta q_\psi \end{pmatrix} = \mathbf{U}^{-1} \mathbf{\Delta q}^{loc} \mathbf{U} \tag{3.25}$$

Voityuk and Rösch [73] have schon that a maximum of charge separation in $\mathbf{\Delta q}^{loc}$ corresponds to the condition

$$\tan(2\eta) = \frac{2\Delta q_{\phi\psi}}{\Delta q_\phi - \Delta q_\psi} \tag{3.26}$$

which yields the following relation for the electronic coupling H_{if}

$$H_{\mathrm{if}} = \frac{(E_\phi - E_\psi)|\Delta q_{\phi\psi}|}{\sqrt{(\Delta q_\phi - \Delta q_\psi)^2 + \Delta q_{\phi\psi}^2}} \tag{3.27}$$

In the case of no involvement of a bridge between the two charge centers, the formula (3.26) takes the simplified form [73]

$$-\Delta q_\phi = \Delta q_\psi = \cos(2\eta) \tag{3.28}$$

$$|\Delta q_{\phi\psi}| = \sin(2\eta) \tag{3.29}$$

and it is enough to compute one of the FCD values, typically the one of the ground state Δq_ϕ. This results in the following expression for the electronic coupling

$$H_{\mathrm{if},approx} = (E_\phi - E_\psi)\sqrt{1 - \Delta q_\phi^2} \tag{3.30}$$

Activation free energy

For the computation of the activation free energy $\Delta A^{\neq}$ two different approaches were considered: a Marcus theory [93] type approach and free energy perturbation

(FEP). [94] In the first case special attention had to be paid to an inclusion of distortions of the potential energy induced by the rather strong electronic couplings present in the cases considered. A parabolic diabatic Hamiltonian between two equivalent sites with a constant coupling H_{if} and a reorganization energy λ

$$\mathbf{H}^{loc}(\xi) = \begin{pmatrix} \lambda\left(\xi + 1/2\right)^2 & H_{\mathrm{if}} \\ H_{\mathrm{if}} & \lambda\left(\xi - 1/2\right)^2 \end{pmatrix} \tag{3.31}$$

was assumed. This Hamiltonian can be diagonalized by a unitary transformation, yielding adiabatic energies of

$$E_\phi(\xi) = \lambda\left(1/4 + \xi^2\right) - \sqrt{H_{\mathrm{if}}^2 + \lambda^2\xi^2} \tag{3.32}$$

$$E_\psi(\xi) = \lambda\left(1/4 + \xi^2\right) + \sqrt{H_{\mathrm{if}}^2 + \lambda^2\xi^2} \tag{3.33}$$

If $\lambda > 2|c|$ then the ground state E_ϕ has two minima, which are located at

$$\xi_{min} = \pm\frac{\sqrt{\lambda^2 - 4H_{\mathrm{if}}^2}}{2\lambda} \tag{3.34}$$

By inserting this value into Eqs (3.32) and (3.33), it can be seen that the adiabatic gap at one of these minima

$$\Delta E_{min} := E_\psi(\xi_{min}) - E_\phi(\xi_{min}) = \lambda \tag{3.35}$$

corresponds precisely to the reorganization energy λ. This means that in a symmetric system the reorganization energy can simply be obtained by computing the vertical excitation energy at one of the minima. In the case of vanishing couplings, Marcus theory states that the activation free energy is obtained as $\Delta A^{\neq} = \frac{\lambda}{4}$. [93] A generalization of this, applicable to the case of non-vanishing couplings, may be written as

$$\Delta A^{\neq} := E_\phi(0) - E_\phi(\xi_{min}) = \frac{\lambda}{4} - H_{\mathrm{if}} + \frac{H_{\mathrm{if}}^2}{\lambda} \tag{3.36}$$

The strength of this type of approach is that this essential thermodynamic property can be obtained by simply computing the vertical excitation energy at one of the minima (and if necessary the couplings as outlined above).

For comparison the activation free energies were also computed by a more direct approach using molecular dynamics (MD). For this purpose $\Delta A^{\neq}$ was split into an external and internal part

$$\Delta A^{\neq} = \Delta A^{\neq}_{ext} + \Delta E^{\neq}_{int} \tag{3.37}$$

The external activation free energy $\Delta A^{\neq}_{ext}$ derives from the solvent-solute and solvent-solvent interactions. It can be computed using classical MD, where in particular the FEP approach [94] is efficient.

The internal activation energy corresponds to the energy related to the change in geometry and to the energy of charge separation. A diabatic correction was included because of the fact that the wavefunction in-vacuo does not correspond to the wavefunction in solution (see also [92]). And $\Delta E^{\neq}_{int}$ is computed as

$$\Delta E^{\neq}_{int} = E^{iso}_{\phi}(0) - E^{iso}_{\eta_{emb}}(\xi_{min}) \tag{3.38}$$

where $E^{iso}_{\phi}(0)$ is simply the energy of the ground state at the symmetric geometry, computed in-vacuo. No diabatic correction had to be performed here for symmetry reasons. $E^{iso}_{\eta_{emb}}(\xi_{min})$ is the in-vacuo energy of the state which corresponds to the diabatic character of the calculation in solution, computed at the minimum geometry optimized in solution. According to the two state model a correction can be performed by considering the mixing angles in the isolated η_{iso} and embedded η_{emb} calculations.

$$E^{iso}_{\eta_{emb}}(\xi_{min}) = E^{iso}_{\phi}(\xi_{min}) \left(\cos\left(\eta_{emb} - \eta_{iso}\right)\right)^2 + E^{iso}_{\psi}(\xi_{min}) \left(\sin\left(\eta_{emb} - \eta_{iso}\right)\right)^2 \tag{3.39}$$

where η_{emb} and η_{iso} correspond to the values obtained according to (Eq. 3.26) (or Eq. (3.28)) for embedded and isolated calculations, respectively, computed at the minimum geometry of the embedded system.

Coarse graining of pointcharges

For QM/MM calculations with a large MM region or even more in ASEP calculations the computation of the QM/MM electrostatic interaction terms (Eq. (2.84)) may constitute a dominant factor of the computation time. However, in most cases the precise position of charges far away from the QM region should not have a significant impact but only their large scale electrostatic moments should be of importance. This motivates the idea of coarse graining the pointcharge distribution, where areas close to the QM region should be described by a high resolution but areas farther away can be given a more approximate treatment. One possible procedure for this purpose has been described in Refs [90, 91]. In this work a

somewhat different approach is chosen with the main difference that a dynamical threshold is used, which means that there is no clear cutoff and no discontinuities in the description. Therefore a smooth transition between parts described more accurately and parts with increased coarse graining is possible. Moreover, an approximate gradient for all original pointcharges can be easily computed.

The main idea of this procedure is that two pointcharges of the same sign i and j were combined and replaced by a charge corresponding to the sum of these two positioned at their center of charge if the distance d_{ij} between them was

$$d_{ij} \leq d_{ij,max} := C\left(\frac{r_i + r_j}{2} - r_0\right) \tag{3.40}$$

where r_i and r_j are the distance of these point charges to the origin and the parameters r_0 and C represent the radius of the (spherical) molecular cavity and the fineness of the procedure, respectively. Firstly, pointcharges were sorted according to their r_i values. Then the procedure was carried in out an iterative way: starting from the outside, a charge i was compared with the following charges j. If Eq. (3.40) was fulfilled, the charges were combined. If on the other hand the pre-screening condition

$$(r_i - r_j)^2 \leq d_{ij,max} \tag{3.41}$$

was no longer fulfilled pointcharge i was set aside and the procedure was continued with the charge $i+1$. This process was iterated until no more pairs of pointcharges that satisfied Eq. (3.40) could be found.

An example application of this procedure as applied to a distribution of pointcharges obtained from 100 independent molecular dynamics frames is shown in Figure 3.4. It can be seen that in the vicinity of the central molecule the fine structure of the distribution is retained. By contrast, when moving farther apart from the central region the initial dense distribution of pointcharges is significantly coarse grained.

In the case of a non-spherical molecule the procedures described above would not directly yield a uniform reduction around the whole molecule. Pointcharges positioned along the long axis would be overly coarse grained, while the ones along the short axis may be kept unnecessarily at a high resolution. For this purpose a customized scaling along the three coordinate axes can be specified in order to yield an approximately spherical cavity (Figure 3.5). In this scaled coordinate

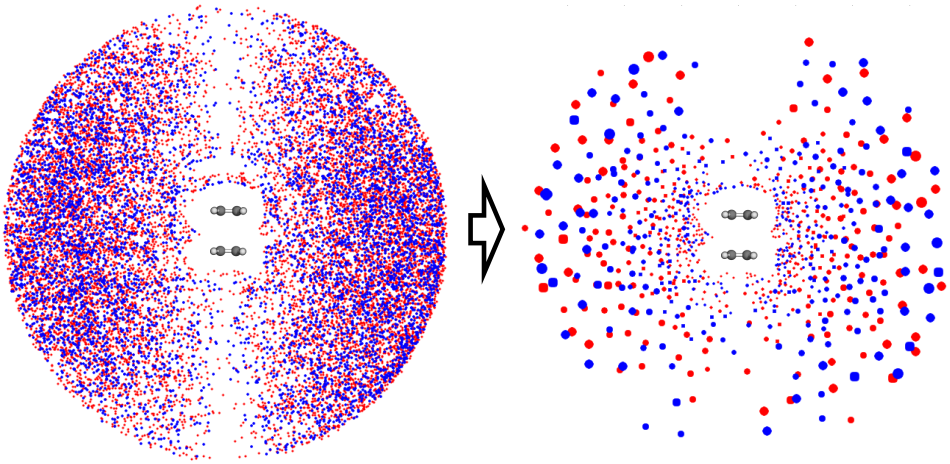

Figure 3.4: *Example of coarse graining of a pointcharge distribution.*

system a pointcharge reduction as explained above may be carried out providing equal treatment along the coordinate axes. The final coarse grained potential is obtained after rescaling the pointcharges to the original coordinate system.

If the coarse graining procedure is to be applied to dynamics simulations then it would be of importance to have gradients available, at least in an approximate fashion. These can be computed by the following considerations. Assuming that a set of point charges with indices $i_1, \ldots, i_m$ had been combined to one pointcharge, and that for this combined charge an energy gradient $\bigtriangledown_c E$ was obtained from the electronic structure calculation - then approximate gradients $\bigtriangledown_{i_k} E$ for the individual point charges in this set can be computed according to

$$\bigtriangledown_{i_k} E = \bigtriangledown_c E \frac{q_{i_k}}{\sum_{l=1}^{m} q_{i_l}} \tag{3.42}$$

where q_{i_k} is the charge of the pointcharge indexed i_k. It may be pointed out here that only the part of the gradient relating to the QM/MM solute-solvent interaction, which should be small by construction, is approximated. The MM solvent-solvent gradient contributions can still be computed in the full set of atoms. Moreover, the solvent dynamics usually do not proceed in a completely deterministic fashion in any case due to a thermostat. Thus, it can be assumed that these approximate gradients yield satisfactory results in many cases while significantly lowering the computational cost.

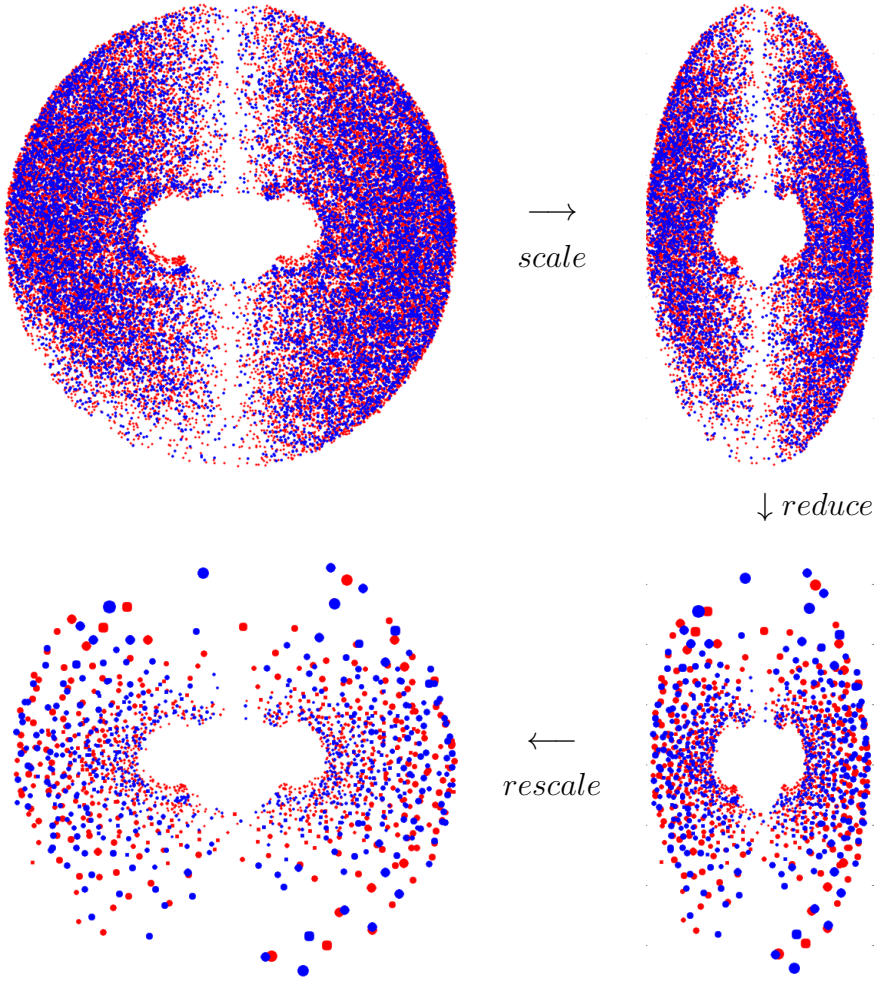

Figure 3.5: *Pointcharge reduction in the case of an elliptical molecular cavity.*

3.5.3 Computational Details

The $[Et–Et]^+$ and $[FA–Et–Et–FA]^+$ systems were arranged as symmetric face-to-face stacks arranged with the z-axis perpendicular to the molecular plane with intermolecular stacking distances of 3.5 Å. The stacks were solvated in a spherical droplet containing about 1000 water molecules. Electronic structure calculations were performed using the CASSCF method with three active electrons in four active orbitals with state-averaging over two states. For $[Et–Et]^+$ the 6-311+G* basis set was used, for $[FA–Et–Et–FA]^+$ the 6-31G* basis set. Dynamics calculations were performed with the COLUMBUS program package [36, 41, 80, 83] using the newly improved gradients described in Section 3.2. Molecular dynamics were performed with TINKER [95] using the OPLSAA forcefield. [96] The initial solvated structures were created using PACKMOL. [97]

Geometry optimizations in solution were carried out using an ASEP formalism (see alse Refs [90, 91]). For this purpose after equilibration a 100 ps MD run was performed and one frame per ps was sampled. These pointcharges were scaled and considered as one combined potential. A reduction according to Eq. (3.40) was performed where $C = 0.02$ and $r_0 = 5.0$Å. Using this external potential a geometry optimization of the stack was performed. Additional harmonic restrains to secure the relative positions of the individual molecules were included as described in Section 3.3. Using the new structure and fitted CHELPG charges [98] another MD sampling run was performed and the procedure repeated until no significant changes were observed in the optimization (requiring about two or three cycles). These optimizations were performed for the localized minimum structure and for the symmetric transition state. In the latter case an additional symmetrization of the external charges were performed to assure a symmetric structure.

Free energy perturbation was carried out using the ASEP optimized structures. An interpolation between the minimum and TS, considering structures and CHELPG charges, was performed using the single topology approach (cf. [94]). Thermalization runs were performed at interpolation values of λ_{FEP}= 0.25, 0.65, 0.90 allowing for a more thorough sampling of the area with more charge separation. Using these sets of configurations sampling in the forward and reverse directions was performed at λ_{FEP}= 0.00, 0.50, 0.80, 1.00.

Dynamics simulations were carried out following the procedures described in Ref. [62]. For the initial conditions of the dynamics intramolecular motions of the central region were considered as quantum mechanical zero point vibrations, whereas solvent modes were considered by classical dynamics. In the present case, the equilibration was performed with respect to the neutral system. And the dynamics represented the vertical ionization process. Non-adiabatic interactions were considered using the local diabatization methd as described in Section 3.4. To follow the ionization process the electric field due to the point charges was computed at five distinct points around the origin and the z-direction of this field was plotted. 20 trajectories for $[Et\text{–}Et]^+$ and 29 for $[FA\text{–}Et\text{–}Et\text{–}FA]^+$ were considered.

3.5.4 Results and Discussion

Stationary points and electronic couplings

As a first step, the stationary points on the potential energy surface were examined and different methods for estimating the electronic couplings were evaluated (Table 3.2). For this purpose structures were optimized in solution using the ASEP formalism described above and the electronic coupling at these optimized structures was evaluated. In the case of the symmetric TS structure, the coupling is simply given as half the energy gap. This amounted to 0.637 eV for $[Et\text{–}Et]^+$ and 0.634 eV for $[FA\text{–}Et\text{–}Et\text{–}FA]^+$. These values are almost identical, illustrating the fact that the two additional FA molecules on the outside of the charged ethylene molecules only have a negligible effect on the coupling. For $[Et\text{–}Et]^+$ at its minimum structure the charge was almost completely localized ($|\Delta q| > 0.9$). This means that the large energy gap obtained is deriving mostly from the difference in site energies. A direct estimation of the coupling only from the energy gap is not possible in such a case. However, the formulas (3.30) and (3.27) can be applied yielding values of 0.459 eV and 0.559 eV, respectively. A discrepancy remains, which is probably related to the strong localization of the charge. In the case of $[FA\text{–}Et\text{–}Et\text{–}FA]^+$ the localization of the charge is less pronounced ($|\Delta q| \approx 0.7$). Eqs (3.30) and (3.27) lead to the identical value of 0.600 eV, which is also similar to the coupling obtained at the TS.

Table 3.2: *Adiabatic energy gaps, fragment charge differences and estimated electronic couplings of the QM/MM calculations.*

	$[Et–Et]^+$		$[FA–Et–Et–FA]^+$	
	TS	min.	TS	min.
ΔE (eV)	1.274	3.032	1.268	1.750
Δq_ϕ (a.u.)	0	0.953	0	0.728
Δq_ψ (a.u.)	0	-0.907	0	-0.721
$\Delta q_{\phi\psi}$ (a.u.)	1.005	0.369	0.996	0.683
$H_{\mathrm{if},approx}$ (eV) [a]	-	0.459	-	0.600
H_{if} (eV) [b]	0.637	0.559	0.634	0.600

[a] computed according to Eq. (3.30)

[b] computed according to Eq. (3.27)

It is interesting to consider the influence of the solvent on the couplings. For this purpose the couplings were also computed without the influence of the pointcharges (Table 3.3) using the same geometries as in Table 3.2. For the TS structures very similar results were obtained. By contrast in the case of minimum structures a significantly increased charge delocalization was observed, represented by lower Δq values, and lower energy gaps (ΔE). However, by applying Eqs (3.30) or (3.27) very similar results for the coupling as in the above case are obtained. In summary it could be shown that the couplings do not experience a strong dependence on either the geometry or the solvent. This suggests that in practical calculations either of these values can be taken to represent the coupling.

Activation Free Energy

In a next step the activation free energy was computed according to the Marcus theory type formula Eq. (3.36), Table 3.4. For this purpose the reorganization energy λ was computed according to Eq. (3.35) (i.e. the vertical excitation energy at the minimum geometry). For the coupling the value of the TS in the QM/MM calculations (Table 3.2) was considered. In both cases it can be seen that a quite substantial value of λ is counterbalanced by a strong diabatic coupling. In the $[Et–Et]^+$ case there is still a significant free energy barrier of 0.255 eV remaining

Table 3.3: *Adiabatic energy gaps, fragment charge differences and estimated electronic couplings of the QM calculations.*

	$[Et\text{–}Et]^+$		$[FA\text{–}Et\text{–}Et\text{–}FA]^+$	
	TS	min.	TS	min.
ΔE (eV)	1.312	1.171	1.294	1.239
Δq_ϕ (a.u.)	0	0.154	0	0.134
Δq_ψ (a.u.)	0	-0.148	0	-0.133
$\Delta q_{\phi\psi}$ (a.u.)	1.003	0.991	0.995	0.985
$H_{\mathrm{if},approx}$ (eV) [a]	0.656	0.578	0.647	0.614
H_{if} (eV) [b]	0.656	0.579	0.647	0.614

[a] computed according to Eq. (3.30)

[b] computed according to Eq. (3.27)

Table 3.4: *Activation free energy as obtained by a QM/MM ASEP calculation in connection with Marcus theory.*

	$[Et\text{–}Et]^+$	$[FA\text{–}Et\text{–}Et\text{–}FA]^+$
λ (eV)	3.032	1.750
H_{if} (eV) [a]	0.637	0.634
$\Delta A^{\neq}$ (eV) [b]	0.255	0.033

[a] using the values of the TS in Table 3.2

[b] computed according to Eq. (3.36)

while for $[FA\text{–}Et\text{–}Et\text{–}FA]^+$ λ and H_{if} approximately cancel each other out yielding a rather flat free energy surface.

For comparison $\Delta A^{\neq}$ was also computed by the somewhat more involved FEP procedure as explained in Section 3.5.3 (Table 3.5). Aside from providing a way of checking the above results, this procedure also gives a possibility to differentiate between the internal and external contributions of the activation free energy. The internal contribution $\Delta E^{\neq}_{int}$ is concerned with the change in geometry as well as with the energy required for charge separation. In the present context this energy is negative considering that because of the strong electronic coupling the isolated system tends to delocalize the charge. The external contribution $\Delta A^{\neq}_{ext}$ is related to the fact that the solvent tends to trap and localize the charge. The total activation free energy is obtained after counterbalancing these two contributions. In the case

Table 3.5: *Activation free energy as obtained by a QM+MM free energy perturbation.*

	$[Et–Et]^+$	$[FA–Et–Et–FA]^+$
$E_\phi^{iso}(0)$	0	0
$E_\phi^{iso}(\xi_{min})$	0.086	0.040
$E_\psi^{iso}(\xi_{min})$	1.257	1.279
η_{iso}	0.710	0.718
η_{emb}	0.189	0.378
$\Delta E_{int}^{\neq}$ (eV)	-0.376	-0.178
$\Delta A_{ext}^{\neq}$ (eV)	0.521	0.213
$\Delta A^{\neq}$ (eV) [a]	0.145	0.035

[a] computed according to Eq. 3.37

of $[Et–Et]^+$ a $\Delta A^{\neq}$ value of 0.145 eV is obtained. In agreement with Table 3.4 there is a significant barrier for charge transfer. Using the Marcus theory approach the estimate of the barrier was somewhat higher. This may be understood by the fact that in the estimation of λ, as a computation of the vertical excitation energy (Eq. 3.35)), no dynamical solvent polarization was included. In spite of being small, dynamical solvent polarizability may have important effects in cases where significant charge shifts occur. And it has been pointed out that non-polarizable forcefields may somewhat overestimate the reorganization energy in this type of calculation. [89] By contrast in the FEP approach there are no computations of vertical excitation energies in solution involved making it more robust with respect to this problem.

For $[FA–Et–Et–FA]^+$ the internal and external contributions cancel each other out almost exactly, yielding a small barrier of 0.035 eV, in good agreement with Table 3.4.

Dynamics

The processes occurring after vertical ionization were examined by explicit QM/MM dynamics simulations to highlight the above considerations in a different framework. Moreover, direct dynamics allow to observe solvent response times. An

example trajectory for the first 500 fs after vertical ionization of $[Et–Et]^+$ in aqueous solution is given in Figure 3.6. The energy gap between the D_0 and D_1 states, the FCD of these states, and a representation of the electric field as induced by the solvent (see Section 3.5.3) is presented. Within about the first 10 fs the charge is localized on one side, yielding an FCD which subsequently oscillates around a value of about 0.75. At a somewhat slower timescale (20 fs) the solvent response can be observed by a an increase in the electric field. The energy gap between the doublet ground and first excited state is initially somewhat above one eV, which can be understood as the gap present due to the electronic coupling (cf. Table 3.2). During the dynamics a quick increase of the energy gap is obtained and a subsequent oscillation around about 1.75 eV occurs. This value is significantly lower than the energy gap of about 3.0 eV at the potential energy minimum (cf. Table 3.2), meaning that this area of the potential surface is not quite reached but the charge remains somewhat more delocalized, as can also be seen by the FCD values.

The time-dependent averages over 20 trajectories of the three values discussed above are presented in Figure 3.7. The average energy gap ΔE at $t = 0$ plus/minus one standard deviation lies at 1.14 ± 0.10 eV. This corresponds closely to the value at the TS (cf. Table 3.2), i.e. the value induced by the electronic coupling alone. This energy is raised in a coherent fashion after vertical excitation, owing to a trapping of the charge and after 32 fs ΔE is increased to 1.65 ± 0.12 eV. After this process the energy gap oscillates in a rather coherent fashion, while always staying above the initial value. Next, the FCD is plotted in Figure 3.7. In this case the absolute value is considered because of the fact that the charge may be localized on either side with equal probability. At $t = 0$ this average absolute shows a rather wide distribution of 0.27 ± 0.19. In the subsequent dynamics the value increases somewhat but no clear coherent dynamics can be observed considering the wide distribution that was already present at the start. Finally the average of the absolute value of the z-component of the solvent induced electric field at the origin is shown. At the start of the dynamics a distribution of 0.013 ± 0.010 a.u. is present which relates to the thermal disorder present. After ionization a quick increase is observed yielding 0.019 ± 0.012 a.u. after 17.5 fs. Subsequently this value increases slightly but a wide distribution remains present. In summary it can be said that there is an initial (sub 30 fs) response of the solvent to the

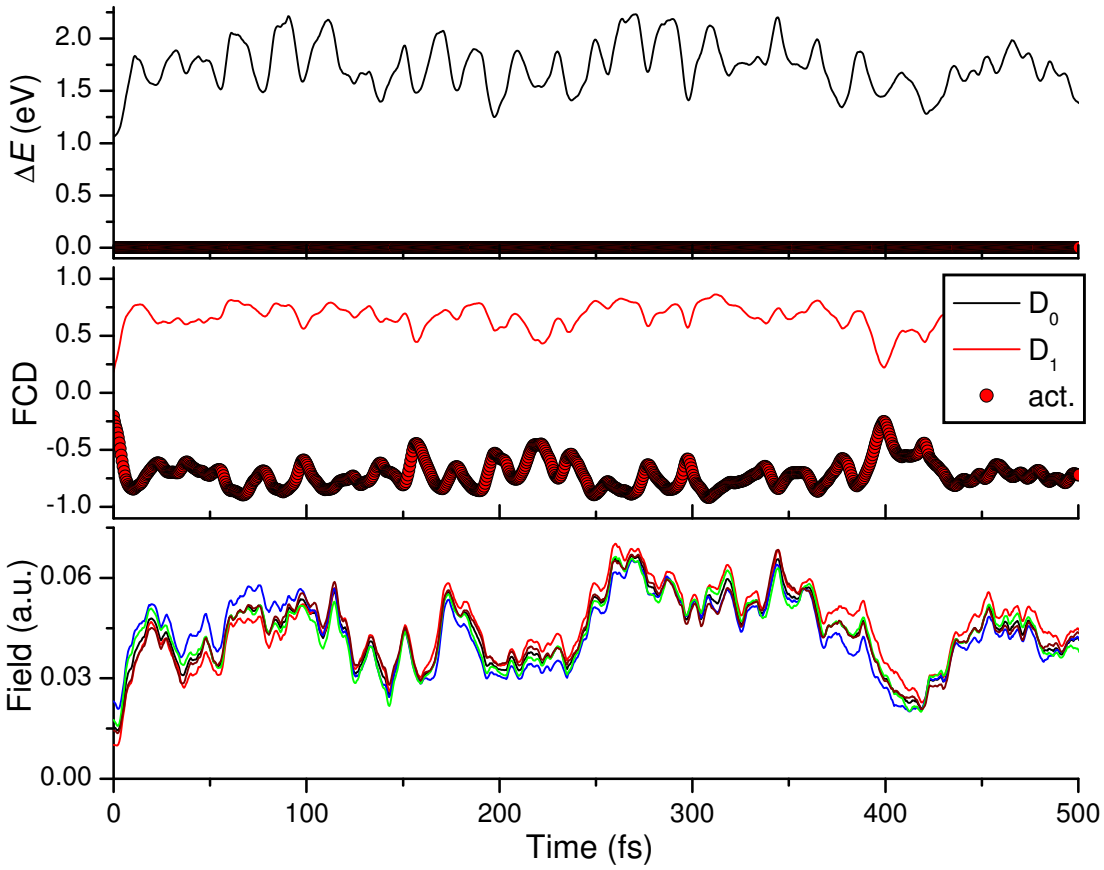

Figure 3.6: *Energy gap, fragment charge differences (FCD) and z-component of the electric field at five distinct points for a* $[Et–Et]^+$ *trajectory in aqueous solution.*

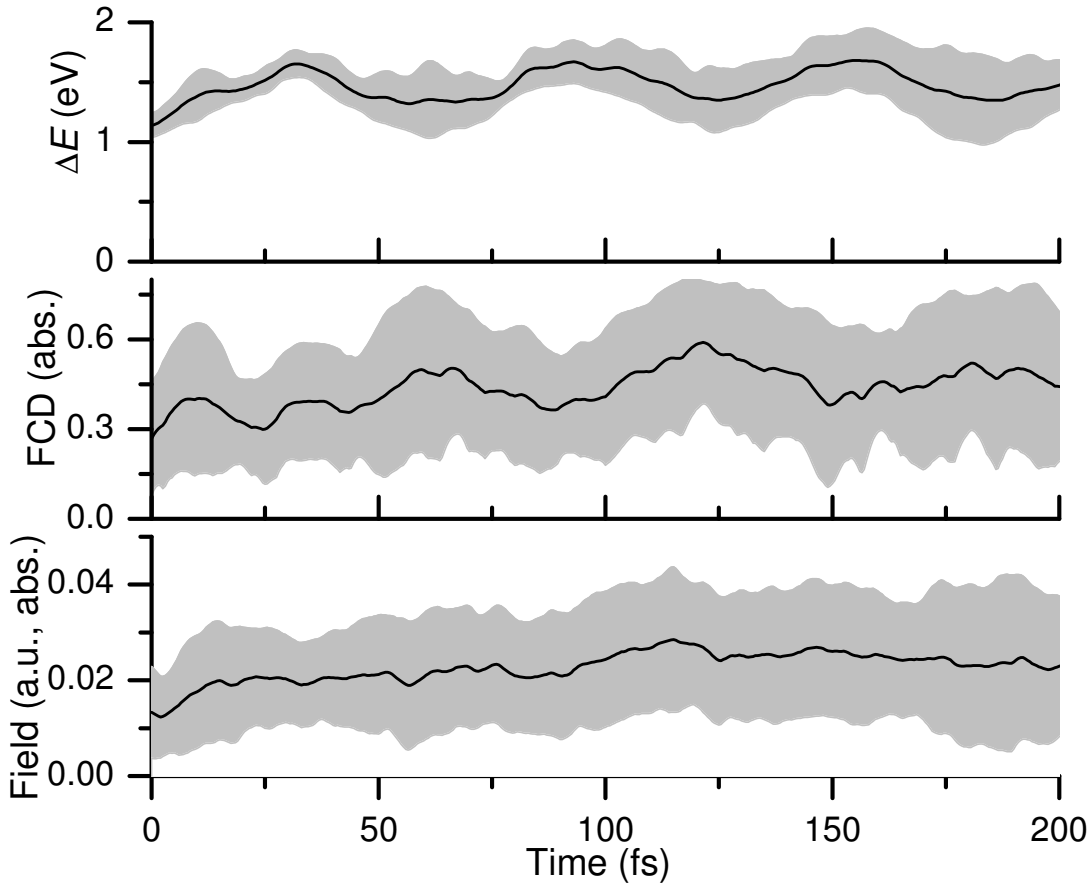

Figure 3.7: *Time evolution of the means of the energy gap, absolute FCD values, and absolute values of the z-component of the electric field at the origin for the* $[Et–Et]^+$ *dynamics in aqueous solution (the standard deviation over trajectories is represented as gray area).*

ionization, which is in particular visible when considering ΔE, and then a slower equilibration process with some oscillations follows.

In Figure 3.8 an example trajectory of $[FA–Et–Et–FA]^+$ after vertical ionization is shown. As explained above the additional formaldehyde molecules shield the charge in a way that the trapping by the solvent is reduced and in connection with the strong coupling no free energy barrier for charge transfer is present (cf. Tables 3.4 and 3.5). Therefore no charge separation occurs in the dynamics but the FCD oscillates around zero, i.e. the charge remains rather delocalized. The field strength is significantly lower as compared to the $[Et–Et]^+$ trajectory (Figure

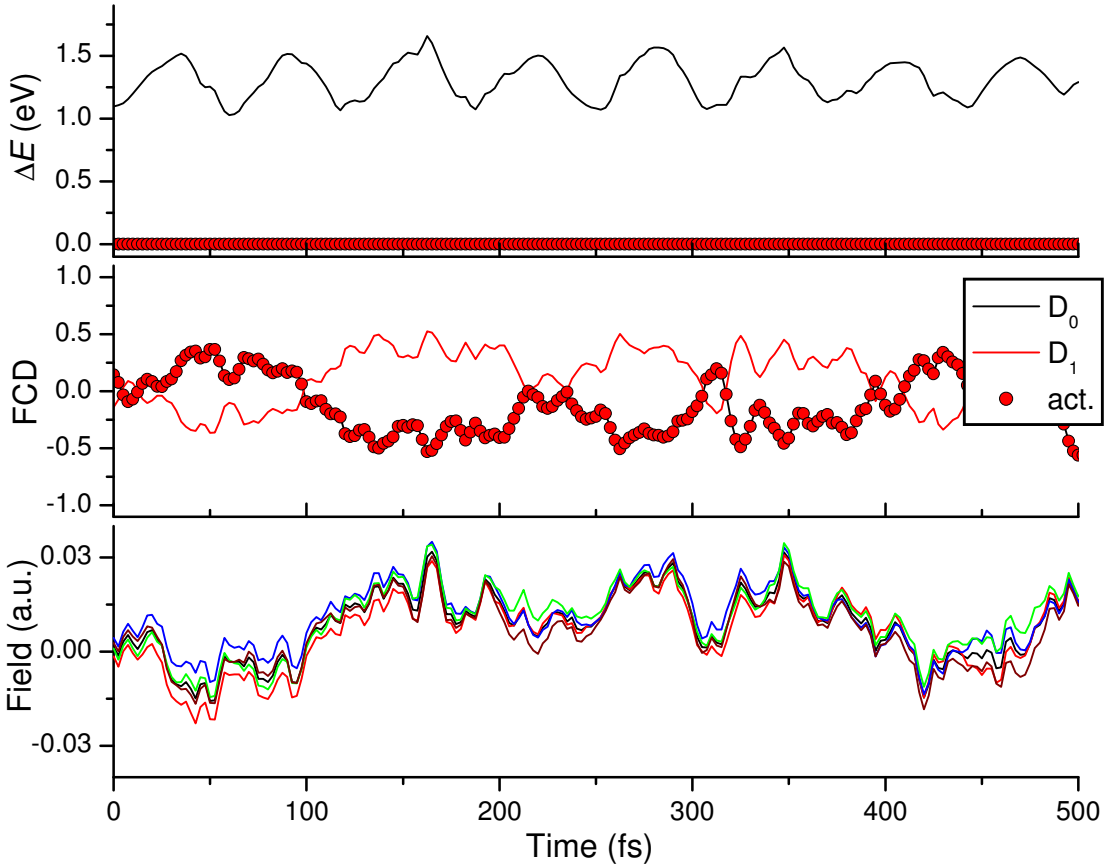

Figure 3.8: *Energy gap, fragment charge differences (FCD) and z-component of the electric field at five distinct points for a* $[FA–Et–Et–FA]^+$ *trajectory in aqueous solution.*

3.6) and oscillations around zero are observed, which are correlated with the FCD oscillations. The energy gap ΔE shows some rather regular oscillations.

The average dynamics for the 29 $[FA–Et–Et–FA]^+$ trajectories are presented in Figure 3.9. At the start of the dynamics ΔE lies at 1.11 ± 0.06 eV, very similar as compared to $[Et–Et]^+$ (Figure 3.7). Then there is again an upward motion and some rather coherent oscillations. The average FCD shows a wide initial distribution almost no change during the dynamics, never reaching a value above 0.44. The solvent induced electric field shows a small initial response to the ionization. Subsequently the average value remains somewhat below that in the $[Et–Et]^+$ case.

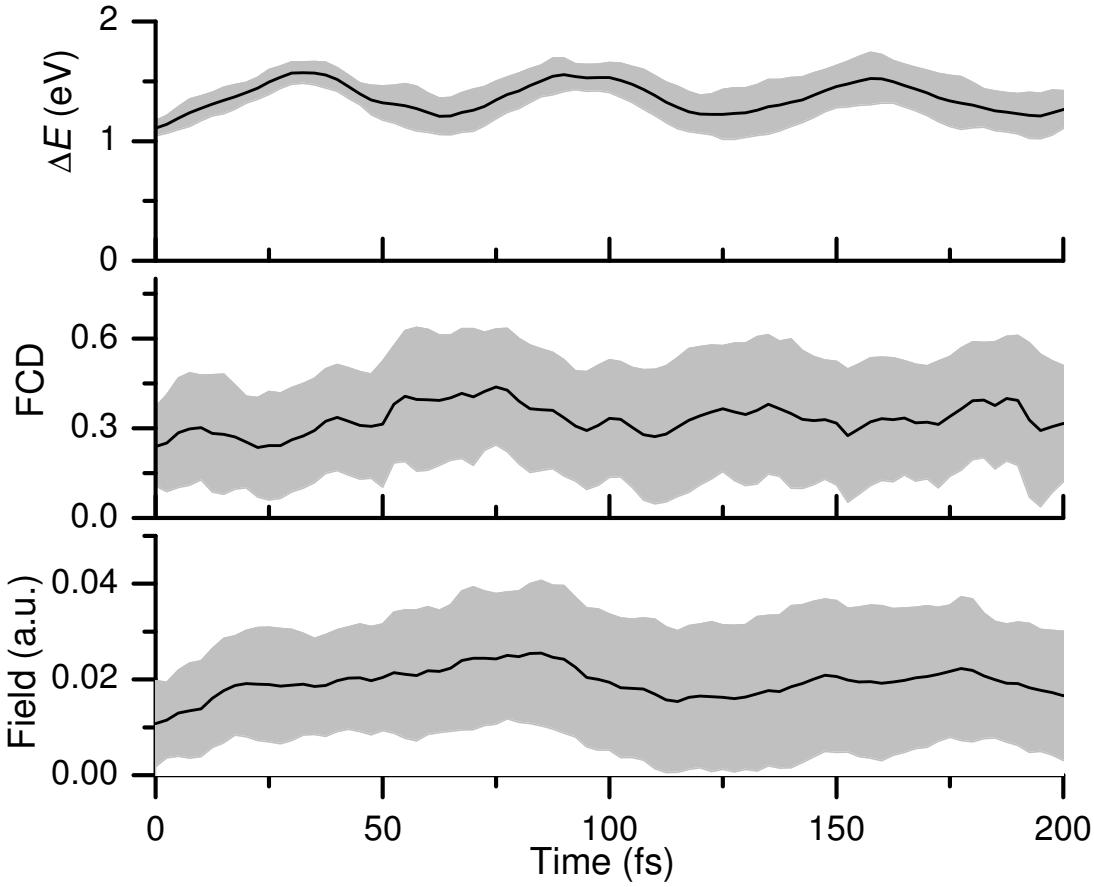

Figure 3.9: *Time evolution of the means of the energy gap, absolute FCD values, and absolute values of the z-component of the electric field at the origin for the* $[FA–Et–Et–FA]^+$ *dynamics in aqueous solution (the standard deviation over trajectories is represented as gray area).*

3.5.5 Summary

Two model systems for charge transfer in solution were considered: the stacked ethylene dimer radical cation $[Et–Et]^+$ and the same system with two stacked formaldehyde molecules on the outside $[FA–Et–Et–FA]^+$. First, different methods based on fragment charge differences [73] for obtaining the electronic coupling were tested, showing good consistency between different methods and structures. Second, the activation free energy for charge transfer were computed by two different methods: a Marcus theory type approach and free energy perturbation. Both methods agreed in the sense that a small free energy barrier for charge transfer was present in the $[Et–Et]^+$ system whereas the free energy surface was almost flat for $[FA–Et–Et–FA]^+$. Explicit QM/MM dynamics simulations of these systems provided a time-dependent description of the processes occurring after vertical ionization. In $[Et–Et]^+$ charge trapping was observed, whereas the charge oscillated more freely in $[FA–Et–Et–FA]^+$.

3.6 Phenomenological Analysis of Excited States

Systems with several coupled chromophores may possess complex excited states. Not only excitonic interactions between locally excited states have to be considered but also charge transfer states come into play. The precise description of these states is not only of highest interest in DNA [3, 4] but also in many other systems. [99–101] However, the required analysis can be quite involved considering that many electronic configurations may play a role. Moreover, if the orbitals are delocalized, it is not straight forward to differentiate between excitonic and charge resonance interactions. In this article an analysis method for such states, as obtained from quantum chemical calculations, based on the one-particle transition density matrix is outlined (see also Section 2.1.5). This quantity contains the essential information that is needed for describing excited states, which are reached by a one-electron transition. Similar analysis methods have been described in Refs [99, 102]. However, I believe that significant new applicability could be provided in this work through connecting different ideas, by providing automatized descriptors and by supplying an interface that may be extended to many electronic structure methods and program packages. In addition the related subject of natural transition orbitals [32–34] is discussed and it is shown how these can be used to get more insight into the structure of excited states.

Four examples were provided: interactions between the n$\pi*$ states in a formaldehyde dimer; excimer formation in the naphthalene dimer; stacking interaction in an adenine dimer and the excitonic band structure of a conjugated phenylene-vinylene oligomer.

My contribution to this project was the design of the method as well as performing illustrative calculations. This work has been accepted for publication by the *Journal of Chemical Theory and Computation* (21 June 2012). [103]

Analysis of excitonic and charge transfer interactions from quantum chemical calculations

Felix Plasser,[a] *Hans Lischka*[a,b]

[a] Institute for Theoretical Chemistry – University of Vienna,

Waehringerstrasse 17, A 1090 Vienna, Austria.

[b] Department of Chemistry and Biochemistry, Texas Tech University, Lubbock, TX 79409-1061, USA.

Email: felix.plasser@univie.ac.at, hans.lischka@ttu.edu

Abstract

A procedure for a detailed analysis of excited states in systems of interacting chromophores is proposed. By considering the one-electron transition density matrix, a wealth of information is recovered that may be missed by manually analyzing the wavefunction. Not only position and spatial extent are given but insight into the intrinsic structure of the exciton is readily obtained as well. For example, the method can differentiate between excitonic and charge resonance interactions even in completely symmetric systems. Four examples are considered to highlight the utility of the approach: interactions between the nπ* states in a formaldehyde dimer; excimer formation in the naphthalene dimer; stacking interaction in an adenine dimer and the excitonic band structure in a conjugated phenylene-vinylene oligomer.

1. Introduction

Excited states in multichromophoric systems have recently gained a substantial amount of interest. One example is DNA, where interactions between nucleobases were shown to significantly alter the excited state behavior as compared to its isolated constitutents.[1,2] In particular the amount of delocalization and the question of whether the resulting states are of excitonic or charge transfer nature and how interconversions could happen, were discussed intensively.[3-7] Another area that has been gaining significant attention is organic electronics. There it is of particular interest to analyze the spatial extent of an exciton and the average electron hole separation, and to understand the processes of charge separation and recombination.[8-11] Both cases are examples where a detailed description of the structure of the exciton is decisive for understanding the processes and where a simple visual analysis of the large number of contributing molecular orbitals and configurations is not only cumbersome but may miss important information. Furthermore, if statistical data are needed it is important to have well defined quantities which are easily used in an automated analysis. In this contribution we will present a strategy for detailed analysis of quantum chemical excited state calculations in dimers, oligomers, and extended systems, which allows drawing a direct relation to physical models.

Our approach is based on an analysis of the one-electron transition density matrices between the ground and electronically excited states. It provides a direct and straightforward procedure to characterize the aforementioned excitonic and charge transfer processes. Related work by Luzanov[12,13] provides a firm mathematical background. Tretiak and Mukamel have formulated a similar analysis specifically for conjugated polymers.[8] As a complimentary approach, a singular value decomposition of the transition density matrix to obtain the natural transition orbitals has been applied by several authors as well.[14-16] In contrast to our methods, also the one-electron difference density matrix has been used to describe electronic transitions.[17] Thus, many of the underlying concepts are already known. However, we believe that building on the above mentioned work we can provide a significant amount of new applicability by connecting the different ideas, by providing compact automatized descriptors and by supplying a programming interface that may be easily extended to many different wave function models and quantum chemistry programs.

In this work the basic procedures and the final formalism will be presented, followed by representative examples which should demonstrate the power and the usefulness of our methods. Firstly, the stacked formaldehyde dimer will be explored, followed by an analysis of excimer formation in the naphthalene dimer. Especially the second example will illustrate the strength of our analysis as compared to the quite involved direct analysis of the electronic wavefunction. Finally, the analysis of two systems of highest current interest, a di-adenine stack in B-DNA geometry and a phenylene-vinylene oligomer, will be presented.

2. Methodology

If two or more chromophores come into contact, not only interactions between the excited states on each chromophore have to be considered, but also charge transfer states come into play. For example in a dimer there are four states per type of monomer transition: a local excitation on

each fragment and two charge transfer states going in either direction (Figure 1).[18] At small intermolecular separations (< 5Å in π-systems[18]) all four states may interact yielding eigenfunctions which can be arbitrary mixtures of these states.[19] The situation becomes more complex if more than two chromophores are involved because a large number of possible local and charge transfer transitions have to be considered. Below, an approach is described for analyzing excited states obtained in quantum chemical computations, which allows reconstructing such contributions systematically. Firstly, the concepts of interest will be briefly illustrated by using a dimer of interacting chromophores. Secondly, based on these considerations, the charge transfer numbers,[12,13] a general measure for decomposing an exciton into locally excited and charge transfer contributions will be considered. Furthermore, strategies for reducing this information in systems with a larger number of chromophores will be discussed. Finally, it will be outlined how natural transition orbitals[14-16] may be used to define an intrinsic measure for resonant delocalization (see also Ref. 20).

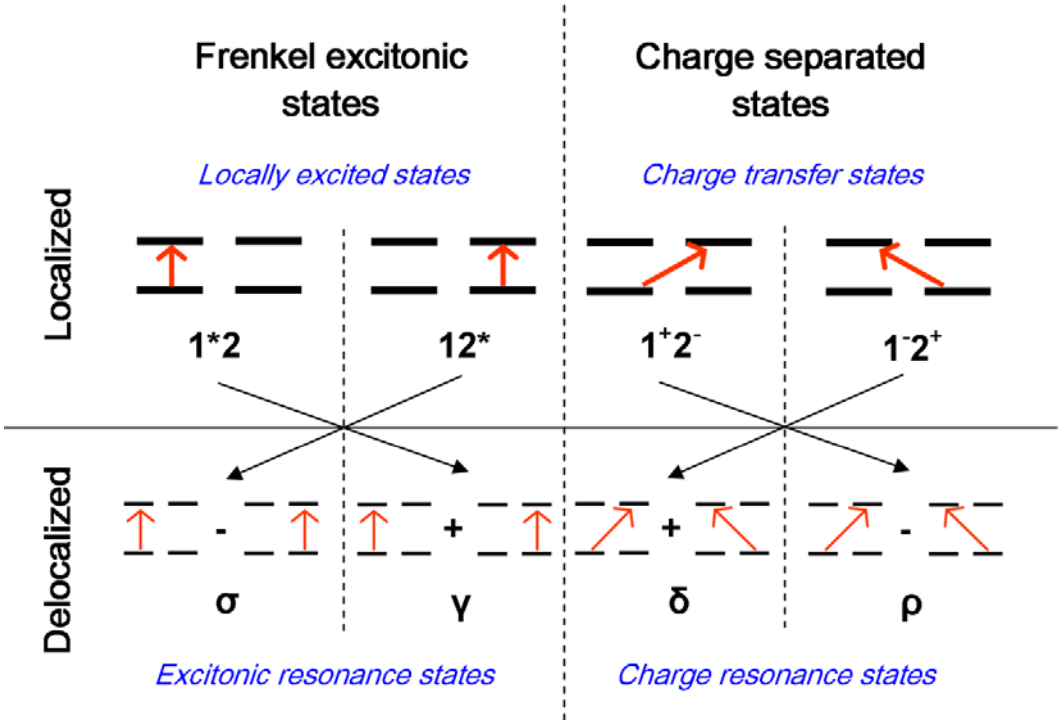

Figure 1. Depiction of dimer excited states arising from one type of transition in the monomer. Localized excited states (top), as well as their linear combinations leading to delocalized states (bottom) are shown.

The nomenclature used in the following text is outlined in Figure 1. The term "Frenkel exciton" refers to excited states where for every transition the *initial* and *final* orbitals are located on the same respective fragment. These may be "locally excited states" with only one fragment involved or "excitonic resonance states" if two or more fragments are involved. Contrary to Frenkel excitons, the term "charge separated states" refers to states where for every transition the *initial* and *final* orbitals are located on different fragments. Such states may exhibit a net transfer of

charge, resulting in a "charge transfer state". Alternatively two opposing charge transfer transitions may come into resonance, producing a charge resonance state without net transfer of charge. In the following discussion these four limiting cases will be considered. In practice also mixtures between these types are possible.

In this context it may be noted that by consideration of summed attachment and detachment densities,[17] which is a complementary way to represent an excitation, it would not be possible to differentiate between excitonic resonance and charge resonance states (Figure 1, bottom): both kinds of states would yield evenly delocalized attachment and detachment densities.

2.1 Introductory example

To illustrate the concepts involved, first the standard model for excited states on two interacting molecules will be briefly reviewed.[18,19] Two molecules "1" and "2" are considered, each with two active orbitals, forming an orthonormal set of four orbitals: i (*initial*) and f (*final*) on fragment 1, i' and f' on 2. The *initial* orbitals are doubly occupied in the ground state whereas the *final* orbitals are unoccupied. Considering these orbitals it is possible to construct four states by single excitations from a Hartree-Fock ground state $|0\rangle$ (cf. Figure 1, top). Using spin-averaged excitation operators (cf. for example Ref. 21) these may be written in a compact form as

$$|1^*2\rangle = 2^{-1/2}E_{\mathrm{fi}}|0\rangle \tag{1}$$

$$|12^*\rangle = 2^{-1/2}E_{\mathrm{f'i'}}|0\rangle \tag{2}$$

$$|1^-2^+\rangle = 2^{-1/2}E_{\mathrm{fi'}}|0\rangle \tag{3}$$

$$|1^+2^-\rangle = 2^{-1/2}E_{\mathrm{f'i}}|0\rangle \tag{4}$$

where E_{rs} denotes the excitation from orbital *s* to *r* (consider Ref. 18 for the explicit expressions of these states). The first two states correspond to locally excited states. The remaining two are charge separated states with a net transfer of a unit charge.

In the presence of symmetry the states $|1^*2\rangle$ and $|12^*\rangle$ as well as $|1^-2^+\rangle$ and $|1^+2^-\rangle$ are pairwise degenerate, yielding delocalized eigenfunctions. At large intermolecular separations these can be clearly divided into two types (cf. Figure 1, bottom): Frenkel excitonic resonance states (where excitations always occur within one fragment)

$$|\sigma\rangle = \frac{1}{\sqrt{2}}(|1^*2\rangle - |12^*\rangle) = \frac{1}{2}(E_{\mathrm{fi}} - E_{\mathrm{f'i'}})|0\rangle = \frac{1}{2}(E_{\mathrm{f^+i^-}} + E_{\mathrm{f^-i^+}})|0\rangle \tag{5}$$

$$|\gamma\rangle = \frac{1}{\sqrt{2}}(|1^*2\rangle + |12^*\rangle) = \frac{1}{2}(E_{\mathrm{fi}} + E_{\mathrm{f'i'}})|0\rangle = \frac{1}{2}(E_{\mathrm{f^-i^-}} + E_{\mathrm{f^+i^+}})|0\rangle \tag{6}$$

and charge resonance states (where excitations always go across fragments)

$$|\delta\rangle = \frac{1}{\sqrt{2}}(|1^-2^+\rangle + |1^+2^-\rangle) = \frac{1}{2}(E_{\mathrm{fi'}} + E_{\mathrm{f'i}})|0\rangle = \frac{1}{2}(E_{\mathrm{f^-i^-}} - E_{\mathrm{f^+i^+}})|0\rangle \tag{7}$$

$$|\rho\rangle = \frac{1}{\sqrt{2}}(|1^-2^+\rangle - |1^+2^-\rangle) = \frac{1}{2}(E_{\mathrm{fi}'} - E_{\mathrm{f}'\mathrm{i}})|0\rangle = \frac{1}{2}(E_{\mathrm{f}^+\mathrm{i}^-} - E_{\mathrm{f}^-\mathrm{i}^+})|0\rangle \tag{8}$$

The states are given here in the localized basis, as well as in a basis of delocalized orbitals defined as $\mathrm{i}^+ = 2^{-1/2}(\mathrm{i} + \mathrm{i}')$, $\mathrm{i}^- = 2^{-1/2}(\mathrm{i} - \mathrm{i}')$, $\mathrm{f}^+ = 2^{-1/2}(\mathrm{f} + \mathrm{f}')$, and $\mathrm{f}^- = 2^{-1/2}(\mathrm{f} - \mathrm{f}')$, cf. Ref 18. It can be seen that a differentiation between $|\sigma\rangle$ and $|\rho\rangle$ or $|\gamma\rangle$ and $|\delta\rangle$ is easily accomplished in the localized basis but quite challenging when delocalized orbitals are present, considering that they consist of the same pair of configurations and only the relative sign differentiates between them.

An interesting observation is that a single excitation between delocalized orbitals, e.g.

$$|\chi^{-/+}\rangle = 2^{-1/2}E_{\mathrm{f}^+\mathrm{i}^-}|0\rangle = 2^{-3/2}(E_{\mathrm{fi}} - E_{\mathrm{fi}'} + E_{\mathrm{f}'\mathrm{i}} + E_{\mathrm{f}'\mathrm{i}'})|0\rangle \tag{9}$$

yields an even mixture of locally excited and charge transfer contributions when written in the localized basis. Considering this, it is only possible to have a pure delocalized Frenkel excitonic or charge resonance state when at least two configurations (and four orbitals) are involved in the way described above. This property will be discussed in more detail in Section 2.4.

In general it is also possible to represent localized states (or directed CT states) in terms of delocalized orbitals, e.g.

$$|1^*2\rangle = 2^{-3/2}(E_{\mathrm{f}^+\mathrm{i}^-} + E_{\mathrm{f}^-\mathrm{i}^+} + E_{\mathrm{f}^-\mathrm{i}^-} + E_{\mathrm{f}^+\mathrm{i}^+})|0\rangle \tag{10}$$

which is even more difficult to understand by a quick inspection. It is therefore apparent that a rigorous analysis method may be of great benefit.

For an analysis of these states, the one-electron transition density matrix with respect to the ground state will be used, cf. Refs 8,12,13. It is defined for an excited state α as

$$D_{rs}^{0\alpha} = \langle 0|E_{rs}|\alpha\rangle \tag{11}$$

where *r* and *s* are two orbital indices. With a single determinant ground state, the transition density matrix simply corresponds to the one-electron excitation operators applied when constructing the excited state. The transition densities obtained in this way for the four localized states (Figure 1, top) are shown in Table 1. The crucial point here is that LE states are represented in the diagonal blocks corresponding to the particular fragment, whereas the CT states correspond to off-diagonal blocks. For the delocalized states (Figure 1, bottom) the transition densities (expressed in localized orbitals) are shown in Table 2. It can be seen that the Frenkel excitonic states $|\sigma\rangle$ and $|\gamma\rangle$ are represented on the diagonal blocks. In contrast, the charge resonance states $|\delta\rangle$ and $|\rho\rangle$ have non-vanishing elements only in the off-diagonal blocks.

Table 1. Transition density matrices ($\mathbf{D}^{0\alpha}$) represented in the localized orbital basis arranged according to (i,f,i',f'), charge transfer number matrices $\mathbf{\Omega}^{0\alpha}$,[a] and descriptors *CT*, *PR*, *POS* [b] and PR_{NTO} [c] of idealized locally excited states $|1^*2\rangle$ and $|12^*\rangle$ and charge transfer states $|1^-2^+\rangle$ and $|1^+2^-\rangle$ in a dimer of interacting molecules.

state	$\|1^*2\rangle$	$\|12^*\rangle$	$\|1^-2^+\rangle$	$\|1^+2^-\rangle$
$\mathbf{D}^{0\alpha}$	$\begin{bmatrix} 0 & \sqrt{2} & 0 & 0 \\ 0 & 0 & 0 & 0 \\ 0 & 0 & 0 & 0 \\ 0 & 0 & 0 & 0 \end{bmatrix}$	$\begin{bmatrix} 0 & 0 & 0 & 0 \\ 0 & 0 & 0 & 0 \\ 0 & 0 & 0 & \sqrt{2} \\ 0 & 0 & 0 & 0 \end{bmatrix}$	$\begin{bmatrix} 0 & 0 & 0 & 0 \\ 0 & 0 & 0 & 0 \\ 0 & \sqrt{2} & 0 & 0 \\ 0 & 0 & 0 & 0 \end{bmatrix}$	$\begin{bmatrix} 0 & 0 & \sqrt{2} & 0 \\ 0 & 0 & 0 & 0 \\ 0 & 0 & 0 & 0 \\ 0 & 0 & 0 & 0 \end{bmatrix}$
$\mathbf{\Omega}^{0\alpha}$	$\begin{bmatrix} 1 & 0 \\ 0 & 0 \end{bmatrix}$	$\begin{bmatrix} 0 & 0 \\ 0 & 1 \end{bmatrix}$	$\begin{bmatrix} 0 & 0 \\ 1 & 0 \end{bmatrix}$	$\begin{bmatrix} 0 & 1 \\ 0 & 0 \end{bmatrix}$
CT	0	0	1	1
PR	1	1	1	1
POS	1	2	1.5	1.5
PR_{NTO}	1	1	1	1

[a] defined in Section 2.2
[b] defined in Section 2.3
[c] defined in Section 2.4

Table 2. Transition density matrices ($\mathbf{D}^{0\alpha}$) represented in the localized orbital basis arranged according to (i,f,i',f'), charge transfer number matrices $\mathbf{\Omega}^{0\alpha}$,[a] and descriptors *CT*, *PR*, *POS* [b] and PR_{NTO} [c] of idealized Frenkel excitonic resonance states σ and γ, as well as charge resonance states δ and ρ in a dimer of interacting molecules.

state	σ	γ	δ	ρ
$\mathbf{D}^{0\alpha}$	$\begin{bmatrix} 0 & 1 & 0 & 0 \\ 0 & 0 & 0 & 0 \\ 0 & 0 & 0 & -1 \\ 0 & 0 & 0 & 0 \end{bmatrix}$	$\begin{bmatrix} 0 & 1 & 0 & 0 \\ 0 & 0 & 0 & 0 \\ 0 & 0 & 0 & 1 \\ 0 & 0 & 0 & 0 \end{bmatrix}$	$\begin{bmatrix} 0 & 0 & 1 & 0 \\ 0 & 0 & 0 & 0 \\ 0 & 1 & 0 & 0 \\ 0 & 0 & 0 & 0 \end{bmatrix}$	$\begin{bmatrix} 0 & 0 & 1 & 0 \\ 0 & 0 & 0 & 0 \\ 0 & -1 & 0 & 0 \\ 0 & 0 & 0 & 0 \end{bmatrix}$
$\mathbf{\Omega}^{0\alpha}$	$\begin{bmatrix} 0.5 & 0 \\ 0 & 0.5 \end{bmatrix}$	$\begin{bmatrix} 0.5 & 0 \\ 0 & 0.5 \end{bmatrix}$	$\begin{bmatrix} 0 & 0.5 \\ 0.5 & 0 \end{bmatrix}$	$\begin{bmatrix} 0 & 0.5 \\ 0.5 & 0 \end{bmatrix}$
CT	0	0	1	1
PR	2	2	2	2
POS	1.5	1.5	1.5	1.5
PR_{NTO}	2	2	2	2

[a] defined in Section 2.2
[b] defined in Section 2.3
[c] defined in Section 2.4

2.2 Charge transfer numbers

Following the above considerations, the one-electron transition density matrix may be seen as a central quantity recovering the excitations leading to a one-electron excited state, cf. Refs 8,12,13. If a basis of orthogonal localized orbitals were available, the following procedure could be envisaged: An element $D_{ab}^{0\alpha,[\mathrm{LO}]}$ of the transition density matrix in this localized basis (the first part of the superscript refers to the transition from the ground state to state α, the second part to the orbital basis) corresponds to a local excitation on a fragment *A* if the orbitals *a* and *b* are both situated on *A* and to a charge transfer excitation if *a* and *b* are on different fragments. A charge transfer number[12] Ω_{AB}^{α} could simply be defined by summing over all contributions on the respective fragments

$$\Omega_{AB}^{\alpha} = \frac{1}{2}\sum_{\substack{a\in A\\ b\in B}} \left(D_{ab}^{0\alpha,[\mathrm{LO}]}\right)^2 \tag{12}$$

If $A \neq B$, this represents the weight of an $A \rightarrow B$ charge transfer, and $\hat{\Omega}_{AA}^{\alpha}$ is the weight of local excitations on *A*. Luzanov has shown that this has in fact properties of a two-particle quantity, describing correlations between the *electron* and *hole* positions,[13] which is crucial for example for differentiating between Frenkel excitonic and charge resonance states (cf. Figure 1). The charge transfer numbers of the four localized dimer states (Figure 1, top) are presented in Table 1. These states can be clearly differentiated, as each state has one unique non-vanishing element of its $\mathbf{\Omega}^{\alpha}$ matrix. For the resonant delocalized states (Figure 1, bottom) always two elements of $\mathbf{\Omega}^{\alpha}$ are non-vanishing (Table 2). For Frenkel excitonic resonance states these are on the diagonal, whereas for charge resonance states the off-diagonal elements are non-vanishing.

For practical calculations Eq. (12) has to be generalized to include non-orthogonality of the atomic orbitals (AO). For this purpose we suggest an analysis in analogy to Mayer's bond order[22] between two atoms μ and ν

$$B_{\mu\nu}^{\alpha} = \sum_{\substack{a\in\mu\\ b\in\nu}} \left(\mathbf{D}^{\alpha\alpha,[\mathrm{AO}]}\mathbf{S}^{[\mathrm{AO}]}\right)_{ab}\left(\mathbf{D}^{\alpha\alpha,[\mathrm{AO}]}\mathbf{S}^{[\mathrm{AO}]}\right)_{ba} = \tag{13}$$

$$= \sum_{\substack{a\in\mu\\ b\in\nu}} \left(\mathbf{D}^{\alpha\alpha,[\mathrm{AO}]}\mathbf{S}^{[\mathrm{AO}]}\right)_{ab}\left(\mathbf{S}^{[\mathrm{AO}]}\mathbf{D}^{\alpha\alpha,[\mathrm{AO}]}\right)_{ab}$$

where $\mathbf{D}^{\alpha\alpha,[\mathrm{AO}]}$ is the (symmetric) one-electron density matrix of a state α in the AO basis and $\mathbf{S}^{[\mathrm{AO}]}$ is the AO overlap matrix. The summations are performed over the basis functions on atoms μ and ν, respectively. Using this form, the charge transfer number between fragments *A* and *B* can be defined by inserting the transition density matrix instead of the state density matrix

$$\Omega_{AB}^{\alpha} = \frac{1}{2}\sum_{\substack{a\in A\\ b\in B}} \left(\mathbf{D}^{0\alpha,[\mathrm{AO}]}\mathbf{S}^{[\mathrm{AO}]}\right)_{ab}\left(\mathbf{S}^{[\mathrm{AO}]}\mathbf{D}^{0\alpha,[\mathrm{AO}]}\right)_{ab} \tag{14}$$

Then, the sum

$$\Omega^{\alpha} = \sum_{A,B}\Omega_{AB}^{\alpha} = \frac{1}{2}\mathrm{Tr}\left(\mathbf{D}^{0\alpha,[\mathrm{AO}]}\mathbf{S}^{[\mathrm{AO}]}\left(\mathbf{D}^{0\alpha,[\mathrm{AO}]}\right)^{\mathrm{T}}\mathbf{S}^{[\mathrm{AO}]}\right) = \tag{15}$$

$$= \frac{1}{2}\mathrm{Tr}\left(\mathbf{D}^{0\alpha,[\mathrm{MO}]}\left(\mathbf{D}^{0\alpha,[\mathrm{MO}]}\right)^{\mathrm{T}}\right)$$

is invariant to any basis set transformation, demonstrating that squared density matrix elements appear to be a useful choice for our analysis (T denotes the matrix transposition and **C** is the AO-MO transformation matrix, see Section 3 for transformation rules). For a normalized CIS wave function, Ω^{α} is exactly one (cf. Ref. 13) and for any other excited state wave function dominated by a one-electron transition, it should be close to one.

In a system of two chromophores the quantity

$$\Delta^{\alpha}q_{12} = (\Omega_{12}^{\alpha} - \Omega_{21}^{\alpha})/\Omega^{\alpha} \tag{16}$$

represents the net charge shifted from fragment 1 to fragment 2 due to the excitation. Such a relation was shown to hold exactly in the case of CIS[12,13] but it should give the correct trend also in cases where the electronic excitation can be described by a one electron transition.

2.3 Collective information

While a density matrix analysis as described above can be used to get detailed analysis of the structures of excited states, cf. Refs 8,13, it is in many cases also highly desirable to have even more compact descriptors. In an extension to the L_d and L_c values of Ref. 8, we will describe how the above information can be compressed to retrieve the most interesting physical information in a compact form. This is of particular importance for polymers or extended systems with a large number of chromophores. In the following we will drop the superscript α for simplicity, but it should be remembered that all these descriptors yield one value per electronic state at every geometry. In all formulas it is assumed that the normalization factor Ω deviates only slightly from one. Otherwise, an analysis based only on the one-electron transition density matrix may not be suitable and generalized expressions using two-electron transition density matrices might be necessary, cf Ref 12.

The quantity *CT* is defined by summing over the off-diagonal elements, yielding

$$CT = \frac{1}{\Omega}\sum_{\substack{A\\ B\neq A}}\Omega_{AB} \tag{17}$$

which corresponds to the total weight of configurations where the *initial* and *final* orbitals are situated on different fragments. *CT* assumes the value one for all completely charge separated states (Figure 1, right) whereas it is zero for locally excited or Frenkel excitonic states (Figure 1, left).

Another interesting question refers to the extent of the delocalization of the excitation over fragments. For this purpose we will use the concept of a participation ratio to compute the number of fragments participating in the excitation, cf. Refs 23,24. To consider the general case of a non-symmetric **Ω** matrix, the definition is split into two parts. The participation ratio of the *initial* orbital or *hole* is defined as

$$PR_{\mathrm{I}} = \frac{\Omega^2}{\sum_A (\sum_B \Omega_{AB})^2} \tag{18}$$

to represent over how many fragments the *hole* is delocalized. The sum in parentheses considers all configurations where the *initial* orbital lies on a specific fragment *A* and goes over final orbitals on any possible fragment.

And in a similar way for the *final* orbital

$$PR_{\mathrm{F}} = \frac{\Omega^2}{\sum_B (\sum_A \Omega_{AB})^2} \tag{19}$$

The average of these two quantities

$$PR = (PR_{\mathrm{I}} + PR_{\mathrm{F}})/2 \tag{20}$$

is used to represent the number of fragments involved in the excited state. Considering the above examples (Section 2.1) this appears to be suitable measure for delocalization, giving *PR* = 1 for all the localized states (Table 1), and *PR* = 2 for all the delocalized states (Table 2).

The above formalism requires the construction of two separate quantities PR_{I} and PR_{F}. This was avoided in Ref. 8 by considering only diagonal elements. The quantity

$$PR_{\mathrm{diag}} = \frac{(\sum_A \Omega_{AA})^2}{\sum_A (\Omega_{AA})^2} \tag{21}$$

would correspond to L_d of Ref. 8 (with the only exception that squared rather than absolute values of density matrix elements are taken here). However, the advantage of the present definition of *PR* is that it is also well defined when the diagonal elements of **Ω** are zero as this is the case in charge transfer and charge resonance states ($|1^-2^+\rangle$ and $|1^+2^-\rangle$ in Table 1; δ and ρ in Table 2).

The coherence length of the excited state, which is related to the average electron-hole separation, can be defined following the ideas of Ref 8 as

$$COH = \frac{1}{PR} \frac{\Omega^2}{\sum_A \sum_B {\Omega_{AB}}^2} \tag{22}$$

Whereas *PR* gives the total spatial distribution of the exciton as a quasiparticle, *COH* relates to the intrinsic structure of the exciton. The measure is largest when locally excited and charge transfer configurations are participating in an equal amount. For loosely bound excitons (all elements of **Ω** are the same value) *COH* = *PR*, whereas for pure Frenkel excitons (only diagonal elements **Ω** are non-zero) *COH* = 1 (cf. Ref 8).

Finally, quantities are described, which are applicable mostly if a linear arrangement of the fragments is present. The average position of the *initial* orbital (*hole*) is computed as

$$POS_{\mathrm{I}} = \frac{\sum_A A(\sum_B \Omega_{AB})}{\Omega} \tag{23}$$

the position of the *final* orbital (*electron*) as

$$POS_{\mathrm{F}} = \frac{\sum_B B(\sum_A \Omega_{AB})}{\Omega} \tag{24}$$

and the mean position as

$$POS = (POS_{\mathrm{I}} + POS_{\mathrm{F}})/2 \tag{25}$$

Considering the idealized dimer states (Table 1 and Table 2), $|1^*2\rangle$ yields *POS* = 1, $|12^*\rangle$ yields *POS* = 2, and all charge transfer and delocalized states show *POS* = 1.5.

The signed net charge transfer length

$$CT_{net} = POS_{\mathrm{F}} - POS_{\mathrm{I}} \tag{26}$$

is computed as the difference between the centers of charge of the *electron* and *hole*. Considering Table 1, $|1^-2^+\rangle$ has CT_{net} = -1, and $|1^+2^-\rangle$ yields CT_{net} = 1. All other states in Table 1 and Table 2 have no net transfer of charge.

2.4 Natural transition orbitals

Natural transition orbitals (NTO) can be used to create a compact representation of an electronic excited state by reducing the number of configurations required to describe the most important features of a transition.[14-16] As opposed to a state density, it is not generally possible to diagonalize a transition density since it is not symmetric. However, a singular value decomposition scheme can be used where the decomposition of the transition density matrix using unitary matrices **U** and **V** may be written as

$$\mathbf{D}^{0\alpha,[\mathrm{MO}]} = \mathbf{U}\mathrm{diag}\left(\sqrt{\lambda_1}, \sqrt{\lambda_2}, \ldots\right)\mathbf{V}^{\mathrm{T}} \tag{27}$$

U denotes a set of *initial* (hole) orbitals, **V** the *final* (electron) orbitals, and the λ_i are giving the weight of the corresponding transition. Typically only a very small number of configurations are necessary to describe the states in this way and plotting the orbitals gives a compact graphical representation of the excited state (as shown for example in Refs 11,15,16,20). In general **U** and **V** are different. However, in the case of a CIS type wavefunction (where only the occupied-

virtual block of $\mathbf{D}^{0\alpha,[\mathrm{MO}]}$ is non-vanishing) it is possible to choose **U** = **V** due to degenerate singular values. Then the natural transition orbitals are in fact identical to the natural orbitals of the corresponding CIS wavefunction.[25]

An interesting property of this decomposition, that has been pointed out in Ref. 20, is that for resonant delocalized states always two significant non-vanishing singular values are present. This is represented in Eqs (5)-(8): Two excitation operators are needed for constructing the excited state. This is true independent of whether localized or delocalized orbtials are used (cf. Ref 18) and there is no orbital basis that could be used to construct the excited state with only one transition. To formalize this concept, we use a participation ratio[23,24] expression for the number of singular values:

$$PR_{\mathrm{NTO}} = \frac{(\sum_i \lambda_i)^2}{\sum_i \lambda_i^2} = \frac{4\Omega^2}{\sum_i \lambda_i^2} \tag{28}$$

where the second equality holds because of the fact that the λ_i are the eigenvalues of the product matrix $\mathbf{D}^{0\alpha,[\mathrm{MO}]}\left(\mathbf{D}^{0\alpha,[\mathrm{MO}]}\right)^T$. The analogous expression was called the collectivity index in Ref 13. It is a lower bound to the number of non-zero singular values (N_{SVD})[13] where PR_{NTO} = N_{SVD} only in the case that all non-zero singular values have the same magnitude. In this sense PR_{NTO} counts how many different NTOs are participating and thus how many transitions are necessary to describe the excited state. In combination with the considerations at the beginning of this paragraph, PR_{NTO} could be seen as an intrinsic measure giving information about electronic resonances that does not require the definition of any fragments. A decrease of PR_{NTO} can have two different implications. In the first case this decrease could coincide with a localization of the exciton and therefore a decrease in *PR* (Eq. (20)). On the other hand, if a large value of *PR* coincides with a low PR_{NTO}, this means that a larger spatial delocalization is combined with a coherent homogeneous excitation which should concur with a large coherence length *COH* (Eq. (22)). An example for this situation is the $|\chi^{-/+}\rangle$ state given in Eq. (9). Further formal discussion of these relations are given in the Supporting Information (S5). Note that the number of non-zero singular values (and thus PR_{NTO}) was also considered as a measure of electron correlation in the excited state wavefunction.[25] In the present context this can be understood by the fact that an excitonic or charge resonance state requires some additional electron correlation as compared to a homogeneous excitation (the *electron* and *hole* move in a somewhat correlated fashion as they are always on the same or on different fragments, respectively).

3. Computational details

As first example a stacked arrangement of two face-to-face formaldehyde molecules at their ground state minimum geometries, separated by 3.5 Å in a parallel arrangement was considered. The calculations of the electronic states were performed using multi-reference configuration interaction with single and double excitations (MR-CISD), using a complete active reference space of eight electrons in six orbitals (π, n, π* on each molecule). The orbitals were generated by using a complete active space self-consistent field wave function with eight electrons and six orbitals (CASSCF(8,6)) in the same active space as selected for the MR-CISD reference space

given just above. Averaging over the first three states was performed and the aug-cc-pVDZ basis set was used.[26] Energies, density matrices, and analytic non-adiabatic coupling vectors at the MR-CISD level were computed with the COLUMBUS 7.0 program package.[27-32]

The electronic states of the remaining systems (naphthalene dimer, di-adenine stack, and the phenylene-vinylene oligomer $(PV)_6P$) were treated using the algebraic diagrammatic construction to second order (ADC(2))[33] with the resolution of the identity approximation (RI).[34-37] The geometry of the naphthalene dimer was constructed by first optimizing the monomer at the RI-MP2/SVP[38] level and then placing two monomers in a face-to-face arrangement. The calculations were performed in D_{2h} symmetry where the long and short molecular axes were arranged in x- and y-direction, respectively, and the z-axis was perpendicular to the molecular planes. The aug-cc-pVDZ basis set[26,39] was used, considering that diffuse functions are necessary to guarantee a correct orbital overlap interaction for large intermolecular distances.[40] The geometry for the adenine dimer was constructed by first optimizing the adenine monomer at the RI-MP2/SVP[38] level and then inserting this structure by a least squares fit[41] into an arrangement of idealized B-DNA geometry, as created with the "Nucleic" program distributed with Tinker.[42] Vertical excitations for the dimer were computed at the RI-ADC(2)/TZVP[43] level. RI-MP2/SV(P) ground state geometry optimization was performed for $(PV)_6P$. For vertical excitations and the excited state optimization the RI-ADC(2)/SV(P) method was used. The structure was restricted to C_{2h} symmetry for computational efficiency. All RI-MP2 and RI-ADC(2) calculations were performed using TURBOMOLE 6.3.[44]

Corrections for basis set superposition error (BSSE) [45] are quite important in the description of excimers,[46] considering the fact that intermolecular separations may be significantly smaller than in ground state complexes. Unfortunately, in the case of strongly interacting chromophores a consistent definition of a counterpoise correction[45] is quite challenging. In the case of separated Frenkel excitonic and charge transfer contributions, it is conceivable to compute a state specific correction by considering appropriate locally excited and ionic states of the monomer. However, if different monomer states interact and excitonic and CT contributions mix (cf. Section 4.2) such a task does not seem feasible. Thus, in case of the naphthalene dimer the total energies of all excited states were corrected with the counter-poise correction computed for the ground state, as a compromise. The assumption behind this is that one electron promoted into a valence orbital should only have a minor contribution to the BSSE as opposed to the remaining electrons, which are largely unaffected by the excitation. The BSSE corrected total energy of state α in the dimer $E^{\alpha}_{\text{dimer,corr}}$ was computed from the uncorrected energy $E^{\alpha}_{\text{dimer}}$ as

$$E^{\alpha}_{\text{dimer,corr}} = E^{\alpha}_{\text{dimer}} + 2\left(E^{0}_{\text{mon.,[mon.]}} - E^{0}_{\text{mon.,[dim.]}}\right) \qquad (29)$$

where $E^{0}_{\text{mon.,[mon.]}}$ and $E^{0}_{\text{mon.,[dim.]}}$ are the MP2 ground state energies of one of the equivalent monomers using the AO basis set of the monomer and dimer respectively. It may be noted here that in this approach vertical excitation energies are uncorrected.

Fragments, as necessary for the summations in Sec. 2.3, were assigned as follows. In the first three cases the fragments corresponded to the two separate molecules in the dimer. For $(PV)_6P$ we formally cut the C=C double bonds of the vinyl moieties, to obtain the fragment definitions. This choice was done in order to obtain a set of analogous fragments, which also preserved the overall symmetry of the system.

For the MR-CISD calculations the exact one-electron transition density matrices as given by the COLUMBUS program system were used. Considering that for ADC(2) calculations these were not available to us, the singly excited cluster amplitudes were chosen instead to represent the excitation. This choice was taken considering the close relationship between these quantities and because of the fact that it is just these amplitudes which are usually considered for manually analyzing excited states. To reduce inconsistencies normalization against the sum of the weights Ω (Eq. (15)) was performed. Moreover it was checked that this normalization factor was always close to one. Whereas exact transition density matrices would be desirable if available, we want to point out that this approximate method opens a pathway that significantly enhances the general applicability and ease of implementation of our analysis procedure.

MO-coefficients were obtained in terms of Cartesian atomic orbitals in MOLDEN format[47] as supplied by COLUMBUS and TURBOMOLE. The MO-AO transformations of density and overlap matrices were performed according to Ref. 48:

$$\mathbf{D}^{[\mathrm{AO}]} = \mathbf{C}\mathbf{D}^{[\mathrm{MO}]}\mathbf{C}^{\mathrm{T}} \tag{30}$$

$$\mathbf{S}^{[\mathrm{AO}]} = \mathbf{C}^{-1,\mathrm{T}}\mathbf{S}^{[\mathrm{MO}]}\mathbf{C}^{-1} = \mathbf{C}^{-1,\mathrm{T}}\mathbf{C}^{-1} \tag{31}$$

which lead to the following expressions for the matrix products of Eq. (14)

$$\mathbf{D}^{[\mathrm{AO}]}\mathbf{S}^{[\mathrm{AO}]} = \mathbf{C}\mathbf{D}^{[\mathrm{MO}]}\mathbf{C}^{\mathrm{T}}\mathbf{C}^{-1,\mathrm{T}}\mathbf{C}^{-1} = \mathbf{C}\mathbf{D}^{[\mathrm{MO}]}\mathbf{C}^{-1} \tag{32}$$

$$\mathbf{S}^{[\mathrm{AO}]}\mathbf{D}^{[\mathrm{AO}]} = \mathbf{C}^{-1,\mathrm{T}}\mathbf{D}^{[\mathrm{MO}]}\mathbf{C}^{\mathrm{T}} \tag{33}$$

where $\mathbf{C}$ is the MO-coefficient matrix and the overlap in the MO basis $\mathbf{S}^{[\mathrm{MO}]}$ is a unit matrix.

Some of the mathematical formulas were derived or verified by using the MATHEMATICA 5.2[49] program. An efficient implementation of the matrix operations was achieved by using the NumPy tools.[50] Plotting of the computed natural transition orbitals was performed with the Jmol program package.[51] The code described here is freely available and is currently distributed as a test version,[52] providing interfaces to the COLUMBUS and TURBOMOLE programs for applications with the CASSCF, MR-CI, ADC(2), CC2 and time-dependent density functional theory (TDDFT) methods.

4. Results and discussion

4.1 The formaldehyde dimer

In this section the interaction between the lowest excited states of two stacked formaldehyde molecules, which are of nπ* character, is considered. An asymmetry, leading to nonequivalence of the two monomers and a corresponding localization of the excitation, is introduced by altering the asymmetric stretch coordinate

$$\Delta R = 2^{-1/2}\left(R_{CO,1} - R_{CO,2}\right) \tag{34}$$

in the two CO distances. A more detailed explanation of the underlying physical models in such a case is given in Ref 40. Here only the most important results are presented. In Figure 2 potential curves along ΔR, the *POS* value and the non-adiabatic coupling projected onto ΔR, i.e. $\left\langle \varphi_1 \left| \frac{\partial}{\partial(\Delta R)} \varphi_2 \right. \right\rangle$ (where φ_1 and φ_2 are the wavefunctions of the two electronic states), are presented for the S_1 and S_2 states of the formaldehyde dimer. At the symmetric geometry there is a small gap of 0.0216 eV between S_1 and S_2, which derives from the excitonic coupling. At this point, the S_1 and S_2 wave functions are evenly delocalized (POS_1=POS_2=1.5, *PR*=2.0). A large component of the non-adiabatic coupling vector between these two states along the ΔR direction (268/Å) indicates that the wave functions should change rapidly upon displacement. Accordingly, if the symmetry is lifted by bond length alternation, the two excited states quickly localize and already at ΔR=0.005Å the states are almost completely localized on either molecule (POS_1=1.04). Also the non-adiabatic coupling is reduced substantially.

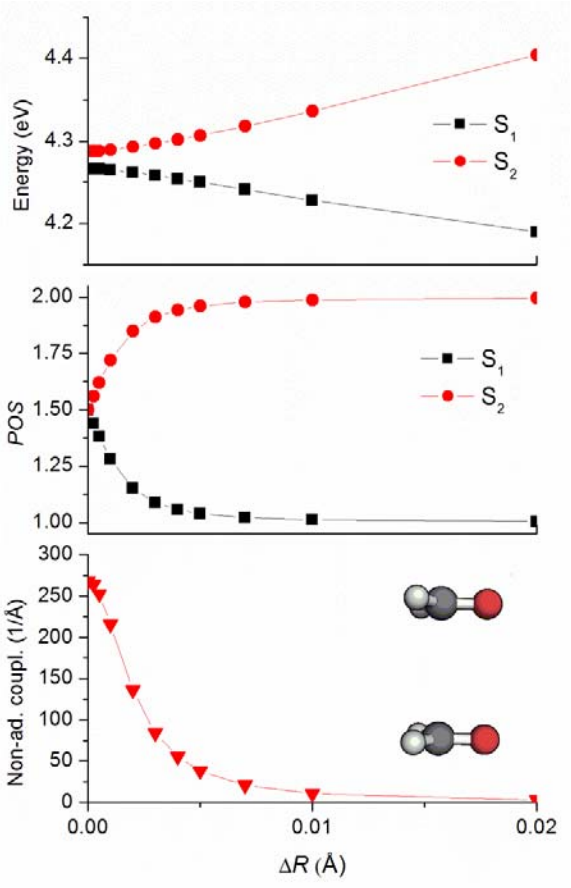

Figure 2. MR-CISD state energies, position values (*POS*) and non-adiabatic couplings projected onto ΔR for two interacting nπ* states of two stacked formaldehyde molecules separated by a distance of 3.5Å.

In Table 3 a collection of complementary descriptors is presented for three different ΔR values. The small *CT* value found over the whole range of ΔR values considered indicates that the states

are of Frenkel excitonic nature, without significant charge transfer interactions. Next, the excitonic participation ratio *PR* is shown. *PR*=2.00 at ΔR=0 reflects that due to symmetry the excited states are completely delocalized over the two fragments. At ΔR=0.005Å the wave function is already almost completely localized (*PR*=1.08). The natural transition orbital participation ratio PR_{NTO}, giving the number of configurations minimally necessary to describe a state, is about two for the delocalized states, and goes to one as the excited states are localized. This is just what corresponds to the idealized model.[18,20] The fact that *PR* is somewhat lower than two at ΔR=0 is probably due to orbital interactions and it is reflected by the fact that the *CT* value is not completely vanishing.

Table 3. Charge transfer (*CT*), excitonic participation ratio (*PR*), and natural transition orbital participation ratio (PR_{NTO}) for the S_1 state of two stacked formaldehyde molecules separated by a distance of 3.5Å at different values of the bond length alternation ΔR.

ΔR (Å)	*CT*	*PR*	PR_{NTO}
0	0.005	2.00	1.95
0.002	0.005	1.35	1.33
0.005	0.004	1.08	1.08

4.2 The naphthalene dimer

The naphthalene dimer is an interesting benchmark system where the interactions between excitonic and charge resonance states and the formation of a strongly stabilized excimer has been reported.[18,19] In the present investigation the eclipsed dimer was chosen and the dependence of excited states on the intermolecular distance was considered. Excited states were computed at the RI-ADC(2)/aug-cc-pVDZ level. Because of the symmetry all states are evenly delocalized in this system (*PR*=2, *POS*=1.5). And the amount of charge separation *CT* remains the main feature of interest. It should be noted here that also all orbitals and densities are delocalized and therefore an identification of charge separated configurations is not trivial. The problem was solved by East and Lim[18] through an analysis, involving a careful inspection of the symmetry properties of all the orbitals involved. It will be shown how the same results can be obtained by simply considering the *CT* value defined above. Moreover, the *CT* value provides a well defined quantifier for measuring the gradual mixing between excitonic and charge resonance contributions, which will be illustrated for the case of excimer formation.

In Table 4 a summary of the lowest energy singlet $\pi\pi^*$ excited states at an intermolecular distance of 5.0 Å is presented. The Rydberg states, which are also present at this energy range, are not shown. First it can be seen that the states are clearly separated into Frenkel type excitonic resonance states (*CT* ≈ 0) and charge resonance states (*CT* ≈ 1). Mixing between these types of states occurs only at smaller intermolecular separations (cf Refs 18,19), a process which will be described later. The first two excited states (1^1B_{2g}, 1^1B_{3u}) are of Frenkel type (*CT* = 0.0). An analysis of the orbitals and transition moments shows that these states are deriving from the lowest singlet excited state (S^{01+}, ^1L_b) of naphthalene, forming the $^1\sigma^{01+}$ and $^1\gamma^{01+}$ states in the nomenclature of Ref. 18 (cf. Figure 1). The 1^1B_{2g} state has zero oscillator strength for symmetry

reasons and for 1^1B_{3u} this value is also almost vanishing. This is in agreement with the small exciton splitting of only 0.0087 eV between these two states. The natural transition orbital participation ratio PR_{NTO} is about four for these two states: two configurations are already needed to describe the corresponding monomer states[18] and this value is doubled in the resonant delocalized state. The next two excited states (1^1B_{3g}, 1^1B_{2u}) are again of Frenkel type ($CT = 0.0$). Both states derive from the S_2 (S^{00}, ^1L_a) state of naphthalene and may be designated as the $^1\sigma^{00}$ / $^1\gamma^{00}$ excitonic pair. The oscillator strength of the γ state is 0.144, and an excitonic splitting of 0.049 eV is present. Considering the remaining states, it may be observed that the 3^1B_{2u} and 3^1B_{3g} states are composed of the same orbital contributions as 1^1B_{3g} and 1^1B_{2u} but that they show $CT \approx 1$. They are the charge resonance states related to S^{00} (designated $^1\delta^{00}$ and $^1\rho^{00}$). Thus in summary a complete set of four excited states deriving from the S^{00} monomer transition could be identified (cf. Figure 1, bottom). PR_{NTO} reveals that for all four of the resonant states in the S^{00} series two configurations are significantly involved, which is consistent with the idealized case[18,20] shown in Eqs. (5)-(8). Here it may be noticed that the singular value decomposition reduced the number of configurations need to describe the excited state: Whereas $7b_{1g}$-$10b_{2g}$ and $7b_{1g}$-$11b_{2g}$ amount to two different configurations in Hartree-Fock orbitals, these are reduced to one configuration where the virtual NTO is a linear combination of the $10b_{2g}$ and $11b_{2g}$ orbitals. The 3^1B_{2g} and 3^1B_{3u} states form another pair of excitonic resonance states ($^1\sigma^{01-}$ / $^1\gamma^{01-}$). In agreement with the larger oscillator strength of the γ state (2.700), the excitonic splitting is also larger (0.324 eV). The final state shown (4^1B_{3g}) is again of Frenkel excitonic type, and may be designated $^1\sigma^{11}$. In the energetic region considered here only two states (3^1B_{2u}, 3^1B_{3g}) with non-vanishing CT contribution, belonging to the S^{00} monomer state, were found. The charge resonance combinations of the S^{01+}, S^{01-}, and S^{11} monomer states lie at higher energies and are not presented in Table 4. For a discussion of these states, the reader is referred to Ref. 18.

Table 4. Excitation energies (ΔE, eV), oscillator strengths (f), charge transfer values, natural transition orbital participation ratios, and type assignments of the 9 lowest energy ππ* states of the stacked naphthalene dimer at an intermolecular separation of 5.0 Å.

State	ΔE	f	Dominant contributions[a]	CT	PR_{NTO}	type[b]
1^1B_{2g} (S_1)	4.386	0	$11b_{1u}$-$11b_{3u}$ (0.49) $7a_u$-$11b_{2u}$ (0.45) $7b_{1g}$-$11b_{3g}$ (0.44)	0.00	3.93	$^1\sigma^{01+}$
1^1B_{3u} (S_2)	4.394	0.00002	$11a_g$-$11b_{3u}$ (-0.47) $7a_u$-$11b_{3g}$ (0.47) $7b_{1g}$-$11b_{2u}$ (0.43)	0.00	4.00	$^1\gamma^{01+}$
1^1B_{3g} (S_3)	4.709	0	$7a_u$-$11b_{3u}$ (0.72) $7b_{1g}$-$10b_{2g}$ (0.46) $7b_{1g}$-$11b_{2g}$ (0.38)	0.01	2.00	$^1\sigma^{00}$
1^1B_{2u} (S_4)	4.759	0.144	$7b_{1g}$-$11b_{3u}$ (0.67) $7a_u$-$10b_{2g}$ (0.50) $7a_u$-$11b_{2g}$ (0.42)	0.00	2.14	$^1\gamma^{00}$
3^1B_{2g} (S_{12})	5.789	0	$7a_u$-$11b_{2u}$ (0.53) $11b_{1u}$-$11b_{3u}$ (-0.53) $7b_{1g}$-$11b_{3g}$ (0.35)	0.04	3.54	$^1\sigma^{01-}$
3^1B_{2u} (S_{13})	5.867	0.0003	$7b_{1g}$-$11b_{3u}$ (-0.61) $7a_u$-$10b_{2g}$ (0.55) $7a_u$-$11b_{2g}$ (0.41)	0.94	2.00	$^1\delta^{00}$
3^1B_{3g} (S_{14})	5.874	0	$7b_{1g}$-$10b_{2g}$ (0.59) $7a_u$-$11b_{3u}$ (-0.57) $7b_{1g}$-$11b_{2g}$ (0.46)	0.95	1.95	$^1\rho^{00}$
3^1B_{3u} (S_{17})	6.113	2.700	$7b_{1g}$-$11b_{2u}$ (0.53) $11a_g$-$11b_{3u}$ (0.48) $7a_u$-$11b_{3g}$ (0.38)	0.08	3.85	$^1\gamma^{01-}$
4^1B_{3g} (S_{20})	6.283	0	$11b_{1u}$-$11b_{2u}$ (0.69) $11a_g$-$11b_{3g}$ (-0.53) $11b_{1u}$-$12b_{2u}$ (-0.30)	0.03	1.95	$^1\sigma^{11}$

[a] Dominant contributions to the excitation, coefficient in parentheses.

[b] Nomenclature according to Figure 1 and Ref. 18.

Next, the geometry dependence of the excited states with respect to the intermolecular distance of the naphthalene molecules is examined. And in particular it will be outlined how the four

states deriving from the S^{00} monomer state interact to form the strongly stabilized excimer. For this purpose the excited state energies and *CT* and PR_{NTO} properties of these states are presented in Figure 3. Potential curves of the 1^1B_{2g} and 1^1B_{3u} states are presented for comparison. At 5.0 Å and longer intermonomer separations, a clear distinction between Frenkel excitonic and charge separated states, as described above, can be seen. 1^1B_{3g} and 1^1B_{2u} form the almost degenerate excitonic $^1\sigma^{00}$ / $^1\gamma^{00}$ pair with $CT \approx 0$ whereas for the corresponding charge resonance states 3^1B_{3g} ($^1\rho^{00}$) and 3^1B_{2u} ($^1\delta^{00}$) $CT \approx 1$. At this large separation all these states show $PR_{\mathrm{NTO}} \approx 2$ (with deviations less than 0.2). When the intermolecular distance is decreased, a splitting between 1^1B_{3g} and 1^1B_{2u} as well as 3^1B_{3g} and 3^1B_{2u} is observed due to excitonic and charge resonance interactions, respectively. At the same time also the excitonic splitting between the 1^1B_{2g} and 1^1B_{3u} states is raised. As the distance is decreased further, the B_{2u} states (Figure 3, red) retain their diabatic character, i.e. $CT(1^1B_{2u}) \approx 1$, $CT(3^1B_{2u}) \approx 0$ and their PR_{NTO} stays at about two, also indicating that no changes occur. There is only a small spike in *CT* at 4.7 Å which seems to be caused by an interaction with a Rydberg state. It may be noted that at very small intermolecular separations the *CT* value of 3^1B_{2u} goes slightly below zero, whereas the one of 1^1B_{2u} goes above one. This result is present because of slightly negative Ω_{AB}^{α} values, which according to Eq. (14) may be obtained if the overlap is strong. It is related to the existence of negative Mulliken populations.[53] In spite of being an artifact in the present context it should not affect any of the qualitative implications of the results. The situation is more complicated for the B_{3g} states (Figure 3, black). 1^1B_{3g} does not remain a pure Frenkel exciton but it gains part of the charge transfer character of 3^1B_{3g}, which means that these states are no longer well defined as $^1\sigma^{00}$ and $^1\rho^{00}$ states. Additionally at 3.8 Å there is an avoided crossing between 3^1B_{3g} and 4^1B_{3g}. 4^1B_{3g} becomes now the continuation of the $^1\rho^{00}$ state, which can be seen by the fact that the *CT* values of these two states cross. Interestingly PR_{NTO} shows a spike at the avoided crossing for the two states involved because of the fact that two configurations mix at this point. At about 3.5 Å intermolecular separation the 1^1B_{3g} and 1^1B_{2g} states cross, making 1^1B_{3g} the lowest singlet excited state overall (cf. Ref. 18). The excimer minimum lies at 3.2 Å intermolecular separation. It forms a deep potential well on the 1^1B_{3g} potential surface, stabilized by 1.38 eV with respect to infinite separation. This value should be seen as an estimate, considering that a precise calculation of the interaction energy is highly challenging. Already at the ground state minimum the MP2 method overestimates the interaction energy by about 0.1 to 0.2 eV compared to the much more computationally intensive CCSD(T) reference,[54] and the discrepancies may be somewhat enhanced at smaller separations and for excited states. Moreover, basis set superposition effects play a significant role at such small intermolecular separations.[46] The counterpoise correction term for the ground state, $2\left(E^0_{\mathrm{mon.,[mon.]}} - E^0_{\mathrm{mon.,[dim.]}}\right) = 0.435$ eV (Eq. (29)), was added but this is just an approximation for the excimer state. However, in spite of a possible error of a few tenths of an eV, it can be assumed that the description of the physical processes and the changes occurring in the electronic structure are qualitatively correct.

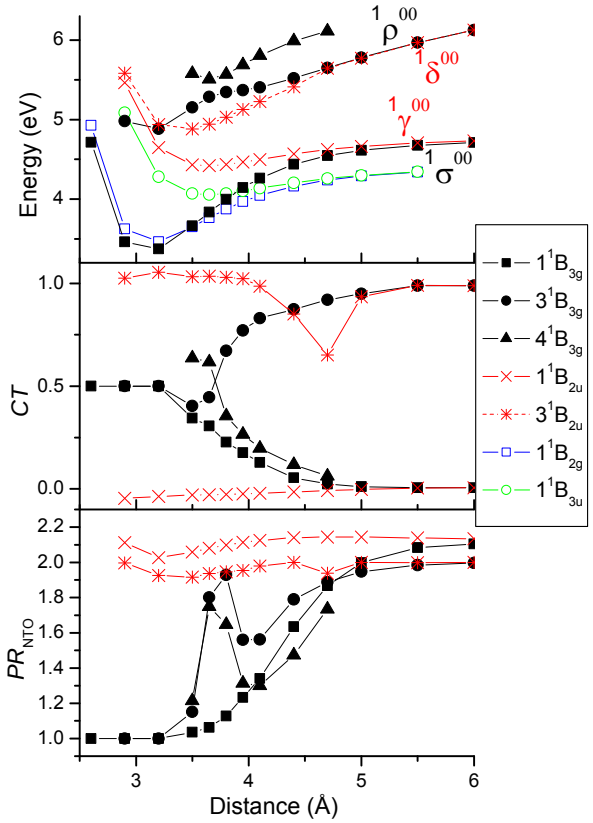

Figure 3. Counterpoise corrected state energies relative to the ground state at infinite separation, charge transfer values (*CT*), and NTO participation ratios (PR_{NTO}) for the lowest singlet ππ* states of B_{3g} (black) and B_{2u} (red) symmetry of a face-to-face stacked naphthalene dimer at different intermolecular distances. The energies of the lowest singlet excited states of B_{2g} (blue) and B_{3u} (green) symmetry are presented as well. The state labels correspond to the assignments at 5.0 Å, whenever crossings between Rydberg and ππ* states occurred, the indices where adjusted accordingly.

When approaching the excimer minimum, the *CT* values of the two B_{3g} states converge to 0.5, i.e. there is an equal probability for the *electron* and *hole* to be on the same or different molecules. The 1^1B_{3g} state is now described by only one configuration (corresponding to the $7a_u$-$11b_{3u}$ transition in Table 4), which means that PR_{NTO} is reduced to one. According to Eq. (9), this situation may also be understood in the sense that the excimer state is an equal mixture of all four states in the upper part of Figure 1 (1*2, 12*, 1^+2^-, 1^-2^+). Thus, in accordance with Refs 18 and 55, excitonic and CT interactions are both active in the stabilization of the excimer. In the language of Ref. 8 this situation also means that the coherence size now spans both molecules (*COH*=2 according to Eq (22)). In this sense, the excimer can neither be explained by excitonic coupling nor by charge transfer but only a coherent interaction, leading to a homogenous excited state, can induce this strong stabilization.

4.3 Nucleobase stacks

The nature of excited states in nucleobases has been intensively discussed using a large variety of experimental and computational methods. A question of particular importance was over how many bases the excited states are distributed and whether base-base interactions were of excitonic or charge transfer type.[3-7] In this section the analysis of a di-adenine stack in idealized B-DNA geometry is performed. The two bases have the same geometry but are not exactly equivalent because of the twisted arrangement. Therefore, the electronic states are not completely delocalized, cf Ref. 56. In Table 5 the excitation energies, oscillator strengths and statistical descriptors of the first 10 excited states of the stacked dimer are shown. Additionally, the type of the excitation (nπ* or ππ*), obtained from visual analysis of the orbitals, is presented. The eight lowest energy states can be identified with excitonic combinations of the four lowest states of the isolated adenine.[57] S_1 and S_2 form a pair of corresponding nπ* states, separated by a gap of 0.0091 eV. Considering the fact that the states are almost completely delocalized ($POS \approx 1.5$), the excitonic coupling between these two states can be obtained as 0.0045eV, which is similar to the value of 0.006 eV of Ref 56. For these states $PR_{NTO} \approx 2.0$, which corresponds to idealized simple excitonic states. The following four states, S_3-S_6, are of ππ* nature and derive from the L_a and L_b states of adenine. S_7 and S_8 form another pair of nπ* states. These states are somewhat more localized, so that the splitting of 0.019 eV is in part due to asymmetry and in part due to the excitonic coupling. S_9 is an almost complete charge transfer state (CT=0.92). Compared to the naphthalene dimer example, there are no charge resonance interactions here but the charge transfer is directed ($CT_{net} = -0.92 = -CT$). This is also reflected by the large dipole moment μ = 12.2 D. Finally a partially delocalized nπ* state (S_{10}) can be seen. In summary, it could be shown how a large amount of quantitative physical information could be extracted from this system. A more extended study using these procedures to analyze realistic DNA fragments has been submitted for publication.[58]

Table 5. Excitation energies (ΔE, eV), oscillator strengths (f), dipole moments (μ, D) statistical descriptors, and type assignments for the first 10 excited states of a di-adenine stack in B-DNA geometry.

State	ΔE	f	μ	POS	PR	CT	CT_{net}	PR_{NTO}	type
S_1	5.013	0.009	2.84	1.56	1.97	0.02	0.01	1.98	nπ*
S_2	5.022	0.001	2.99	1.45	1.98	0.02	0.01	1.99	nπ*
S_3	5.104	0.046	4.57	1.80	1.48	0.04	-0.02	1.54	ππ*
S_4	5.193	0.054	4.46	1.36	1.84	0.03	0.00	2.75	ππ*
S_5	5.225	0.007	5.62	1.43	1.96	0.03	0.00	3.26	ππ*
S_6	5.307	0.345	4.95	1.39	1.90	0.03	0.00	2.07	ππ*
S_7	5.724	0.005	3.64	1.11	1.25	0.02	0.01	1.23	nπ*
S_8	5.743	0.001	2.87	1.89	1.25	0.01	-0.01	1.24	nπ*
S_9	5.854	0.015	12.20	1.49	1.09	0.92	-0.92	1.07	ππ* (CT)
S_{10}	6.128	0.000	4.39	1.85	1.34	0.03	-0.01	1.47	nπ*

4.4 Poly-phenylene-vinylene conjugated organic polymers

Recently, conjugated organic polymers have attracted a lot of interest for applications in photovoltaic devices.[10,59] And it is of particular interest to get a clear insight into the excited states involved. These are in many cases quite complex, considering that usually many molecular orbitals are involved, and that different exciton bands may overlap. An analysis in terms of transition density matrices[8] is therefore convenient by reducing the representation to a form independent of the number of orbitals involved. Additionally, as shown below, it may also give insight into excitonic structure, which would be hidden by simply considering orbitals. We performed RI-ADC(2) calculations on a phenylene-vinylene oligomer $(PV)_6P$ (see Figure 4) at its S_0 and S_1 minimum geometries, as reported in detail in Ref. 60.

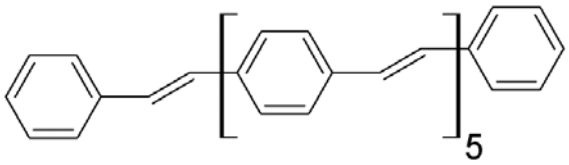

Figure 4. Structural formula of the phenylene-vinylene oligomer $(PV)_6P$.

In Table 6 information about the excited states of $(PV)_6P$ at the ground state minimum is presented. S_1 (1^1B_u) is the bright state, carrying almost all the oscillator strength. The number of fragments participating in this excited state (*PR*) is 5.53. This state shows a significant coherence length (*COH*=3.90), which means that this state has a large *electron-hole* separation and cannot be viewed as a Frenkel exciton over PV units. This state is dominated by one major transition ($14b_g$-$14a_u$) and accordingly PR_{NTO} is low at 1.59. In the last row of Table 6, the plot of the **Ω** matrix with respect to the 7 fragments is shown. The diagonal length represents the spatial extent of the excitons, whereas the off-diagonal elements, corresponding to charge transfer configurations, mark coherences between the fragments.[8] The S_1 state shows a diagonal length over a large part of the system. The off-diagonal components indicate that there is a significant amount of *electron-hole* separation at least between neighboring PV units. S_2 (2^1A_g) and S_3 (2^1B_u) show a very similar structure to S_1, only that one and two nodal planes are present. These can therefore be interpreted as higher states of the same exciton band. Interestingly S_4 (3^1A_g) shows a completely different structure with a significantly more pronounced charge separation and no nodal plane. Moreover, its coherence length is significantly larger (*COH*=4.98). Apparently it is the first state of a different exciton band. S_5 (4^1A_g) could be seen as the next state in the initial exciton band. S_6 (3^1B_u) has a somewhat different character with a significantly lowered coherence length (*COH*=2.20) and is therefore more closely related to an ideal Frenkel exciton, cf Ref 8. Note that the presence of three distinct exciton bands corresponds nicely to results obtained using solid state physics methodology.[61]

Table 6. Excitation energies (ΔE, eV), oscillator strengths (f), statistical descriptors, dominant contributions to the excitation, and plots of **Ω** for the lowest singlet excited states of $(PV)_6P$ at the ground state minimum geometry.

	S_1 (1^1B_u)	S_2 (2^1A_g)	S_3 (2^1B_u)	S_4 (3^1A_g)	S_5 (4^1A_g)	S_6 (3^1B_u)
ΔE	3.154	3.557	3.995	4.225	4.392	4.468
f	5.66	0	0.61	0	0	0.02
PR	5.53	6.32	6.69	5.14	6.30	3.80
COH	3.90	3.38	3.03	4.98	3.04	2.20
PR_{NTO}	1.59	2.14	2.99	2.39	4.00	4.16
Dom. contr.[a]	$14b_g$-$14a_u$ (0.86)	$13a_u$-$14a_u$ (0.65)	$13b_g$-$14a_u$ (0.55)	$13a_u$-$14a_u$ (0.53)	$13a_u$-$15a_u$ (0.41)	$8b_g$-$14a_u$ (0.47)
	$13a_u$-$15b_g$ (-0.40)	$14b_g$-$15b_g$ (-0.63)	$13a_u$-$15b_g$ (0.54)	$14b_g$-$15b_g$ (0.55)	$13b_g$-$15b_g$ (0.40)	$14b_g$-$19a_u$ (0.29)
	$13b_g$-$15a_u$ (-0.22)	$13b_g$-$15b_g$ (0.22)	$14b_g$-$15a_u$ (-0.50)	$13b_g$-$15b_g$ (0.35)	$14b_g$-$16b_g$ (0.36)	$14b_g$-$20a_u$ (-0.26)
Ω						

[a] Dominant contributions to the excitation, coefficient in parentheses.

In order to rationalize the results presented above, the orbitals involved in the excited states will be considered. In this context it is of particular interest how the difference between the 2^1A_g and 3^1A_g states can be understood. The dominant contributions to the excitations are given in Table 6. The corresponding orbitals are shown in Figure 5. What can be seen, is that the 2^1A_g and 3^1A_g excited states consist of the same configurations with almost identical weights. Only the signs of the components differ. As shown in Eqs (5)-(8) and Ref. 18, such differences can have a significant influence on the properties of the excited state. It is however quite difficult to deduce any of these properties in a canonical orbital representation.

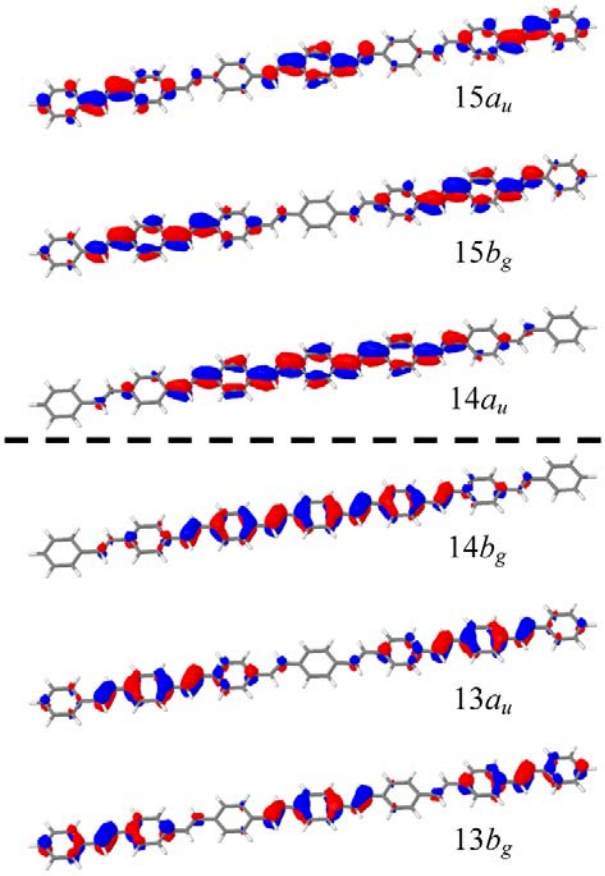

Figure 5. Frontier Hartree-Fock orbitals of $(PV)_6P$ at the optimized ground state geometry.

To get a different perspective of these states, the natural transition orbitals (Eq. (27)) are plotted in Figures 6 and 7. In this representation a clear difference is visible. The 2^1A_g state (Figure 6) can be represented by two transitions involving orbitals that are fairly evenly localized over the whole system except for the central phenyl moiety. This is in agreement with the structure and nodal plane of **Ω** as shown in Table 6. It can be seen that the two main *initial* and *final* orbitals are each of very similar shape with the only difference being the symmetry with respect to a rotation around the center of the molecule. It may thus be understood that the excitation could also be represented by two rather localized excitations on either half of the molecule. More information about this fact and orbital plots are given in the Supporting Information (S6). The natural transition orbitals of 3^1A_g (Figure 7) have a significantly different structure. In the first transition, shown at the top, the *initial* orbital is clearly localized in the center of the molecule, whereas the *final* orbital is distributed over the sides. The second contribution shows the opposite feature. In both cases it is seen that there is a significant participation of the central phenylene, which corresponds to the fact that there is no clear nodal structure of **Ω** in Table 6. The fact that the *initial* and *final* orbitals are always localized on different fragments corresponds to the off-diagonal size in **Ω** and to the larger *COH* value.

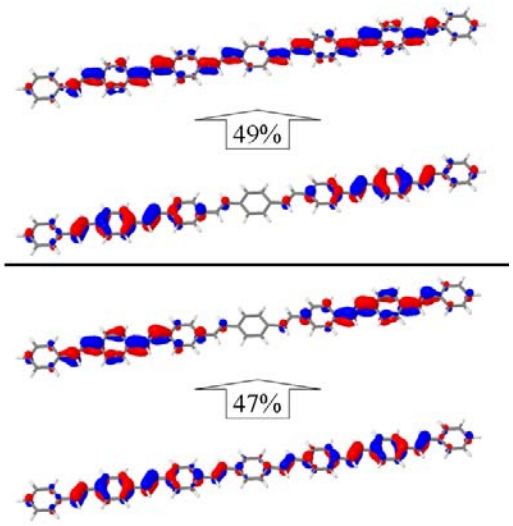

Figure 6. Plots of the two dominant pairs of natural transition orbitals for the 2^1A_g state of $(PV)_6P$.

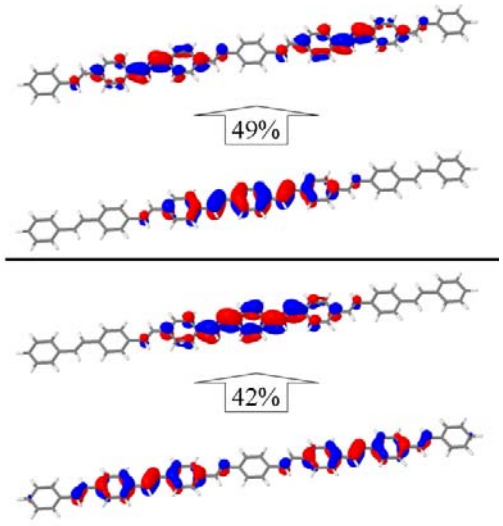

Figure 7. Plots of the two dominant pairs of natural transition orbitals for the 3^1A_g state of $(PV)_6P$.

To examine a possible localization of the excitation, a geometry optimization in the 1^1B_u state was performed (Table 7). Compared to the ground state minimum the 1^1B_u state is somewhat contracted upon relaxation (PR is lowered to 5.01) but remains delocalized over several fragments. This is consistent with Ref. 11 where the analysis was performed in terms of nuclear geometry. The coherence length is somewhat increased (*COH*=4.21) and PR_{NTO} lowered, reflecting the formation of a more homogeneous coherent excited state. Interestingly the 3^1A_g

state is strongly stabilized and moves below the 2^1B_u state. The 3^1B_u state here appears to be of the same character as 3^1A_g only that it has a nodal plane.

Table 7. Excitation energies (ΔE, eV), oscillator strengths (f), statistical descriptors, and plots of $\mathbf{\Omega}$ for the lowest excited states of $(PV)_6P$ at the S_1 (1^1B_u) minimum geometry.

	S_1 (1^1B_u)	S_2 (2^1A_g)	S_3 (3^1A_g)	S_4 (2^1B_u)	S_5 (3^1B_u)	S_6 (4^1A_g)
ΔE	2.665	3.281	3.621	3.771	4.021	4.217
f	5.37	0	0	0.98	0.01	0
PR	5.01	6.26	4.68	6.67	5.74	6.70
COH	4.21	3.69	4.48	3.28	4.20	3.22
PR_{NTO}	1.29	2.06	2.15	2.93	2.68	4.01
$\mathbf{\Omega}$						

5. Conclusions

We presented a scheme for the analysis of one-electron singlet excited states in dimers, oligomers and extended molecular systems. Through an analysis of the one-electron transition density matrix, significant new insight can be gained over a manual wavefunction analysis. Quantities of immediate physical interest like charge separation, exciton delocalization, and coherence can be obtained through partial summation schemes. The method is readily automatized, providing a route for statistical analysis. The general formulation of the equations allows an application to a wide variety of wave function models. So far implementations are available for the CASSCF, MR-CI, CC2, ADC(2), and TDDFT methods. Fundamental limitations are related only to the physical properties of the excited state (i.e. only one-electron excited states can be analyzed). To show the applicability of this method, we presented results on several classes of systems using different correlated ab-initio wave function models.

First, for methodological purposes, excitonic interactions between the nπ* states of two face-to-face stacked formaldehyde molecules were considered. It was shown how a displacement from the symmetric geometry lead to a localization of the wave function. This process was analyzed using the above mentioned techniques. In addition it was pointed out how the change in the wave function properties could be related to the ab-initio non-adiabatic coupling vectors.

The example of a π-stacked naphthalene dimer was used to examine the performance of our analysis scheme for states, which were completely delocalized due to symmetry. In this case a differentiation between Frenkel excitonic and charge resonance states is particularly challenging because of the fact that all orbitals are evenly distributed over both fragments. The automatized analysis gave results consistent with the formal considerations of Ref 18. Moreover, by systematically following the change in the wave function, when the intermolecular separation was lowered, interesting new insight into the process of excimer formation could be obtained. A mixing between excitonic and charge resonance character (cf. Refs 18,55), yielding a

homogeneous and coherent excited state, was identified as possible cause for the strong stabilization of the excimer.

Using two stacked adenine molecules, it was shown how the analysis scheme can also be readily applied to systems with a number of interacting excited states of different character. A collection of different physical descriptors could be provided for a compact representation of the states. It was found that the lowest eight singlet excited states were excitonic combinations of the four lowest monomer states, with only a few percent of charge resonance character. The next state, S_9, was identified as a pure charge transfer state.

A phenylene-vinylene oligomer was considered to test the performance of our analysis with respect to conjugated π-systems. An analysis of the vertical excitations revealed details of the excitonic structure, which remained hidden by a simple consideration of the canonical orbitals. Excited states, belonging to three different distinct exciton bands,[61] could be identified. The difference could be represented by the $\mathbf{\Omega}$ matrix, and was also shown graphically in the natural transition orbital[14-16] representation. An analysis of the excited states at the S_1 minimum was presented as well.

This work was intended as a methodological outline of the working equations and as a tentative collection of potential applications of this method. More detailed investigations on the systems described are in progress.

6. Acknowledgment

We thank I. Burghardt for discussions and for pointing out Ref. 61 to us. F. Plasser is a recipient of a DOC fellowship of the Austrian Academy of Sciences. This work has been supported by the Austrian Science Fund within the framework of the Special Research Program and F41 Vienna Computational Materials Laboratory (ViCoM). Support was also provided by the Robert A. Welch Foundation under Grant No. D-0005. The authors also acknowledge the technical support and computer time at the Vienna Scientific Cluster (project nos. 70019 and 70151).

7. Supporting Information Available

Cartesian coordinates of the molecular structures considered (S1-S4), mathematical discussion of the relations between *PR*, *COH*, and PR_{NTO} (S5), localization of the PPV NTOs (S6).

8. References

(1) Middleton, C. T.; de La Harpe, K.; Su, C.; Law, Y. K.; Crespo-Hernandez, C. E.; Kohler, B. *Annu. Rev. Phys. Chem.* **2009**, *60*, 217-239.

(2) Markovitsi, D.; Gustavsson, T.; Banyasz, A. *Mutat. Res., Rev. Mutat. Res.* **2010**, *704*, 21-28.

(3) Crespo-Hernandez, C.; Cohen, B.; Kohler, B. *Nature* **2005**, *436*, 1141-1144.

(4) Markovitsi, D.; Talbot, F.; Gustavsson, T.; Onidas, D.; Lazzarotto, E.; Marguet, S. *Nature* **2006**, *441*, E7-E7.

(5) Buchvarov, I.; Wang, Q.; Raytchev, M.; Trifonov, A.; Fiebig, T. *Proc. Natl. Acad. Sci. U. S. A.* **2007**, *104*, 4794-4797.

(6) Takaya, T.; Su, C.; de La Harpe, K.; Crespo-Hernandez, C.; Kohler, B. *Proc. Natl. Acad. Sci. U. S. A.* **2008**, *105*, 10285-10290.

(7) Markovitsi, D.; Vaya, I.; Gustavsson, T.; Miannay, F. A.; Douki, T. *J. Am. Chem. Soc.* **2010**, *132*, 11834-11835.

(8) Tretiak, S.; Mukamel, S. *Chem. Rev.* **2002**, *102*, 3171-3212.

(9) Wu, C.; Malinin, S. V.; Tretiak, S.; Chernyak, V. Y. *J. Chem. Phys.* **2008**, *129*, 174112.

(10) Brédas, J.-L.; Norton, J. E.; Cornil, J.; Coropceanu, V. *Acc. Chem. Res.* **2009**, *42*, 1691-1699.

(11) Nayyar, I.; Batista, E.; Tretiak, S.; Saxena, A.; Smith, D.; Martin, R. *J. Phys. Chem. Letters* **2011**, *2*, 566-571.

(12) Prezhdo, O. V.; Luzanov, A. V. *Int. J. Quantum Chem.* **2005**, *102*, 582-601.

(13) Luzanov, A. V.; Zhikol, O. A. *Int. J. Quantum Chem.* **2010**, *110*, 902-924.

(14) Luzanov, A. V.; Sukhorukov, A. A.; Umanskii, V. E. *Theor. Exp. Chem.* **1976**, *10*, 354-361.

(15) Martin, R. L. *J. Chem. Phys.* **2003**, *118*, 4775-4777.

(16) Mayer, I. *Chem. Phys. Lett.* **2007**, *437*, 284-286.

(17) Head-Gordon, M.; Grana, A. M.; Maurice, D.; White, C. A. *J. Phys. Chem.* **1995**, *99*, 14261-14270.

(18) Lim, E. C.; East, A. L. L. *J. Chem. Phys.* **2000**, *113*, 8981-8994.

(19) Scholes, G. D.; Ghiggino, K. P. *J. Phys. Chem.* **1994**, *98*, 4580-4590.

(20) Mayer, I. *Chem. Phys. Lett.* **2007**, *443*, 420-425.

(21) Shepard, R. In *Ab Initio Methods in Quantum Chemistry II*; Lawley, K. P., Ed.; Wiley: New York, 1987, p 63-200.

(22) Mayer, I. *Chem. Phys. Lett.* **1983**, *97*, 270-274.

(23) Pipek, J.; Mezey, P. G. *Int. J. Quantum Chem.* **1988**, *34*, 1-13.

(24) Czader, A.; Bittner, E. R. *J. Chem. Phys.* **2008**, *128*, 035101.

(25) Surjan, P. R. *Chem. Phys. Lett.* **2007**, *439*, 393-394.

(26) Dunning, T. H. *J. Chem. Phys.* **1989**, *90*, 1007-1023.

(27) Lischka, H.; Shepard, R.; Brown, F. B.; Shavitt, I. *Int. J. Quantum Chem.* **1981**, *S15*, 91-100.

(28) Shepard, R.; Lischka, H.; Szalay, P. G.; Kovar, T.; Ernzerhof, M. *J. Chem. Phys.* **1992**, *96*, 2085-2098.

(29) Lischka, H.; Dallos, M.; Shepard, R. *Mol. Phys.* **2002**, *100*, 1647-1658.

(30) Lischka, H.; Dallos, M.; Szalay, P. G.; Yarkony, D. R.; Shepard, R. *J. Chem. Phys.* **2004**, *120*, 7322-7329.
(31) Muller, T. *J. Phys. Chem. A* **2009**, *113*, 12729-12740.
(32) Lischka, H.; Shepard, R.; Shavitt, I.; Pitzer, R. M.; Dallos, M.; Mueller, T.; Szalay, P. G.; Brown, F. B.; Ahlrichs, R.; Boehm, H. J.; Chang, A.; Comeau, D. C.; Gdanitz, R.; Dachsel, H.; Ehrhardt, C.; Ernzerhof, M.; Hoechtl, P.; Irle, S.; Kedziora, G.; Kovar, T.; Parasuk, V.; Pepper, M. J. M.; Scharf, P.; Schiffer, H.; Schindler, M.; Schueler, M.; Seth, M.; Stahlberg, E. A.; Zhao, J.-G.; Yabushita, S.; Zhang, Z.; Barbatti, M.; Matsika, S.; Schuurmann, M.; Yarkony, D. R.; Brozell, S. R.; Beck, E. V.; Blaudeau, J.-P.; Ruckenbauer, M.; Sellner, B.; Plasser, F.; Szymczak, J. J. *COLUMBUS, an ab initio electronic structure program, release 7.0* **2011**, www.univie.ac.at/columbus.
(33) Trofimov, A. B.; Schirmer, J. *J. Phys. B: At., Mol. Opt. Phys.* **1995**, *28*, 2299-2324.
(34) Weigend, F.; Haser, M.; Patzelt, H.; Ahlrichs, R. *Chem. Phys. Lett.* **1998**, *294*, 143-152.
(35) Hättig, C.; Weigend, F. *J. Chem. Phys.* **2000**, *113*, 5154-5161.
(36) Hättig, C.; Köhn, A. *J. Chem. Phys.* **2002**, *117*, 6939-6951.
(37) Hattig, C. *Advances in Quantum Chemistry, Vol 50* **2005**, *50*, 37-60.
(38) Schafer, A.; Horn, H.; Ahlrichs, R. *J. Chem. Phys.* **1992**, *97*, 2571-2577.
(39) Weigend, F.; Kohn, A.; Hattig, C. *J. Chem. Phys.* **2002**, *116*, 3175-3183.
(40) Plasser, F.; Lischka, H. *J. Chem. Phys.* **2011**, *134*, 034309.
(41) Karney, C. F. F. *J. Mol. Graphics Modell.* **2007**, *25*, 595-604.
(42) Ponder, J. W.; Richards, F. M. *J. Comput. Chem.* **1987**, *8*, 1016-1024.
(43) Schafer, A.; Huber, C.; Ahlrichs, R. *J. Chem. Phys.* **1994**, *100*, 5829-5835.
(44) Ahlrichs, R.; Bar, M.; Haser, M.; Horn, H.; Kolmel, C. *Chem. Phys. Lett.* **1989**, *162*, 165-169.
(45) Boys, S. F.; Bernardi, F. *Mol. Phys.* **1970**, *19*, 553-566.
(46) Olaso-Gonzalez, G.; Merchan, M.; Serrano-Andres, L. *J. Am. Chem. Soc.* **2009**, *131*, 4368-4377.
(47) Schaftenaar, G.; Noordik, J. H. *J. Comput.-Aided Mol. Des.* **2000**, *14*, 123-134.
(48) Shepard, R. In *Modern Electronic Structure Theory*; Yarkony, D. R., Ed.; World Scientific: Singapore, 1995, p 345-458.
(49) Wolfram Research, Inc., Mathematica, Version 5.2, Champaign, IL, 2005.
(50) Jones, E.; Oliphant, T.; Peterson, P.; et-al *SciPy: Open source scientific tools for Python* **2001-**, http://www.scipy.org/.
(51) *Jmol: an open-source Java viewer for chemical structures in 3D*, http://www.jmol.org/.
(52) Plasser, F. *Wave Function Analysis Tools: Computational tools for analyzing molecular orbitals and electronic wavefunctions* **2012**, http://homepage.univie.ac.at/felix.plasser/download.html.
(53) Ammeter, J. H.; Buergi, H. B.; Thibeault, J. C.; Hoffmann, R. *J. Am. Chem. Soc.* **1978**, *100*, 3686-3692.
(54) Tsuzuki, S.; Honda, K.; Uchimaru, T.; Mikami, M. *J. Chem. Phys.* **2004**, *120*, 647-659.
(55) Das, A.; Mahato, K. K.; Chakraborty, T. *J. Chem. Phys.* **2001**, *114*, 6107-6111.
(56) Nachtigallova, D.; Hobza, P.; Ritze, H. *Phys. Chem. Chem. Phys.* **2008**, *10*, 5689-5697.
(57) Perun, S.; Sobolewski, A. L.; Domcke, W. *J. Am. Chem. Soc.* **2005**, *127*, 6257-6265.
(58) Plasser, F.; Aquino, A. J. A.; Lischka, H. *J. Phys. Chem. A, submitted for publication.*
(59) Shang, Y.; Li, Q.; Meng, L.; Wang, D.; Shuai, Z. *Theor. Chem. Acc.* **2011**, *129*, 291-301.
(60) Panda, A.; Burghardt, I.; Plasser, F.; Aquino, A. J. A.; Lischka, H. *to be published.*
(61) Kirova, N. *Polym. Int.* **2008**, *57*, 678–688.

3.7 The UV Absorption Spectrum of Alternating DNA Duplexes

In this work the absorption spectrum of alternating DNA duplexes was examined. The electronic structure was described at the correlated ab-initio ADC(2) level, environmental effects were included by a QM/MM electrostatic embedding approach (Figure 3.10), and a phenomenological analysis of the excited states was performed according to the tools introduced in Section 3.6. Moreover, for a realistic simulation of the spectra extensive sampling of intra- and intermolecular degrees of freedom was performed.

This paper sheds new light on the absorbing states in DNA. It could be shown that, when all factors leading to disorder are considered, the states are rather localized and do not form extended excitons. Charge transfer states are in the higher energy range of the spectrum but they can be stabilized through dynamical charge separation. Moreover, it was found that intramolecular contributions play the most important part with respect to spectral broadening.

The in-vacuo calculations and testing of the methods were carried out by A. J. A. Aquino. After this it was my task to devise an analysis strategy and also to carry out the QM/MM calculations. The paper was submitted to the *Journal of Physical Chemistry A* (17 May 2012). [104]

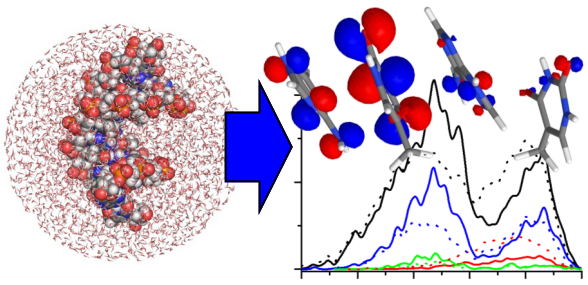

Figure 3.10: *Schematic depiction of the QM/MM methodology used for the computation of the UV absorption spectra of alternating DNA duplexes.*

The UV absorption spectrum of alternating DNA duplexes – analysis of excitonic and charge transfer interactions

Felix Plasser,[a] *Adelia J. A. Aquino,*[b,c] *Hans Lischka*[a,c]

[a]Institute of Theoretical Chemistry, University of Vienna, Währingerstraβe 17, A-1090, Vienna, Austria

[b]Institute of Soil Research, University of Natural Resources and Life Sciences, Peter-Jordan-Straβe 82, A-1190, Vienna, Austria

[c]Department of Chemistry and Biochemistry, Texas Tech University, Lubbock, TX 79409-1061, USA

Abstract

A detailed investigation of the excited states accessed by UV absorption in alternating DNA duplexes was performed by means of an extensive sampling of intra- and intermolecular degrees of freedom. The excited states were computed using the algebraic diagrammatic construction method to second order (ADC(2)). A realistic DNA environment was included through an electrostatic embedding QM/MM coupling scheme. The results indicate that (i) most excited states are delocalized over at most two bases, (ii) charge transfer states are located at higher energies than the bright states in the Franck-Condon region, but (iii) coupling between locally excited and charge transfer states may provide a route to dynamical charge separation, and (iv) spectral broadening is mainly caused by intramolecular vibrations.

1. Introduction

Deoxyribonucleic acid (DNA) plays a central role in biology as the carrier of the genetic code. Absorption of UV light can potentially damage DNA leading to mutations, genomic instability or carcinogenesis.[1] A major defense mechanism against these possibilities is based on ultrafast decay, converting the electronic excitation energy into hot vibrational motion in the ground state.[2-9] When studying the photophysics of DNA, collective behavior and interactions between nucleobases are considered to play a decisive role. Whereas isolated nucleobases decay on a picosecond time scale, single and double stranded DNA show additional transients with a 10-100 ps lifetime and even nano second components were found.[8,10-14] Both, excitonic delocalization[12,13,15-18] and interbase charge transfer[10,19-21] are being considered as processes arising due to base-base interactions, which may be responsible for the above mentioned change in dynamical behavior. A wide range of different results concerning excitonic delocalization has been reported. In single-stranded homoadenine polymers the delocalization was estimated at around three bases and it was pointed out that delocalization should be smaller in alternating sequences.[12,20,22] A computational study reported excitonic delocalization of at least two bases in dCdG polymers.[23] In contrast to these estimates of rather small delocalization degrees, others of six bases and more have been reported as well for poly-dA and poly-dGdC.[16,18] Moreover, from time-dependent fluorescence anisotropy studies on different base sequences, possible signatures of excitonic dynamics and excitation energy transfer between the bases were reported.[13,15,18] The existence of charge transfer states, on the other hand, is considered of highest importance as well, as they may lead to exciplexes which could act as trapping sites.[8,10] In this case there is some discrepancy as far their energetic ordering with respect to the bright states is concerned. Studies using time-dependent density functional theory (TDDFT) tended to place charge transfer states at lower or comparable energies as the bright states,[20,24,25] whereas they were found at somewhat higher energies in wave function based ab-initio studies.[17,26]

Even though the role of excitonic and charge transfer states has been discussed extensively in the literature, the information deduced from experiment is rather indirect and computational studies have the possibility to furnish a large amount of additional interesting information. Exciton theory, as one option (cf. Refs 16,23,27,28), provides a convenient tool for modeling electronic spectra and dynamical processes. These studies gave interesting insight but require tedious investigations to obtain the necessary parameterization. These approaches concentrate on statistical broadening and static disorder and do not consider the explicit sampling of the many internal degrees of freedom in the system. Furthermore, the excitonic models considered only one or a few $\pi\pi^*$ states per monomer, ignoring mixing to other states of $\pi\pi^*$ or $n\pi^*$ character. Finally, an inclusion of charge transfer configurations is challenging within such an approach, and was only performed in one of these studies.[28] Compared to parameterized exciton theory, quantum chemical calculations on the excited states of particular molecular systems offer the possibility of including excitonic and CT interactions at the same level in an integrated way based on well tested computational models. A number of different calculations on DNA fragments have been performed (cf. Ref 29). The TDDFT approach, as one powerful option, allows treating DNA fragments efficiently[20,22,25] but care has to be taken in computing charge transfer states correctly[26,30,31] and special calibration is needed for obtaining accurate results.[20] In contrast to TDDFT, methods such as the second order approximate coupled cluster model CC2[32] or algebraic diagrammatic construction to second order ADC(2)[33] approaches offer the possibility of balanced calculations of excitonic and charge transfer states without any particular bias to either side. Additionally, usage of the resolution of the identity (RI)[34] approximation allows for efficient calculations on sufficiently

large molecular systems to study stacking effects in the excited states. A systematic gas phase RI-CC2 study gave detailed insight into the different components of interbase coupling and other parameters,[35] and comparisons of different ab-initio methods on stacked dimers in comparison to selected functionals used in TDDFT calculations were performed as well.[26,36] Water solvation in the QM calculations was included by explicit solvent[20] and by polarizable continuum methods.[25,26] Molecular dynamics simulations were performed for sampling purposes.[16,20,22,23,27] Moreover, it was shown that environmental fluctuations may lead to significant changes in orbital energies in DNA[37] and that in particular the CT states were sensitive to the particular water configuration.[20] Thus, an accurate treatment of the interplay between thermal flexibility and restrains from stacking interactions and the backbone is necessary to obtain accurate relative positions of DNA bases as this may affect the interbase coupling significantly.[16,35,36]

In this work a detailed computational analysis of the initial distribution of excited states in DNA accessed through UV absorption will be performed, where in particular the amount of excitonic delocalization and charge transfer will be considered. In the light of the above considerations we designed our study to comply with the following points: (i) a reliable description of the excited states giving a balanced treatment of excitonic and CT interactions, (ii) a fully integrated description of the DNA environment, (iii) consistent sampling of intra- and intermolecular degrees of freedom, and (iv) development and application of methods to analyze the complex pattern of the excited-state wavefunctions. A QM/MM strategy has been adopted to address these points based on a DNA dodecamer (Figure 1). The QM part of the entire complex is computed at the ADC(2)[33] level with the strong advantages in terms of balanced description of excitonic and charge transfer states already mentioned above.

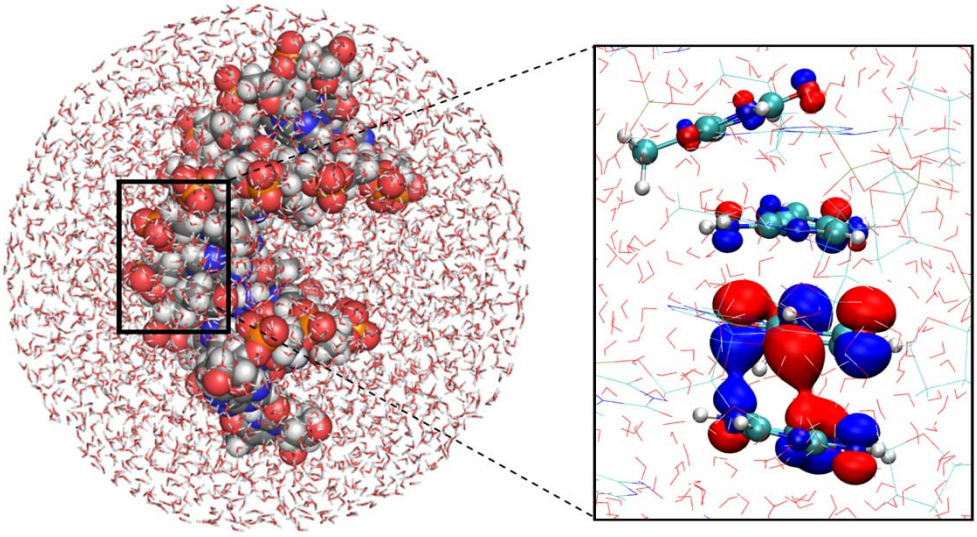

Figure 1. Depiction of the QM/MM methodology used in this work. Configurational sampling was performed by molecular dynamics simulations of a DNA dodecamer duplex solvated in a water droplet (left). ADC(2) calculations using electrostatic embedding were performed (right).

In the present simulations, the $(dAdT)_6 \cdot (dAdT)_6$ and $(dGdC)_6 \cdot (dGdC)_6$ alternating duplexes were chosen. The QM region consisted of two stacked bases (AT and CG, respectively) as well as four stacked bases (TATA, CGCG). Stacked bases rather than Watson-Crick paired bases were considered in light of experimental[8,10] and computational[25,28] evidence that the

main interaction is between stacked bases along one strand. Moreover, interstrand CT was considered only important in homopolymeric sequences and located at higher energies in alternating duplexes.[20]

2. Computational details

The electronic structure calculations were performed using the RI-ADC(2) method as implemented in the Turbomole 6.3 program package.[33,34,38,39] Calculations on selected structures were made with the SVP basis[40] for comparison reasons. Because of the relatively high computational cost for the sampling of the stacked dimer and tetramer structures in the order of 300-500 structures for each case as described below, the SV basis set[40] was used after verification against SVP results. In all calculations the core orbitals were frozen. In the tetramer spectra calculations the twenty lowest lying σ orbitals were frozen as well for reasons of computational efficiency. Test calculations described in the text below showed minor basis set effects on excitation energies in the order of 0.2 eV.

Base stacks in vacuo were arranged according to an ideal B helix configuration considering one strand. The vibrational broadening of the spectra was computed from the Wigner distribution of the zero point vibrations of the electronic ground state as described in Ref 41. For computations in DNA, mixed initial conditions following Ref. 42 were created. The purpose of this procedure was to treat the intramolecular modes of the molecules in the central region at a quantum mechanical level considering zero point vibrations, whereas low frequency intermolecular modes and environmental degrees of freedom were sampled by classical molecular dynamics (MD). Computations in DNA were performed on $(dAdT)_6 \cdot (dAdT)_6$ and $(dGdC)_6 \cdot (dGdC)_6$ duplexes embedded in a sphere of 3000 waters, neutralized with 22 K^+ counterions. After creation of an initial structure using Packmol,[43] equilibration and sampling was performed by means of a classical molecular dynamics simulation using the Amber-99[44] force field, as implemented in Tinker.[45] Sampling was performed every 0.2 ps. In parallel, the samples of the ground state Wigner distribution for the individual nucleobases in vacuo were constructed. For each of the structures selected from the dynamics simulations, the two and four nucleobases, respectively, obtained from the samples of the Wigner distribution were inserted at their appropriate places into the DNA structure using a quaternion least squares fit, cf. Refs 46-48. Then a 1 ps MD run was performed in order to relax the environment according to the small changes induced by the Wigner sample, while the structures and positions of the inserted bases were kept fixed. Finally, the atomic positions of the last MD step was used to perform a QM/MM calculation on the vertical excitation energies. The inserted stacked dimer and tetramer, respectively, connected to the sugar/phosphate backbone using a link hydrogen atom techninque,[49,50] constituted the QM region and the remaining atoms were included in the QM calculation by means of electrostatic embedding as point charges using their Amber99 values. The charge of the carbon atom forming the link atom on the MM side was set to zero, and in order to maintain the original neutral charge of the overall system, the excess charge (i.e. the sum of the deleted charge of the MM-link atom and the partial charge corresponding to the atoms in the QM region) were equally distributed onto the three atoms bonded to the MM-link atom (cf. Ref. 51).

The spectra simulation was performed using the program system Newton-X.[41,52] 300-500 distinct molecular geometries and environmental configurations were chosen. A phenomenological broadening of 0.05 eV was applied. Resulting distributions were normalized to put the different calculations on the same scale. For dimers ten excited states

were computed, for tetramers twenty. The spectra were constructed considering vertical excitation energies and oscillator strengths at the displaced structures. In addition, a density of transitions (DOT) was computed. In this case, the same methodology as for the spectra, only with a formal unit oscillator strength, was used. For plotting, the density of transition was rescaled in order to have the same total area as the spectrum.

An automated analysis of the excited states was performed according to a recently developed scheme of analyzing the one-electron transition density matrix[53] using previous work by Tretiak[54] and Luzanov.[55] This method provides well defined descriptors for properties like the position, delocalization and charge transfer character of the wave function even in difficult cases (e.g. delocalized orbitals, many contributing configurations). First, charge transfer numbers for an excited state α are computed

$$\Omega_{AB}^{\alpha} = \frac{1}{2}\sum_{\substack{a\in A\\ b\in B}} \left(\mathbf{D}^{0\alpha,[\mathrm{AO}]}\mathbf{S}^{[\mathrm{AO}]}\right)_{ab}\left(\mathbf{S}^{[\mathrm{AO}]}\mathbf{D}^{0\alpha,[\mathrm{AO}]}\right)_{ab} \tag{1}$$

from the transition density matrix between this state and the ground state $\mathbf{D}^{0\alpha,[\mathrm{AO}]}$ and the overlap matrix $\mathbf{S}^{[\mathrm{AO}]}$, both expressed in the atomic orbital (AO) basis. The summations go over the basis functions on fragments *A* and *B*, respectively. Using the charge transfer numbers, the position of the exciton in the dimer or tetramer can be defined as

$$POS^{\alpha} = \frac{\sum_A A \sum_B (\Omega_{AB}^{\alpha} + \Omega_{BA}^{\alpha})}{2\Omega^{\alpha}} \tag{2}$$

where the summation indices *A* and *B* go over the two or four molecules of the QM region and the symbol Ω^{α} is used to represent the normalization factor

$$\Omega^{\alpha} = \sum_{A,B} \Omega_{AB}^{\alpha} \tag{3}$$

For a state α localized only on one fragment *C*, i.e. $\Omega_{CC}^{\alpha} = \Omega^{\alpha}$ and all other elements of the $\mathbf{\Omega}^{\alpha}$ matrix are vanishing, it follows that $POS^{\alpha} = C$. For states that are distributed over several fragments, the POS^{α} value corresponds to the weighted average of the indices of theses fragments. The excitonic delocalization may be defined as a participation ratio expression

$$PR^{\alpha} = \frac{(\Omega^{\alpha})^2}{2}\left(\frac{1}{\sum_A (\sum_B \Omega_{AB}^{\alpha})^2} + \frac{1}{\sum_B (\sum_A \Omega_{AB}^{\alpha})^2}\right) \tag{4}$$

States localized on only one fragment *C* ($\Omega_{CC}^{\alpha} = \Omega^{\alpha}$) or charge transfer states between two fragments *C* and *D* ($\Omega_{CD}^{\alpha} = \Omega^{\alpha}$, $C \neq D$) exhibit $PR^{\alpha} = 1$. By contrast, for delocalized Frenkel excitonic states or charge resonance states, $PR^{\alpha} > 1$, according to the number of fragments involved. Finally the weight of charge transfer configurations is determined according to

$$CT^{\alpha} = \frac{1}{\Omega^{\alpha}} \sum_{\substack{A,B\\ B\neq A}} \Omega_{AB}^{\alpha} \tag{5}$$

This measure is zero for localized or delocalized Frenkel excitonic states (all off-diagonal elements of $\mathbf{\Omega}^{\alpha}$ are vanishing), whereas it is one for charge transfer or charge resonance states (all diagonal elements of $\mathbf{\Omega}^{\alpha}$ are vanishing). For notational brevity the α superscript, designating the excited state, will be omitted in the following text whenever explicit reference to the state is not needed.

A decomposition of the spectra based on the *PR* and *CT* values was performed (see below). The thresholds were chosen to give a meaningful representation of the underlying distribution. *PR* < 1.5 is seen as fairly localized, whereas *PR* > 2.5 can be considered as a significantly delocalized state. As a threshold for CT states, *CT* > 0.5 was chosen, i.e. states that contained at least 50% CT character.

Furthermore, to estimate excitonic couplings between neighboring molecules, a transformation based on the *POS* value was applied, in analogy to the use of fragment charge differences in charge transfer couplings.[56,57] The model assumes that two adiabatic states Ψ_i^{ad} and Ψ_j^{ad} are obtained through a unitary transformation applied to two localized diabatic states, positioned on neighboring fragments *k* and *k*+1

$$\begin{pmatrix}\Psi_i^{\mathrm{ad}}\\ \Psi_j^{\mathrm{ad}}\end{pmatrix} = \mathbf{U}\begin{pmatrix}\Psi_k^{\mathrm{loc}}\\ \Psi_{k+1}^{\mathrm{loc}}\end{pmatrix} \tag{6}$$

$$\mathbf{U} = \begin{pmatrix}\cos(\eta) & -\sin(\eta)\\ \sin(\eta) & \cos(\eta)\end{pmatrix} \tag{7}$$

The *POS* values of Ψ_k^{loc} and $\Psi_{k+1}^{\mathrm{loc}}$ are *k* and *k*+1, respectively, by definition. The values for the adiabatic states (POS^i, POS^j) are obtained by the transformation

$$\begin{pmatrix}POS^i & POS^{ij}\\ POS^{ij} & POS^j\end{pmatrix} = \mathbf{U}^{-1}\begin{pmatrix}k & 0\\ 0 & \mathrm{k}+1\end{pmatrix}\mathbf{U} \tag{8}$$

which can be explicitly rewritten as

$$2k + 1 - POS^i = POS^j = k + \cos^2(\eta) \tag{9}$$

To apply this model for extracting diabatic couplings from the quantum chemical computations, it was first necessary to identify pairs of states Ψ_i^{ad} and Ψ_j^{ad}, which approximately satisfied the underlying assumption of the model. The condition for this was that the left side of equation Eq. (9) was satisfied for these states, as well as that these states had similar *PR* and *CT* values and orbital contributions to the electronic transition. Then Eq. (9) was applied to compute η and subsequently **U**. Then, the diabatic localized Hamiltonian $\mathbf{H}^{\mathrm{loc}}$ was computed by transforming the diagonal matrix containing the adiabatic energies of the two states (E_i, E_j)

$$\mathbf{H}^{\mathrm{loc}} = \mathbf{U}\begin{pmatrix}E_i & 0\\ 0 & E_j\end{pmatrix}\mathbf{U}^{-1}. \tag{10}$$

The excitonic coupling between the localized states H_{if} (i.e. the off-diagonal element of $\mathbf{H}^{\mathrm{loc}}$) is explicitely given as

$$H_{\mathrm{if}} = \cos(\eta)\sin(\eta)\left(E_i - E_j\right) \tag{11}$$

Molecular visualization and graphical analysis were primarily performed with the PyMOL,[58] VMD,[59] and Jmol[60] packages.

3. Results and discussion

3.1 poly-(dAdT)·(dAdT) duplexes

Figure 2 shows the computed spectra (solid lines) of AT and TATA stacked complexes in vacuo. In both cases a broad peak around 5.5 eV is found in the spectrum. The maximum is located at somewhat higher energies in the tetramer. For comparison, also the total density of transitions (dotted lines), i.e. the spectrum without weighting by the oscillator strengths, is shown to highlight the dark states. This second distribution is significantly broader, which means that there are hidden dark states both at lower and higher energies than the main contributions of the bright states. States with significant charge transfer character ($CT > 0.5$) only play a minor role in the absorption spectrum, which means that they cannot be directly excited by UV light. In the DOT charge transfer states are present in the range of 6.0 – 6.5 eV and a more detailed analysis shows that in the tetramer about 13% of the states considered exhibit $CT > 0.5$. However, these states are lying at energies above the first absorption maximum. In the dimer spectrum almost no delocalized states ($PR > 1.5$) are present. In the tetramer spectrum these account also for only about 15% of the states. However, due to their larger oscillator strengths (i.e. the intensity of the $PR > 1.5$ contribution to the spectrum is significantly larger than the respective contribution to the density of transitions) they are responsible for almost half of the intensity at the absorption maximum. Larger oscillator strengths were to be expected, considering that according to Förster theory brighter states should interact stronger and should therefore also yield more delocalized excitons. At the red and blue edges of the spectrum, the relative importance of delocalized states is significantly diminished. Furthermore, there are almost no excited states (<1%) with a delocalization over more than two and a half bases ($PR > 2.5$).

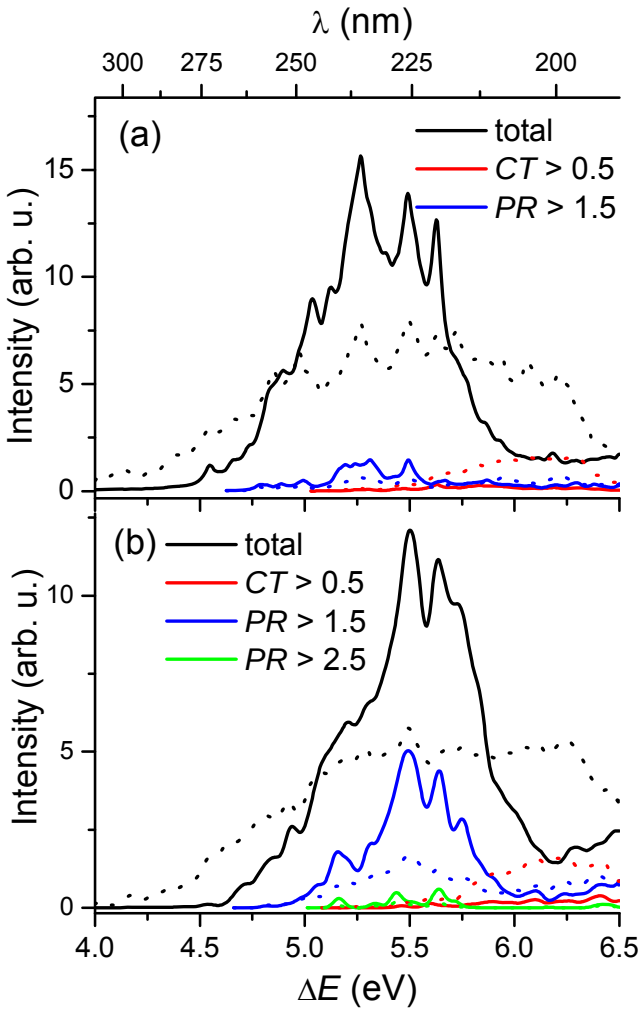

Figure 2. Decomposition of the absorption spectra (solid lines) and densities of transition (dotted lines) of an AT (a) and a TATA (b) nucleobase stack in vacuo.

In Figure 3 the spectra of the AT and the TATA stacks embedded in the poly-(dAdT)·(dAdT) duplex are shown. These spectra are redshifted by ~0.3-0.5 eV with respect to the complexes in vacuo, and again the tetramer spectrum is at somewhat higher energies than that of the dimer. Compared to the DOT shown in Figure 2, there are no low-energy dark states found now. This is probably due to the fact that nπ* transitions are blueshifted by hydrogen bonding and are now located in the energy range of the bright ππ* states. The maximum of the tetramer QM/MM spectrum lies at 5.2 eV (240 nm). This is about 0.5 eV higher than the experimental maximum of the poly-(dAdT)·(dAdT) duplex.[61] In Figure 3 also a second peak in the lower wave length UV range is visible, cf. Ref 61. This difference to the vacuum spectrum (Figure 2) relates to the fact that the high energy area is not completely sampled with the limited number of excited states considered here. Due to a different state ordering, apparently more high energy bright states are included in the QM/MM simulation, whereas in vacuo more dark states are present. To support this hypothesis, we have verified that the second peak emerges also in vacuo if more states are considered. However, since we wanted to concentrate on the first absorption band, the full sampling of the second band, which would also involve substantially higher computational cost, is not further pursued. Charge transfer states play a secondary role even in the spectra including the DNA

environment; they have lower oscillator strengths and are located at higher energies relative to the first absorption peak. In DNA delocalized states play a somewhat more important role as compared to the spectra in-vacuo. About 30% of the states show PR > 1.5 and because of their higher oscillator strengths, these amount to more than half of the intensity at the absorption maximum of the tetramer. In most cases considered, they extend over neighboring adenine and thymine bases, rather than second neighboring bases of the same kind. In other words: introducing a thymine spacer almost completely decouples the two adenine bases.[62] There are almost no states with $PR > 2.5$ (about 3%), which means that the majority of the excited states are at most delocalized between two bases. Figure 4 shows the distribution of the *CT* values in the spectrum of the embedded TATA stack. About 60% of the excited states considered exhibit $CT < 0.1$. Then, states with a strong mixing between locally excited and charge transfer contributions follow (i.e. the *CT* value is neither close to zero corresponding to only locally excited configurations nor close to one indicating a pure CT state), and about 15% of the states exhibit significant charge separation ($CT > 0.5$). It should be noted that a simple Frenkel exciton model, neglecting charge transfer interactions, may be insufficient to describe these last 40% of the states.

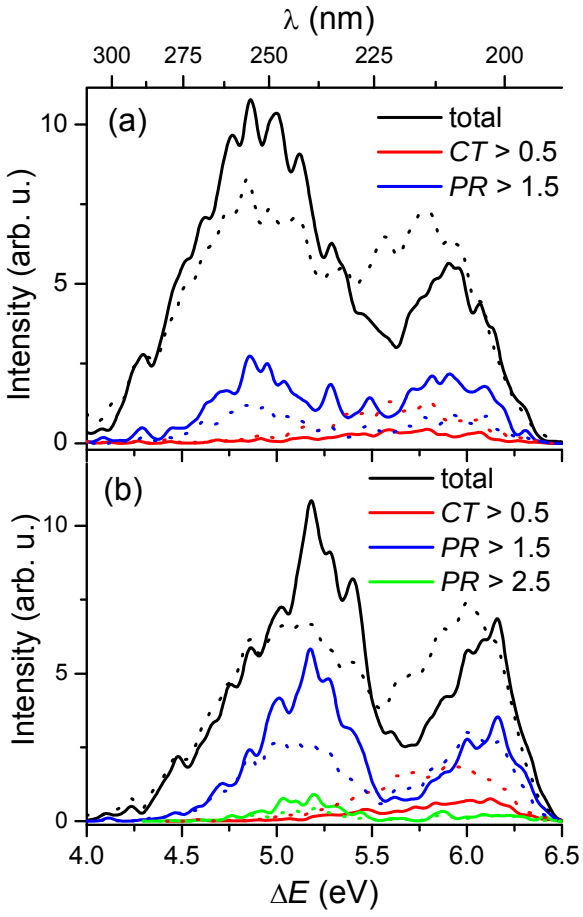

Figure 3. Decomposition of the QM/MM absorption spectra (solid lines) and densities of transition (dotted lines) of an AT (a) and a TATA (b) base stack embedded in a $(dAdT)_6 \cdot (dAdT)_6$ duplex.

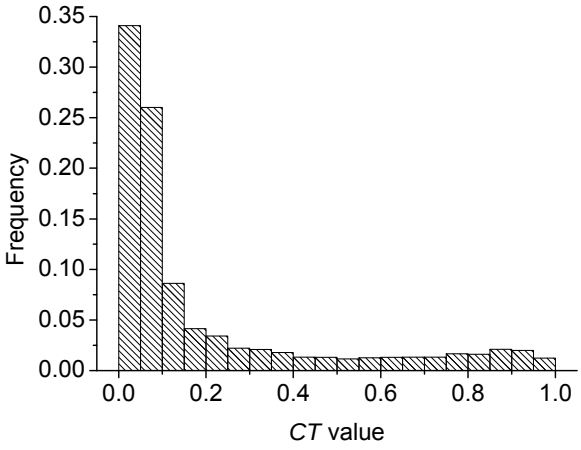

Figure 4. Distribution of *CT* values in the absorption spectrum of a TATA base stack embedded in a $(dAdT)_6 \cdot (dAdT)_6$ duplex.

To get more insight into the character of the excited states, one representative configuration of the embedded TATA stack was analyzed in more detail (Table 1). Aside from the

excitation energies and oscillator strengths, the descriptors for position (*POS*), excitonic participation ratio (*PR*), and charge transfer character (*CT*) are given. The type of the excited state is assigned as well. The lowest excited state (S_1) at this configuration is an nπ* state of the thymine at position three (T3). S_2 and S_3 amount to a pair of excitonic states formed of the ππ* state of the other thymine residue (T1) and the ππ* (the bright L_a) state of the adjacent adenine (A2). They are separated by a gap of 0.154 eV. Using Eq. (11), this amounts to an inter-chromophore coupling of about 0.065 eV. This large value is consistent with the substantial oscillator strength of S_3 (0.242). The ππ* (L_b) state of A2 remains fairly isolated at S_7. The two ππ* states of A4 couple with the ππ* state of T3 to form three delocalized excitonic states: S_4, S_5 and S_9. Above 5.5 eV, two charge transfer states are present: S_{11} ($A2^+T3^-$) and S_{13} ($A4^+T3^-$). Aside from the states mentioned, there is a large number of localized nπ* states. Furthermore, S_{18} and S_{19} form a pair of delocalized nπ* states, probably due to an accidental degeneracy, separated by 0.020 eV (with a coupling of about 0.009 eV). To estimate the effects of environment, the excited states of the isolated molecule at the same geometry were computed as well. Electronic states computed in DNA environment and in vacuo were related to each other based on the analysis of the electronic wavefunction, and wherever this was possible the energy of the corresponding isolated state ($\Delta E_{SV,isol}$) is given as well in Table 1. It can be observed that the DNA environment significantly destabilizes all the nπ* states (by about 0.4 eV). This strong shift is due to hydrogen bonding interactions and agrees well with previous experience.[63-65] The ππ* states seem largely unaffected by environmental effects and no clear trend is present here. The vertical excitation energies of the charge transfer states are almost not affected here. However, it should be noted that they might be somewhat stabilized by an environmental model including the electronic response of the environment to the excitation, cf. Refs 21,25.

Table 1. Excitation energies (ΔE, eV), oscillator strengths (*f*), statistical descriptors, and type assignments at the ADC(2)/SV level for the first 20 excited states of a TATA base stack (designated T1, A2, T3, A4) embedded in a $(dAdT)_6 \cdot (dAdT)_6$ duplex solvated in water computed at one selected geometry.

State	ΔE_{SV}	*f*	*POS*	*PR*	*CT*	type	$\Delta E_{SV,isol}$[a]	ΔE_{SVP}[b]
S_1	4.679	0.001	2.99	1.04	0.03	n(T3)-π*(T3)	4.261	4.453
S_2	4.833	0.052	1.79	**1.63**	0.02	π(A2)-π*(A2) / π(T1)-π*(T1)	4.823[c]	4.604
S_3	4.986	**0.242**	1.29	**1.63**	0.02	π(T1)-π*(T1) / π(A2)-π*(A2)	5.242[c]	4.768
S_4	5.039	0.027	3.31	**2.35**	0.07	π(T3)-π*(T3) / π(A4)-π*(A4)	5.161[c]	4.824
S_5	5.095	0.029	3.69	**1.63**	0.04	π(A4)-π*(A4) / π(T3)-π*(T3)	5.044[c]	4.935
S_6	5.121	0.017	1.06	1.13	0.02	n(T1)-π*(T1)	4.718	4.925
S_7	5.150	0.033	2.11	1.42	0.05	π(A2)-π*(A2)	5.112[c]	4.981[c]
S_8	5.193	0.002	2.04	1.06	0.03	n(A2)-π*(A2)	4.752	5.118
S_9	5.265	**0.283**	3.73	**1.60**	0.04	π(A4)-π*(A4) / π(T3)-π*(T3)	5.317[c]	5.012[c]
S_{10}	5.330	0.029	3.98	1.04	0.02	n(A4)-π*(A4)	4.779	5.230
S_{11}	5.559	0.005	2.52	1.08	**0.95**	π(A2)-π*(T3)	5.581	5.208
S_{12}	5.583	0.000	3.00	1.04	0.03	n(T3)-π*(T3)	5.239	5.248
S_{13}	5.700	0.014	3.39	1.26	**0.81**	π(A4)-π*(T3)	5.665	5.388
S_{14}	5.937	0.010	1.04	1.06	0.06	n(T1)-π*(T1)	5.742	5.644
S_{15}	6.127	0.021	3.06	1.21	0.17	n(T3)-π*(T3)		5.742
S_{16}	6.175	0.022	4.00	1.01	0.01	n(A4)-π*(A4)	5.671	
S_{17}	6.214	0.012	1.95	1.16	0.14	n(A2)-π*(A2)	5.898	
S_{18}	6.248	0.005	2.33	**1.83**	0.08	n(A2)-π*(A2) / n(T3)-π*(T3)	5.812[c]	
S_{19}	6.267	0.021	2.69	**2.01**	0.10	n(T3)-π*(T3) / n(A2)-π*(A2)		
S_{20}	6.332	**0.150**	1.52	**1.76**	0.17	π(T1)-π*(T1) / π(A_2)-π*(T1)		

[a] ADC(2)/SV excitation energy of the corresponding state in the isolated tetramer of the same geometry.

[b] QM/MM excitation energy of the corresponding state at the ADC(2)/SVP level.

[c] Only an approximate assignment was possible.

Next, the reasons for spectral broadening in the poly-(dAdT)·(dAdT) duplex are examined. In particular the contributions of environmental fluctuations and intra- and intermolecular motions will be analyzed, and the effect of quantum mechanical zero-point vibrations will be highlighted. Initially, the first absorption band of a stack in vacuo with fixed intermolecular degrees of freedom (Figure 2) and the QM/MM simulation, where also interbase motions are considered (Figure 3) are compared. It can be seen that aside from the general overall shift, the peak shapes are very similar. This already suggests that intramolecular motions are the decisive factor in spectral broadening, whereas both interbase motions and environmental motions play only a minor role in this context. To get a more detailed insight into this phenomenon, a spectrum of AT in DNA with frozen intramolecular degrees of freedom was

computed (Figure 5 (a)). This was achieved by replacing the adenine and thymine fragments of the QM part in each MD snapshot with the ground state equilibrium geometries of the adenine and thymine molecules. For each of these structures the electronic excitations were computed. In this way the computed spectrum included solvent and backbone rearrangements, as well as relative base-base movements, but no intramolecular motions of the bases. The resulting spectrum looks completely different as compared to the full simulation (Figure 3 (a)). The broad peak is now split up into three well separated components, corresponding to the adenine $\pi\pi^*$ (L_b), thymine $\pi\pi^*$, and adenine $\pi\pi^*$ (L_a) states. The spectral broadening for these peaks is on the order of only about 0.1 eV. Next we examined the result obtained when only classical contributions to intramolecular motions are considered, i.e. the calculation of electronic excitations is directly performed at the configuration of the MD snapshot without considering the quantum mechanical zero point vibrations (Figure 5 (b)). In this case the state energies overlap again, forming one broad peak. However, the result is significantly different from the full simulation (Figure 3 (a)). The peak is blueshifted by about 0.5 eV, and additionally, its shape is completely different with a somewhat narrower peak and a broad plateau. In summary, we can conclude that intramolecular motions, resulting from quantum mechanical zero-point vibrations, are the dominant factor in determining the spectral shape, which is in line with the experimental observation that the spectrum of the duplex is very similar to the sum of its constituents.[61] These vibrations should be active also after UV absorption, and the strong coupling to the excited states could lead to sub-picosecond excitation energy transfer between the bases as suggested from experimental investigations.[11,15]

QM/MM excitation energies were also computed at the ADC(2) level using the SVP basis containing polarization functions. Respective ΔE_{SVP} values are given in the last column of Table 1. There is a general decrease of about 0.2 eV found for the SVP results in comparison to the SV data. But aside from that, the results are consistent, and in particular the state ordering is almost identical. Additionally, the QM/MM spectrum of the embedded AT stack (Figure 3, (a)) was recomputed at the ADC(2)/SVP level (Figure 6). The two figures agree well in all main features (peak positions, peak heights, and distribution into the different components); it is only found that the SVP spectrum is shifted to lower energies by about 0.1 or 0.2 eV as observed for the calculation reported in Table 1. In summary it can be concluded that basis set effects should not play a large role in the general interpretation of the spectra except for the fact that excitation energies are overestimated by about 0.2 eV as compared to SVP and probably somewhat more as compared to the complete basis set limit. In this sense the shift of 0.5 eV with respect to the experimental absorption spectrum[61] is probably to a large part due to basis set effects.

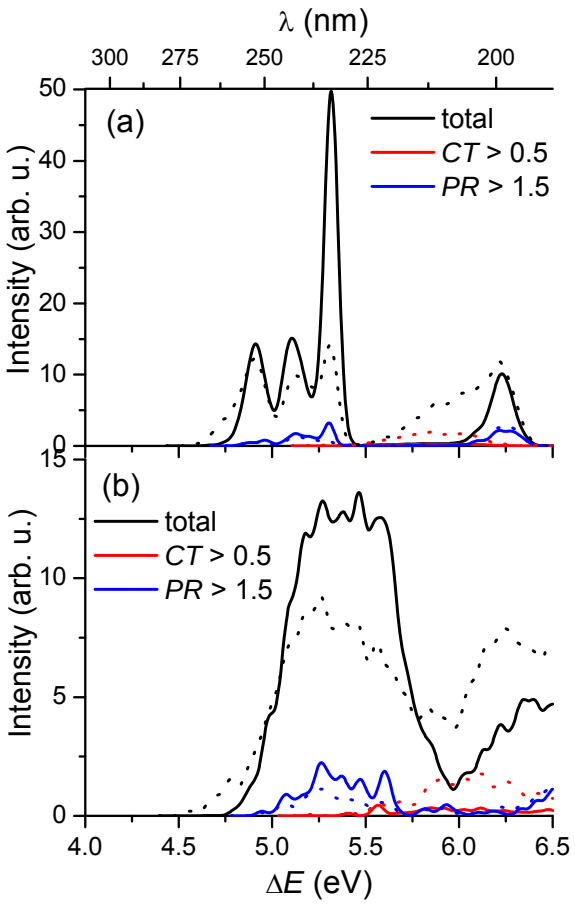

Figure 5. Decomposition of the QM/MM absorption spectra (solid lines) and densities of transition (dotted lines) of an AT base stack embedded in a $(dAdT)_6 \cdot (dAdT)_6$ duplex with frozen intramolecular coordinates (a) and only consideration of the classical contributions to intramolecular motions (b).

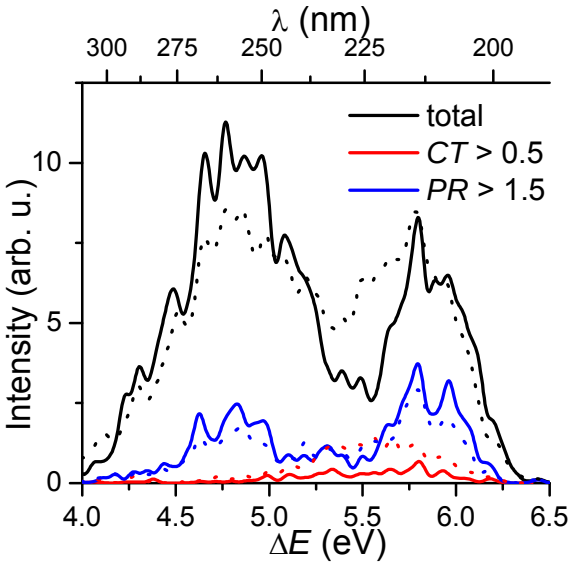

Figure 6. Decomposition of the QM/MM absorption spectrum (solid lines) and density of transition (dotted lines) of an AT base stack embedded in a $(dAdT)_6 \cdot (dAdT)_6$ duplex, computed at the ADC(2)/SVP level.

3.2 poly-(dGdC)·(dGdC) duplexes

The spectra for the GC and the CGCG stacks in vacuo are shown in Figure 7. Compared to those for the adenine-thymine stacks, they are significantly broader. However, the decomposition of the spectra into their different contributions is similar to the corresponding ones of the adenine-thymine case. Charge transfer states ($CT > 0.5$) again play only a minor role (10% in the tetramer) and are located at higher energies. Just as in the TATA case only a small fraction of the excited states are delocalized, e.g. in the tetramer only about 13% of the excited states considered show $PR > 1.5$. Again, these have oscillator strengths somewhat higher than average, which can be seen from the fact that the spectrum lies above the normalized DOT, in accordance with Förster theory. However, as opposed to the TATA case the enhancement is not as strong and only about a third of the intensity at the absorption maximum is due to delocalized states.

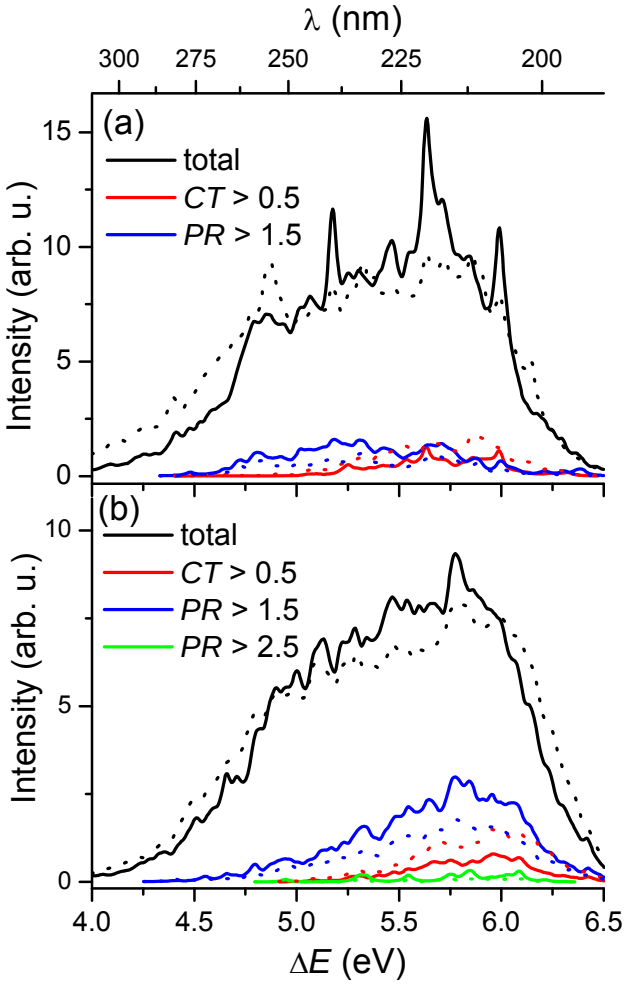

Figure 7. Decomposition of the absorption spectra (solid lines) and densities of transition (dotted lines) of a GC (a) and a CGCG (b) base stack in vacuo.

After embedding GC and CGCG, respectively, into the hydrated duplex, the shape of the absorption spectra is somewhat altered (Figure 8) and the spectra exhibit more pronounced peaks at the center of the band. In the tetramer spectrum the absorption maximum is located at about 5.4 eV (230 nm), which is ~0.5 eV above the experimental value.[14] Charge transfer states play only a minor role and are located in the high energy part of the spectrum. States delocalized over two bases are more pronounced as compared to the spectra in vacuo: in the tetramer 37% of the excited states show PR > 1.5 (as opposed to 13% in vacuo). They peak at the absorption maximum, where they make up about half of the intensity. Again, there are almost no states (only about 4%) with three bases participating (*PR* > 2.5). At the red edge of the spectrum, the states are mostly localized on one base. The distribution of *CT* values of the embedded tetramer is presented in Figure 9. About 50% of the states show Frenkel excitonic character (*CT* < 0.1) and there are about 12% true charge transfer states (*CT* > 0.5).

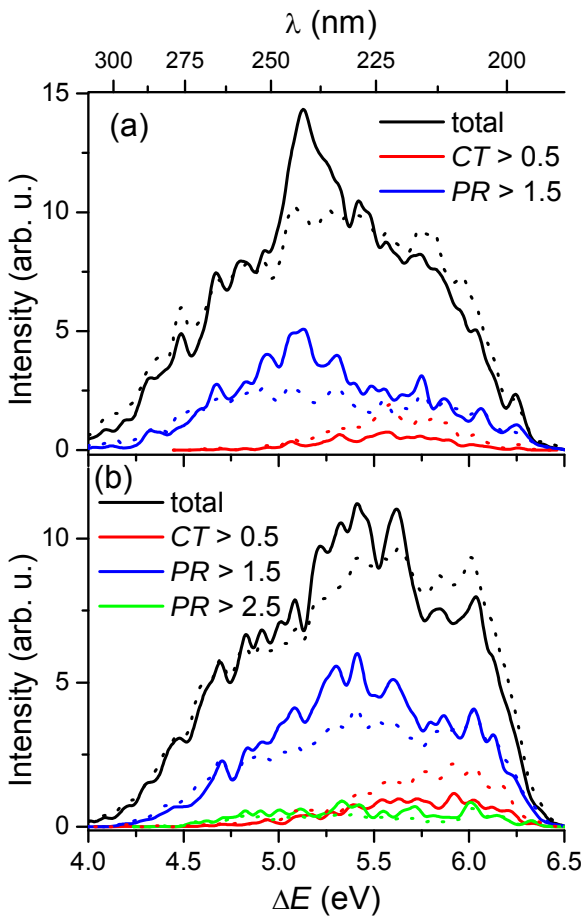

Figure 8. Decomposition of the QM/MM absorption spectra (solid lines) and densities of transition (dotted lines) of an GC (a) and a CGCG (b) base stack embedded in a $(dGdC)_6 \cdot (dGdC)_6$ duplex.

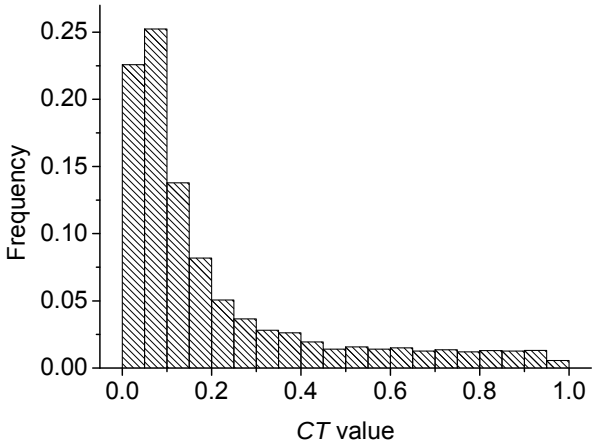

Figure 9. Distribution of *CT* values in the absorption spectrum of a CGCG base stack stack embedded in a $(dGdC)_6 \cdot (dGdC)_6$ duplex.

A detailed analysis of the excited states at one representative configuration of the embedded CGCG stack is shown in Table 2. The four lowest excited states are formed from ππ* states on the four bases. The S_1 and S_2 excitations are located on the neighboring guanine G4 and cytosine C3 residues, respectively. S_3 and S_4 form a resonant pair on C1 and G2 separated by a gap of 0.072 eV, which according to Eq. (11) corresponds to a coupling of about 0.030 eV. The S_5 and S_{10} states are nπ* states localized on the cytosine residues. S_6, S_7, S_9, S_{13} form a set of four localized ππ* states on the four bases. The lowest lying charge transfer state (S_8), in the direction from G2 to C3, is located at an excitation energy of 5.284 eV. S_{11} and S_{12} comprise a set of weakly coupled (< 0.001 eV) nπ* states, which are delocalized due to the fact that their site energies are by chance nearly degenerate. Two localized states follow. S_{15} and S_{16} again derive from a pair of nearly degenerate nπ* states, which are somewhat more strongly coupled (0.007 eV). S_{17} is the next charge transfer state, followed by three localized states. An excited state calculation was performed for the same geometry in vacuo as well. A direct relation to the states computed at QM/MM level was not always possible because different mixings between configurations were obtained. Wherever possible, this value is given in Table 2 ($\Delta E_{SV,isol}$). Just like for TATA, it can be observed that the nπ* states are strongly destabilized by solvation and hydrogen bonding (by about 0.5 eV). In contrast, the ππ* states deviate in both directions and respective shifts are not quite as pronounced. The

charge transfer state (S_8) was found at about the same energy in the isolated complex. To test for basis set effects, the QM/MM energies at the ADC(2)/SVP (ΔE_{SVP}) were computed (Table 2). Again, there is a general quite consistent decrease of about 0.2 eV found for ΔE_{SVP} (last column) as opposed to those of the SV results (second column).

Table 2. Excitation energies (ΔE, eV), oscillator strengths (f), statistical descriptors, and type assignments at the ADC(2)/SV level for the first 20 excited states of a CGCG base stack (designated C1, G2, C3, G4) embedded in a $(dGdC)_6 \cdot (dGdC)_6$ duplex solvated in water computed at one selected geometry.

State	ΔE_{SV}	f	*POS*	*PR*	*CT*	type	$\Delta E_{SV,isol}$[a]	ΔE_{SVP}[b]
S_1	4.619	**0.135**	3.99	1.02	0.02	π(G4)-π*(G4)	4.579	4.479
S_2	4.719	0.019	2.96	1.14	0.12	π(C3)-π*(C3)	4.421	4.520
S_3	4.804	0.003	1.23	**1.54**	0.07	π(C1)-π*(C1) / π(G2)-π*(G2)	4.510[c]	4.642
S_4	4.876	**0.121**	1.81	**1.68**	0.06	π(G2)-π*(G2) / π(C1)-π*(C1)	4.913[c]	4.703
S_5	4.971	0.020	3.01	1.13	0.09	n(C3)-π*(C3)		4.781
S_6	5.167	**0.227**	3.92	1.17	0.03	π(G4)-π*(G4)	5.191[c]	4.932
S_7	5.269	**0.178**	1.06	1.11	0.07	π(C1)-π*(C1)		5.051
S_8	5.284	0.050	2.56	1.23	**0.87**	π(G2)-π*(C3)	5.343	4.980
S_9	5.358	0.080	3.04	1.24	0.14	π(C3)-π*(C3)		5.078
S_{10}	5.475	0.008	1.05	1.08	0.05	n(C1)-π*(C1)	5.107	5.246
S_{11}	5.553	0.005	3.69	**1.68**	0.02	n(G4)-π*(G4) / n(C3)-π*(C3)	4.830[c]	5.350[c]
S_{12}	5.554	0.014	3.20	**1.61**	0.04	n(C3)-π*(C3) / n(G4)-π*(G4)		5.288[c]
S_{13}	5.558	**0.184**	2.09	1.47	0.08	π(G2)-π*(G2)	5.514[c]	5.293
S_{14}	5.661	0.029	2.98	1.12	0.07	n(C3)-π*(C3)	5.070	5.455
S_{15}	5.676	0.012	1.18	1.41	0.05	n(C1)-π*(C1) / n(G2)-π*(G2)	4.918[c]	5.506
S_{16}	5.693	0.002	1.82	**1.51**	0.07	n(G2)-π*(G2) / n(C1)-π*(C1)	5.185[c]	5.483
S_{17}	5.784	0.002	3.44	1.15	**0.89**	π(G4)-π*(C3)		5.526
S_{18}	5.824	**0.423**	1.10	1.19	0.08	π(C1)-π*(C1)		5.602
S_{19}	5.921	0.073	1.06	1.10	0.08	π(C1)-π*(C1)		5.739
S_{20}	6.025	**0.327**	3.00	1.23	0.13	π(C3)-π*(C3)		

[a] ADC(2)/SV excitation energy of the corresponding state in the isolated tetramer of the same geometry.

[b] QM/MM excitation energy of the corresponding state at the ADC(2)/SVP level.

[c] Only an approximate assignment was possible.

3.3 Excitonic delocalization and charge transfer

A major outcome of our study based on sampling of intra- and intermolecular vibrational modes is that in alternating duplexes excited states are mostly localized between two

neighboring bases. Previous estimates based on experiments and parameterized exciton models range from two or three[12,20,22,23] to six or eight[16,18] monomer units. Our calculations show quite conclusively that the lower end of this range is more realistic. The hypothesis of rather localized states is also in agreement with the observation that excited state lifetimes are nearly independent of the helix conformation and the base-pairing motif in $d(GC)_9 \cdot d(GC)_9$.[66] Evidence for sub picosecond energy transfer, which has been obtained from fluorescence anisotropy studies, was seen as indication for strongly delocalized states.[15] However, the strong coupling between the electronic state energies and intramolecular motions (as seen in Figure 5) indicates that energy transfer is not a purely electronic process but strongly correlated to intramolecular vibrations, which operate on just that ultrafast time scale.

The computation of charge transfer states is a challenge with any computational strategy. Particular problems are the failure of standard TDDFT functionals and the necessity for a high level description of environmental polarization, cf. Ref 29. An initial TDDFT study of poly-dA placed charge transfer states well below the localized and Frenkel excitonic states.[24] However, this behavior was later attributed to the insufficiency of PBE0 in describing charge transfer states, and subsequent TDDFT,[20,25] complete active space perturbation-theory to second order (CASPT2)[17] and RI-CC2[26] studies found charge transfer states at about the same energy as the lowest $\pi\pi^*$ transitions or somewhat higher, in accordance with our current investigations. It is interesting to note that the relative position of the charge transfer states is found to be quite independent of the model used in our calculations (vacuum or QM/MM, dimer or tetramer). Thus, Coulomb effects of the DNA environment and in particular the extra degree of dynamic polarizability, present through the additional bases in the tetramer, does not significantly alter the energy of the charge transfer states. To estimate the magnitude of stabilization of the CT states due to electronic polarization not explicitly included in our force field, one could consider results reported from calculations using a polarizable continuum model (PCM). In linear-response PCM calculations for water and other solvents only small redshifts (0.1-0.2 eV) were obtained.[26] A somewhat larger value was reported when using state-specific PCM in aqueous solution, where an additional stabilization energy of 0.5 eV, resulting from the state-specific solvation, was computed.[21,25] However, for partially charge separated states as they occur in the present investigations (cf. Figure 4 and Figure 9) and considering the fact that the dielectric constant of water is certainly an upper limit for the local dielectric constant in DNA, the actual shift may well be smaller even though a conclusive answer is still to be found. Whereas charge transfer states thus appear to be located at higher energies in the Franck-Condon region, they may well be stabilized in the dynamical processes after photoexcitation, e.g. through interbase motions[67] or solvent reorganization. The strong mixing between Frenkel and CT states, which can be deduced from the fact that there is a wide range of such mixed states ($0.1 < CT < 0.9$ in Figure 4 and Figure 9; and Ref. 21), could provide a direct route from bright states into trapped charge transfer states by dynamical charge separation.[28,67]

4. Conclusions

Extended atomistic simulations of the UV absorption spectrum of $(dAdT)_6 \cdot (dAdT)_6$ and $(dGdC)_6 \cdot (dGdC)_6$ alternating duplexes, respectively, have been performed using a QM/MM scheme with an extended QM part including four stacked nucleobases in the central region of the duplex. As quantum chemical method the RI-ADC(2) method has been chosen which is free of artifacts concerning charge transfer states and is supposed to provide within the possibilities of computational methods available for the relatively large molecular systems

encountered here a balanced description of these states in comparison to locally excited and delocalized excitonic states.

Based on these calculations our main conclusions about the properties of the absorbing states in alternating duplexes are

- In the majority of the cases, the excited states are either localized on one or two nucleobases. The computed distribution of delocalized states is peaking at the absorption maximum.
- In the Franck-Condon region, i.e. the configurational space immediately accessed after UV absorption, charge transfer states are located in the higher energy range of the spectrum somewhat above the major portion of the energy distribution of the bright states.
- There is a significant coupling between locally excited and charge separated states, yielding a large number of states of partial CT character. This could provide a route to dynamical charge separation and excimer formation.
- Spectral broadening leading to one broad peak is largely caused by intramolecular vibrations. In other words: there is a strong electron-phonon coupling between intramolecular vibrations and excited state energies. This suggests that even the first ultrafast processes are coupled to nuclear vibrations and no purely electronic dynamics is present.

Acknowledgment

This work has been supported by the Austrian Science Fund within the framework of the Special Research Program and F41 Vienna Computational Materials Laboratory (ViCoM). Support was also provided by the Robert A. Welch Foundation under Grant No. D-0005. The calculations were performed at the Vienna Scientific Cluster (project nos. 70019 and 70151). F. Plasser is a recipient of a DOC fellowship of the Austrian Academy of Sciences.

References

(1) Pfeifer, G. P.; You, Y. H.; Besaratinia, A. *Mutat. Res., Fundam. Mol. Mech. Mutagen.* **2005**, *571*, 19.

(2) Ullrich, S.; Schultz, T.; Zgierski, M. Z.; Stolow, A. *Phys. Chem. Chem. Phys.* **2004**, *6*, 2796.

(3) Perun, S.; Sobolewski, A. L.; Domcke, W. *J. Am. Chem. Soc.* **2005**, *127*, 6257.

(4) Canuel, C.; Mons, M.; Piuzzi, F.; Tardivel, B.; Dimicoli, I.; Elhanine, M. *J. Chem. Phys.* **2005**, *122*, 074316.

(5) Marian, C. M. *J. Chem. Phys.* **2005**, *122*, 104314.

(6) Merchan, M.; Gonzalez-Luque, R.; Climent, T.; Serrano-Andres, L.; Rodriuguez, E.; Reguero, M.; Pelaez, D. *J. Phys. Chem. B* **2006**, *110*, 26471.

(7) Hudock, H. R.; Levine, B. G.; Thompson, A. L.; Satzger, H.; Townsend, D.; Gador, N.; Ullrich, S.; Stolow, A.; Martinez, T. J. *J. Phys. Chem. A* **2007**, *111*, 8500.

(8) Middleton, C. T.; de La Harpe, K.; Su, C.; Law, Y. K.; Crespo-Hernandez, C. E.; Kohler, B. *Annu. Rev. Phys. Chem.* **2009**, *60*, 217.

(9) Barbatti, M.; Aquino, A. J. A.; Szymczak, J. J.; Nachtigallová, D.; Hobza, P.; Lischka, H. *Proc. Natl. Acad. Sci. U. S. A.* **2010**, *107*, 21453.

(10) Crespo-Hernandez, C.; Cohen, B.; Kohler, B. *Nature* **2005**, *436*, 1141.

(11) Kwok, W. M.; Ma, C. S.; Phillips, D. L. *J. Am. Chem. Soc.* **2006**, *128*, 11894.

(12) Buchvarov, I.; Wang, Q.; Raytchev, M.; Trifonov, A.; Fiebig, T. *Proc. Natl. Acad. Sci. U. S. A.* **2007**, *104*, 4794.

(13) Markovitsi, D.; Gustavsson, T.; Talbot, F. *Photochem. Photobiol. Sci.* **2007**, *6*, 717.

(14) Vaya, I.; Miannay, F.; Gustavsson, T.; Markovitsi, D. *ChemPhysChem* **2010**, *11*, 987.

(15) Onidas, D.; Gustavsson, T.; Lazzarotto, E.; Markovitsi, D. *Phys. Chem. Chem. Phys.* **2007**, *9*, 5143.

(16) Czader, A.; Bittner, E. R. *J. Chem. Phys.* **2008**, *128*, 035101.

(17) Olaso-Gonzalez, G.; Merchan, M.; Serrano-Andres, L. *J. Am. Chem. Soc.* **2009**, *131*, 4368.

(18) Markovitsi, D.; Gustavsson, T.; Banyasz, A. *Mutat. Res., Rev. Mutat. Res.* **2010**, *704*, 21.

(19) Takaya, T.; Su, C.; de La Harpe, K.; Crespo-Hernandez, C.; Kohler, B. *Proc. Natl. Acad. Sci. U. S. A.* **2008**, *105*, 10285.

(20) Lange, A.; Herbert, J. *J. Am. Chem. Soc.* **2009**, *131*, 3913.

(21) Santoro, F.; Barone, V.; Lami, A.; Improta, R. *Phys. Chem. Chem. Phys.* **2010**, *12*, 4934.

(22) Tonzani, S.; Schatz, G. C. *J. Am. Chem. Soc.* **2008**, *130*, 7607.

(23) Emanuele, E.; Zakrzewska, K.; Markovitsi, D.; Lavery, R.; Millie, P. *J. Phys. Chem. B* **2005**, *109*, 16109.

(24) Santoro, F.; Barone, V.; Improta, R. *Proc. Natl. Acad. Sci. U. S. A.* **2007**, *104*, 9931.

(25) Santoro, F.; Barone, V.; Improta, R. *ChemPhysChem* **2008**, *9*, 2531.

(26) Aquino, A. J. A.; Nachtigallova, D.; Hobza, P.; Truhlar, D. G.; Hattig, C.; Lischka, H. *J. Comput. Chem.* **2011**, *32*, 1217.

(27) Emanuele, E.; Markovitsi, D.; Millié, P.; Zakrzewska, K. *ChemPhysChem* **2005**, *6*, 1387.

(28) Bittner, E. R. *J. Photochem. Photobiol., A* **2007**, *190*, 328.

(29) Plasser, F.; Barbatti, M.; Aquino, A. J. A.; Lischka, H. *Theor. Chim. Acta* **2012**, *131*, 1073.

(30) Dreuw, A.; Head-Gordon, M. *J. Am. Chem. Soc.* **2004**, *126*, 4007.

(31) Hieringer, W.; Görling, A. *Chem. Phys. Lett.* **2006**, *419*, 557.

(32) Christiansen, O.; Koch, H.; Jorgensen, P. *Chem. Phys. Lett.* **1995**, *243*, 409.
(33) Trofimov, A. B.; Schirmer, J. *J. Phys. B: At., Mol. Opt. Phys.* **1995**, *28*, 2299.
(34) Hättig, C.; Weigend, F. *J. Chem. Phys.* **2000**, *113*, 5154.
(35) Nachtigallova, D.; Hobza, P.; Ritze, H. *Phys. Chem. Chem. Phys.* **2008**, *10*, 5689.
(36) Kozak, C.; Kistler, K.; Lu, Z.; Matsika, S. *J. Phys. Chem. B* **2010**, *114*, 1674.
(37) Kubar, T.; Elstner, M. *J. Phys. Chem. B* **2008**, *112*, 8788.
(38) Hattig, C. *Advances in Quantum Chemistry, Vol 50* **2005**, *50*, 37.
(39) Ahlrichs, R.; Bär, M.; Häser, M.; Horn, H.; Kölmel, C. *Chem. Phys. Lett.* **1989**, *162*, 165.
(40) Schafer, A.; Horn, H.; Ahlrichs, R. *J. Chem. Phys.* **1992**, *97*, 2571.
(41) Barbatti, M.; Granucci, G.; Persico, M.; Ruckenbauer, M.; Vazdar, M.; Eckert-Maksic, M.; Lischka, H. *J. Photochem. Photobiol., A* **2007**, *190*, 228.
(42) Ruckenbauer, M.; Barbatti, M.; Muller, T.; Lischka, H. *J. Phys. Chem. A* **2010**, *114*, 6757.
(43) Martinez, J. M.; Martinez, L. *J. Comput. Chem.* **2003**, *24*, 819.
(44) Kollman, P. A.; Wang, J. M.; Cieplak, P. *J. Comput. Chem.* **2000**, *21*, 1049.
(45) Ponder, J. W.; Richards, F. M. *J. Comput. Chem.* **1987**, *8*, 1016.
(46) Karney, C. F. F. *J. Mol. Graphics Modell.* **2007**, *25*, 595.
(47) Plasser, F.; Barbatti, M.; Aquino, A. J. A.; Lischka, H. *J. Phys. Chem. A* **2009**, *113*, 8490.
(48) Plasser, F. Dynamics simulation of excited state intramolecular proton transfer (http://othes.univie.ac.at/4414/). Master Thesis, 2009.
(49) Field, M. J.; Bash, P. A.; Karplus, M. *J. Comput. Chem.* **1990**, *11*, 700.
(50) Bakowies, D.; Thiel, W. *J. Phys. Chem.* **1996**, *100*, 10580.
(51) Nicoll, R. M.; Hindle, S. A.; MacKenzie, G.; Hillier, I. H.; Burton, N. A. *Theor. Chem. Acc.* **2001**, *106*, 105.
(52) Barbatti, M.; Granucci, G.; Ruckenbauer, M.; Plasser, F.; Pittner, J.; Persico, M.; Lischka, H. *NEWTON-X: a package for Newtonian dynamics close to the crossing seam* **2011**, www.newtonx.org.
(53) Plasser, F.; Lischka, H. *J. Chem. Theory Comput.*, *submitted for publication*.
(54) Tretiak, S.; Mukamel, S. *Chem. Rev.* **2002**, *102*, 3171.
(55) Luzanov, A. V.; Zhikol, O. A. *Int. J. Quantum Chem.* **2010**, *110*, 902.
(56) Voityuk, A. A.; Rosch, N. *J. Chem. Phys.* **2002**, *117*, 5607.
(57) Plasser, F.; Lischka, H. *J. Chem. Phys.* **2011**, *134*, 034309.
(58) Schrodinger, LLC. The PyMOL Molecular Graphics System, Version 1.1 The PyMOL Molecular Graphics System, Version 1.1, 2008.
(59) Humphrey, W.; Dalke, A.; Schulten, K. *Journal of Molecular Graphics* **1996**, *14*, 33.
(60) Jmol. : an open-source Java viewer for chemical structures in 3D. http://www.jmol.org/.
(61) Markovitsi, D. *Pure Appl. Chem.* **2009**, *81*, 1635.
(62) Nielsen, L. M.; Holm, A. I. S.; Hoffmann, S. V.; Nielsen, S. B. *J. Photochem. Photobiol., A* **2011**, *220*, 1.
(63) Wesolowski, T. A. *J. Am. Chem. Soc.* **2004**, *126*, 11444.
(64) Santoro, F.; Barone, V.; Gustavsson, T.; Improta, R. *J. Am. Chem. Soc.* **2006**, *128*, 16312.
(65) Szymczak, J. J.; Muller, T.; Lischka, H. *Chem. Phys.* **2010**, *375*, 110.
(66) de La Harpe, K.; Crespo-Hernandez, C. E.; Kohler, B. *ChemPhysChem* **2009**, *10*, 1421.
(67) Starikov, E. B.; Cuniberti, G.; Tanaka, S. *J. Phys. Chem. B* **2009**, *113*, 10428.

Chapter 4

Conclusions

This study was concerned with the quantum mechanical simulation of electronic defects in DNA. Special challenges in the context of the chosen topic were complex open-shell electronic wavefunctions, non-adiabatic interactions between electronic and nuclear degrees of freedom, and the description of environmental effects. Both, method development targeting these points and applied simulations were performed.

Non-adiabatic effects can usually be treated efficiently by the surface hopping approach. However, it was observed that the standard approach of considering non-adiabatic coupling vectors fails in the case of weakly interacting chromophores owing to highly peaked interactions. To overcome this problem a locally diabatic approach for propagating the electronic wavefunction was implemented and tested, showing impressive stability (Section 3.4). Furthermore, it was highlighted that a simple manual analysis of excited states may not be suitable for systems containing several coupled chromophores. Such an analysis would not only be cumbersome but significant information may be lost if partially delocalized orbitals are not considered correctly. For this purpose an analysis strategy based on the one-particle transition density matrix was devised, tested and applied to a number of interesting molecules (Section 3.6). Furthermore, significant development effort was devoted to electronic energy gradients and non-adiabatic couplings at the SA-MCSCF level (Section 3.2). Finally, connections between direct dynamics of charge transfer and Marcus theory were made as far as both non-adiabatic effects

(Section 3.3) and the description of the solvent were concerned (Section 3.5) and good agreement was found.

Based on the method development and evaluation described above, larger systems of immediate interest were considered. First, excimer formation in the π-stacked naphthalene dimer was examined at the ADC(2) level (Section 3.6). It was observed that the strong stabilization of the excimer goes along with mixing between locally excited and CT configurations, ultimately leading to a homogeneous excited state extended over the whole system. This suggests that excimer formation is not induced either by pure excitonic or CT interactions but by a coherent interaction, which might even be associated with chemical bonding. In this context it is of special interest, whether these considerations are also relevant for π-stacked DNA bases and whether they may even shed new light on excimer states or on photoproduct formation. As a second system the hydrogen bonded 2-pyridone dimer, a model for hydrogen bonded DNA base pairs, was considered and surface hopping dynamics at the TDDFT/BHLYP level were performed (Section 3.4). In this case an interesting interplay between energy transfer and a possible proton-coupled electron transfer (PCET) were observed. In the latter case the importance of non-adiabatic effects related to the electron transfer could be highlighted, reducing the PCET efficiency as compared to the simple adiabatic picture. Finally, realistic simulations of the UV absorption spectrum of alternating DNA duplexes were performed, using a QM/MM methodology with extensive sampling of intra- and intermolecular coordinates (Section 3.7). These simulations gave new insight into questions that were discussed intensively in literature, with our main results about the UV absorbing excited states being: they are rather localized, CT states are high in energy, but these may couple to the locally excited states, and spectral broadening is induced mostly by intramolecular vibrations.

Acknowledgements

First, I would like to thank my supervisor Prof. Hans Lischka who provided me with enough guidance but also some freedom to complete this work in the present form. In spite of being in foreign countries for the most part of my thesis, he was always easy to reach and happy to discuss the different topics.

With respect to the work on COLUMBUS I would like to thank in particular Dr. Thomas Müller. He always quickly replied to my many emails, which helped me through problems and to understand the structure of the COLUMBUS code in detail. Furthermore, I had interesting discussions with Dr. Ron Shepard on my research visit to Argonne National Laboratory. And I want to acknowledge Dr. Bernhard Sellner's work with respect to the installation of the parallel COLUMBUS program. Many interesting calculations performed since were possible thanks to his efforts.

I would like to thank Prof. Maurizio Persico and Dr. Giovanni Granucci for a productive and enjoyable research visit to Pisa. In addition Dr. Jiří Pittner and Dr. Mario Barbatti helped me with the local diabatization project.

Dr. Matthias Ruckenbauer helped me use the tools for QM/MM dynamics, which he developed. Moreover, Dr. Hasan Pašalić helped me use the TINKER program, in particular with respect to free energy perturbation calculations.

Dr. Adélia Aquino provided me with the initial calculations on DNA stacks for spectra generation. Furthermore, I had interesting discussions with Prof. Irene Burghardt regarding the nature of excitons.

I also want to thank Prof. Leticia González for providing an easy transition after she moved to Vienna, for including me in the group and organizing interesting

seminars. I had many discussions and received help for solving everyday problems also from Dr. Jaroslaw Szymczak, Dr. Daniel Tunega, Sebastian Mai, and Leon Freitag.

I want to thank Claire for always being supportive of my interest in research and for not hesitating to move to Germany with me for my next research appointment. Thanks to my family and thanks to everyone who showed interest in the project.

Financial support through a DOC fellowship of the Austrian Academy of Sciences and from the Austrian Science Fund (FWF) within the framework of the Special Research Program and F41 Vienna Computational Materials Laboratory (ViCoM) is gratefully acknowledged.

Bibliography

[1] Pfeifer, G. P.; You, Y. H.; Besaratinia, A. *Mutation Research, Fundamental and Molecular Mechanisms of Mutagenesis*, **2005**, *571*(1-2), 19–31.

[2] Heller, A. *Faraday Discussions*, **2000**, *116*, 1–13.

[3] Middleton, C. T.; de La Harpe, K.; Su, C.; Law, Y. K.; Crespo-Hernandez, C. E.; Kohler, B. *Annual Review of Physical Chemistry*, **2009**, *60*, 217–239.

[4] Markovitsi, D.; Gustavsson, T.; Talbot, F. *Photochemical and Photobiological Sciences*, **2007**, *6*(7), 717–724.

[5] Endres, R.; Cox, D.; Singh, R. *Reviews of Modern Physics*, **2004**, *76*(1), 195–214.

[6] Ullrich, S.; Schultz, T.; Zgierski, M. Z.; Stolow, A. *Physical Chemistry Chemical Physics*, **2004**, *6*, 2796–2801.

[7] Crespo-Hernndez, C. E.; Cohen, B.; Hare, P. M.; Kohler, B. *Chemical Reviews*, **2004**, *104*(4), 1977–2020.

[8] Perun, S.; Sobolewski, A. L.; Domcke, W. *Journal of the American Chemical Society*, **2005**, *127*(17), 6257–6265.

[9] Merchan, M.; Gonzalez-Luque, R.; Climent, T.; Serrano-Andres, L.; Rodriguez, E.; Reguero, M.; Pelaez, D. *The Journal of Physical Chemistry B*, **2006**, *110*(51), 26471–26476.

[10] Hudock, H. R.; Levine, B. G.; Thompson, A. L.; Satzger, H.; Townsend, D.; Gador, N.; Ullrich, S.; Stolow, A.; Martnez, T. J. *The Journal of Physical Chemistry A*, **2007**, *111*(34), 8500–8508.

[11] Barbatti, M.; Aquino, A. J. A.; Szymczak, J. J.; Nachtigallova, D.; Hobza, P.; Lischka, H. *Proceedings of the National Academy of Sciences, USA*, **2010**, *107*(50), 21453–21458.

[12] Serrano-Andres, L.; Merchan, M. *Journal of Photochemistry and Photobiology C: Photochemistry Reviews*, **2009**, *10*(1), 21 – 32.

[13] Crespo-Hernandez, C.; Cohen, B.; Kohler, B. *Nature*, **2005**, *436*(7054), 1141–1144.

[14] Kwok, W. M.; Ma, C. S.; Phillips, D. L. *Journal of the American Chemical Society*, **2006**, *128*(36), 11894–11905.

[15] Buchvarov, I.; Wang, Q.; Raytchev, M.; Trifonov, A.; Fiebig, T. *Proceedings of the National Academy of Sciences, USA*, **2007**, *104*(12), 4794–4797.

[16] Vaya, I.; Miannay, F.; Gustavsson, T.; Markovitsi, D. *ChemPhysChem*, **2010**, *11*(5), 987–989.

[17] Santoro, F.; Barone, V.; Lami, A.; Improta, R. *Physical Chemistry Chemical Physics*, **2010**, *12*(19), 4934–4948.

[18] Jortner, J.; Bixon, M.; Langenbacher, T.; Michel-Beyerle, M. E. *Proceedings of the National Academy, USA*, **1998**, *95*(22), 12759–12765.

[19] Giese, B.; Amaudrut, J.; Kohler, A.; Spormann, M.; Wessely, S. *Nature*, **2001**, *412*(6844), 318–320.

[20] Barnett, R. N.; Cleveland, C. L.; Joy, A.; Landman, U.; Schuster, G. B. *Science*, **2001**, *294*(5542), 567–571.

[21] O'Neil, M. A.; Barton, J. K. *Journal of the American Chemical Society*, **2004**, *126*(37), 11471–11483.

[22] Kubar, T.; Elstner, M. *Journal of Physical Chemistry B*, **2008**, *112*(29), 8788–8798.

[23] Kravec, S. M.; Kinz-Thompson, C. D.; Conwell, E. M. *The Journal of Physical Chemistry B*, **2011**, *115*(19), 6166–6171.

[24] Kumar, A.; Sevilla, M. D. *The Journal of Physical Chemistry B*, **2011**, *115*(17), 4990–5000.

[25] Wu, J.; Walker, V. E. J.; Boyd, R. J. *The Journal of Physical Chemistry B*, **2011**, *115*(12), 3136–3145.

[26] Improta, R.; Barone, V. *Angewandte Chemie International Edition*, **2011**, *50*(50), 12016–12019.

[27] Sobolewski, A. L.; Domcke, W.; Hattig, C. *Proceedings of the National Academy of Sciences, USA*, **2005**, *102*(50), 17903–17906.

[28] Worth, G. A.; Cederbaum, L. S. *Annual Review of Physical Chemistry*, **2004**, *55*, 127–158.

[29] Szabo, A.; Ostlund, N. S. *Modern Quantum Chemistry*. MacGraw-Hill, Inc., 1989.

[30] Knowles, P.; Schütz, M.; Werner, H.-J. in *Modern Methods and Algorithms of Quantum Chemistry*, Grotendorst, J., Ed. Jülich Supercomputing Centre, 2000.

[31] Shepard, R. in *Ab Initio Methods in Quantum Chemistry II*, Lawley, K. P., Ed., pp 1–62. Wiley, 1987.

[32] Luzanov, A. V.; Sukhorukov, A. A.; Umanskii, V. E. *Theoretical and Experimental Chemistry*, **1976**, *10*(4), 354–361.

[33] Martin, R. L. *Journal of Chemical Physics*, **2003**, *118*(11), 4775–4777.

[34] Mayer, I. *Chemical Physics Letters*, **2007**, *443*(4-6), 420–425.

[35] Hohenberg, P.; Kohn, W. *Physical Review B*, **1964**, *136*(3B), 864.

[36] Shepard, R. *International Journal of Quantum Chemistry*, **1987**, *31*(1), 33–44.

[37] Hättig, C. in *Multiscale Simulation Methods in Molecular Sciences, Lecture Notes*, Grotendorst, J.; Attig, A.; Bügel, S.; Marx, D., Eds. Jülich Supercomputing Centre, 2009.

[38] Szalay, P. G.; Bartlett, R. J. *The Journal of Chemical Physics*, **1995**, *103*(9), 3600–3612.

[39] Schmidt, M. W.; Gordon, M. S. *Annual Review of Physical Chemistry*, **1998**.

[40] Lischka, H.; Dallos, M.; Szalay, P. G.; Yarkony, D. R.; Shepard, R. *Journal of Chemical Physics*, **2004**, *120*(16), 7322–7329.

[41] Lischka, H.; Shepard, R.; Brown, F. B.; Shavitt, I. *International Journal of Quantum Chemistry*, **1981**, *15*, 91–100.

[42] Werner, H.-J. in *Ab Initio Methods in Quantum Chemistry II*, Lawley, K. P., Ed., pp 63–200. Wiley, 1987.

[43] Shavitt, I. in *Lecture Notes in Chemistry*, pp 51–99. 1981.

[44] Muller, T. *Journal of Physical Chemistry A*, **2009**, *113*(45), 12729–12740.

[45] Moller, C.; Plesset, M. S. *Phys. Rev.*, **1934**, *46*, 618–622.

[46] Weigend, F.; Haser, M. *Theoretical Chemistry Accounts*, **1997**, *97*(1-4), 331–340.

[47] Stanton, J. F.; Bartlett, R. J. *The Journal of Chemical Physics*, **1993**, *98*(9), 7029–7039.

[48] Christiansen, O.; Koch, H.; Jorgensen, P. *Chemical Physics Letters*, **1995**, *243*(5-6), 409–418.

[49] Hattig, C.; Weigend, F. *Journal of Chemical Physics*, **2000**, *113*(13), 5154–5161.

[50] Trofimov, A. B.; Schirmer, J. *Journal of Physics B*, **1995**, *28*(12), 2299–2324.

[51] Hattig, C. *Advances in Quantum Chemistry*, **2005**, *50*, 37–60.

[52] Parr, R. G.; Yang, W. *Density-Functional Theory of Atoms and Molecules*. Oxford University Press, 1989.

[53] Kohn, W.; Sham, L. J. *Physical Review*, **1965**, *140*(4A), 1133.

[54] Zeller, R. in *Multiscale Simulation Methods in Molecular Sciences, Lecture Notes*, Grotendorst, J.; Attig, A.; Bügel, S.; Marx, D., Eds. Jülich Supercomputing Centre, 2009.

[55] Perdew, J.; Burke, K.; Ernzerhof, M. *Physical Review Letters*, **1996**, *77*(18), 3865–3868.

[56] Lee, C.; Yang, W.; Parr, R. G. *Physical Review B*, **1988**, *37*, 785–789.

[57] Becke, A. D. *Journal of Chemical Physics*, **1993**, *98*(2), 1372–1377.

[58] Casida, M. in *Recent advances in density functional methods, Part I*, Chong, D., Ed., pp 155–192. World Scientific Singapore, 1995.

[59] Dreuw, A.; Head-Gordon, M. *Journal of the American Chemical Society*, **2004**, *126*, 4007–4016.

[60] Slavicek, P.; Martinez, T. J. *The Journal of Chemical Physics*, **2006**, *124*(8), 084107–10.

[61] Bakowies, D.; Thiel, W. *The Journal of Physical Chemistry*, **1996**, *100*(25), 10580–10594.

[62] Ruckenbauer, M.; Barbatti, M.; Muller, T.; Lischka, H. *The Journal of Physical Chemistry A*, **2010**, *114*(25), 6757–6765.

[63] Cossi, M.; Barone, V.; Cammi, R.; Tomasi, J. *Chemical Physics Letters*, **1996**, *255*(46), 327–335.

[64] Klamt, A.; Schuurmann, G. *Journal of the Chemical Society, Perkin Transactions 2*, **1993**, pp 799–805.

[65] Day, P. N.; Jensen, J. H.; Gordon, M. S.; Webb, S. P.; Stevens, W. J.; Krauss, M.; Garmer, D.; Basch, H.; Cohen, D. *Journal of Chemical Physics*, **1996**, *105*(5), 1968–1986.

[66] Wesolowski, T. A.; Warshel, A. *Journal of Physical Chemistry*, **1993**, *97*(30), 8050–8053.

[67] Neugebauer, J. *ChemPhysChem*, **2009**, *10*, 3148–3173.

[68] Verlet, L. *Physical Review*, **1967**, *159*(1), 98.

[69] Van Voorhis, T.; Kowalczyk, T.; Kaduk, B.; Wang, L. P.; Cheng, C. L.; Wu, Q. *Annual Review of Physical Chemistry*, **2010**, *61*, 149–170.

[70] Koppel, H. *Faraday Discuss.*, **2004**, *127*, 35–47.

[71] Granucci, G.; Persico, M.; Toniolo, A. *Journal of Chemical Physics*, **2001**, *114*, 10608–10615.

[72] Dillon, J.; Yarkony, D. R.; Schuurman, M. S. *Journal of Chemical Physics*, **2011**, *134*(4), 044101.

[73] Voityuk, A. A.; Rosch, N. *Journal of Chemical Physics*, **2002**, *117*(12), 5607–5616.

[74] Hsu, C. *Accounts of Chemical Research*, **2009**, *42*(4), 509–518.

[75] Tully, J. C. *Faraday Discussions*, **1998**, *110*, 407–419.

[76] Barbatti, M.; Granucci, G.; Persico, M.; Ruckenbauer, M.; Vazdar, M.; Eckert-Maksic, M.; Lischka, H. *Journal of Photochemistry and Photobiology A-Chemistry*, **2007**, *190*(2-3), 228–240.

[77] Nelson, T.; Fernandez-Alberti, S.; Chernyak, V.; Roitberg, A. E.; Tretiak, S. *Journal of Chemical Physics*, **2012**, *136*(5), 054108.

[78] Ben-Nun, M.; Quenneville, J.; Martinez, T. J. *Journal of Physical Chemistry A*, **2000**, *104*(22), 5161–5175.

[79] Plasser, F.; Barbatti, M.; Aquino, A. J. A.; Lischka, H. *Theoretical Chemistry Accounts*, **2012**, *131*, 1073.

[80] Lischka, H.; Shepard, R.; Shavitt, I.; Pitzer, R. M.; Dallos, M.; Mueller, T.; Szalay, P. G.; Brown, F. B.; Ahlrichs, R.; Boehm, H. J.; Chang, A.; Comeau, D. C.; Gdanitz, R.; Dachsel, H.; Ehrhardt, C.; Ernzerhof, M.; Hoechtl, P.; Irle, S.; Kedziora, G.; Kovar, T.; Parasuk, V.; Pepper, M. J. M.; Scharf, P.; Schiffer, H.; Schindler, M.; Schueler, M.; Seth, M.; Stahlberg, E. A.; Zhao, J.-G.; Yabushita, S.; Zhang, Z.; Barbatti, M.; Matsika, S.;

Schuurmann, M.; Yarkony, D. R.; Brozell, S. R.; Beck, E. V.; Blaudeau, J.-P.; Ruckenbauer, M.; Sellner, B.; Plasser, F.; Szymczak, J. J. Columbus: An ab initio electronic structure program, release 7.0, www.univie.ac.at/columbus, 2011.

[81] Lischka, H.; Shepard, R.; Pitzer, R. M.; Shavitt, I.; Dallos, M.; Mueller, T.; Szalay, P. G.; Seth, M.; Kedziora, G. S.; Yabushita, S.; Zhang, Z. Y. *Physical Chemistry Chemical Physics*, **2001**, *3*(5), 664–673.

[82] Shepard, R.; Lischka, H.; Szalay, P. G.; Kovar, T.; Ernzerhof, M. *Journal of Chemical Physics*, **1992**, *96*(3), 2085–2098.

[83] Lischka, H.; Dallos, M.; Shepard, R. *Molecular Physics*, **2002**, *100*(11), 1647–1658.

[84] Handy, N. C.; Schaefer, H. F. III. *The Journal of Chemical Physics*, **1984**, *81*, 5031–5033.

[85] Helgaker, T.; Jensen, H. J. A.; Jorgensen, P.; Olsen, J.; Ruud, K.; Agren, H.; Andersen, T.; Bak, K. L.; Bakken, B.; Christiansen, O.; Dahle, P.; Dalskov, E. K.; Enevoldsen, T.; Heiberg, H.; Hettema, H.; Jonsson, D.; Kirpekar, S.; Kobayashi, R.; Koch, H.; Mikkelsen, K. V.; Norman, P.; Packer, M. J.; Saue, T.; Taylor, P.; Vahtras, O. Dalton, an ab initio electronic structure program, release 1.0, 1997.

[86] Karlstrom, G.; Lindh, R.; Malmqvist, P.-A.; Roos, B. O.; Ryde, U.; Veryazov, V.; Widmark, P.-O.; Cossi, M.; Schimmelpfennig, B.; Neogrady, P.; Seijo, L. *Computational Materials Science*, **2003**, *28*(2), 222–239.

[87] Plasser, F.; Lischka, H. *Journal of Chemical Physics*, **2011**, *134*(3), 034309.

[88] Plasser, F.; Granucci, G.; Persico, M.; Pittner, J.; Lischka, H. *Journal of Chemical Physics*, **2012**. submitted for publication.

[89] Blumberger, J. *Physical Chemistry Chemical Physics*, **2008**, *10*(37), 5651–5667.

[90] Sanchez, M. L.; Martin, M. E.; Aguilar, M. A.; Olivares del Valle, F. J. *Journal of Computational Chemistry*, **2000**, *21*(9), 705–715.

[91] Galván, I. F.; Sánchez, M. L.; Martín, M. E.; Olivares Del Valle, F. J.; Aguilar, M. A. *Journal of Chemical Physics*, **2003**, *118*, 255–263.

[92] Subotnik, J. E.; Cave, R. J.; Steele, R. P.; Shenvi, N. *The Journal of Chemical Physics*, **2009**, *130*(23), 234102.

[93] Marcus, R. A. *Angewandte Chemie, International Edition in English*, **1993**, *32*(8), 1111–1121.

[94] Kollman, P. *Chemical Reviews*, **1993**, *93*(7), 2395–2417.

[95] Ponder, J. W.; Richards, F. M. *Journal of Computational Chemistry*, **1987**, *8*(7), 1016–1024.

[96] Jorgensen, W. L.; Maxwell, D. S.; Tirado-Rives, J. *Journal of the American Chemical Society*, **1996**, *118*(45), 11225–11236.

[97] Martinez, J. M.; Martinez, L. *Journal of Computational Chemistry*, **2003**, *24*(7), 819–825.

[98] Breneman, C. M.; Wiberg, K. B. *Journal of Computational Chemistry*, **1990**, *11*(3), 361–373.

[99] Tretiak, S.; Mukamel, S. *Chemical Reviews*, **2002**, *102*(9), 3171–3212.

[100] Escudero, D.; Gonzalez, L. *Journal of Chemical Theory and Computation*, **2012**, *8*, 203–213.

[101] Bixner, O.; Lukeš, V.; Mančal, T.; Hauer, J.; Milota, F.; Fischer, M.; Pugliesi, I.; Bradler, M.; Schmid, W.; Riedle, E.; Kauffmann, H. F.; Christensson, N. *The Journal of Chemical Physics*, **2012**, *136*(20), 204503.

[102] Luzanov, A. V.; Zhikol, O. A. *International Journal of Quantum Chemistry*, **2010**, *110*(4), 902–924.

[103] Plasser, F.; Lischka, H. *Journal of Chemical Theory and Computation*, **2012**. accepted for publication, DOI:10.1021/ct300307c.

[104] Plasser, F.; Aquino, A. J. A.; Lischka, H. *Journal of Physical Chemistry A*, **2012**. submitted for publication.

Felix Plasser

Institute for Theoretical Chemistry, University of Vienna
Währingerstr. 17, 1090 Wien
felix.plasser@univie.ac.at
http://homepage.univie.ac.at/felix.plasser/

WORK EXPERIENCE

Graduate student (part time since 2007) 2009-Present
University of Vienna, Institute for Theoretical Chemistry
in the field of Quantum Chemistry and Chemical Dynamics

EDUCATION

PhD, Theoretical Chemistry 2009-2012
University of Vienna, Institute for Theoretical Chemistry
Thesis: "Quantum mechanical simulations of defect dynamics in DNA and model systems" with Prof. Hans Lischka

Master of Science, Chemistry 2007-2009
University of Vienna, Institute for Theoretical Chemistry
Master Thesis: "Dynamics simulation of excited state intramolecular proton transfer" with Prof. Hans Lischka

Bachelor of Science, Chemistry 2004-2008
University of Technology, Vienna

Supplementary courses, Mathematics 2005-2011
Studies of linear algebra, calculus, and discrete mathematics
University of Technology and Vienna University

Secondary School Graduation (Matura) 1995-2003
Schottengynmasium, Vienna
Completed summa cum laude ("ausgezeichneter Erfolg")

INTERNATIONAL RESEARCH EXPERIENCE

Texas Tech University, TX, USA March 2011
One month stay in the group of Prof. Bill Hase

University of Pisa March 2010
Two week visit to Prof. Mauricio Persico regarding non-adiabatic dynamics

Argonne National Laboratory, IL, USA November 2009
One month visit to Dr. Ron Shepard on the topic of MR-CI gradients

Academy of Sciences of the Czech Republic 2009
Several visits to the group of Prof. Pavel Hobza

University of Illinois, Urbana-Champaign July/August 2008
Work on cytosine dynamics with Prof. Todd Martinez

Austrian Research Centers Seibersdorf August 2007
Work on in-silico protein ligand docking with Dr. Thomas Stockner

QUALIFICATIONS AND AWARDS

Two year *DOC fellowship* of the Austrian Academy of Sciences — 2010-2012

Sponsorship by the Austrian *Pro Scientia* program — 2009-2012

TUtheTOP high potential program of the TU Vienna — 2007/2008

Chemistry / Mathematics Olympiad — 2002/2003

- Chemistry: first place in Vienna
- Chemistry: fifth place at the national competition
- Mathematics: fifth place in Vienna

WYSE competition, IL — 2000/2001

- Chemistry: third place at Sectionals
- Mathematics: participation in the State competition

LANGUAGE SKILLS

English: excellent knowledge of English (after a one year stay in the USA and many visits to English speaking countries)

French: three years in secondary school

Latin: six years in secondary school

Publication List

1. Plasser, F.; Lischka, H. "Analysis of excitonic and charge transfer interactions from quantum chemical calculations" *Journal of Chemical Theory and Computation*, **2012**. accepted for publication, DOI: 10.1021/ct300307c.

2. Kungwan, N.; Plasser, F.; Aquino, A. J. A.; Barbatti, M.; Wolschann, P.; Lischka, H. "The effect of hydrogen bonding on the excited-state proton transfer in 2-(2'-hydroxyphenyl)benzothiazole: a TDDFT molecular dynamics study." *Physical Chemistry Chemical Physics*, **2012**, *14*, 9016–9025.

3. Plasser, F.; Barbatti, M.; Aquino, A. J. A.; Lischka, H. "Electronically excited states and photodynamics: a continuing challenge." *Theoretical Chemistry Accounts*, **2012**, *131*, 1073.

4. Plasser, F.; Lischka, H. "Semiclassical dynamics simulations of charge transport in stacked π-systems." *Journal of Chemical Physics*, **2011**, *134*(3), 034309.

5. Plasser, F.; Barbatti, M.; Aquino, A. J. A.; Lischka, H. "Excited-state diproton transfer in [2,2'-bipyridyl]-3,3'-diol: the mechanism is sequential, not concerted." *The Journal of Physical Chemistry A*, **2009**, *113*(30), 8490–8499.

6. Aquino, A. J. A.; Plasser, F.; Barbatti, M.; Lischka, H. "Ultrafast excited-state proton transfer processes: energy surfaces and on-the-fly dynamics simulations." *Croatica Chemica Acta*, **2009**, *82*(1), 105–114.

7. Plasser, F.; Aquino, A. J. A.; Lischka, H. "The UV absorption spectrum of

alternating DNA duplexes - analysis of excitonic and charge transfer interactions" *Journal of Physical Chemistry A*, **2012**. submitted for publication.

8. Plasser, F.; Granucci, G.; Persico, M.; Pittner, J.; Lischka, H. "Surface hopping dynamics using a locally diabatic formalism: charge transfer in the ethylene dimer cation and excited state dynamics in the 2-pyridone dimer" *Journal of Chemical Physics*, **2012**. submitted for publication.

9. Lumpi, D.; Horkel, E.; Plasser, F.; Lischka, H.; Fröhlich, J. "Synthesis, spectroscopy and computational analysis of photoluminescent bis(aminophenyl)-substituted thiophene derivatives" *Journal of Physical Chemistry A*, **2012**. submitted for publication.

10. Plasser, F.; Pasalic, H.; Gerzabek, M. H.; Libisch, F.; Reiter, R.; Müller, T.; Burgdörfer, J.; Lischka, H. "The Multiradical Character of One- and Two-Dimensional Graphene Nanoribbons" in preparation.

11. Georgieva, I.; Plasser, F.; Aquino, A. J. A.; Lischka, H. "Theoretical (MRCIS) study of intramolecular charge transfer excited state process in 4-(Dimethylamino)benzonitrile with inclusion of solvent effects" in preparation.

12. Panda, A. N.; Burghardt, I.; Plasser, F.; Aquino, A. J. A.; Lischka, H. "The effects of torsions on the excited states of phenylene-vinylene oligomers" in preparation.

13. Daily, A.; Shtepani, S.; Plasser, F.; Windus, T. L.; Hase, W. L.; Lischka, H. "Benchmark Calculations on the Lowest Electronic Excitations in Oligophenylenevinylenes" in preparation.

14. Ramert, A.; Plasser, F.; Lischka, H. "The Rydberg states of morpholine derivatives - a computational study" in preparation.